Precision Higgs Coupling Measurements in $H \to WW^* \to l\nu l\nu$ Final State with the ATLAS Detector at the LHC

by

HEE YEUN KIM

Presented to the Faculty of the Graduate School of
The University of Texas at Arlington in Partial Fulfillment
of the Requirements
for the Degree of

DOCTOR OF PHILOSOPHY

THE UNIVERSITY OF TEXAS AT ARLINGTON

May 2015

To my family

ACKNOWLEDGEMENTS

I started this journey five and a half years ago for the satisfaction of my passion to physics, but I would not have been able to carry out taking any further steps without the people around me.

My advisor, Dr. Jaehoon Yu, has given me the advice and guidance needed to move forward through all these years. He gave me a chance and the courage to pursue my dream and supported me to spread my wings for the new world. I learned many lessons to be successful not only in this profession but also in life. This valuable advice led me finding the right attitude toward questions as a physicist and as a good human being.

I would like to thank UTA physics department and the High Energy Physics (HEP) group for all the support throughout this journey. Dr. Alex Weiss and Dr. Kaushik De who lead the department and the group, respectively, have my sincere gratitude for their generous support for me. My academic advisors, Dr. Asok Ray and Dr. Qiming Zhang have helped me very much to maintain my academic career. Dr. Ray, I miss your quantum classes and I will remember you. I appreciate Dr. Andy White, Dr. Chris Jackson, Dr. Sangwook Park and Dr. Biagio Di Micco for serving on my defense committee and for their valuable opinions for the defense and dissertation.

I want to thank Giulio Usai, Justin Griffiths and all other postdocs at UTA HEP group who walked along with me through out this long journey. Justin, you opened a door for me to the world of programming and trained me to perform what I needed to do. I know Giulio is very patient to wait for me to understind Tile calorimeter in ATLAS and

play my role in MobiDICK team in ATLAS. My thanks also goes to my classmates at UTA in the past and present, Smita, Last, Daniel, Harsha, Prasad, Ian, John, Carlos, Kapil, Sunil and many others, the time with you was incredibly fun and a blessing.

I would like to extend my fullest gratitude to my colleagues in HSG3 group at CERN; Biagio, Aaron, Corrinne, Tatsuya, Nikolina, Jonathan, Magda, Cecilia, Li, Tae, Olivier and so many others. Without their help, I would not have been able to do what I have done. Aaron, you helped me to survive in the statistics world. Corrinne, Tatsuya and Olivier, special thanks to you for leading the HSG3 group and for cooperating on my work in the long process.

I would like to give my heartfelt thanks to Biagio without whom I could not have accomplished all my work. He was my essential mentor for the research with unlimited energy and help during my residence at CERN. He even flew over to UTA to serve on my defense committee despite a long-distance trip from Rome and a rare Texas ice storm. Biagio, I was very happy when I worked with you, and thank you very much for being there with me. You lifted me up and gave me the strength and the confidence to stand on my own.

My innermost thanks goes to my family. My husband, Yong Seon, I confess that I owe you a huge debt of gratitude for your love and support. It is never easy to give up all your time and effort for my dream. I still remember what you told me when we left for CERN three years ago, that I just needed to think about what I wanted to do and keep going. I know you always stand up for me, and it gave me the strength to complete this long journey.

My deepest gratitude also goes to my parents. There is no way I would be able to repay their patience and support coming from the unconditional love for me. I really appreciate what they have done for me. Thanks to their faith in me, they made me to realize my dream. I would like to thank my sister and brother as well, for their trust in me

and for keeping our family together in Korea. I would like to express my deep respect to my parents-in-law. Without their understanding, I could not have made this happen.

And my son, Ryan. I ran this journey for my dearm but did not ask if you were willing to take all these adventures. Your mom is very happy and thanks you that you adapt yourself very well to new environments. My only wish for you is being healthy and happy. I really appreciate this precious chance to meet you as my son in this life.

The greatest thing I have ever learned from this long journey is how much I am loved, and it gave me a strong will to overcome all obstacles that I could face in my life. I will remember this journey throughout my life.

March 5, 2015

ABSTRACT

Precision Higgs Coupling Measurements in $H \to WW^* \to lvlv$

Final State with the ATLAS Detector at the LHC

Hee Yeun Kim, Ph.D.

The University of Texas at Arlington, 2015

Supervising Professor: Dr. Jaehoon Yu

The Standard Model (SM) is a gauge theory that describes the fundamental particles of matter and the forces between these particles. It has been tested to a very high precision in the past several decades, except for the observation of the Higgs particle, because of a ramification of the Higgs mechanism. After the discovery of the Higgs particle in July 2012, at the Large Hadron Collider (LHC) at the European organization for Nuclear Research (CERN), subsequent studies have been focused on confirming whether the newly discovered particle is consistent with the SM Higgs, in particular its spin and its couplings strengths. In this thesis, the Higgs coupling properties are measured using $H \to WW^* \to \ell\nu\ell\nu$ final state. The $H \to WW^* \to \ell\nu\ell\nu$ channel has a large branching ratio, thus it provides a large amount of Higgs signal and more precise Higgs property measurements. The overall significance of Higgs particle observation in this channel is 6.1σ while the expected significance is 5.8σ at the mass $m_H = 125.36$ GeV. The overall signal strength is measured to be $\mu = 1.09\ ^{+0.23}_{-0.21}$ while $\mu_{\mathrm{ggF}} = 1.02\ ^{+0.29}_{-0.26}$ for the gluon-gluon fusion and $\mu_{\mathrm{VBF}} = 1.27\ ^{+0.53}_{-0.45}$ for the vector boson fusion production mode. The results of the signal strength are used to measure the Higgs couplings to fermions and to gauge bosons under

the SM Higgs hypothesis. The measured relative Higgs coupling strength to fermions is $\kappa_F = 0.93^{+0.32}_{-0.23}$ and the one to bosons is $\kappa_V = 1.04 \pm 0.11$. This study also presents the measured inclusive cross-sections for thegluon-gluon fusion (ggF) and the vector boson fusion (VBF) production modes as well as the fiducial cross-sections of a ggF production mode of $H \to WW^* \to \ell\nu\ell\nu$.

TABLE OF CONTENTS

LIST OF ILLUSTRATIONS

LIST OF TABLES

CHAPTER 1

Introduction

The Standard Model (SM) [1] is a gauge theory that describes the fundamental particles of matter and the forces between these particles. It has been tested to a very high precision in the past several decades, except for the Higgs mechanism [2]. After the Higgs discovery [3] in July 2012 at the Large Hadron Collider (LHC) [4] at the European Organization for Nuclear Research (CERN) [5], subsequent Higgs particle studies focus on the measurement of its properties, including the spin and coupling strengths to determine the nature of the discovered particle.

In this thesis, the Higgs coupling property measurements using $H \to WW^* \to \ell\nu\ell\nu$ final state are presented. The $H \to WW^* \to \ell\nu\ell\nu$ channel has a larg branching fraction and provides the largest amount of signal among the final states for more precise Higgs property measurements. This study is divided into sub-categories to optimize signal to backgrounds ratio. The results of these sub-analyses are combined and to extract the signal yield the Profile Likelihood method [6, 7] is used. The results of the signal yield are used to measure the Higgs coupling strength to fermions and gauge bosons under the SM Higgs hypothesis. The results are interpreted as measurements of the Higgs coupling constants to fermions and weak bosons. This study also measures the inclusive cross-sections for the gluon-gluon fusion (ggF), the vector boson fusion (VBF) production modes and the fiducial cross-sections of a ggF signal region in $H \to WW^* \to \ell\nu\ell\nu$.

Chapter 2 discusses the theory behind the Higgs mechanism and the Higgs study at the LHC, followed by an overview of the apparatus in chapter 3. Chapter 4 explains how the major physical objects used in this analysis are reconstructed and selected. Chapter 5

describes the statistical concepts and the statistical treatments used in this study. Chapter 6 and 7 present details of the $H \to WW^* \to \ell\nu\ell\nu$ analysis and the results of coupling strength and cross section measurements, followed by conclusions in chapter 8.

CHAPTER 2

The Standard Model of Particle Physics

The Standard Model (SM) [1] is the gauge theory which describes the fundamental particles and their interactions, with the exception of gravity. The SM consists three generations of leptons and quarks and their force mediators (gauge bosons) as shown in Fig 2.1. This model has been well adopted to explain the particle physics world, however, the mechanism by which these particles have mass was not known. In 1964, several theoretical particle physicists, including P. Higgs and F. Englert, suggested a brilliant idea to explain this. This theory has been known as the Higgs mechanism [2] which introduced a new particle called the Higgs boson.

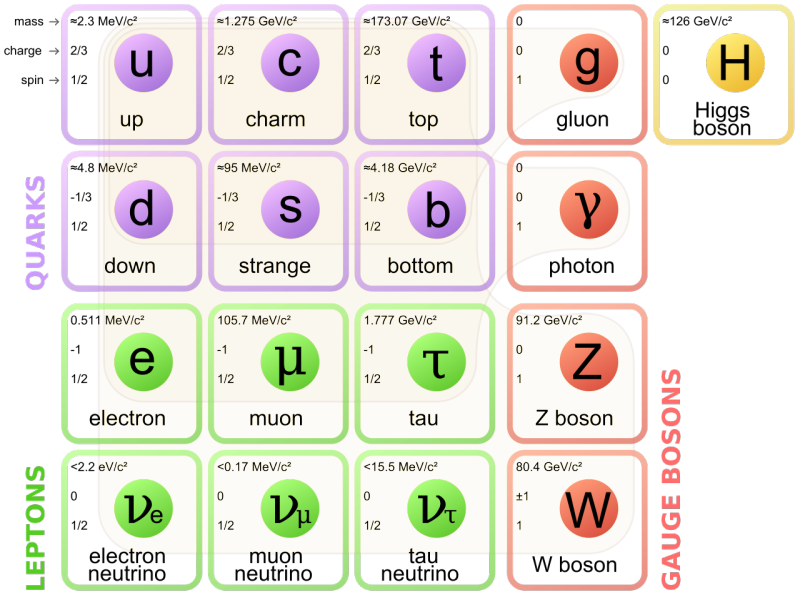

Figure 2.1: The Standard Model of elementary particles, with the three generations of matter, gauge bosons in the fourth column, and the Higgs boson [8].

For nearly 50 years, experimental particle physicists had been looking for this particle, and finally, in 2012, the LHC at CERN claimed the discovery of a scalar particle that appears consistent with the SM Higgs boson.

The SM is built on the following gauge symmetry

$$SU(3) \times SU(2) \times U(1) \tag{2.1}$$

with $SU(3)$ representing the strong interaction of quantum chromodynamics (QCD) and $SU(2) \times U(1)$ corresponds to the electroweak interaction. The gauge symmetry is broken in the electroweak interaction and gauge bosons acquire mass through the Higgs mechanism.

2.1 Fermions and Gauge Bosons

Fermions are spin 1/2 particles and are divided into two different categories, quarks and leptons. Quarks come in two types, the up-type and its corresponding down-type. The up-type quarks are up (u), charm (c) and top (t), and the down-type quarks are down (d), strange (s) and bottom (b). Leptons also have two types, charged leptons and neutral leptons. The charged leptons are electron (e), muon (μ) and tau (τ) and the neutral leptons correspond to each charged lepton, electron neutrino (ν_e), muon neutrino (ν_μ) and tau neutrino (ν_τ). Quarks have fractional charges, +2/3 for the up-type and -1/3 for the down-type, while all the charged leptons have charge -1. Each of all quarks and leptons has its own anti-particle that has the same mass and spin properties but opposite charge (such as positron ($+e$) for the electron ($-e$)).

Gauge bosons are force carriers that mediate the interactions between fermions, and their spins are 1. Gluons mediate the strong interaction that acts on quarks. The strong interaction is described by QCD in $SU(3)$ gauge group. Photons meditate the electromagnetic force while $W^\pm$ and Z bosons are responsible for the weak interaction. The unification

of the electromagnetic and the weak interactions is described by $SU(2) \times U(1)$. The gluon and the photon have no electrical charge and are massless while the $W^{\pm}$ and Z bosons have charges ± 1 and 0, respectively.

2.2 The Higgs Mechanism

The Higgs mechanism [2] describes how fermions and gauge bosons obtain masses. This mechanism has been introduced and has been developed more than five decades ago by several theorists including P. Higgs and F. Englert. In 2012, the theory finally was proved experimentally through the discovery of a Higgs particle at the CERN. P. Higgs and F. Englert were awarded the 2013 Nobel Prize in physics for their discovery of this mechanism.

The Higgs mechanism begins with the concept of spontaneous symmetry breaking. When we write a Lagrangian that is invariant under the $\phi \rightarrow -\phi$ transformation, the Lagrangian can take the form of a complex $\lambda\phi^4$, as follows. Note that following explainations are developed under a toy model for understanding of how the Higgs mechanism works.

$$L = T(\phi) - V(\phi) = \partial_\mu \phi \partial^\mu \phi - m^2\phi^2 + \lambda\phi^4 \tag{2.2}$$

As seen in Eq. 2.2, there are only even powers and even derivative terms, thus, it does not changed under the $\phi \rightarrow -\phi$ transformation. However, when we consider the minimum potential energy, this Lagrangian does not satisfy the same symmetry because $\phi = 0$ is not the actual minimum anymore. In Eq. 2.2, the first term is the kinematic energy terms, and the second and third terms are the potential energy terms. The minimum potential energy is at the point where its derivative with respect to ϕ is 0.

$$\frac{\partial V}{\partial \phi} = 0 \tag{2.3}$$

A good example of this is the Lagrangian under chiral symmetry in which the left-handed and right-handed parts of Dirac fields transform independently as follows

$$L = \frac{1}{2}(\partial_\mu \phi)^2 - \frac{1}{2}m^2\phi^2 - \frac{1}{4}\lambda\phi^4 \tag{2.4}$$

where the potential energy term is $V(\phi) = \frac{1}{2}m^2\phi^2 + \frac{1}{4}\lambda\phi^4$. Its derivative is

$$\frac{\partial V}{\partial \phi} = m^2\phi + \lambda\phi^3 = \phi(m^2 + \lambda\phi^2). \tag{2.5}$$

Two solutions can be obtained to meet this condition. One solution is $\phi = 0$ when $m^2 > 0$. The ϕ^4 term is the self-coupling term with the coupling constant λ. The other solution can be obtained from $m^2 + \lambda\phi^2 = 0$, where the solutions are

$$\phi = \pm\sqrt{\frac{-m^2}{\lambda}} = \pm v. \tag{2.6}$$

For this case, the minimum potential energy is not at $\phi = 0$ but at $\phi = \pm v$, that means, the lagrangian is no longer invariant under $\eta \rightarrow -\eta$ when it is expressed as a function of η through the substitution $\phi = \phi_0 + \eta$. This phenomenon is due to the shape of the Higgs potential that resembles a Mexican hat [9] as shown in Fig 2.2. These two solutions are illustrated on the left-hand side in Fig 2.2.

Since we now have the real minimum at the solution points in Eq. 2.6, the $\phi = 0$ point is now unstable. If there is a particle at this point, it would hardly stay but would rather move along the slope in any direction toward the real minima $\phi = \pm v$ under very little perturbation. Now adding the fluctuation term to the solution, we can write the solution as

$$\phi(x) = \pm v + \eta(x). \tag{2.7}$$

If we only takes the positive solution, $\phi(x) = v + \eta(x)$, the Lagrangian can be re-written

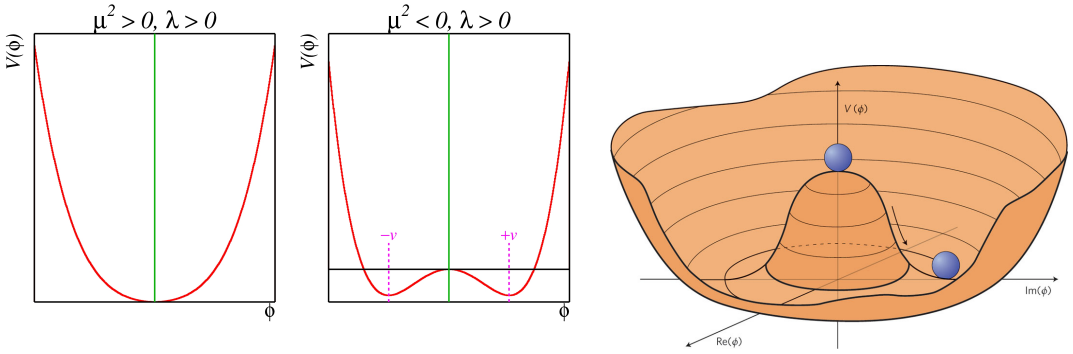

Figure 2.2: Solutions for the given Lagrangian in Eq.2.5, a simple solution when $m^2 > 0$ is $\phi = 0$ (left) and two solutions are available as given in Eq.2.6 when $m^2 < 0$ (middle). These solution are for the spontaneous symmetry breaking and called the "Mexican Hat" that shown in the right of the figure (right).

$$L = \frac{1}{2}(\partial_\mu \eta)^2 - \lambda v^2 \eta^2 - \lambda v \eta^3 - \frac{1}{4}\lambda \eta^4 \tag{2.8}$$

This is the final Lagrangian of the spontaneous symmetry breaking that consists of 4 terms: the kinematic energy term $\frac{1}{2}(\partial_\mu \eta)^2$, the mass term $\lambda v^2 \eta^2$, and the third and fourth terms are for the coupling terms for three and four legs, respectively.

The Higgs mechanism is one example of a spontaneous symmetry breaking of the non-abelian model that does not commute any of two elements in the group. Consider a complex scalar field ϕ that interacts with electromagnetic fields and also coupled to itself. The Lagrangian for this case can be written as

$$L = -\frac{1}{4}(F_{\mu\nu})^2 + \mid D_\mu \phi \mid^2 - V(\phi) \tag{2.9}$$

where, $D_\mu = \partial_\mu - iqA_\mu$. Since the Lagrangian is invariant under the $U(1)$ transformation, the solution is given as the $\phi \rightarrow e^{i\alpha(x)}$ and the gauge field $A_\mu(x) \rightarrow A_\mu(x) + \mathrm{d}_\mu \theta$ is introduced to maintain the invariance of the solution in the field. The chosen potential form is

$$V(\phi) = \frac{m^2}{2v}(\phi^* \phi - v^2)^2. \tag{2.10}$$

Based on Eq. 2.6, $\phi = \pm\nu$ is the solution for the vacuum state. However, it can be perturbed by the real field $h(x)$. Thus the solution for minimum potential is given as

$$< \phi >= \nu + \frac{h(x)}{\sqrt{2}}. \tag{2.11}$$

The real field $h(s)$ is the Higgs field. Then the potential energy is

$$V = m^2h^2 + \frac{m^2h^2}{2\nu^2}(\sqrt{2}\nu h + \frac{h^2}{4}). \tag{2.12}$$

The $D_\mu = \partial_\mu + iqA_\mu$ with given solution , $D_\mu\phi$, is now

$$D_\mu\phi = (\partial_\mu - iqA_\mu)(\nu + \frac{h(x)}{\sqrt{2}}) = \frac{1}{\sqrt{2}}\partial_\mu h - iq\nu A_\mu - \frac{iqh}{\sqrt{2}}A_\mu. \tag{2.13}$$

The the term $\mid D_\mu\phi \mid^2$ in Eq. 2.9 becomes

$$D_\mu\phi D^\mu\phi = \frac{1}{2}\partial_\mu h\partial^\mu h + q^2\nu^2A_\mu A^\mu + \sqrt{2}q^2\nu hA_\mu A^\mu + \frac{q^2h}{2}A_\mu A^\mu. \tag{2.14}$$

Then the Lagrangian becomes

$$\begin{aligned} L &= -\frac{1}{4}(F_{\mu\nu})^2 + \mid D_\mu\phi \mid^2 - V(\phi) \\ &= \frac{1}{2}\partial_\mu h\partial^\mu h + q^2\nu^2A_\mu A^\mu + \sqrt{2}q^2\nu hA_\mu A^\mu + \frac{q^2h}{2}A_\mu A^\mu \\ &- m^2h^2 - \frac{m^2h^2}{2\nu^2}(\sqrt{2}\nu h + \frac{h^2}{4}) - \frac{1}{4}(F_{\mu\nu})^2. \end{aligned}$$

This is the Lagrangian for the Higgs mechanism. Each term in this Lagrangian represents a specific physics interaction. The first terms to notice are is the terms that include the Higgs field h(x).

$$L^h_{free} = \frac{1}{2}\partial_\mu h\partial^\mu h - m^2h^2. \tag{2.15}$$

These terms look similar to a Klein-Gordon equation with a scalar Higgs field $h(x)$ and a Higgs mass $\sqrt{2}m$.

The gauge boson terms are:

$$L^B_{free} = -\frac{1}{4}(F_{\mu\nu})^2 + q^2\nu^2 A_\mu A^\mu. \tag{2.16}$$

The first term of L^B_{free} is the kinematic energy which is present for massless gauge bosons regardless of symmetry breaking. However, by adopting the real field $h(x)$, this solution gets a perturbation term, $\nu \rightarrow \nu + h(x)$. Hence it introduces a mass term for the gauge bosons, $q^2\nu^2 A_\mu A^\mu$. Then the mass is $M = \sqrt{2}q\nu$.

The rest of the equation corresponds to the coupling. The Higgs self–coupling term and Higgs-gauge field coupling term are give as follows :

$$L^h_{self} = \frac{m^2h^2}{2\nu^2}(\sqrt{2}\nu h + \frac{h^2}{4}) \tag{2.17}$$

$$L^{gauge}_{coup} = \sqrt{2}q^2\nu h A_\mu A^\mu + \frac{q^2h}{2}A_\mu A^\mu = q^2 A_\mu A^\mu(\sqrt{2}\nu h\frac{h}{2}). \tag{2.18}$$

The Higgs boson couples most strongly to the most massive SM particles.

2.3 Higgs boson production at the LHC

Higgs production at the LHC is dominated by the ggF process, which is induced via the top-quark loop. The second largest production mode is the VBF in that two vector bosons are initially produced from the interaction with two initial state quarks and are found to produce the Higgs particle. The associated vector boson mode (VH) is also a part of the LHC Higgs production, through $q\bar{q} \rightarrow V^* \rightarrow VH$ Bremsstrahlung-like process. Smaller production modes can also be exploit, like the $t\bar{t}H$ through $gg/q\bar{q} \rightarrow t\bar{t}$ process. The Feynman diagrams for these are presented in Fig 2.3. The corss sections of different production modes at the Higgs mass 125 GeV [10] are summarized in Table 2.1 and are also seen in Fig 2.4. The Higgs particle decays to many different final states. The $H \rightarrow WW^*$ channel is a good candidate channel to observe the Higgs particle thanks to its

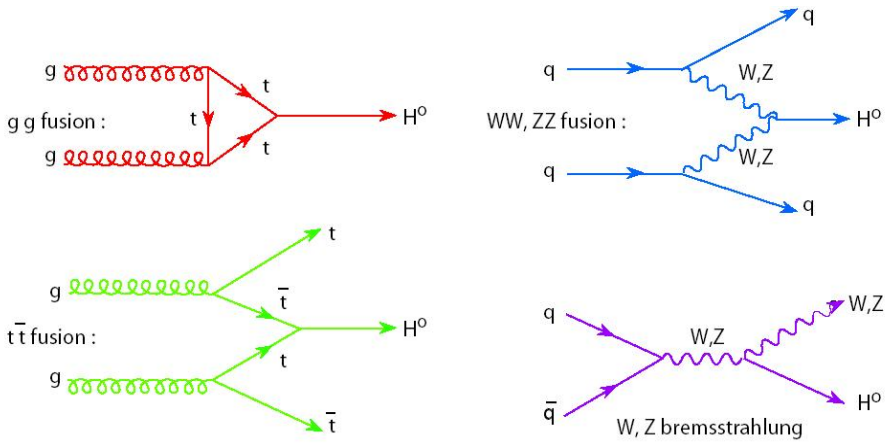

Figure 2.3: Feynman diagrams for various Higgs production modes at the LHC.

high branching ratio. As seen in Fig 2.5, it is ranked on the second largest following the $b\bar{b}$ around $m_H = 125$ GeV.

Table 2.1: Summary of the cross sections of major production modes in the LHC for the 7 and 8 TeV at the Higgs mass 125 GeV [10].

cross section (σ)	7 TeV	8 TeV
ggF	15.13 pb	19.3 pb
VBF	1.2 pb	1.6 pb
VH	0.9 pb	1.1 pb
$t\bar{t}H$	0.09 pb	0.1 pb

Discovery of the Higgs Particle

On the 4th of July 2012, CERN announced the discovery of a Higgs-like particle. This was a historic moment for particle physics because the SM received its final missing piece of the puzzle to complete. Two major experiments at the LHC, A Torodial LHC Apparatus (ATLAS) and Compact Muon Solienoid (CMS), performed independent searches and observed the Higgs signal in the same Higgs mass range [3, 11, 12]. The results from these

two experiments were cross-checked to ensure the results. The mass measured through the ATLAS detector is $m_H = 126.0$ GeV $\pm 0.4(stat.) \pm 0.4(sys.)$ while that of the CMS detector is $m_H = 125.3$ GeV $\pm 0.4(stat.) \pm 0.5(sys.)$.

Fig 2.6 shows the exclusion limits for the ATLAS and CMS SM Higgs boson searches [3, 11, 12] at the time, where a clear excess around 125 GeV forbid the ruling out of a Higgs particle.

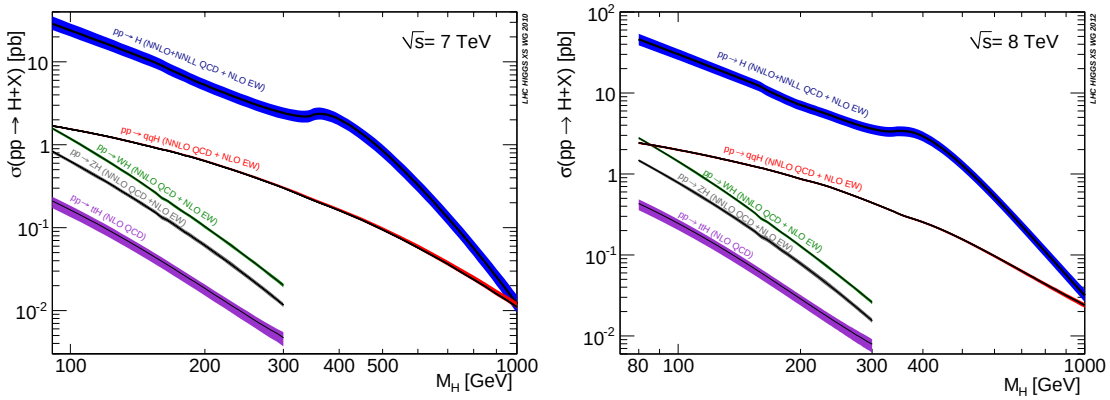

Figure 2.4: The Higgs cross section at the $\sqrt{s} = 7$ and 8 TeV center of mass energy in the LHC [10].

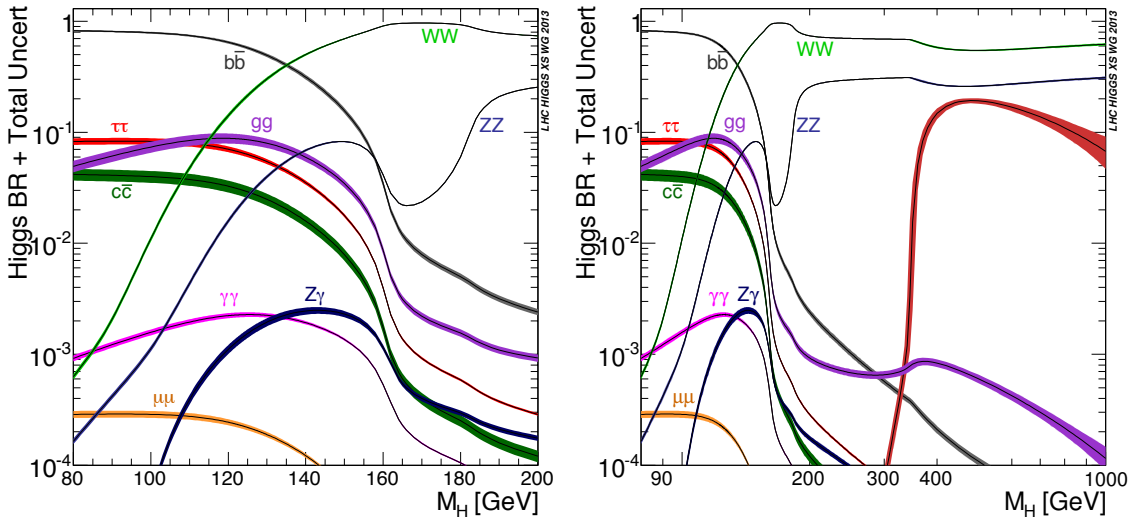

Figure 2.5: The Standard Model Higgs boson decay branching ratio at the low Higgs mass rage (left) and up to the high Higgs mass rage (right).

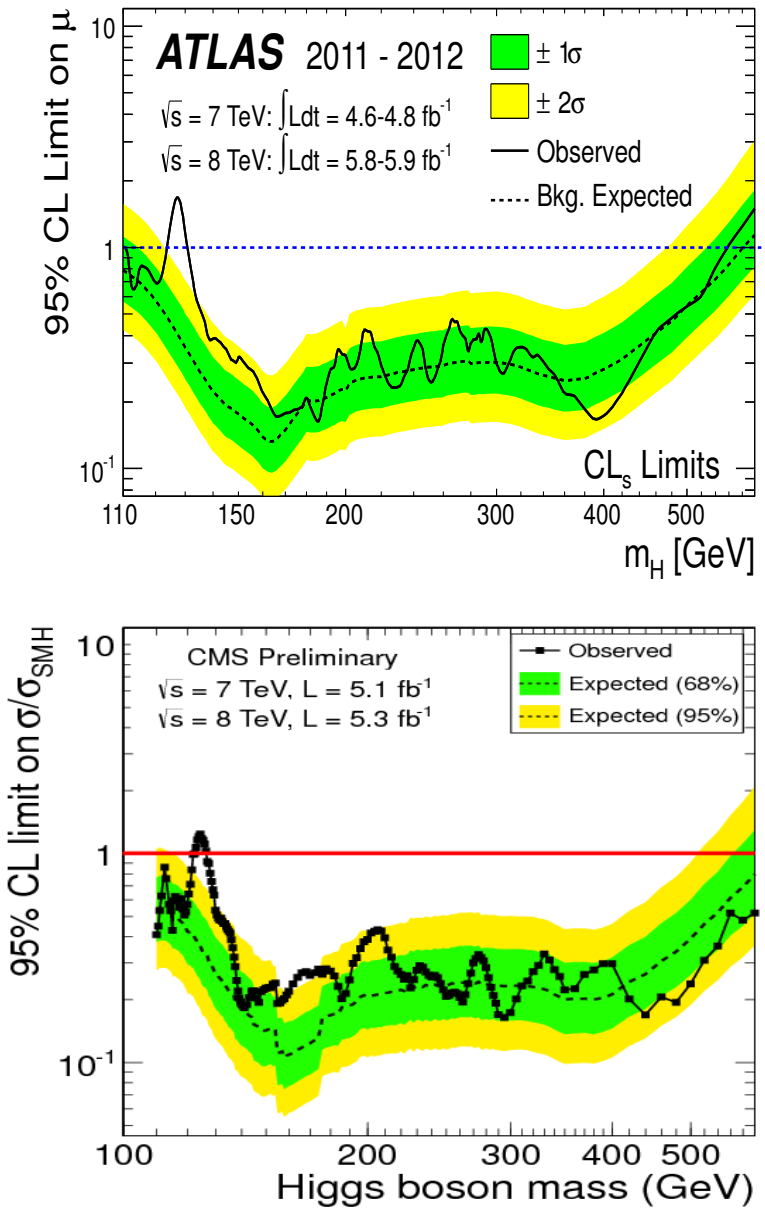

Figure 2.6: The exclusion limits (CLs) plots of the 2012 Higgs boson discovery from the ATLAS experiment and the CMS experiment in the LHC using $H \to ZZ \to 4\ell$ and $H \to \gamma\gamma$ final states as well as $H \to WW^* \to \ell\nu\ell\nu$.

CHAPTER 3

The Apparatus

3.1 The Large Hadron Collider

The Large Hadron Collider (LHC) is designed to supply high energy collisions for particle physics experiments. It uses the existing 26.7 km tunnel of the Large Electron-Positron (LEP) collider that was installed and used from 1989 to until 2000 [4] by the European Organization for Nuclear Research (CERN) [5]. The LHC started its operation in 2009 with low collision energy, at the center of mass energy ($\sqrt{s} = 900\,\text{GeV}$). Along the LHC beam circumference, there are 4 major detectors. Two general purpose detectors, A Toroidal LHC Apparatus (ATLAS) and Compact Muon Solenoid (CMS), and two special objective detectors, A Large Ion Collider Experiments (ALICE) for a quark-gluon plasma studies using heavy ion collisions and LHC-beauty (LHCb) for b-physics using low luminosity. The location of these detectors is shown in the Fig. 3.1. The LHC operated with a center of mass energy ($\sqrt{s}$) of 7 TeV in 2011 and 8 TeV in 2012. A tremendous amount of data has been collected by the detectors and ATLAS detected and analyzed 5.25 fb^{-1} of 7 TeV and 21.7 fb^{-1} of 8 TeV data.

The LHC uses protons extracted from hydrogen atoms to form beams and after a series of accelerations [4], these beams are injected into the LHC. The beam injection process accelerates the protons to have a desired energy through a sequence of accelerators in the injection chain. A linear particle accelerator, called Linac2, accelerates the protons to an energy of 50 MeV. Then the protons are injected to the Proton Synchrotron Booster (PSB) that boosts the proton to an energy of 1.4 GeV followed by the Proton Synchrotron (PS) where 1.7×10^{11} proton are grouped and accelerated up to an energy of 25 GeV.

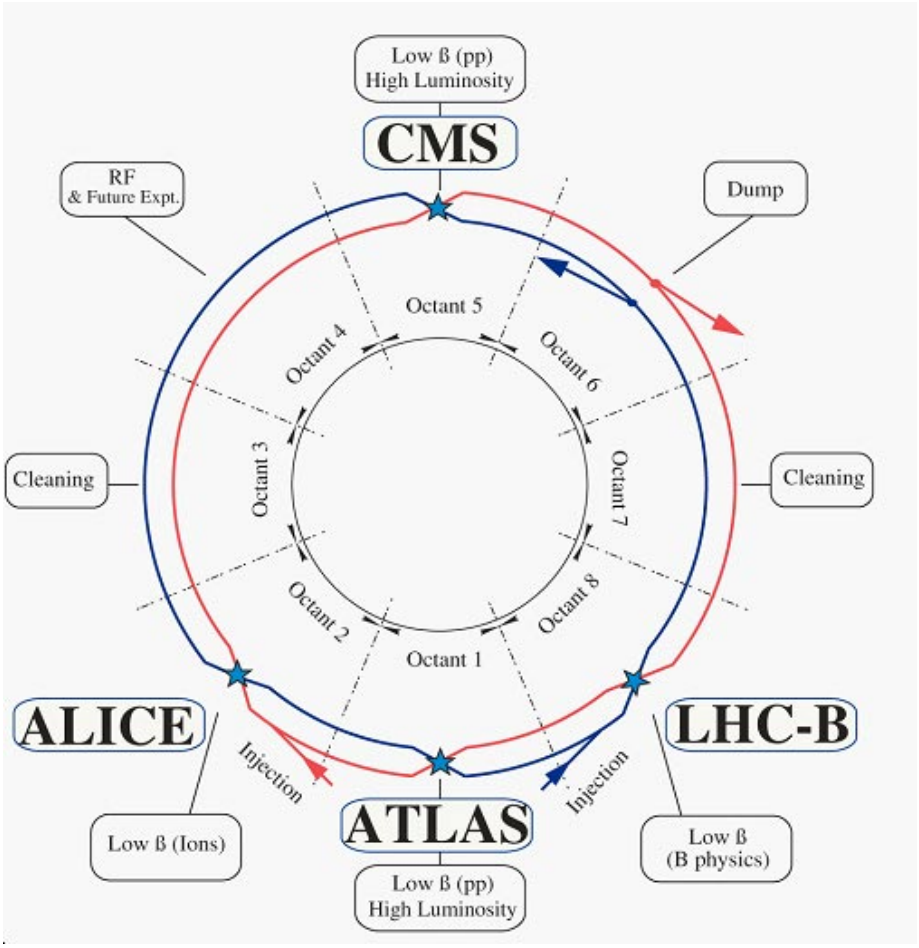

Figure 3.1: Schematics layout of the LHC [4].

Then, these proton are injected to the Super Proton Synchrotron (SPS) and are accelerated to an energy of 450 GeV. Protons are finally transferred to the two rings of the LHC both in a clockwise and anticlockwise direction. After another 20 25 min. the protons reach the desirable energy. Fig. 3.2 shows the injection chain.

As seen in Fig. 3.2, the LHC consists of eight octant sections. The four detectors are located each in a different octant, two of octant-sections are reserved for the cleaning and one section is for the Radio Frequency (RF) cavities and the last one section is for beam dumping. The RF system in the LHC is in used for accelerating protons and for increasing luminosity in collision. The RF cavities generate a longitudinal voltage so

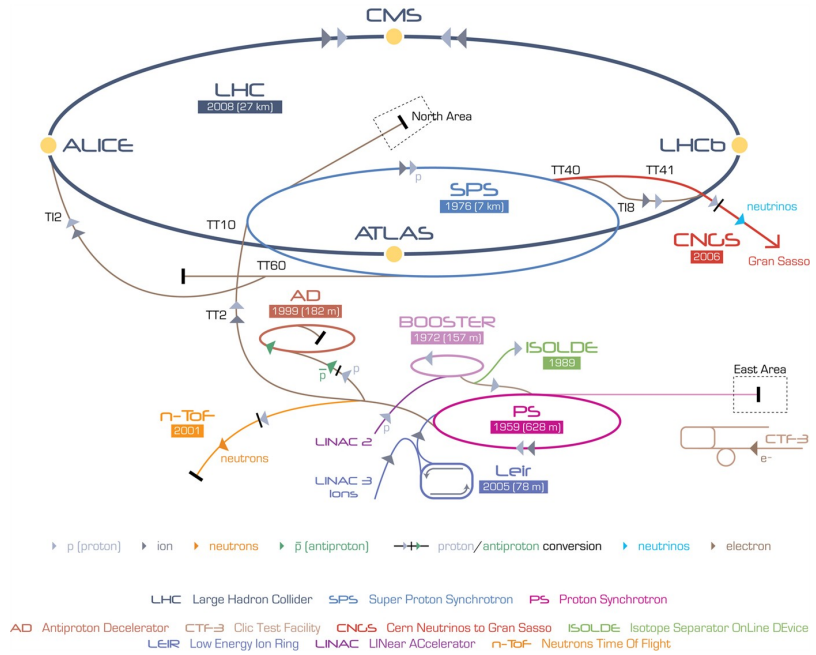

Figure 3.2: The sequence layout of LHC beam injection procedure [4].

the entering protons experience an acceleration, so that the particle sees an accelerating voltage at the gap, and the voltage then cancels out as the particle goes around the rest of the machine [13]. Therefore, and oscillating voltage is applied to make protons always in the acceleration mode, to ensure that protons are always accelerated. The RF frequency must have an integer multiple of the revolution frequency, $f_{RF} = hf_{rev}$, which depends on the particles revolution frequency and hence its momentum. Therefore, the integer number h is

$$h = harmonic\ \ number = \frac{f_{RF}}{f_{rev}} = \frac{T_{rev}}{T_{RF}} = T_{rev} \cdot f_{RF} \tag{3.1}$$

where T_{rev} is the period of protons that is given as the length of LHC divide by the speed of particles, and the f_{RF} of the LHC is 400 MHz. Then, the harmonic number of LHC h is 35640. Protons are exactly in sync with the RF, thus, there are 35640 possible phases in the

RF and each proton bunch is synchronized with one phase, called buckets. However, not all the buckets are filled with proton groups but only 2808 buckets are filled with protons.

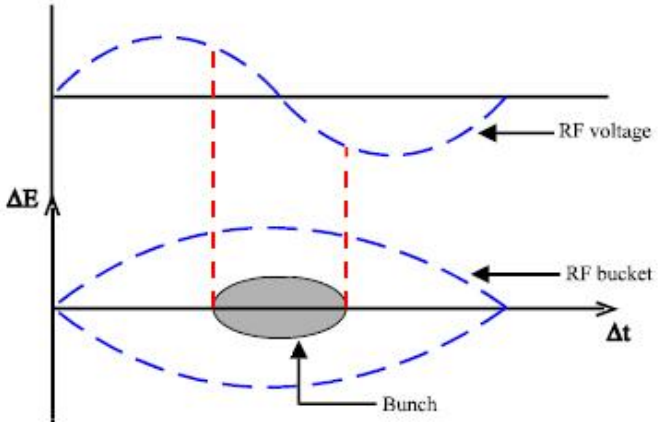

Figure 3.3: The RF bucket and bunch in LHC [13].

These filled RF buckets are called bunches, as shown in Fig. 3.3. Each bunch is separated by 2.5 *ns*, called as a bunch spacing and the distance between the bunches are 7.5 *m*.

The LHC is required to control the beam behavior while the protons travel through the LHC vacuum pipes. There are two behaviors to be controlled in order to maintain circulating beams with high beam intensity. One is a circular movement along with the beam pipes and the other one is a beam focusing. The LHC magnetic system consists of 1232 dipole and 392 quadruple magnets. Dipole magnets provide a magnetic field to sustain a circular path. According to the Lorentz force, the centripetal force F_c is

$$F_c = q \times v \times B \tag{3.2}$$

but also, the centripetal force, F_c

$$F_c = \frac{mc^2}{r} = \frac{E}{r} = 4 \times 10^{-10} N \tag{3.3}$$

so, the magnetic field of the dipole magnets is

$$B = \frac{F_c}{q \times v} = \frac{4 \times 10^{-10} N}{(1.6 \times 10^{-19} C) \times c} \approx 8.33 \ \ T \tag{3.4}$$

The dipole magnetic field is generated through the 160 superconducting cables that circulate each beam pipe with about 11800 A electric current applied on them. In addition to that, quadruple magnets are used to make beams to focus the beams. Protons moves along with circumference of the accelerator, their paths are not stay with the central trajectory. A pair of quadruple magnet systems work together to keep the protons bunched: the first quadruple focuses the beam width while the second system focuses the beam height. A diagram of the two magnet systems is in the Fig. 3.4.

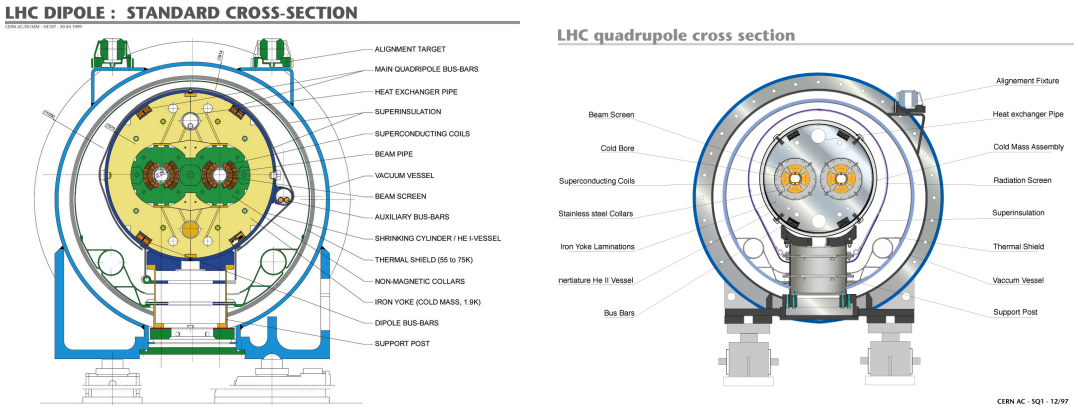

Figure 3.4: LHC di- (left) and quadru- (right) pole cross section [14, 15].

Positions of protons, then, are expressed with displacement from central path (x), and angle with respect to central path (x), as shown at the top in Fig. 3.5. The behavior of the protons are calculated with simple harmonic motion (SHM), thus the solution of the motion can be written:

$$x = Acos(\frac{\omega}{V}S + \phi) \quad , \quad x' = -A\frac{\omega}{V}sin(\frac{\omega}{V}S + \phi) \tag{3.5}$$

Therefore, this can be shown in a phase space plot: x *vs* x', as shown in the bottom of Fig. 3.5.

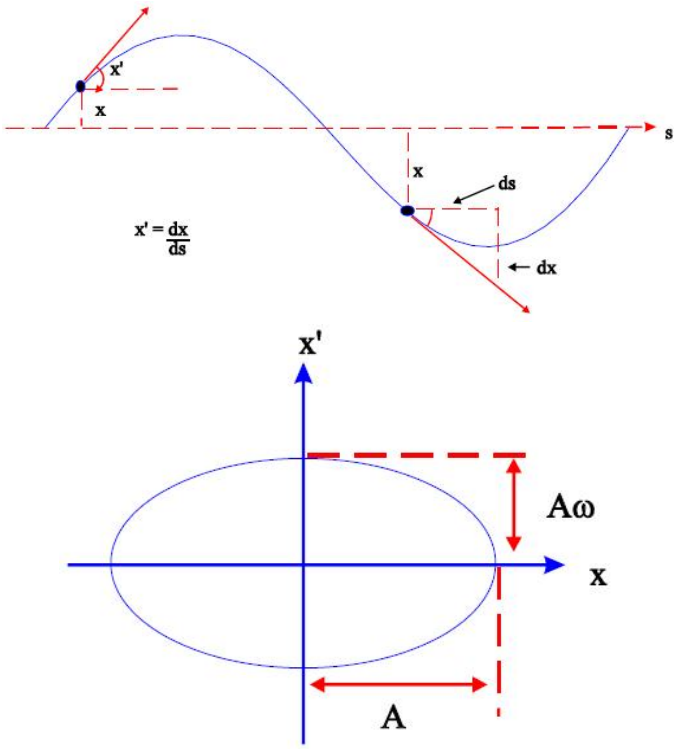

Figure 3.5: The position of protons along the beam line [13].

The particles moves along with the this phase space, say $k(s)$, with different amplitudes and different angles. Outside of $k(s) = 0$, no quadruple magnet force exerts. The general equation for transverse motion:

$$\frac{d^2x}{ds^2} + k(s) \cdot x = 0 \tag{3.6}$$

For the solution of Eq. 3.6, three new parameters are introduced, the emittance ε, the amplitude modulation $\beta(s)$ and the phase advance $\Psi(s)$. The ε is the transverse length of the phase space respect to x-axis and the $\beta(s)$ is the modulation of amplitude due to

the changing focusing strength. The $\Psi(s)$ is the phase advance depending on focusing strength. with these parameters the solution can be written as:

$$x = \sqrt{\varepsilon\beta(s)}\, cos(\Psi(s)+\pi) \quad , \quad x' = -\sqrt{\frac{\varepsilon}{\beta(s)}}\, sin(\Psi(s)+\pi) \tag{3.7}$$

Therefore, the bottom figure of Fig. 3.5 is expressed by follows :

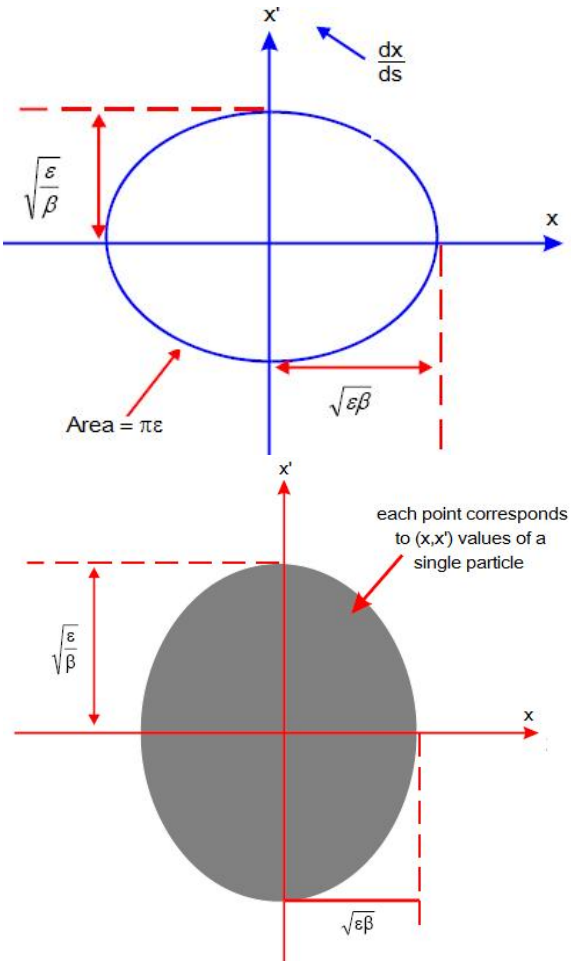

Figure 3.6: The position of protons along the beam line [13].

However, the actual emittance that is used in the real calculation, the emittance is area of the ellipse that contains a certain portion of the particles, i.e. 95 % of emittance that

has 95% particles, as shown in the bottom plot of the 3.6. Therefore, the beam dimension is $2\sqrt{\varepsilon\beta(s)}$, and the approximate cross section is $4\ \varepsilon\beta\ \ =\ \ 4\pi\sigma^2$. Therefore, the β is

$$\beta = \frac{\pi\sigma^2}{\varepsilon} \tag{3.8}$$

So, the β is about the width of the beam divided by the emittance. Therefore, the β is low, the beam is squeezed and it the β is high, the beam is wide and straight. The amplitude fraction at the interaction point, β^*, is defined the distance the focus point that the beam width is twice as wide as the focus point, as shown in Fig. 3.7. β^* is used instead of β.

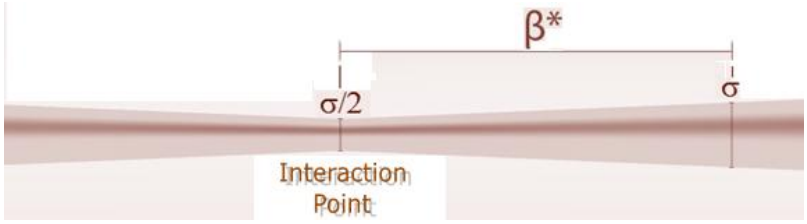

Figure 3.7: The illustration of the β^* [13].

3.1.1 Luminosity

The Luminosity is a measurement of the number of collisions that can be produced in a detector cm^2 per second. It is proportional with number of particles in a bunch and inversely proportion with the cross section which is a measurement of the probability that an events occurs.

$$L = \frac{f \cdot N^2}{4 \cdot \pi \cdot \sigma^2} = \frac{f \cdot\ N_1\ N_2}{4\pi\sigma_1\sigma_2} \tag{3.9}$$

where, N is number of protons and f is the bunches crossing frequency. The Luminosity can be written again with the relationship $\pi\ \sigma^2 = \varepsilon\ \beta$.

$$L = \frac{f\, N_1\, N_2}{4 \cdot \varepsilon \cdot \beta^*} \tag{3.10}$$

where $f = f_{rev} \cdot n_b \cdot F$. The f_{rev} is the revolution frequency and the n_b is the number of bunches in the LHC ring. Then, the Luminosity is

$$L = \frac{f_{rev}\, n_b\, N_1\, N_2}{4 \cdot \varepsilon \cdot \beta^*} \cdot F \tag{3.11}$$

F is the geometrical reduction rate depends on the injection angle of particles and the *r.m.s.* of bunch length. σ_* is the transverse RMS beam size at the IP.

$$\mathrm{F} = (1 + \left(\frac{\theta_c \sigma_z}{2\sigma^*}\right)^2)^{-1/2} \tag{3.12}$$

Equation 3.11 is the instantaneous luminosity, thus the cumulative luminosity over the running time is $\mathcal{L} = \int \mathrm{L}\ \mathrm{dt}$. The design luminosity was $10^{34} cm^{-2} \cdot s^{-1}$, we never have achieved this luminosity yet.

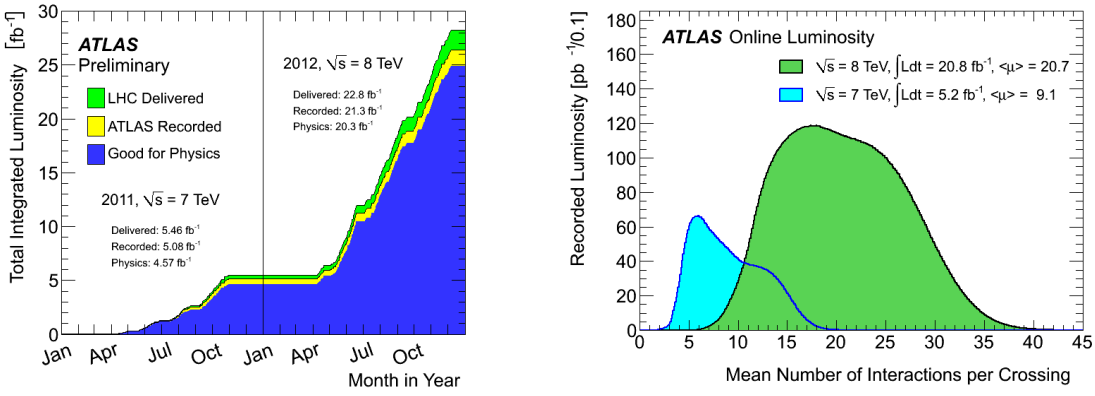

Figure 3.8: Total Integrated Luminosity and Data Quality in 2011 and 2012 (left) and Number of Interactions per Crossing (right) of the LHC [16].

The left figure in Fig. 3.8 shows the integrated luminosity that was collected in 2011 and 2012 by ATLAS (yellow), the data used for physics (blue), and the accumulated luminosity

delivered by the LHC (green), over the years. The average the number of collision in one bunch crossing (μ) is defined in equation 3.13

$$\mu = \frac{L\sigma_{inel}}{\mathrm{nf_{rev}}}. \tag{3.13}$$

where σ_{inel} is the inelastic cross section.

3.2 The ATLAS Detector

A Toroidal LHC Apparatus (ATLAS) is the one of the LHC general purpose detectors. The layout of ATLAS is shown in Fig 3.9. The substructures of ATLAS are the Inner Detector(ID) for vertex and track reconstruction, a Liquid Argon (LAr) Electromagnetic (EM) calorimeter for the electron/photon energy measurement, a tile and LAr hadronic calorimeters for the hardonic particle measurement and a muon spectrometer for the Muon tracking built with eight air-core magnet system in the barrel and the end-cap areas. In addition, there is a forward detector system for luminosity measurement.

The coordinate system of ATLAS is following the Fig 3.10. The origin of the ATLAS coordinate system follows that the z-axis is parallel with the beam direction, the x-axis points to the center of LHC and the y-axis points upward. The azimuthal angle ϕ is defined in the x-y plane and the polar angle θ is the angle between the beam axis and some vector originating at the origin. However, η is used in preference to θ since eta is a longitudinal boost invariant (assuming mass $<<$ E). The distance between objects also can be expressed by η and ϕ which is represented by ΔR, $\Delta R = \sqrt{\Delta\phi^2 + \Delta\eta^2}$. The x-y plane is the transverse plane to reflect the momentum, the energy and the missing energy. Often times energy, momentum, and mass is projected on the the transverse plane and is called: p_{T}, E_{T}, m_{T}, $E_{\mathrm{T}}^{\mathrm{miss}}$, etc. This is done since initially there is no momentum in the

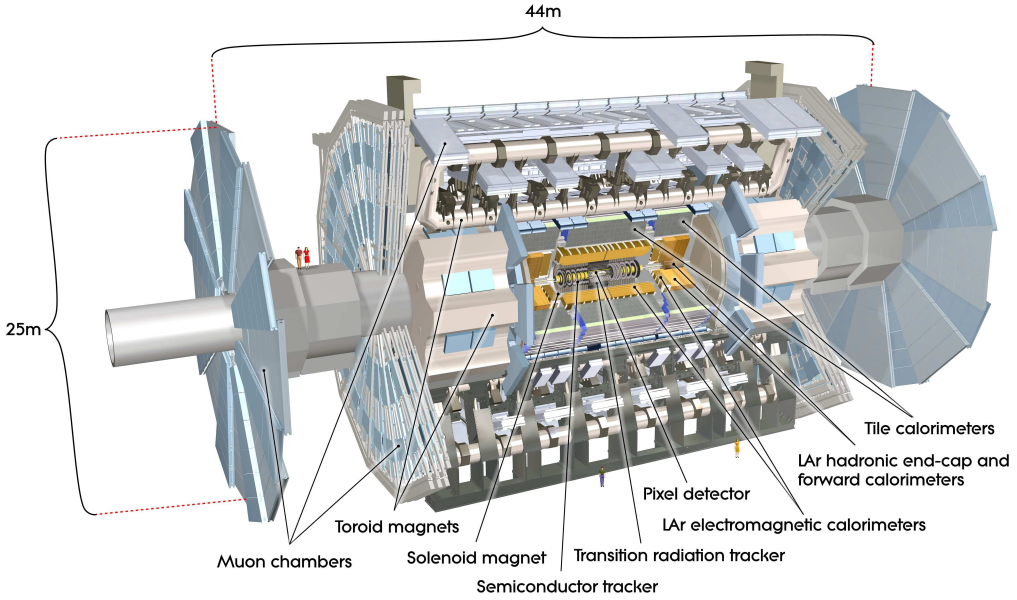

Figure 3.9: Cut-away view of the ATLAS detector. The dimensions of the detector are 25 m in height and 44 m in length. The overall weight of the detector approximately 7000 tonnes [17].

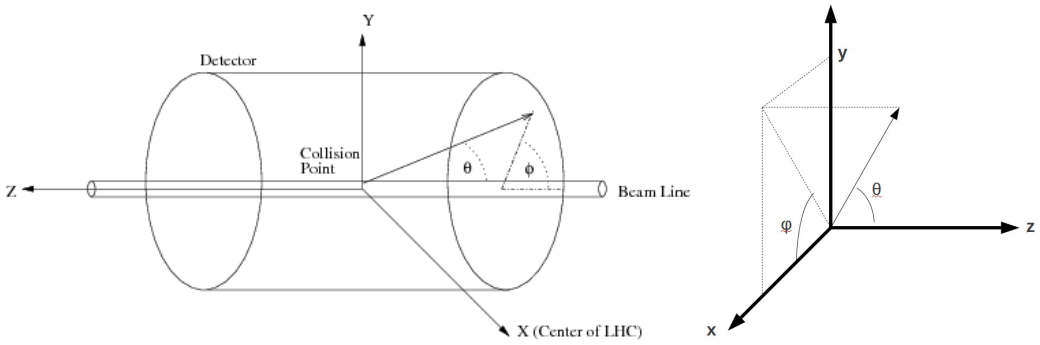

Figure 3.10: The ATLAS detector coordinate system. The z-axis is parallel with the beam line and the x-y plan is the transverse to the beam direction, where x-axis points to the center of the LHC and the y-axis is defined as pointing upward [17].

transverse beam prior to a collision. The detector is divided into two areas: A-side and C-side by the transverse plane at the Interaction point (IP).

3.2.1 Magnets

The ATLAS magnet system consists of two different types of magnets, a solenoid and a toroid. In Fig 3.11, the red cylindrical shape in the very inner range represents the a central solenoid (CS) which is aligned with the beam axis and provides a 2 T magnetic field to the inner detector. This magnets are located beneath the LAr EM calorimeter. The barrel toroid (BT) system located in the muon spectrometer (MS). Two end-cap toroids (ECT) are also within the muon spectrometer system. The BT and ECT are eight-fold azimuthal symmetry that surrounds the calorimeter system.

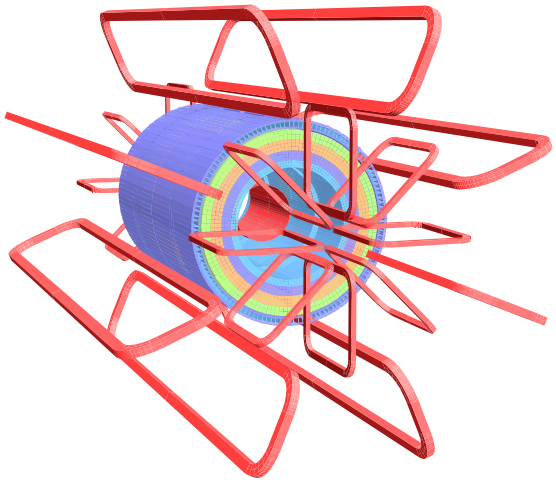

Figure 3.11: Geometry of magnet windings and tile calorimeter steel. The eight barrel toroid coils, with the end-cap coils interleaved are visible. The solenoid winding lies inside the calorimeter volume [17].

3.2.2 Inner Detector

The Inner Detector (ID) is 6.2 m $\times$ 2.1 m in the length (L)$\times$ radial distance (R) and is shielded by a 2 T solenoid field. It is configured three sub detector components, a pixel detector, a Silicon microstrip semi-Conduction Trackers (SCT), and a Transition Radiation Tracker (TRT). The pixel and the SCT are responsible for the momentum and the vertex

measurements, the electron identifications and the pattern recognition. The TRT is able to detect the transition radiation of passing particles. The spacial coverage of the ID is $|\eta| < 2.5$ while TRT covered $|\eta| < 2$.

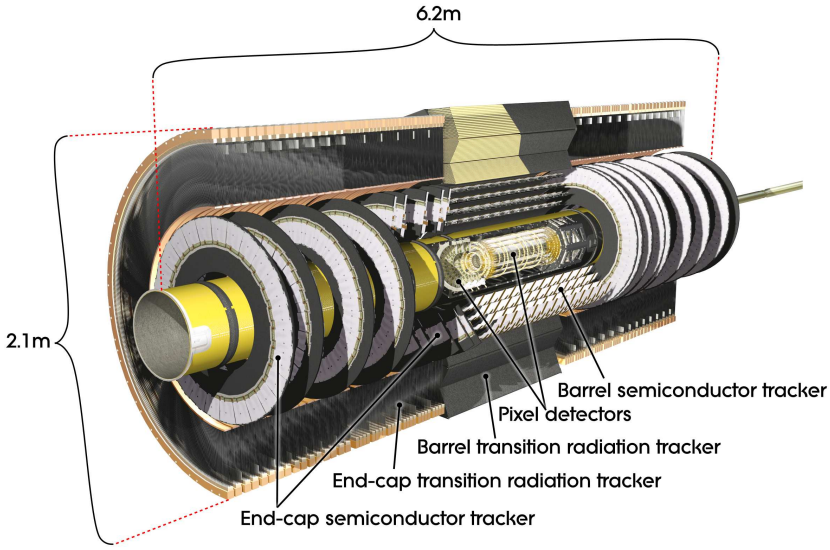

Figure 3.12: The inner detector schematics of ATLAS [17].

In the barrel area, the three pixel detector layers exist around the beam pipe, up to the most outer layers extending up to R = 122.5 mm and the four layers of SCT cover up to R = 514 mm after the pixel detector. The TRT in the barrel extends out to the R = 1082 mm. In the end-cap area, disk shape components are arranged in the perpendicular to the beam axis. Thus, the coverage of ID in the end-cap is different with the ones in the barrel area. Table 3.1 summarizes the main parameter of the ID and Fig 3.13 and 3.14 visualize the ID structure.

The pixel detector has the finest granularity with a minimum pixel size in R-$\phi \times z$ of $50 \times 400\,\mu m^2$. The intrinsic accuracy is R-$\phi \times z$ of $10 \times 115\,\mu m^2$ in both barrel and end-cap area. About 80.4 million readout channels are connected to the pixel detector. The pixel detector measures the track impact parameter d^0 and z^0, the transverse and longitudinal

Table 3.1: Main parameter of the inner detector system

Item	Position	Radial extension (mm)	$\|\eta\|$ coverage
Pixel	3 cylindrical layers (Barrel)	$50.5 < R < 122.5$	< 1.7
	2×3 disks (End-cap area)	$88.8 < R < 149.6$	1.7 - 2.5
SCT	4 cylindrical layers (Barrel)	$299 < R < 514$	< 1.4
	2×9 disks (End-cap area)	$275 < R < 560$	1.4 - 2.5
TRT	73 straw planes (Barrel)	$563 < R < 1066$	< 0.7
	160 straw planes (End-cap area)	$644 < R < 1004$	0.7 - 2.5

position to the beam axis at the point of closest approach, respectively, and identifies short life time particles like b-hadrons and τ leptons.

The SCT provides additional information on vertex measurement and track position, and has eight strips on each of four layers crossing on their edges. The strips are small-angle (40 mrad) stereo strips and consist of two 6.4 cm long daisy-chained sensors with a strip pitch of $80\mu m$ in the barrel region. In the end-cap region, a set of strips spreads radially with the angle of 40 mrad. The average pitch of the strips is approximately $80\mu m$. The intrinsic accuracy per module is R-$\phi \times z$ of $17 \times 580\ \mu m^2$ and is connected with about 6.3 million readout channels. The TRT is located at the most outer layer of the ID and supplies additional information of the coordinates and particle identification. The TRT is made with the 4 mm diameter straw tubes which are parallel with the beam axis and covers $|\eta| < 2.0$. The TRT only provides the R-ϕ information and its intrinsic accuracy per tube is 130 μm. In the barrel, the straw tubes are 144 cm long, and their wires are divided into two halves at $|\eta| = 0$. In the end-cap area, they are 37 cm long and are arranged radially in wheels. The connected readout channels are about 351,000.

3.2.3 Calorimeter

There are two major sub-detector systems within the calorimeter system. The liquid argon (LAr) electromagnetic (EM) calorimeter located in the inner area, and the hadronic

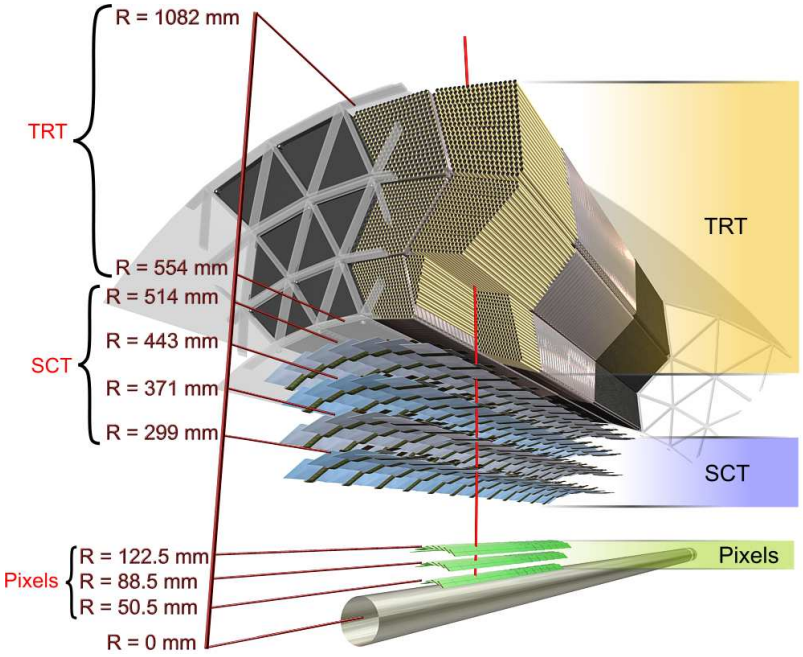

Figure 3.13: Layout of the ID in the barrel showing the Pixel, SCT and TRT detector [17].

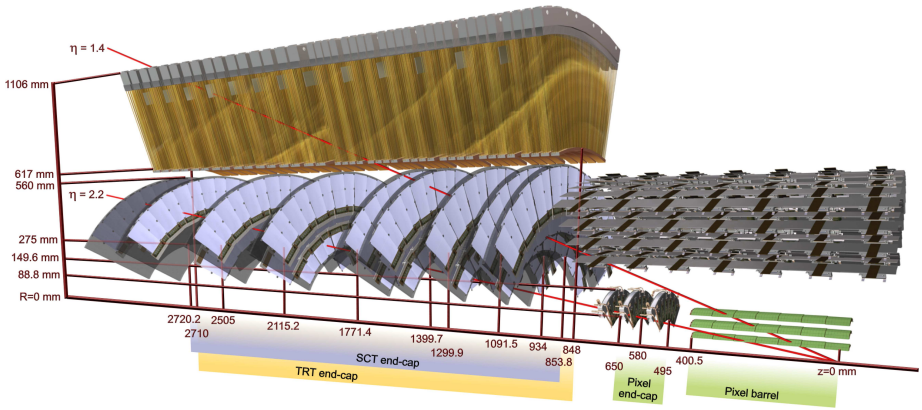

Figure 3.14: Layout of the ID in the end-cap region and showing the sensors and structural elements traversed by two charged tracks of 10 GeV p_{T} in the end-cap inner detector (η = 1.4 and 2.2) [17].

calorimeter system that lies outside the EM calorimeter. The forward detector is located in the central area of the end-cap region. The calorimeter detector measures the energy deposition of the all electromagnetic and hadronic particle activities. Therefore, the depth of the calorimeter is the key design point. The total depth of the LAr EM calorimetor is >

22 (24) radiation lengths and approximately 9.7 (10) interaction lengths (λ) in the barrel (end-cap). The full depth at $\eta = 0$ is 11λ, 1.3 λ from the outer support. Fig 3.15 shows the schematics of the calorimeter system.

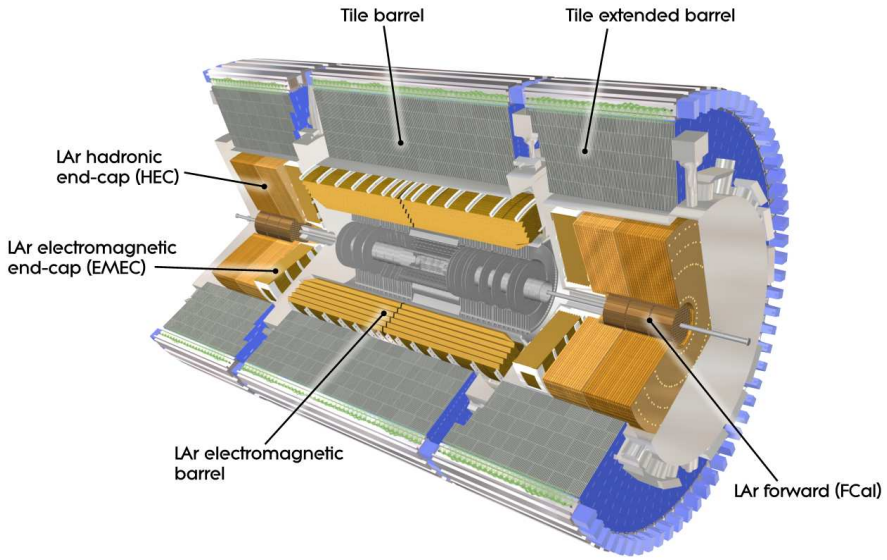

Figure 3.15: The layout of the Calorimeter system. The barrel area consist of the liquid argon (LAr) electromagnetic (EM) calorimeter and the tile calorimeter. In the end-cap area, LAr EM (EMEC), LAr hadronic detector (HEC) and LAr forward (FCal) are surrounded by tile extended barrels [17].

The liquid argon (LAr) electromagnetic (EM) calorimeter in the barrel area (EMB) covers $|\eta| < 1.475$, while the one in the end-cap (EMEC), covers $1.375 < |\eta| < 3.2$. The EM calorimeter uses a lead-LAr detector that is made with accordion-shaped capstan electrodes in the azimuthal symmetric. The lead absorber plates cover a full area and are optimized as a function of η based on the EM calorimeter performance in the energy resolution. It provides physics in the $|\eta| < 2.5$ while a pre-sampler detector compensates the energy loss by electrons and photons in $|\eta| < 1.8$.

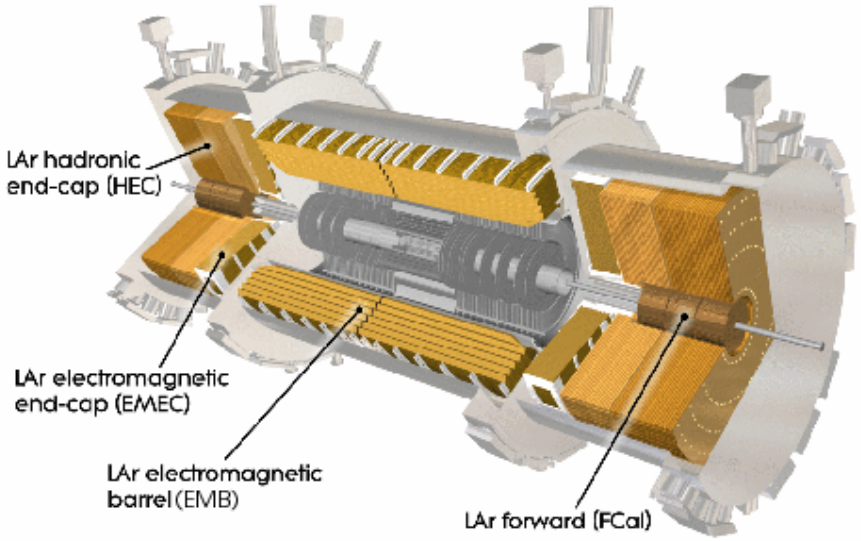

Figure 3.16: The liquid argon (LAr) electromagnetic (EM) calorimeter : a cylinder shapes of LAr EM in the barrel area (EMB) is centralized in the figure and the disk-shape of LAr EM (EMEC) and LAr hadronic detector (HEC) in the end-cap are arranged on perpendicular to the beam axis. The LAr forward (FCal) is located in the central area of the end-cap area which covers 3.1 $< |\eta| <$ 4.9 [17].

The hadronic calorimeter surrounds the EM calorimeter and is divided into several sub-detector system. The LAr hadronic calorimeters in the end-cap region (HEC) covers the region of 1.5 $< |\eta| <$ 3.2 and the LAr forward calorimeter (FCal) covers the region 3.1 $< |\eta| <$ 4.9. In the barrel area, the tile calorimeter covers $|\eta| <$ 1.0 and covers 0.8 $< |\eta| <$ 1.7 in the two extended areas (the end-cap region), as seen in Fig 3.17a. The tile calorimeter uses steel as the absorber and scintillating tiles as the active material. Sixty four modules are radially spread in the transverse plane. Detailed schematics of each modules are described in Fig 3.17b.

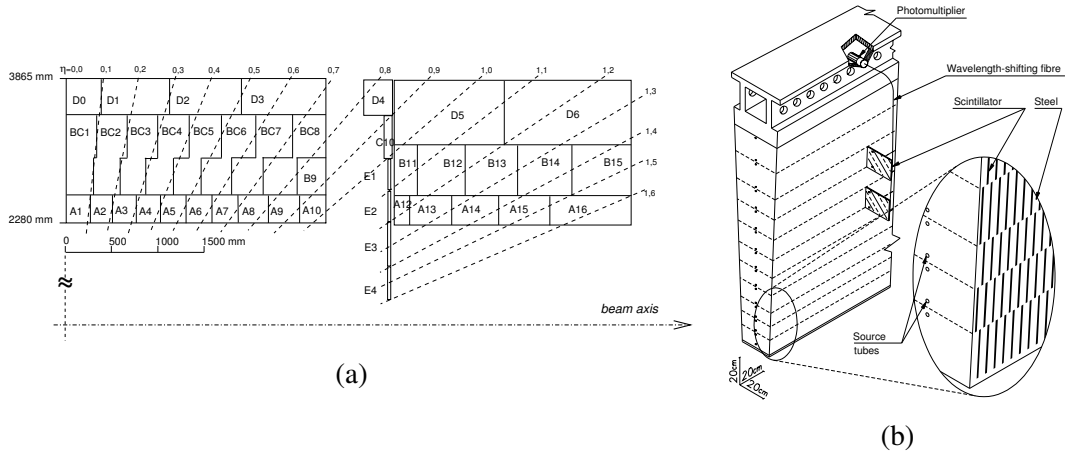

(a) (b)

Figure 3.17: The detail schematics of the hadronic calorimeter. (a) Segmentation in depth and eta of the tile-calorimeter modules in the central (left) and extended (right) barrels. The bottom of the picture corresponds to the inner radius of the tile calorimeter. The tile calorimeter is symmetric about the interaction point at the origin. (b) Schematic showing how the mechanical assembly and the optical readout of the tile calorimeter are integrated together. The various components of the optical readout, namely the tiles, the fibres and the photomultipliers, are shown.

3.2.3.1 MobiDICK4

As seen in the Figure 3.17b, each tile calorimeter module has a mounted electronic readout in the most outer layer including photo multipliers tubes (PMTs). During the first Long Shutdown (LS1), all those electronics are maintained and are upgraded to prepare for the next run resuming in 2015. MobiDICK4 is an upgraded version of the stand-alone test-bench for the full certification of the front-end electronics of the TileCal in the ATLAS experiment [18]. MobiDICK4 communicates with a laptop through the front-end Graphical User Interface (GUI) that is implemented in the test machine. An Ethernet connection with the back-end server makes it available to access the Embedded System on a Field Programmable Gate Array (FPGA). While the MobiDICK4 software keeps the client-sever architecture of previous versions, the server platform has been replaced to

utilize a System on Chip (SoC) platform, as opposed to the Versa Module Europa (VME) modules to the modernize the hardware.

The MobiDICK4 performs independent tests on each electronics of the TileCal modules with implemented functionalities supported by daughter-boards, including High-voltage and LED boards. As Pot's convert the light to the electrical pulse, the signals are also added in groups of towers in η by analogue summation cards and their signals are transmitted to the Level 1 Trigger through dedicated cables. Digitized data in groups of 3 PMTs are read-out by one Data Management Unit (DMU). Two DMUs are mounted on a digitizer board which is equipped with a TTCrx chip. Up to eight digitizer boards' read-out linked to the one module, called as a super-drawer. Finally an Interface Board pack transmits the data to the back-end sever and receives Trigger Timing and Control (TTC) commands from it. MobiDICK4 has specific tests that target the certification of each of these components. With the light and the electrical signal from daughter-boards, the MobiDICK4 is able to benchmark the real collision situation in the LHC.

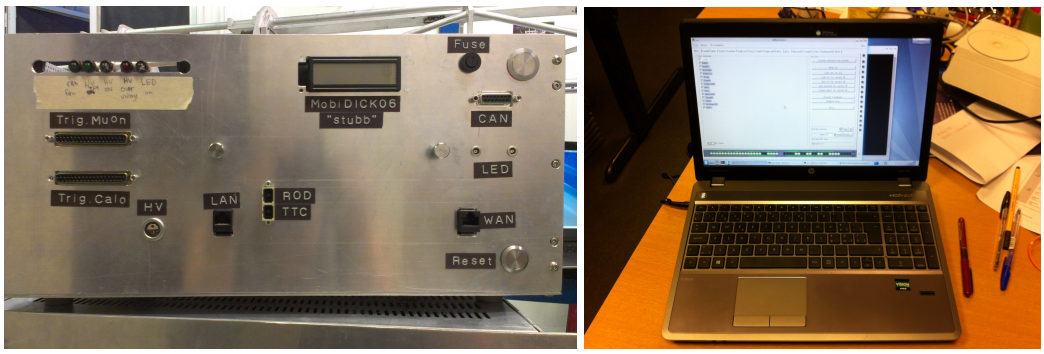

Figure 3.18: The MobiDICK4 hardware box (left) and the associated lepton (right). They communicates through an Internet which access to the GUI interface implemented in the MobiDICK4 [18].

In order to analyze the performance of electronics in the super-drawers, hence, the analogue-digital-converter (ADC) boards are essential role in the given purpose. Thus,

developing and optimizing the ADC board are essential steps in the project. The sample outputs from the ADC board are inverted. Up to 128 samples are stored in the FPGA at a time. Fig 3.20 shows an example of one sampling for the pulse shape measurement at different charge injection times. In the figure, the pulse shape measurement of the tower and muon output of the super-drawer performed by MobiDICK4 are sampling with a known charge at different time offsets. As expected, muon output has a slightly wider distribution, compared with tower measurement.

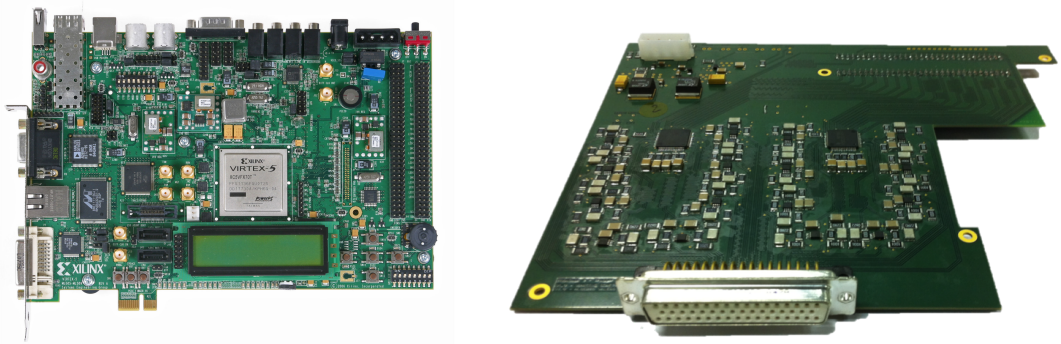

Figure 3.19: The MobiDICK4's mother board (left) and the ADC board (right). The mother board controls all the functionalities of MobiDICK4. The ADC boards make possible to perform the key tests to certify electronics of each calorimeter modules [18].

The uniformity of the ADC channels is shown in Fig 3.21. The top plot in each channels test is the reconstructed response versus channels and the bottom is the deviation from the mean. Fig 3.21 and 3.22 show all the channels of the ADC board that are tested and are reconstructed by two different methods: the Flat Filter and the Optimal Filter. Both Flat Filter and Optimal Filter responses agree. As we see in the Fig 3.22, the linearity of the reconstructed energy as a function of different charges is very good for both Flat and Optimal Filters. Therefore, the difference between these two methods is not significant. The responses of the ADC channel for a given charge are uniform overall. Differences between the two ADC boards can be further improved by inter-calibration if needed.

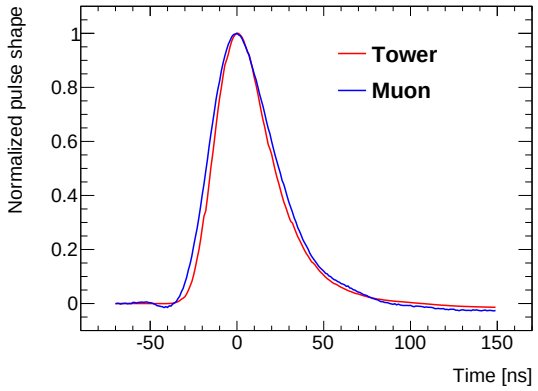

Figure 3.20: ADC pulse shape measurement example with a time variation of the charge injection [18].

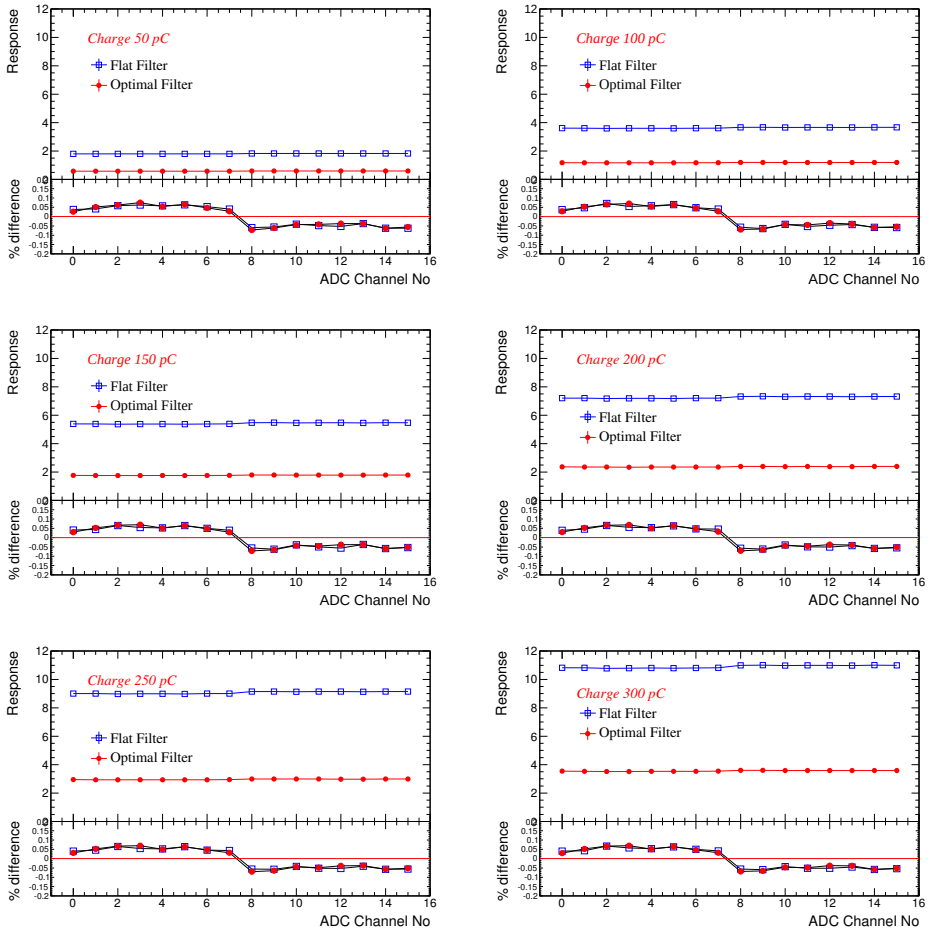

Figure 3.21: Uniformity of the channels in the ADC board reconstructed at the given charge which is varied from 50 to 300 pC [18].

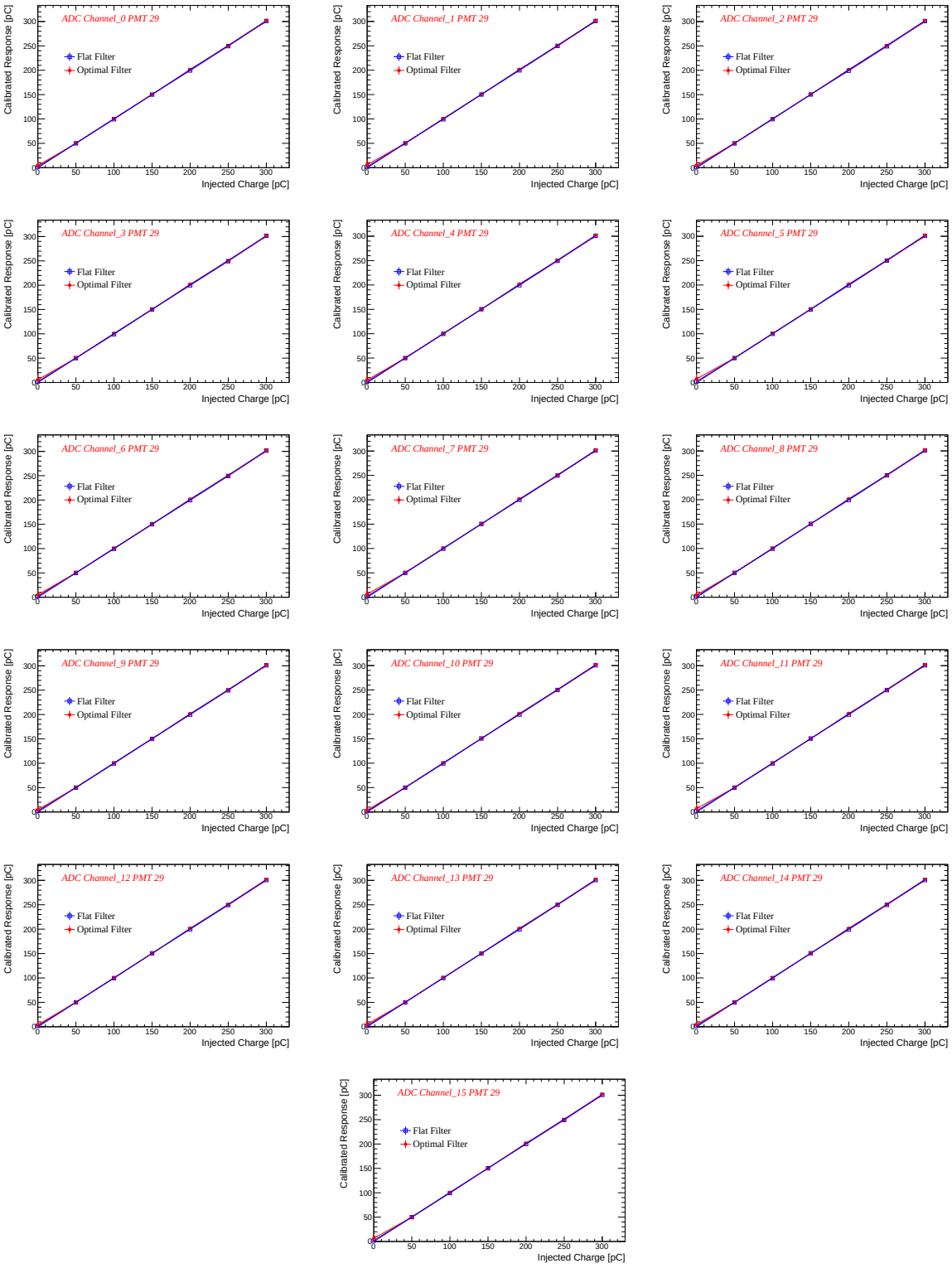

Figure 3.22: Calibrated responses of all ADC channels as a function of injected charge. It presents results of two different filers [18].

3.2.4 Muon Spectrometer

Since muons are minimum ionizing particles, they are able to travel through the calorimeter with minimal energy loss. The muons spectrometer (MS) measures the muons paths and momentum with high precision in the range $|\eta| < 2.7$. From magnets located nearby, the muons spectrometer is supplied a magnetic field. The barrel toroids provides the magnetic field in the $|\eta| < 1.4$ and two end-cap magnets provides the magnetic field in the $1.6 < |\eta| < 2.7$. The range $1.4 < |\eta| < 1.6$ is referred as the transition region where magnet deflection is provided by two magnet systems, as shown in the Fig 3.23.

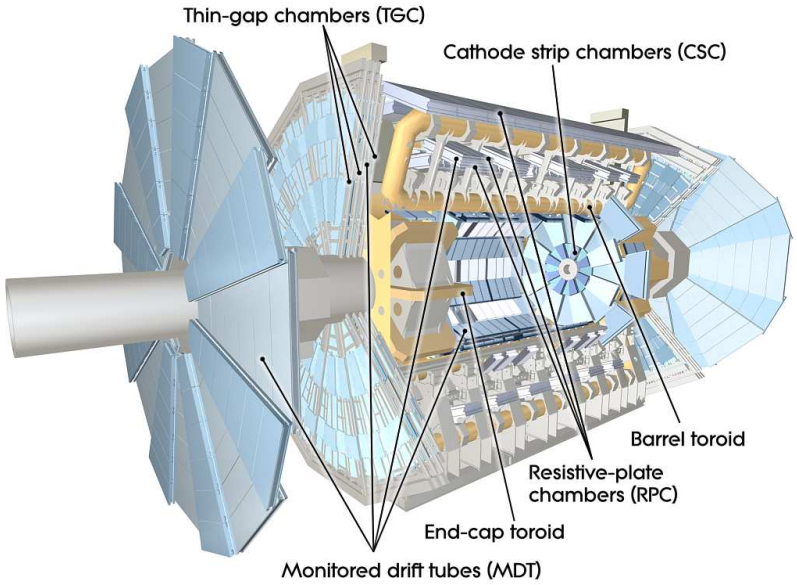

Figure 3.23: The layout of the muon spectrometer [17].

There are two precision-tracking chambers in the Muon detector, the monitored drift tubes (MDT) and the cathode strip chambers (CSC). Over most of the η range, the precision measurement is done with MDT. However, the cathode strip chambers (CSC) is used to measure the principal bending direction by the magnetic field for the large η, $2.0 < |\eta| < 2.7$. The independent mechanical structure of the MDT, three to eight layers of

drift tubes operated at an absolute pressure of 3 bar, assure a robust and reliable operation. The CSC is the multiwired proportional chamber that is symmetric on ϕ and the layers of CSC provides the η information.

Two trigger chambers are available, the resistive plate chambers (RPC) and the thin gap chambers (TGC) which cover the ranges: $|\eta| <$ 1.05 and 1.05 $< |\eta| <$ 2.4, respectively. The information given by the trigger chambers aims to be used for three purposes: providing bunch-crossing identification, providing well-defined p_{T} thresholds, and measuring the muon coordinate in the direction orthogonal to that determined by the precision-tracking chambers.

3.2.5 Forward Detectors

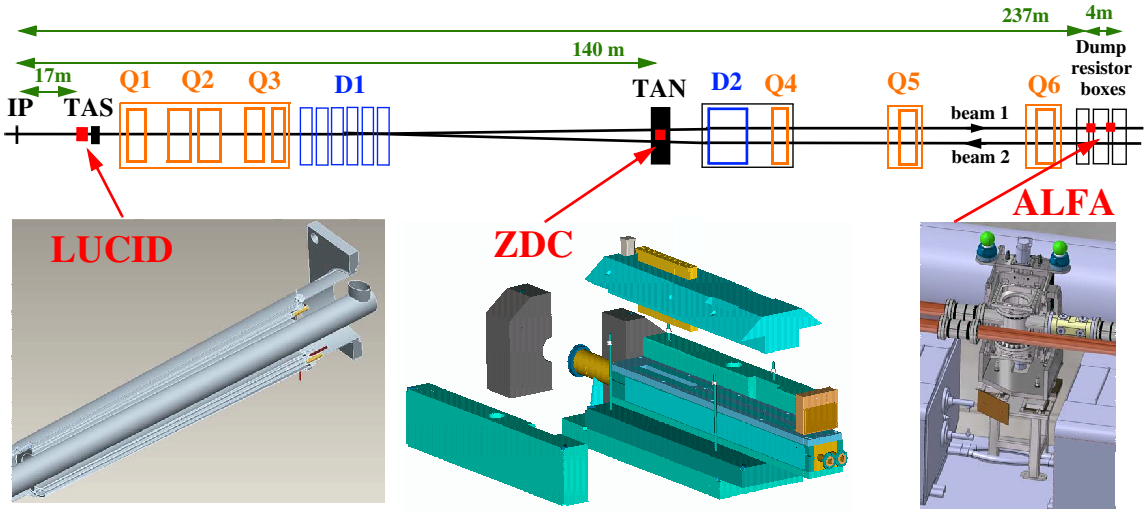

Figure 3.24: Three sub detectors of the forward detector [17].

The forward detector systems are mainly considered to enhance luminosity measurements. The three subsystems are: Luminosity measurement using Cerenkov Integrating Detector (LUCID), Absolute Luminosity For ATLAS (ALFA) and the Zero-Degree Calorimeter (ZDC). LUCID lies at ± 17 m from the IP and detects inelastic p-p scattering

in the very large η region (the forward direction) to mainly monitor the online relative-luminosity for ATLAS. At $\pm 240\ m$ from the IP, the ALFA consisting of scintillating fibre trackers lies at a very close distance to the beam lines, as close as 1 mm. The ZDC was put at $\pm 140\ m$ from the IP. Layers of alternating quartz rods and tungsten plates are the materials for the ZDC and the ZDC has a power to measure neutral particles at pseudorapidities $|\eta| \geq 8.2$.

3.2.6 Trigger System

The trigger system in ATLAS aims to collect meaningful events from the raw collision information due to the limitation of the data storage capacity and the rate at which the data can be written to disk. The collision rate at the LHC is 40 MHz. Since each event size is approximately 1.3 Mbyte, about 1 PB/sec of storage are needed to store them all. Indeed, not all events are physically meaningful. Thus, the ATLAS trigger system reduces to the affordable rate to 200 Hz which is about 300 MB/sec data storage is acquired. The trigger system consists of three distinct levels to manage this complexity: Level-1 (L1), Level-2 (L2) and event filter. The L2 and event filter are all together called as the High-Level Trigger (HLT). Fig 3.25 is visualized the flow of the ATLAS trigger system.

The **L1 trigger** searches for high p_{T} objects, such as muons, electrons/photons, jets, and τ-leptons decaying into hadrons as well as large missing transverse energy ($E_{\mathrm{T}}^{\mathrm{miss}}$) and large total transverse energy. The L1 trigger's events rate is about 75 kHz and within 2.5 μs after the bunch crossing, the decision is made to recorded or not. There are 3 subsystems in the L1 trigger system; the Calorimeter Trigger (L1Calo), the Muon Trigger (L1Muon) and the event-decision part implemented in the Central Trigger Processor (CTP). The L1Calo decision is based on the information from analogue electronics on detector sums signals to form trigger towers. Theses signals are digitized by the pre-processor performing the bunch-crossing identification which is essential to have correct

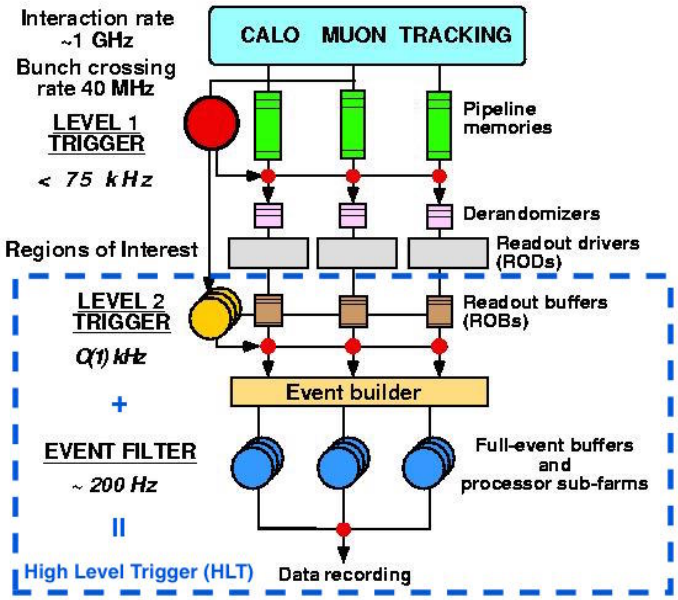

Figure 3.25: The ATLAS trigger system flow chart [17].

associate bunch crossing for the signals. A Cluster Processor identifies specific objects electrons/photons and hereon/τ-leptons using a "sliding window" algorithm that defines an $\eta - \phi$ area in the detector, the calorimeter. This region, called a region of interest (ROI), comprises about 2-3% of the full data within an event. A Jet/Energy Processor identifies jet candidates and evaluates the sum of transverse component for $E_{\mathrm{T}}^{\mathrm{miss}}$. With the given thresholds, jets and $E_{\mathrm{T}}^{\mathrm{miss}}$ are discriminated by comparing with it. The merged L1Calo information is sent to the the Central Trigger Processor. The Muon trigger algorithms are based on hit on middle RPC / TGC station called "coincidence window" within a geometrical track whose width is related to the DPT threshold applied. Six coincidence windows (low/high) coincidence window thresholds are defined. The multiplicity of those information is sent to the Central Trigger Processor. The Central Trigger Processor manages to combine all the signal up to 256 different trigger types. This makes up the L1 trigger menu. Those decisions are stored in the pipeline memories of the sub-detector front-end electronics to pass to the L2 trigger system.

The **HLT system**, which includes the L2 and the event filter trigger system, runs on a cluster of commercial computers farms. here is associated software that is utilized to make HLT decision is designed based on the ATLAS offline Athena frame work. At the level of the **L2 trigger** system. the data is stored in the Read-Out-Buffers (ROB) when the decision is made. The L2 trigger is interested in the RoI information which is already built in the L1 trigger level. Once the RoI builder located at the boundary between the L1 and L2 trigger systems receives the RoI information from the different sources and merges them into the single structure at the L1 trigger rate. The L2 trigger system reduces the data provided from the L1 to an event rate about 3.5 kHz within a latency of 40 ms. The data from L2 trigger system are used in the **event filter trigger** system to make a final decision to write on disks. Unlike the L2 trigger, the events filter can access the full event and nearly replicates full ATLAS event reconstruction. The final event rate is 200 Hz after the EF.

CHAPTER 4

Event Generation and Reconstruction

4.1 Event Generation

Due to the complexity of the ATLAS detector, event simulations are requested to perform the physics analysis. The generation procedure consists of several steps, the hard scatter of the collision, parton shower (PS), hadronization and underlying event (UE), followed by detector simulation and digitization procedures. The colliding protons comprise many quarks (anti-quarks) and gluons. Therefore, in an event that, the constituent of protons decay into many partons in the inelastic scatterings and they share the initial colliding proton momentum. To reconstruct those events with higher accuracy, many generators are available to model these processes as close as possible to reality. The choice of Monte Carlo (MC) tools depends on the purposes of what to reconstruct and how much further complexity to considered. Fig 4.1 shows the process of the events generation.

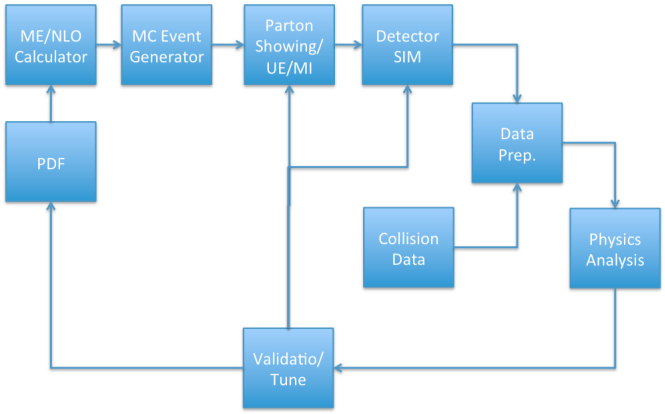

Figure 4.1: The diagram of the event simulation and the data reconstruction sequence in the ATLAS experiment.

It describes the one possible event from the initial hard collision moment to the hadronization level of decay process. To predict this process, the Parton Distribution Functions (PDFs) [19] is used to predict the generation ratio of those partons by the MC tools.

Parton Distribution Function

It is the theoretical probability of finding a particle with a certain momentum fraction x at scale Q^2 [19]. Each parton has its own Parton Distribution Function (PDFs), f, as shown in Eq. 4.1.

$$f_a(x_a, Q^2) \quad , \quad where \quad a = q,\ g \tag{4.1}$$

For a precise modeling, the PDFs are essential inputs. The PDFs calculations are done with the Dokshitzer-Gribov-Lipatov-Altarelli-Parisi (DGLAP) evolution equation [20]. Since, QCD does not predict parton contents of the protons, the shapes of the PDFs are determined by a fit to data from experimental observable in various processes. Two major PDFs are used in this study that are MSTW [21] and CTEQPDFs [22]. The choice of the PDFs would be different as needed.

4.1.1 Hard Scatter

The hard scatter is the big momentum exchange made between the parton-parton. This interaction happens within very small distance, hence partons are modeled as a free particle and use perturbation theory. In contrast to, the soft interactions that dominate interactions in the events exchange a small energy, which cannot be described with the perturbation theory. However, since it is not always clear what exactly happen in the events, one needs to estimate what portion of hard or soft scatter would happen by scaling the boundary between those two interactions. This scale factor is called “factorization

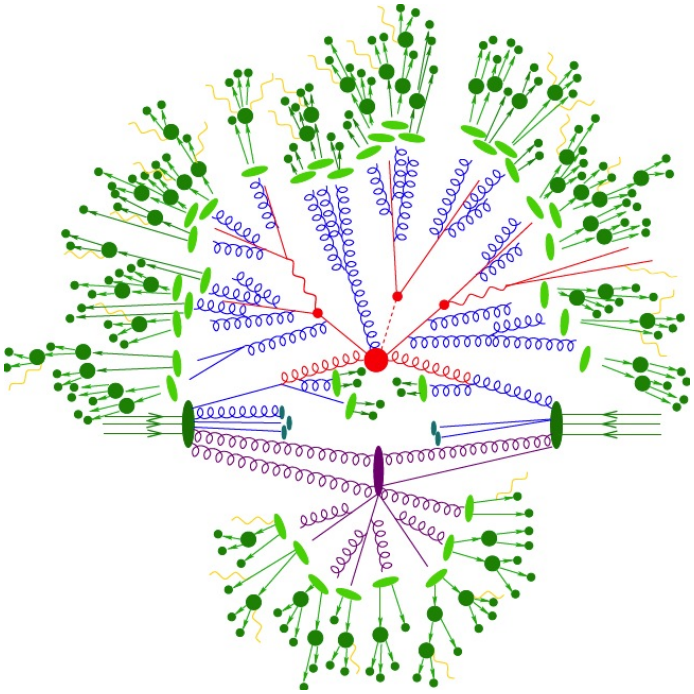

Figure 4.2: Visualization of interactions and decays in the collision events.

scale" factor, μ_F. A nominal setup is $\mu_F = \mu_R = Q$, where μ_R is the normalization scale factor.

4.1.2 Parton Shower

The parton shower (PS) is the higher order correction of the hard scatter. The hard scatter used at Matrix Element (ME) at leading-order (LO) or next-leading-order (NLO) level. To predict the LHC events precisely, the PS is used. Since this level of process is not possible to calculate exactly, the approximation is made and inputs to estimate are angles they radiate and the ratio of momentum they share. Only the collinearly radiated particles are taken into the account and do with a loop level $2 \rightarrow n$ perturbation calculations.

4.1.3 Hardronization

The hardronization is the generation process of the hadrons from the quarks and gluons due to the color confinement in the gauge theory. Two methods are used to described

the hadronization process, the Lund String Model [23] and the Cluster Model [24]. The Lund String Model forms a narrow tube between the hadrons except the highest gluon due to the gluon self-interaction. The tube configuration with thickness of the order of 1 fm when the separation of the sources becomes much larger than this. If the potential energy reaches to the level of the hadron mass, the string is about to break at some point along its length. The Cluster Model is determined on the confinement property of QCD. The process happens at less energy level than the hard scatter scale, Therefore, partons are clustered in colourless groups with an invariant mass distributions that are independent of the hard scattering process. Hence, gluons should decay in the $q\bar{q}$ pairs for clustering, called *proto − hadrons*. Further hadron decays are consequently happening after that.

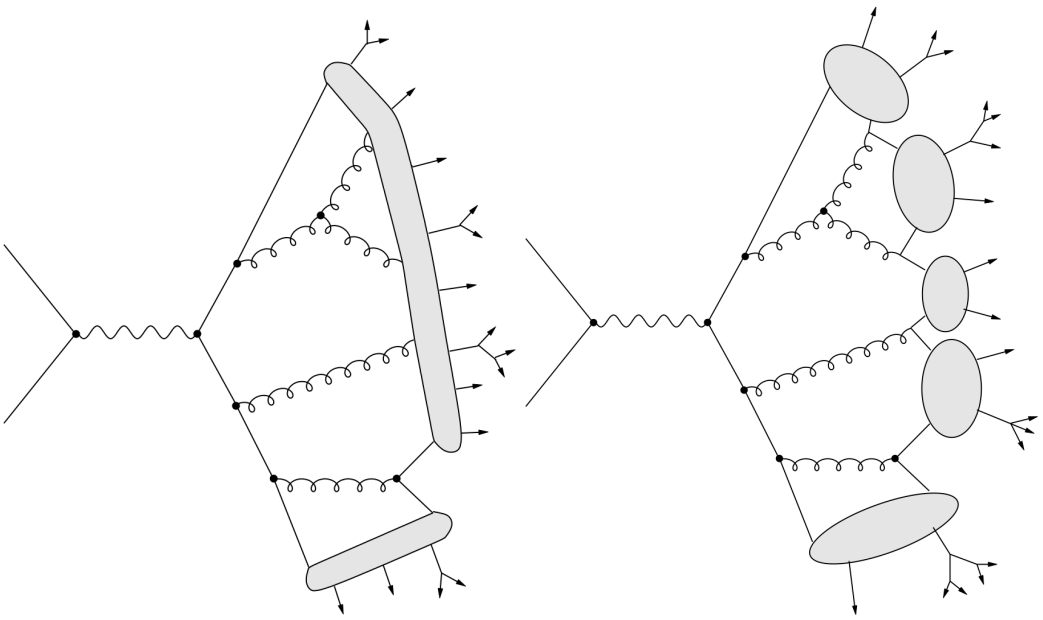

Figure 4.3: The diagram of the two modeling method, the Lund String Model (left) and the Cluster Model (right).

4.1.4 Underlying Event and Pile-up

The underlying events (UE) are particle interactions that are not happen in the hard scattering and are including multiple parton interactions and beam remnants. Since this process cannot be calculated with the perturbation theory, it uses an approximation method to describe. Multiple parton hard-scatterings are the events in which two or more distinct hard parton interactions occurring simultaneously in a single hadron-hadron collision. [26]. The LHC has an environment to produce this process easily since the cross-section increase as the collision energy increasing. Beam remnants are generated when some partons do not take active part in the hard scatter process.

There are two kinds of pileup: in-time pileup and out-of-time pileup [25]. In-time-pileup is additional proton-proton collisions occurring in a same bunch-crossing as the collision of interest. The out-of-time pile-up is additional proton-proton collisions occurring in bunch-crossings just before and after the collision of interest. Therefore, there would be a un-wanted interactions potentially affect to reconstruct real interaction points in the events.

4.1.5 Generators and Detector Simulation

Different kinds of event generator are used to simulate physics processes with their specializing characteristics. Some are described below :

- POWHEG [27] : is the hard scatter generator at the next-to-leading-order (NLO) order in QCD. The tool interfaces with HERWIG and PYTHIA for the parton shower and the hadronization.
- PYTHIA [28, 29] : is a leading-logarithm (LL) event generator in that semi- and non-perturbative phenomena models are implemented. It is widely used to simulate all collision processes including PS in $2 \rightarrow$ n perturbations. It uses the Lund string

hadronization model to model hadronization. The tools also used to model underlying events including in-time pile-up.

- HERWIG [30] : is a leading order $2 \to 2$ processes generator. It simulates the hadronization and the UE using the cluster model. The JIMMY [31] package is used to correct HERWIG to model the UE. JIMMY calculates the multi-parton cross section as a function of the hard scatter process, PDFs, and area overlap between colliding protons.
- SHERPA [32] : is a general purpose generator to model at the leading order (LO). It calculates at the matrix-element (ME) level to match parton showers and to remove overlap diagrams. Combining with PYTHIA or HERWIG, it provides a better approximation to simulate full events with the hadronization or at the UE level.
- ALPGEN [33] : is used for modeling multi-parton hard processes at the LO. Since the tool has advantages in simulating muti-jet final state events, POWHEG or PYTHIA is combined with ALPGEN in many cases. Due to the fixed order QCD matrix element are implemented in ALPGEN, it can provide a better approximation. Thus, it is used to produce W/Z bosons with many jets.
- ACERMC [34] : is a hard scatter generator. It could be combine with POWHEG or PYTHIA for the PS and the hadronization. The tool has been used to generate events containing W/Z bosons with jets.
- GG2VV [35] : models the gluon generation that produce WW and ZZ events. The tool includes a box diagram for the process.

To simulate behaviors of particles going through the detector, GEANT4 [36] is used . It adopts the full ATLAS information, i.e. the coordinate system, the temperature, the voltage settings and so on. It has a choice of modeling details, $FullSim$ and $ATLFAST-II simulation$ [37, 38]. In the $FullSim$, it simulates under the consideration of all the sub detector detail information and the energy deposition information of each sub detectors, such as the associated energy, the position and the time, are recorded as hits. Those hits

are later digitized. The full simulation is useful to study of the tracking performance of the detector, the energy and $E_{\mathrm{T}}^{\mathrm{miss}}$ resolution, the photon conversion, the lepton/photon identification, the jet clustering and so on. Thus, the result models are very precise and accurate even though it takes time. The $ATLFAST-II simulation$ contains less information than the $FullSim$ and treats a condensed geometry information. This simulation method aims to reduce the simulation time of which more than 90% is spent inside the calorimeter systems [39]. This algorithm uses the Fast ATLAS Tracking Simulation (Fatras) [40] for simulating Inner Detector (ID) and the Muon Spectrometer (MS) tracks utilizing geometrical details of the simulated detector area. The Fast Calorimeter Simulation (FastCaloSim) for simulating calorimeter deposits approximated sizes and shapes of shower based on the input particles. The $ATLFAST-II simulation$ is more useful when a large amount of physics samples are produced, like many backgrounds samples for the Higgs study, or the SUSY study.

4.1.6 Digitization

The hits generated at the simulation stage are digitized to mimic the real data collection procedure. The information in the hits are converted to the detector response signal called digits. Just like the real data collected from the detector and stored in the readout devices, those digits are recorded in the data format, Raw Data Objects (RDO) by a digitization software specified to sub detectors. This procedure is called the digitization [37]. The RDO passes to the trigger system of ATLAS to be used.

4.2 Object Reconstruction

4.2.1 Tracks and Vertex

When particles interact, the point it happens is referred as a vertex. The vertex also can be from underlying events or any hadronic decays, like jets. A vertex associated with

a hard collision is called as a primary vertex (PMV). A simple schematics of vertices are shown in the Fig 4.4.

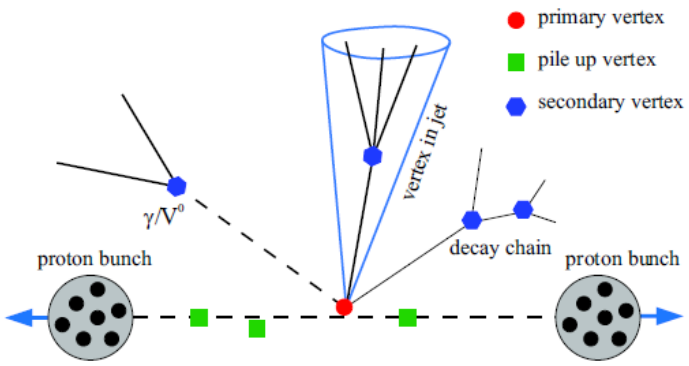

Figure 4.4: Simple schematics of the vertices. The primary vertex (PMV) is represented by a red dot while the second vertex represents with a blue dots. The vertex associated with underlying events are represented with the green dots.

Trajectories being generated as the particles travel after the interactions, traces are left in the sub-detectors. Patterns and distances are different with the passing particle momentum and charges, as described in Fig 4.5. Tracks are used to refer to these traces.

To reconstruct the tracks, there are two algorithms exist: the inside-out track reconstruction and the outside-in track reconstruction. The inside-out sequence starts from the hit in the inner silicon detectors (Pixel and SCT). The first step of the inside-out track reconstruction is the formation of "SpacePoint" objects which are the hit information converted from the silicon detector measurements. Once the SpacePoint seeds are found, the primary ID pattern recognition starts to find hits toward the outer part of the ID. The absence of the hit where it is expected in a track trajectory is called a hole. For the performance of a successful building track, it should be satisfy a certain quality criteria, which called a simplified Kalman filtering that tests the track and accept parameter set with the smallest χ^2. The outside-in sequence starts from the hit in TRT. It starts from the most outer layers of the ID and extends to search the track candidates toward to the Pixel and

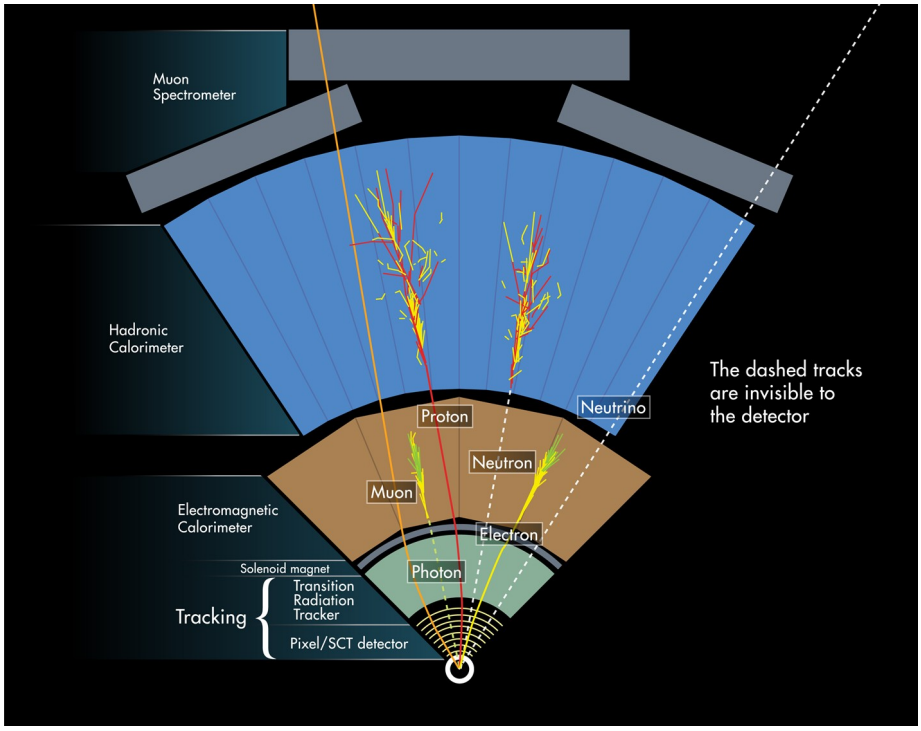

Figure 4.5: Traces of particles in ATLAS. The different types of particles made different trace shapes and distances as they travel ATLAS detector.

SCT. This method is used for the case that tracks are not found in the inner detector or tracks are hard to reconstruct from the silicon detector, like from ambiguous hits or secondary hits. Since the ID is under the influence of the solenoid magnets, the path of the tacks are helical, and the helical trajectories of tracks are parameterized in ATLAS software as a five-dimensional vector in the following form [41]:

$$\tau = (d_0, z_0, \phi_0, \theta, q/p). \tag{4.2}$$

where the five track parameters are :

- d_0 : The transverse impact parameter, defined as the distance of the closest approach of a particle to the PMV in the R-ϕ plane.
- z_0 : The longitudinal impact parameter defined as the distance of the closest approach of a particle to the PMV in the z plane.

- q/p: The curvature describes the charge of the track multiplied by the track momentum.
- ϕ : The coordinate of the track at particles point of the closest approach to the PMV.
- θ : The θ coordinate of the track at the particles point of closest approach to the PMV.

4.2.2 Electrons

Electrons are reconstructed with the information collected from the electromagnetic (EM) calorimeter and the inner detector (ID) tracks [42]. Once the energy that deposited in the EM clusters, which is 3×5 rectangular shape cell groups that are consisted of 0.025 × 0.025 segments in the $\eta \times \phi$ plane, is reconstructed and select the seed if the cluster is $E_{\mathrm{T}} < 3\,\mathrm{GeV}$. The η range is $|\eta| < 2.47$ excluding the transition region between the barrel and end-cap EM calorimeters, $1.37 < |\eta| < 1.52$. the cluster is matched to an inner detector track with an $\Delta\eta \times \Delta\phi = 0.05 \times 0.1$ size sliding window. Since about 20% of energy lose happens when electrons pass the ID tracks before they reach the EM calorimeter due to Bremsstrahlung radiation, a correction procedure is considered to improve the modeling resolution. A Gaussian Sum Filter (GSF) Technique [43] is used for this purpose. This technique uses a Gaussian sum filter to fit all the electron candidates' tracks. Hence, the reconstructed energy difference between the ID tracks and the EM calorimeter is reduced and the resolution of impact parameter and the electron direction are increased. When this correction is done, the refitted tracks are matched to the EM calorimeter information for the electron reconstruction. This procedure is called outside-in reconstruction.

The selected electrons are classified into certain categories depending on how electron-like or jet-like they are. There are two main methods that are used to make this selection. The first method is the cut-based on the shower shape, on the reconstructed track and

the combined reconstruction. Four sets of cuts are categorized depending on the signal efficiency and jet rejection requirements :

- "loose cuts" : a group of the simple shower shape cuts, energy deposition shower shape in the middle layer of EM, and very loose matching cuts between the calorimeter cluster and the reconstructed track. This gives a high efficiency but low background rejection.
- "medium cuts" : in addition to the loose cuts, the medium cuts add the information of the first layer in the EM and the track quality cuts.
- "tight cuts" : a tighter track-matching criteria, the cut on the energy-to-momentum ratio, the more number of hits in the vertex-layer on the track (to reject the photon conversions), are a higher ratio between the high and low threshold hits in the TRT detector (to reject the charged hadron backgrounds) added to the medium cuts.
- "multilepton" [44] : special designed category for the 2012 analysis that developed in the context of searches for multi-lepton final states, exploiting specific cuts on high/low Bremsstrahlung categories using GSF information. Since the complexity of the 8 TeV analysis due to the pile-up, the increasing number of events and so on, this cut is optimized for the low energy electrons in the $H \rightarrow ZZ* \rightarrow 4l$ analysis. This has a almost same level of efficiency with loose cuts but higher rejection on the background.

The second method is the multi-variate electron identification criteria that combined with the likelihood method [45]. The signal and background PDFs of the discriminating variables extracted from the data is used for given electrons. The bremsstrahlung effects are also included. Additional variables are added to boost up the power of the discrimination. The loose, medium, and very tight LH categories are available to use.

Besides the electron identification, the electron isolation cuts [46] are designed to have a further rejection of hadronic jets mis-identification of electrons. One with calorimeter based and one with track based isolation are used.

- Calorimeter based isolation : $E_T^{cone\Delta R}$, the sum of the transverse energy deposited in the calorimeter cells in a cone of ΔR around the electron except the $\Delta\eta \times \Delta\phi = 0.125 \times 0.175$ around the electron cluster to correct the energy leakage from the electron to the isolation cone.
- Track based isolation : The track isolation variable $P_T^{cone\Delta R}$, the sum of the transverse momentum of the tracks with $p_{\mathrm{T}} > 0.4$ GeV in a cone of ΔR around the electron, excluding the track of the electron itself. The tracks should be associated to the PMV and satisfy minimal quality requirements.

4.2.3 Muons

Muons from LHC are distributed in the broad range of energy spectrum. The information from the muon spectrometer (MS) has been used to reconstruct muons, moreover further precision are made with the combined information of the ID. The momentum of the muon is corrected for deposition in the calorimeter. The best measurement of low to intermediate momentum muons are done with ID while muon spectrometer takes care of higher momentum ones. As seen in Fig 4.6, a muon interaction power with metal gets lower at the muon momentum around 1 GeV and gets higher in $\sim$ TeV range. Since the measured muon in the ATLAS is 3 GeV to 3 TeV, the high transverse momentum muon can go further even though its track leaves about 3 GeV energy in the calorimeter, which is taken into account in the reconstruction. Therefore, the track reconstruction in the ID and MS are used to reconstruct the muons by measuring the momentum. Three track reconstruction strategies are available to use as followed :

- Stand-alone : only use the muon spectrometer information to reconstruct the muon track over $|\eta| < 2.5$.
- Combined : combination of a muon-spectrometer track with an inner-detector track over the range $|\eta| < 2.5$
- Segment tag : combination of an inner-detector track with a muon-spectrometer segment

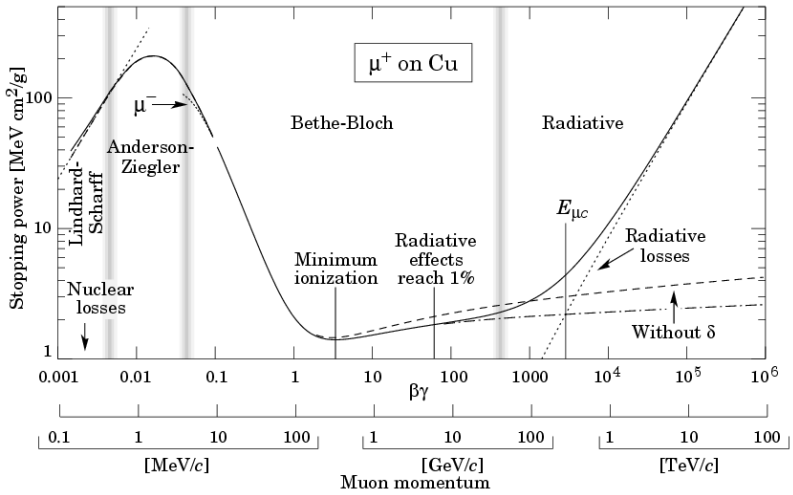

Figure 4.6: Stopping power for positive muons in copper [47].

The used muon reconstruction method is Statistical Combination (STACO) [48] combined algorithm that that reconstructs the muons by matching the reconstructed ID track and the muon spectrometer (MS) track in the $|\eta|$ region ≤ 2.5. The trajectories that left in the three layers of MS tracks has been reconstructed as a seed. The trajectories are traced back to the initial interaction point. The ID tracks should satisfy the following requirement: the sum of pixel hits and dead pixel sensors crossed by the track must be greater than zero, the sum of SCT hits and dead SCT sensors crossed by the track must be greater than four, the number of missing hits in a crossed sensor which is not dead ("holes") must be less than three, and a successful TRT extension must be found if

the track is within the acceptance of the TRT. This algorithm is used χ^2_{match} that define as $\chi^2_{\text{match}} = (T_{MS} - T_{ID})^T (C_{MS} - C_{ID})^{-1} (T_{MS} - T_{ID})$. T where T is the vector of five track parameters which is previously defined in Section 4.2.1 and C is its co-variance matrix. The lowest χ^2_{match} will be the final muon track and the final track vector of those five parameters is $T = (C_{ID}^{-1} + C_{MS}^{-1})^{-1} (C_{ID}^{-1} T_{ID} + C_{MS}^{-1} T_{MS})$.

4.2.4 Jets

Hadronized partons travelling up to the tile calorimeter and showering with deposited energy in the tile calorimeter cells are defined as jets. To reconstruct this objects, there are two algorithms are studied. The first method is the fixed cone algorithm [49] that sum the 4-vectors of the particles within a specific cone size ΔR, typically 0.4 or 0.6, around the seed objects. The k_T clustering algorithm [50] works by either combining two proto-jets or declaring a given jet as a final jet based on Eq. 4.3. If $d_{ij} < d_i$, the jets are merged, otherwise, jet i is declared a jet

$$d_{ij} = \min(p_{T,i}^2, p_{T,j}^2) \frac{\Delta R_{ij}}{R}, \quad where \quad d_i = p_{T,i}^2 \tag{4.3}$$

An anti-k_T algorithm takes the inverse of p_{T} in the k_T algorithm, thus,

$$d_{ij} = \min(p_{T,i}^{-2}, p_{T,j}^{-2}) \frac{\Delta R_{ij}}{R}, \quad where \quad d_i = p_{T,i}^{-2}. \tag{4.4}$$

The fixed cone algorithm is not infrared and collinear safe; two jets can be merged due to soft radiation between the two jets. The resultant jet axis would then be about this soft radiation. Hence, the anti-k_T algorithms are mainly used, specially, the anti-k_T algorithms with the $\Delta R = 0.4$ [51] is the nominal algorithm in the analysis. In Fig 4.7, the anti-k_T algorithm have finer clusters than the k_T algorithm.

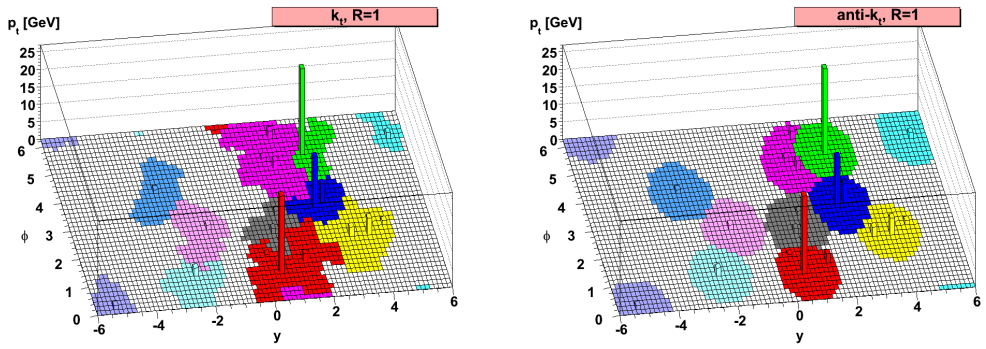

Figure 4.7: Comparison between the k_T (left) and the anti-k_T algorithm (right) [50].

The topo-cluster method is used as an input in ATLAS. The topo-cluster method builds clusters based on the energy deposition in the calorimeter cells. Once identified seeds cells are selected with energy significant excess more than 4σ over the noise level, nearby cells are added to the seeds to form clusters. Extra cells at the boundary regions are also added for the final cluster. After the cluster formation, merging and splitting process is done to maximize the energy deposition in the cluster. Each clusters are calibrated based on the their energy density, calorimeter depth, isolation respect to nearby clusters and so on. The local cluster weighting calibration (LCW) [52] is used for the calibration.

The Jet Energy Fraction (JVF) is used to remove the jets from the pile-up, as it is defined

$$\mathrm{JVF} = \left| \frac{\Sigma_{\mathrm{tracks}} \mathrm{p}_{\mathrm{T}}^{\mathrm{PV}}}{\Sigma_{\mathrm{tracks}} \mathrm{p}_{\mathrm{T}}^{\mathrm{all}}} \right| \tag{4.5}$$

where JVF = 1 means the jet is from the PMV and JVF = -1 indicates no matching tracks and the JVF = 0 mean that the jet is from pile-up vertices. Therefore, jets are required JVF $>$ 0.5 to identify jets that is from the PMV) [53]. This is efficient for suppressing pile-up jets. Identification of the jets originating from b-quark is necessary for the high p_{T} physics and the multivariate MV1 algorithm is the nominal strategy to tag the b-jets. The MV1

takes b jet as a signal and treats other light flavor quarks induced jets as backgrounds [54] and the output of training is a tag weight for the $b-$ tagging.

4.2.5 Missing Transverse Energy

From the conservation of momentum laws, $E_{\mathrm{T}}^{\mathrm{miss}}$ can be calculated by subtracting amount of the other reconstructed hard objects, like electrons, muons, from the initial momentum. Thus, $E_{\mathrm{T}}^{\mathrm{miss}}$ represents existing of undetectable particles [55]. The calculation of $E_{\mathrm{T}}^{\mathrm{miss}}$ is

$$E_{x(y)}^{miss} = E_{x(y)}^{miss,e} + E_{x(y)}^{miss,\gamma} + E_{x(y)}^{miss,\tau} + E_{x(y)}^{miss,jets} + E_{x(y)}^{miss,CellOut\_Eflow} + E_{x(y)}^{miss,\mu}, \tag{4.6}$$

where each terms are calculated by the negative sum of the corresponding objects cell energies in the $|\eta| < 4.9$, except $E_{x(y)}^{miss,\mu}$ is $|\eta| < 2.7$. The $E_{\mathrm{T}}^{\mathrm{miss}}$ muon is calculated from the momentum of muons using MS tracks matching to the tracks of ID and muon spectrometers to qualify muons and to avoid the contribution from the fake muons. A correction for the energy loss in the cryostat caused by a gap between the EM and tile calorimeter has to be considered. It turns out about ~5% with $p_{\mathrm{T}} > 500\,\mathrm{GeV}$ in each jets. If the pile-up suppression correction terms, $E_{x(y)}^{miss,jets,JVFCut}$ and $E_{x(y)}^{miss,CellOut\_Eflow\_STVF}$, are added to this $E_{\mathrm{T}}^{\mathrm{miss}}$, the corrected $E_{\mathrm{T}}^{\mathrm{miss}}$ will be :

$$E_{x(y)}^{miss,STVF} = E_{x(y)}^{miss,e} + E_{x(y)}^{miss,\gamma} + E_{x(y)}^{miss,\tau} + E_{x(y)}^{miss,jets,JVFCut} + E_{x(y)}^{miss,CellOut\_Eflow\_STVF} + E_{x(y)}^{miss,\mu}, \tag{4.7}$$

where, STVF stands for the Soft Term Vertex Fraction. However, the calo-based $E_{\mathrm{T}}^{\mathrm{miss}}$ still is affected by pile-up. Pile-up has little dependence on the track-based $E_{\mathrm{T}}^{\mathrm{miss}}$ since it matches the tracks to the PMV. This $E_{\mathrm{T}}^{\mathrm{miss}}$ is denoted by $p_{\mathrm{T}}^{\mathrm{miss}}$. To calculate a total $p_{\mathrm{T}}^{\mathrm{miss}}$, following definition is used :

$$\vec{E}_{\mathrm{T}}^{\mathrm{miss,track,jetCorr}} = -\sum_{\text{i trks}} \vec{p}_{\mathrm{T}}^{\,i} + \sum_{\text{j jets}} \left(\vec{p}_{\mathrm{T}}^{\,j,\mathrm{trk}} - \vec{p}_{\mathrm{T}}^{\,j,\mathrm{calo}} \right), \tag{4.8}$$

where $\vec{p}_{\mathrm{T}}^{\,j,\mathrm{trk}}$ are all tracks associated to jet j and $\vec{p}_{\mathrm{T}}^{\,j,\mathrm{calo}}$ is the jet area corrected transverse momentum of the jet.

CHAPTER 5

Statistical Methods

In this chapter, statistical tools used at the LHC and particular modeling strategies incorporated within ATLAS are discussed. The probability concepts imposed in this study are based on the frequentist approach that defines [6, 56] :

$$P(A) = \lim_{n\to\infty} \frac{number\ of\ occurrences\ of\ outcome\ A\ in\ n\ measurements}{n} \tag{5.1}$$

In experiment, the probability tends to be a continuous variable. The Probability Density Function (p.d.f) is that the probability to find a single continuous variable x can be found within the infinitesimal interval [x, x+dx], and is denoted by $f(x)$, as represented in Eq. 5.2.

$$P(x \in [x, x + dx]) = f(x)\, dx \tag{5.2}$$

where $f(x)$ is normalized to one within the total space of S :

$$\int_S f(x)\, dx = 1 \tag{5.3}$$

The Poisson distribution is proper to handle independent events, hence, the sum of all events is the combination of the distribution of individual events.

$$Pois(N \mid \nu) = \nu^N \frac{e^{-\nu}}{N!} \tag{5.4}$$

5.1 Profile Likelihood Function

The likelihood function ($\mathcal{L}$) is the probability of a certain parameter or a set of parameters in a given output. A simple practical example is the number of observed events in a single bin N consisting of expected signal events S and background events B. The parameter μ normalizes the S and is called a signal strength, in which $\mu = 0$ represents the background only model (null hypothesis) and $\mu = 1$ corresponds to the SM signal model.

Using the Poisson function, the likelihood function is defined as

$$\mathcal{L}(\mu) = Pois(N \mid \mu S + B) \tag{5.5}$$

Since the N, S and B are constant, the $\mathcal{L}$ is the function of μ. If we have several different analysis categories, the likelihood is expressed by the combination of likelihoods in each categories. The B is normalized with a nomalization factor (θ) that is calculated from Control Region (CR) in the background studies, as represented in Eq. 5.6.

$$\mathcal{L}(\mu, \theta) = \prod_{c \in categories} [Pois(N_c \mid \mu S_c + \theta B_c) \prod_{c \in categories} f(N_{CR,c} \mid \theta B_{CR,c})] \tag{5.6}$$

Among two apart of the Likelihood function, the first Poisson corresponds to the signal-enriched region and the second part is about background treatment. Thus, the signal related parameter μ contains the information in that we are interested. This μ, therfore, can be a Parameter of Interest (POI). The factor θ becomes a nuisance parameter (NP) and the N_{CR} is an auxiliary measurement or a global observable that contains the auxiliary information.

Now, the $\mathcal{L}$ is the function of μ and θ. The multiple-parameter analysis asks more complicated treatment. Unlike with one parameter, in the multiple-parameter analysis, the other parameter's behaviors can affect to the calculation of the $\mathcal{L}$. Each parameters in the list are fully estimated to have a maximized likelihood, and this is called "the Maximum

Likelihood Estimator (MLE)". Therefore, the value of two parameters are determined to maximize the likelihood. The MLE of θ is denoted as $\hat{\theta}$ and the estimated μ is denoted as $\hat{\mu}$.

For finding the maximum of $\mathcal{L}$ in a multiple parameter function, the profile likelihood function is adopted. The profile likelihood function reduces the number of independent parameters by fixing one parameter at where the $\mathcal{L}$ is maximized. Then, the $\mathcal{L}$ becomes a function of only one un-known parameter. For example, when we work with $\mathcal{L}(\mu, \theta)$, a MLE of θ is used, then $\hat{\theta}_\mu$ is a function of mu. Then we can find μ value where the likelihood is maximized and that is represented as $\hat{\mu}$.

The MLE and the profile likelihood are important to define the profile likelihood function ratio (PLR) that is used later as a test statistics.

5.2 Test Statistics

The most common used test statistics in the practical physics is the PLR [56] without including the systematics. To handle with systematics, we have used suxilary measurement. Under the hypothesis testing, the PLR method has the most discriminating power between two different hypotheses. The basic form of PLR is given as follows :

$$\lambda(\mu) = \frac{\mathcal{L}(\mu, \hat{\hat{\theta}})}{\mathcal{L}(\hat{\mu}, \hat{\theta})} \tag{5.7}$$

and the more generic form can be re-defined :

$$t_\mu = -2 \ln \lambda(\mu) \tag{5.8}$$

where t_μ is a test statistics.

The negative logarithm makes possible the t_μ transforming to be like the χ^2 distribution, which is more adoptable formation for statistical treatments to the particle physics,

like the $p-$value and the limit measurement [6]. Higher values of t_μ indicates increasing incompatibility between the data and the μ [56]. The numerical representative of this disagreement is defined as the $p-value$, defined as

$$p_\mu = \int_{t_{\mu,obs}}^{\infty} f(t_\mu \mid \mu) dt_\mu \tag{5.9}$$

where $t_{\mu,obs}$ is a observed t_μ value in the data and $f(t_\mu \mid \mu)$ is a pdf of t_μ under the given signal strength μ.

Since the positive number of signal events are expected to find, the process has $\mu \geq 0$. With considering the case of $\hat{\mu} < 0$ (such that one finds fewer events than even predicted by background processes alone), the nominal likelihood are divided into two categories based on $\hat{\mu}$ value :

$$\tilde{\lambda}(\mu) = \begin{cases} \frac{\mathcal{L}(\mu,\hat{\hat{\theta}}_\mu)}{\mathcal{L}(\hat{\mu},\hat{\theta})}, & \hat{\mu} \geq 0 \\ \frac{\mathcal{L}(\mu,\hat{\hat{\theta}}_\mu)}{\mathcal{L}(0,\hat{\hat{\theta}}(0))}, & \hat{\mu} < 0 \end{cases} \tag{5.10}$$

$\tilde{\lambda}(\mu)$ is used to discriminate from the nominal profile likelihood that the region is not divided. The test statistics have different range for $\hat{\mu}$. The corresponding test statistics are

$$\tilde{t_\mu} = -2ln\tilde{\lambda}(\mu) = \begin{cases} -2ln\frac{\mathcal{L}(\mu,\hat{\hat{\theta}}_\mu)}{\mathcal{L}(0,\hat{\hat{\theta}}(0))}, & \hat{\mu} < 0 \\ -2ln\frac{\mathcal{L}(\mu,\hat{\hat{\theta}}_\mu)}{\mathcal{L}(\hat{\mu},\hat{\theta})}, & \hat{\mu} \geq 0 \end{cases} \tag{5.11}$$

As seen in Eq. 5.10 and Eq. 5.11, $\mu = 0$ is considered a very special case. Rejecting this hypothesis respect to the testing hypothesis has a power to the discovery of a new signal. Therefore, a special notation for the $q_0 = \tilde{t_0}$ is defined as follows :

$$q_0 = \begin{cases} -2\ln\lambda(0), & \hat{\mu} > 0 \\ 0, & \hat{\mu} \leq 0 \end{cases} \tag{5.12}$$

$\lambda(0)$ is the PLR for $\mu = 0$ as defined in Eq. 5.7. Using q_0, Th data shows the disagreement with the background-only hypothesis only if $\hat{\mu} > 0$. However, when the finding

events is much less than the expected number of events, $\hat{\mu}$ is less than 0. For this case, it is treated as $q_0 = 0$. The quantified level of disagreement becomes as follows by using Eq. 5.9.

$$p_0 = \int_{q_0,obs}^{\infty} f(q_0 \mid \mu) dq_0 \tag{5.13}$$

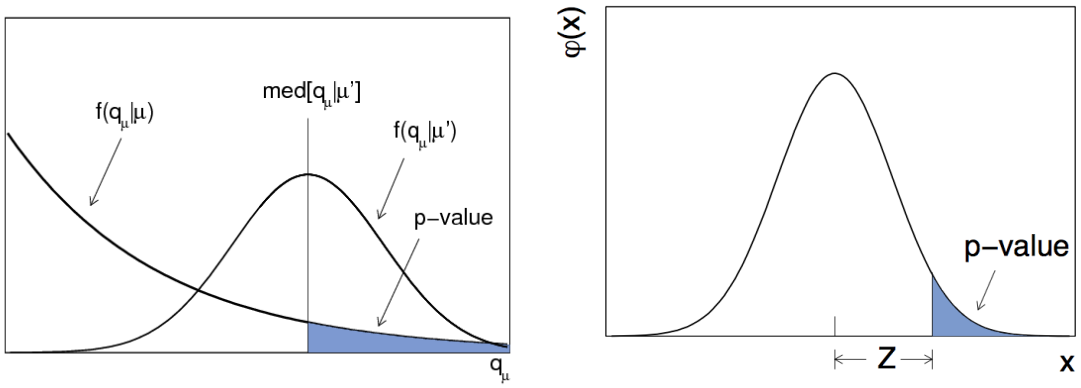

Figure 5.1: Illustration of the relation between the p-value obtained from an observed value of the test statistic t_μ. The standard normal distribution of $\phi(x) = (1/\sqrt{2\pi})e^{(-x^2/2)}$ showing the relation between the significance Z and the p-value.

The $p - value$ is historically expressed in its converted form, so called the $Z - value$ in the unit of σ. The definition is

$$Z = \Phi^{-1}(1 - p_0) \tag{5.14}$$

where Φ^{-1} is the inverse of the cumulative distribution for a unit Gaussian. The significance for the declaration of the discovery is $Z = 5\ \sigma$, corresponding to $p_0 = 2.87 \times 10^{-7}$. Fig. 5.1 illustrates the $p - value$ and the $Z - value$.

When the μ have an upper limit, different test statistics are applied for the different $\hat{\mu}$ region as follows.

$$q_\mu = \begin{cases} -2\ln\lambda(\mu), & \hat{\mu} \le \mu \\ 0, & \hat{\mu} > \mu \end{cases} \tag{5.15}$$

In the case of considering $\hat{\mu} \ge 0$, the variable $\lambda(\mu)$ is replaced by the variable $\tilde{\lambda}(\mu)$. Therefore, the final definition of test statistics, denoted as $\tilde{q}_\mu$, is

$$\tilde{q}_\mu = \begin{cases} -2\ln\frac{\mathcal{L}(\mu,\hat{\hat{\theta}}_\mu)}{\mathcal{L}(0,\hat{\hat{\theta}}(0))}, & \hat{\mu} < 0 \\ -2\ln\frac{\mathcal{L}(\mu,\hat{\hat{\theta}}_\mu)}{\mathcal{L}(\hat{\mu},\hat{\theta})}, & 0 \le \hat{\mu} < \mu \\ 0, & \hat{\mu} \ge \mu \end{cases} \tag{5.16}$$

The CLs is a statistical method for setting upper limits on model parameters [57]. To avoid falsely excluding given a strong deficit, the exclusion limit have limited with $1 - p_b$, as seen from the equation below :

$$CLs = \frac{p_\mu}{1 - p_b} \tag{5.17}$$

where p_b is the $p - value$ that is from the background only hypothesis distribution. The standard confidence level for limits is 5% for the historical reason. Fig. 5.2 shows the concepts of the CLs.

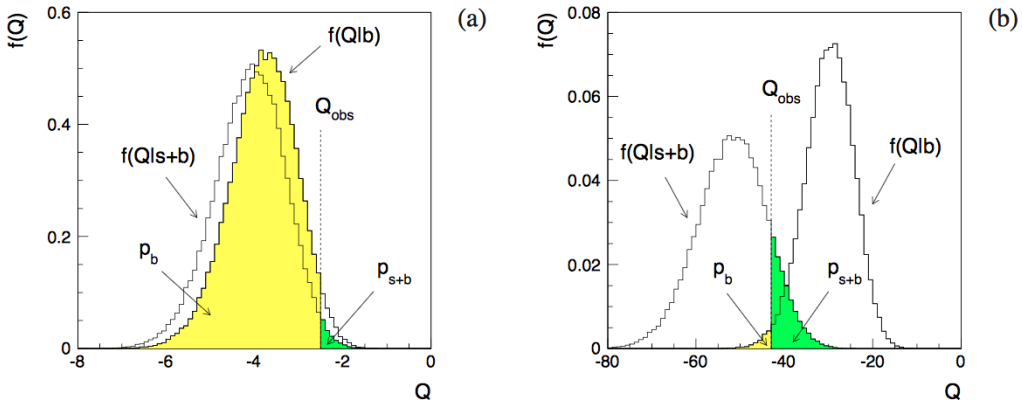

Figure 5.2: (a) Distributions of the statistic Q indicating low sensitivity to the hypothesized signal model and (b) an illustration of the ingredients for the CLs limit.

5.3 Systematic Treatments

The measurements of background and signal events other than a signal region, like a control region, theoretical calculations, are called auxiliary measurements, represented by $N(\tilde{\theta} \mid \theta)$ and the parameters(θ) in this measurement are nuisance parameters that represents the uncertainty. The expected rate is defined :

$$\epsilon(\theta) = \epsilon_0 \nu(\theta) \tag{5.18}$$

where ϵ_0 is the nominal expected rate, and $\nu(\theta)$ is the corresponding function to the nuisance parameter θ. The exact auxiliary measurement can be differ depending on their natures.

Statistical Uncertainties

Statistical uncertainties are mostly coming from the MC uncertainties and are modeled by the Poisson distribution.

$$\begin{aligned} N(\tilde{\theta} \mid \theta) &= P(\tilde{\theta} \mid \theta M) \\ \nu(\theta) &= \theta \end{aligned} \tag{5.19}$$

where M is a nominal value of $\tilde{\theta}$. The number of events of signal and backgrounds that includes those uncertainties would be then :

$$N^{MC}(\vec{\theta}) = N_0^{MC}(\theta) \prod_{\kappa}^{N_{syst}} \theta_\kappa \tag{5.20}$$

where N_0^{MC} is the MC signal and background events of the nominal value of the nuisance parameters.

Normalization Uncertainties

Normalization uncertainties are treated by the Gaussian distribution to normalize the m_{T} distribution.

$$\begin{aligned} N(\tilde{\theta}|\theta) &= G(\tilde{\theta}|\theta, 1) \\ \nu(\theta) &= \kappa^{\theta} \end{aligned} \tag{5.21}$$

The variation of the uncertainty is $\pm 1\sigma$ of the Gaussian. The number of events of signal and backgrounds that includes those uncertainties would be then :

$$N^{MC}(\vec{\theta}) = N_0^{MC}(\theta) \prod_{\kappa}^{N_{syst}} (1 + \epsilon_{\kappa})^{\theta_{\kappa}} \tag{5.22}$$

The nominal values are varied by $(1+\epsilon)^{\theta}$ within the systematic error range and the equation is redefined using $\nu(\theta) = \kappa^{\theta}$, as seen in Eq. 5.23 :

$$\epsilon^{i}_{\kappa_{\pm}} = \frac{N^{i}_{\kappa,exp}(\pm\ 1)}{N^{i}_{\kappa,exp}(0)} \tag{5.23}$$

where i indicates each CR regions.

Shape Uncertainties

Uncertainties from changing the shape of m_{T} distribution is also the Gaussian distribution that are :

$$N^{MC}(\vec{\theta}) = N_0^{MC}(\theta) \prod_{\kappa}^{N_{syst}} (1 + \epsilon_{\kappa}\theta_{\kappa)} \tag{5.24}$$

ϵ_{κ} is setting $\theta = \pm 1\sigma$. Even though it uses the same Gaussian function, the format of function is different with the normalization uncertainty case for the historical reason.

CHAPTER 6

$H \to WW^* \to \ell\nu\ell\nu$ Analysis

6.1 $H \to WW^* \to \ell\nu\ell\nu$ Analysis

At the Higgs mass of 125 GeV, the $H \to WW^* \to \ell\nu\ell\nu$ has comparatively, with respect to the other decay modes, a large branching ratio ($\mathcal{B}$), thus it is a good candidate to search for the Higgs signal at the LHC. The most dominant production mode is the gluon-gluon fusion (ggF). In the SM, the ggF produces the Higgs particle primarily through a top quark loop. The vector-boson fusion (VBF) is the second highest production mode whose cross section is approximately twelve times smaller than the ggF cross section. The VBF is followed by the associated production mode (VH). Therefore, in this study, these production modes are considered as major production modes at the LHC. The Feynman diagrams of the leading order productions are shown in Fig. 6.1.

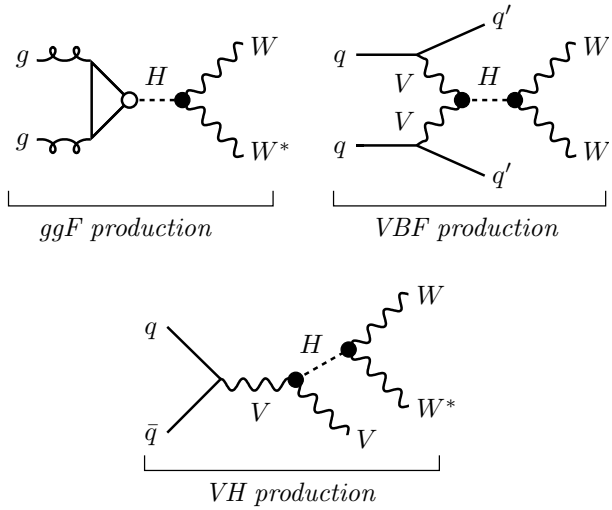

Figure 6.1: Feynman diagrams for the Higgs production modes (ggF, VBF, and VH) at the LHC, where the Higgs coupling vertices to bosons and fermions are indicated by • and ∘, respectively. The V represents a W or Z vector boson in the figure.

6.1.1 Analysis Overview

The analysis strategy is summarized in Fig. 6.2. As the flowchart describes, the analysis is divided into sub-categories based on the lepton flavor combination in the final state ($ee/\mu\mu$ or $e\mu$), the jet multiplicity in the selected events (n_j), and the production modes (ggF and VBF).

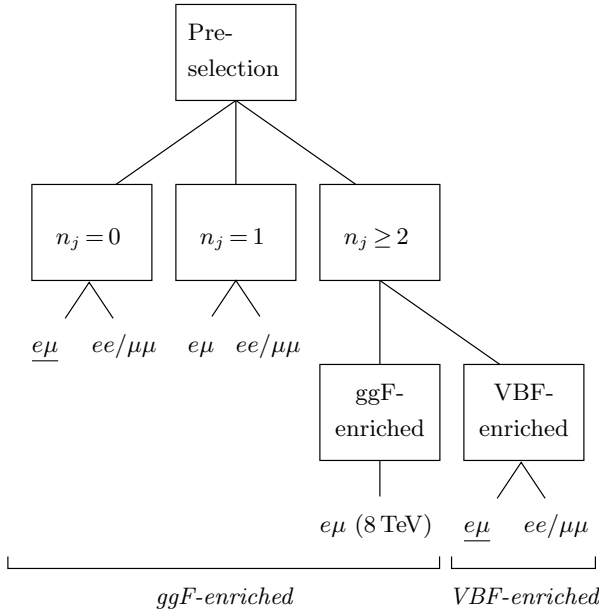

Figure 6.2: Analysis categories based on the jet multiplicity (n_j), the lepton flavour combinations ($e\mu$ and $ee/\mu\mu$) and the production modes (ggF and VBF).

The $H \to WW^* \to \ell\nu\ell\nu$ final state consists of two leptons and two neutrinos from the W boson decays ($W \to \ell\nu$, $l = e, \mu$). Therefore the lepton pair flavor combination can be $ee/\mu\mu$ (Same Flavor, SF) or $e\mu$ (Different Flavor, DF). Also, the number of jets is used to define the analysis categories. In ggF, there are three categories, $n_j = 0$, 1 and $n_j \geq 2$, while in the VBF, only one category exists, $n_j \geq 2$. The ggF $n_j = 0$ and $n_j = 1$ categories is subdivided into SF and DF channels. However, only DF channel is considered in the ggF $n_j \geq 2$ category because of the low sensitivity of the SF channel. The VBF $n_j \geq 2$ events

are subdivided into two categories according to the lepton flavour combination, DF or SF. In this study, regions sensitive to the ggF production are called "ggF-enriched" while those sensitive to VBF are called "VBF-enriched". Unlike the ggF analysis, the VBF analysis uses a Multi Variate Analysis (MVA) based on the boosted decision tree (BDT) algorithm [58]. In the ggF-enriched categories a veto is applied to remove events that pass the VBF selection criteria. The backgrounds for this analysis are listed in Table 6.1 and jet multiplicity distributions are shown in Fig. 6.3 together with the distribution of the number of b-tagged jets (n_b).

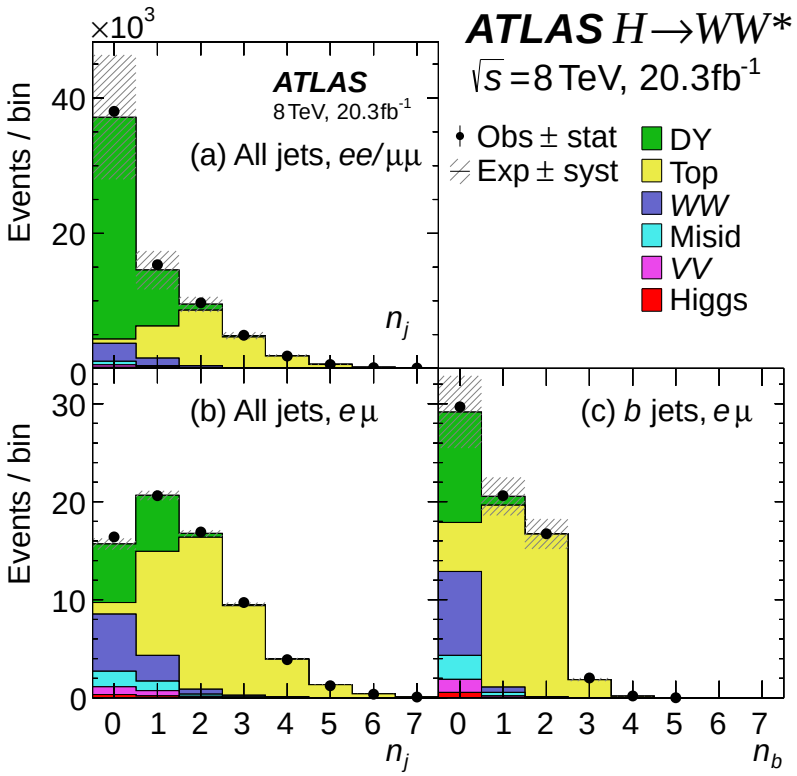

Figure 6.3: Jet multiplicity distributions for all jets (n_j) and b-tagged jets (n_b). The plots are made after applying the preselection criteria common to all jet categories.

The Drell-Yan (DY) process is an important background in all jet bins, neverthless it is particularly abundant in the SF channel, therefore it is treated in different ways in

Table 6.1: The list of backgrounds to the $H \to WW^* \to \ell\nu\ell\nu$, where ℓ is an electron or muon.

Name	Process	Feature(s)
WW	WW	Irreducible
Top quarks		
$t\bar{t}$	$t\bar{t} \to Wb\,W\bar{b}$	Unidentified b-quarks
t	tW	Unidentified b-quark
	$t\bar{b}$, $tq\bar{b}$	q or b misidentified as ℓ; unidentified b-quarks
Misidentified leptons (Misid.)		
Wj	W + jet(s)	j misidentified as ℓ
jj	Multijet production	jj misidentified as $\ell\ell$; misidentified neutrinos
Other dibosons		
VV	$W\gamma$	γ misidentified as e
	$W\gamma^*$, WZ, $ZZ \to \ell\ell\,\ell\ell$	Unidentified lepton(s)
	$ZZ \to \ell\ell\,\nu\nu$	Irreducible
	$Z\gamma$	γ misidentified as e; unidentified lepton
Drell-Yan (DY)		
$ee/\mu\mu$	$Z/\gamma^* \to ee$, $\mu\mu$	Misidentified neutrinos
$\tau\tau$	$Z/\gamma^* \to \tau\tau \to \ell\nu\nu\,\ell\nu\nu$	Irreducible

the DF and SF channels. Top backgrounds, including single-top, are also notable. This background is characterised by the presence of high-momentum jets, neverthless it can be suppressed by vetoing on the presence of b-tagged jets. Top backgrounds represent a high fraction of the background in the $n_j \geq 1$ categories, its reduction is difficult due to inefficiencies in the b-jet identification algorithm. Comparing with DY and top backgrounds, the WW background is difficult to reduce because its final state is identical to the signal. After the removal of DY and top backgrounds, the WW background is the main background in the $n_j = 0$ category which is the most sensitive one. However, due to the spin-0 nature of the SM Higgs [59], the final decay products of the $H \to WW^* \to \ell\nu\ell\nu$ tend to

be more collinear than those of the WW continuum. Therefore, the leptons from the W decay of the signal events lie in the lower range of the distribution of the dilepton system invariant mass ($m_{\ell\ell}$). Therefore the WW background is reduced with an upper cut on $m_{\ell\ell}$. Monte Carlo (MC) samples are used for all backgrounds and normalized to data using special control regions, except for Wj and multi-jet backgrounds that uses only data to extract the rate of misidentifying jets as leptons. The 7 TeV data analysis uses the same methods of the 8 TeV analysis. A profile likelihood fit is performed simultaneously to combine the results from all these categories.

6.1.2 Data and Monte Carlo Samples

6.1.2.1 MC samples

In order to understand the huge number of backgrounds, Monte Carlo (MC) samples are used. The signal and most background samples are produced by various MC tools. A list of the MC tools is summarized in Table 6.2 with the $\sigma \cdot \mathcal{B}$ (cross section $\times$ branching fraction) that is used to normalize each process.

The POWHEG [27] MC which includes the next-to-leading-order (NLO) correction in α_S, is used for the ggF and VBF signal samples and some of the di-boson backgrounds (WZ and ZZ backgrounds) in the higher invariant mass ($m_{\ell\ell}$) regions ($m_{\ell\ell} > 7\,\text{GeV}$ and $m_{\ell\ell} > 4\,\text{GeV}$, respectively). These POWHEG samples are showered with PYTHIA8 [29]. Due to POWHEG+PYTHIA8's inability to produce low $m_{\ell\ell}$ off-shell dilepton pairs, SHERPA [32] is used to model for low $m_{\ell\ell}$ range. SHERPA also produces WW background samples for $n_j \geq 2$. PYTHIA6 [28] is combined with powheg to generate top background samples and a part of WW backgrounds, such as $q\bar{q}/qg \to WW$. ALPGEN [33]+HERWIG [30] provides $W\gamma$ and DY background samples with merged tree-level calculations up to five jets. The pile-up is also modeled with PYTHIA8. The parton distribution function (PDFs) used are CT10 [60] for the

Table 6.2: The list of Monte Carlo generators used to model the signal and background processes with their corresponding cross sections times branching fractions, $\sigma \cdot \mathcal{B}$, for $\sqrt{s} = 8$ TeV.

Process		MC generator	$\sigma \cdot \mathcal{B}$ (pb)
Signal			
ggF	$H \to WW^*$	POWHEG+PYTHIA8	0.435
VBF	$H \to WW^*$	POWHEG+PYTHIA8	0.0356
VH	$H \to WW^*$	PYTHIA8	0.0253
WW			
$q\bar{q} \to WW$ and $qg \to WW$		POWHEG+PYTHIA6	5.68
$gg \to WW$		GG2VV+HERWIG	0.196
$(q\bar{q} \to W) + (q\bar{q} \to W)$		PYTHIA8	0.480
$q\bar{q} \to WW$		SHERPA	5.68
VBS WW+ 2 jets		SHERPA	0.0397
Top quarks			
$t\bar{t}$		POWHEG+PYTHIA6	26.6
Wt		POWHEG+PYTHIA6	2.35
$tq\bar{b}$		ACERMC+PYTHIA6	28.4
$t\bar{b}$		POWHEG+PYTHIA6	1.82
Other dibosons (VV)			
$W\gamma$	($p_{\mathrm{T}}^{\gamma} > 8$ GeV)	ALPGEN+HERWIG	369
$W\gamma^*$	($m_{\ell\ell} \leq 7$ GeV)	SHERPA	12.2
WZ	($m_{\ell\ell} > 7$ GeV)	POWHEG+PYTHIA8	12.7
VBS WZ + 2 jets	($m_{\ell\ell} > 7$ GeV)	SHERPA	0.0126
$Z\gamma$	($p_{\mathrm{T}}^{\gamma} > 8$ GeV)	SHERPA	163
$Z\gamma^*$	(min. $m_{\ell\ell} \leq 4$ GeV)	SHERPA	7.31
ZZ	($m_{\ell\ell} > 4$ GeV)	POWHEG+PYTHIA8	0.733
$ZZ \to \ell\ell\nu\nu$	($m_{\ell\ell} > 4$ GeV)	POWHEG+PYTHIA8	0.504
Drell-Yan			
Z	($m_{\ell\ell} > 10$ GeV)	ALPGEN+HERWIG	16500
VBF Z + 2 jets	($m_{\ell\ell} > 7$ GeV)	SHERPA	5.36

POWHEG and SHERPA samples and CTEQ6L1 [65] for ALPGEN+HERWIG and ACERMC samples. The Z/γ^* sample is re-weighted to MRSTmcal PDF set [66].

6.1.2.2 Data Samples

Data

The full Run-1 data was used with an integrated luminosity of 20.3 fb^{-1} taken at $\sqrt{s} = 8$ TeV in 2012 and 4.5 fb^{-1} at 7 TeV in 2011. In order to maintain the data quality, events in data are analyzed only if they were recorded while the detector was running normally.

Triggers

The details of the trigger requirements for 8 TeV are shown in Table 6.3. The trigger selection efficiency was studied by using a tag-and-probe method with Z/γ^* data samples. The single lepton trigger efficiency is about 70% for $|\eta| < 1.05$ and 90% for $|\eta| > 1.05$ for muons. For electrons, it is about 90% and increases with the transverse momentum (p_{T}).

Table 6.3: The minimum lepton p_{T} trigger requirements for the 8 TeV data (in GeV).

Name	Level-1 trigger	High-level trigger
Single lepton		
e	18 or 30	24i or 60
μ	15	24i or 36
Dilepton		
e, e	10 and 10	12 and 12
μ, μ	15	18 and 8
e, μ	10 and 6	12 and 8

6.1.3 Objects and Events Selection

6.1.3.1 Leptons

The selection of leptons affects the background composition of this analysis; especially for the W+jets, QCD multi-jet, and the WW backgrounds. In this study, we restrict leptons to be either an electron or a muon. Since the combination of leptons in the final state plays a key role for background removals and affects the background rejections, the analysis is sub-divided into categories depending on the lepton flavor combination: $e\mu$ and $ee/\mu\mu$. In addition to the standard ATLAS requirements on leptons, described in Chapter 4, further selections are made on the object reconstruction and identification. In particular cuts on the longitudinal and transverse impact parameters of the associated track, using the variables d_0/σ_{d_0} and $z_0 \sin\theta$. Moreover, cuts are imposed on the calorimeter-based and track-based isolation variables.

Electrons

The electron selection utilizes two different E_{T} ranges. For low E_{T} electrons, $10 < E_{\mathrm{T}} < 25\,\mathrm{GeV}$, the "Very Tight Likelihood (VTLH)" identification [45] is used while for higher E_{T} electrons, the medium cut-based identification is used. For soft electrons, $E_{\mathrm{T}} < 25\,\mathrm{GeV}$, the VTLH is used to reduce backgrounds from light flavor jets and photon conversions while maintaining a reasonable efficiency. However, in the relatively higher E_{T} region, $E_{\mathrm{T}} > 25$ GeV, there is less chance of background objects to be mis-identified as electrons. Thus, the higher efficiency medium cut-based identification is used for high E_{T} electrons. In addition to the two identification algorithms, electrons converted from photons (the conversion flag) are rejected if the associated track did not have a hit in the innermost (b-layer)layer of the pixel detector in ATLAS. The lepton isolation requirements for electrons are specified in Table 6.4. The cone size for calorimeter isolation is 0.3, while the cone size for track based isolation is 0.3 (0.4) for electrons with $E_{\mathrm{T}} > 15$ (< 15) GeV. The

relative calorimeter isolation is required to be $\Sigma E_{\mathrm{T}}/E_{\mathrm{T}} < 0.2 - 0.28$, while the relative track isolation is required to be $\Sigma p_{\mathrm{T}}/E_{\mathrm{T}} < 0.06 - 0.10$ depending on the candidate electron E_{T}. the total electron selection efficiency is summarized in the Table 6.5.

Table 6.4: Electron selection as a function of E_T.

E_T (GeV)	electron ID	calo. isolation topoEtConeCor	track isolation Ptcone	impact parameters
10-15	Very Tight LH	$(\mathrm{iso}(0.3))/E_T < 0.20$	$(\mathrm{iso}(0.4))/E_T < 0.06$	$d_0/\sigma_{d_0} < 3.0$, $z_0 \sin\theta < 0.4$ mm
15-20		$(\mathrm{iso}(0.3))/E_T < 0.24$	$(\mathrm{iso}(0.3))/E_T < 0.08$	
20-25		$(\mathrm{iso}(0.3))/E_T < 0.28$	$(\mathrm{iso}(0.3))/E_T < 0.10$	
> 25	Medium			

Table 6.5: Total electron selection efficiencies and uncertainties for an $m_H = 125$ GeV Higgs signal sample.

E_T	Total Eff.	Iso. unc. (relative)	ID+Rec. unc. (relative)	Total Unc. (relative)
10-15	0.412	0.016	0.016	0.022
15-20	0.619	0.009	0.024	0.025
20-25	0.668	0.008	0.027	0.028
25-30	0.755	0.007	0.014	0.016
30-35	0.770	0.007	0.005	0.009
35-40	0.796	0.006	0.003	0.007
40-45	0.798	0.006	0.002	0.006
45-50	0.813	0.006	0.002	0.006

Muons

For muons, lepton isolation requirements are similar to those for electrons. The relative requirements vary from 0.06 to 0.3 and 0.06 to 0.12 for the calorimeter and track-based isolation, respectively. The muon associated tracks are required to have $d_0/\sigma_{d_0} < 3.0$

and $z_0 \sin\theta < 1.0$. The criteria are summarized in Table 6.6 and the total muon selection efficiency and uncertainty as a function of p_{T} is summarized in Table 6.11.

Table 6.6: Muon selection.

p_T (GeV)	calo. isolation EtConeCor	track isolation Ptcone	impact parameters
10-15	$(\mathrm{iso}(0.3))/p_T < 0.06$	$(\mathrm{iso}(0.4))/p_T < 0.06$	$d_0/\sigma_{d_0} < 3.0$, $z_0 \sin\theta < 1.0$ mm
15-20	$(\mathrm{iso}(0.3))/p_T < 0.12$	$(\mathrm{iso}(0.3))/p_T < 0.08$	
20-25	$(\mathrm{iso}(0.3))/p_T < 0.18$	$(\mathrm{iso}(0.3))/p_T < 0.12$	
> 25	$(\mathrm{iso}(0.3))/p_T < 0.30$		

Table 6.7: Total muon selection efficiencies and uncertainties for an $m_H = 125$ GeV Higgs signal sample.

E_T	Total Eff.	Iso. unc. (relative)	ID+Rec. unc. (relative)	Total Unc. (relative)
10-15	0.574	0.027	< 0.005	0.027
15-20	0.808	0.012	< 0.005	0.013
20-25	0.904	0.007	< 0.005	0.009
25-30	0.924	0.006	< 0.005	0.008
30-35	0.932	0.006	< 0.005	0.008
35-40	0.942	0.005	< 0.005	0.007
40-45	0.943	0.005	< 0.005	0.007
45-50	0.944	0.005	< 0.005	0.007

6.1.3.2 Jets

Since the analysis depends on the number of jets (n_j), the definition of jet is important. In order to have an accurate number of jets in the event, it is important that our jet selection avoids to have jets initiated from pileup vertices. In this analysis, jets are required to satisfy the following criteria::

- $|\eta| < 4.5$

- $p_T > 25$ (30) GeV in the region of $|\eta| < 2.4$ ($2.4 \leq |\eta| \leq 4.5$) for the central jet (the forward jet)
- $|JVF| > 0.5$ for $p_T < 50$ GeV and $|\eta| < 2.4$

The p_{T} requirement for jets is higher in the forward regions in order to suppress pile-up initiated jets. Having the Jet Energy Fraction (JVF) value greater than 0.5 also gives the optimal point to suppress pile-up jets. The JVF is only defined for central jets due to the acceptance of the tracker (see chapter 4.2.4).

b-Jets

The MV1 algorithm [67] is used to identify jets initiated by a b quark. A value of 100 % implies that a jet is very b-like, while the value of 0 % implies the jet is initiated from a light quark or gluon. An operating point of 85% was chosen based on a comprehensive study [68]. Table 6.8 shows the expected significance using 80 and 85% operating points. In order to maximally suppress top backgrounds, the p_{T} threshold for b-tagged jets is 20 GeV rather than 25 GeV.

Table 6.8: Expected significance when using 80% and 85% operating point for the b-tagged jet selection.

operating point	Z_{exp}^{DF0j}	Z_{exp}^{DF1j}	Z_{exp}^{DF01j}	$\hat{\mu}_{exp}^{DF01j}$
85% o.p.	2.32	1.65	2.80	$1^{+0.43}_{-0.38}$
80%	2.32	1.62	2.76	$1^{+0.44}_{-0.38}$

6.1.3.3 Missing Transverse Energy

In addition to the calo-based $E_{\mathrm{T}}^{\mathrm{miss}}$ (defined in chapter 4.2.5), this analysis improves the optimal $E_{\mathrm{T}}^{\mathrm{miss}}$ measurement by utilizing the tracks associated with the primary vertex (PMV). The $E_{\mathrm{T}}^{\mathrm{miss}}$ calculation is the following

$$E_{\mathrm{T}}^{\mathrm{miss}} = -\Big(\sum_{\text{selected obj.}} \boldsymbol{p}_{\mathrm{T}} + \sum_{\text{soft obj.}} \boldsymbol{p}_{\mathrm{T}} \Big), \tag{6.1}$$

when the calorimeter-based measurement is adopted. However, the presence of pile-up lowers the resolution of the $E_{\mathrm{T}}^{\mathrm{miss}}$. By replacing the soft terms in the calorimeter-based $E_{\mathrm{T}}^{\mathrm{miss}}$ with tracks ($p_{\mathrm{T}} > 0.5$ GeV) associated to the PMV, the overall $E_{\mathrm{T}}^{\mathrm{miss}}$ resolution improves by suppressing pileup effects. To distinguish it from the calorimeter-based $E_{\mathrm{T}}^{\mathrm{miss}}$, it is denoted by $p_{\mathrm{T}}^{\mathrm{miss}}$. Tracks associated with leptons or jets are not included in this term. Fig 6.4 shows the comparison between the calorimeter-based $E_{\mathrm{T}}^{\mathrm{miss}}$ and the track-based $p_{\mathrm{T}}^{\mathrm{miss}}$, where it is evident that $p_{\mathrm{T}}^{\mathrm{miss}}$ performs better than $E_{\mathrm{T}}^{\mathrm{miss}}$.

These different definitions of $E_{\mathrm{T}}^{\mathrm{miss}}$ are used to maximize the significance across all categories. Table 6.9 summarizes the $E_{\mathrm{T}}^{\mathrm{miss}}$ used in each analysis.

6.1.3.4 Events Selection

For each jet multiplicity category, special selections are applied in order to maximize the signal-background separation. Table 6.10 shows the detailed criteria for each sub-analysis. Each selection requirement is designed to reduce specific backgrounds.

Preselection

The preselection is performed before event categorization in jet multiplicity. Exactly two oppositely charged leptons satisfying the criteria described in section 4.2.2 through 4.2.3 are required. The leading p_{T} lepton ($p_{\mathrm{T}}^{\ell 1}$), and the sub-leading p_{T} lepton ($p_{\mathrm{T}}^{\ell 2}$) are required to have $p_{\mathrm{T}} > 22$ GeV and $p_{\mathrm{T}} > 10$ GeV, respectively. The invariant mass of the dilepton ($m_{\ell\ell}$) system is required to be larger than 10 GeV for DF and 12 GeV for SF in order to remove low mass Z/γ^* and low-mass meson resonance backgrounds. In the SF channel, $|m_{\ell\ell} - M_Z| > 15$ GeV is imposed and reduces the Z/γ^* background by as much as 90%.

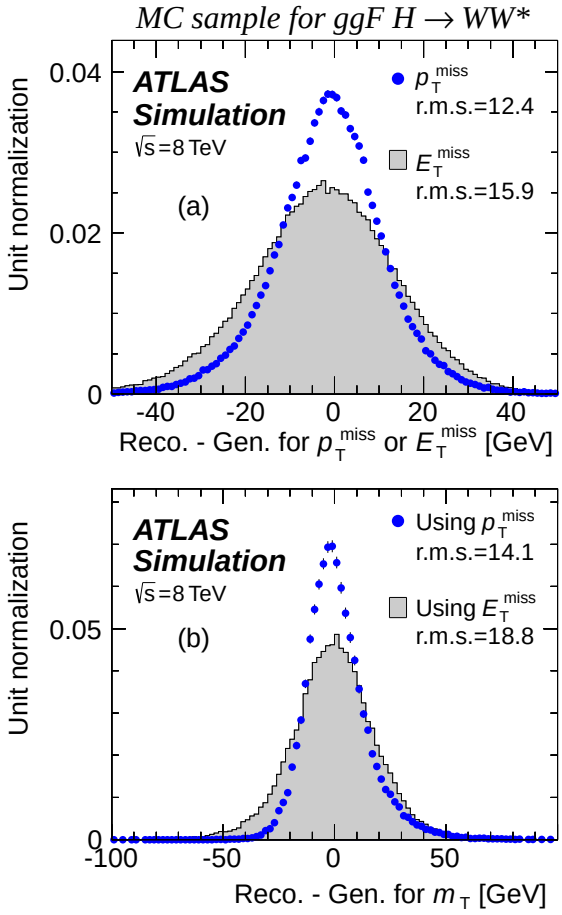

Figure 6.4: Resolutions of (a) $E_{\mathrm{T}}^{\mathrm{miss}}$ or $p_{\mathrm{T}}^{\mathrm{miss}}$ and (b) m_{T} for the ggF signal MC in the $n_j = 0$ category.

Table 6.9: Different $E_{\mathrm{T}}^{\mathrm{miss}}$ used in the $H \to WW^* \to \ell\nu\ell\nu$ analysis.

jet bin	$E_{\mathrm{T}}^{\mathrm{miss}}$ flavour	description
0j $e\mu + \mu e$	$p_{\mathrm{T}}^{\mathrm{miss\,(trk)}}$	track-based $E_{\mathrm{T}}^{\mathrm{miss}}$ with calorimeter jets
0j $ee + \mu\mu$	$p_{\mathrm{T,rel}}^{\mathrm{miss\,(trk)}}$,$E_{\mathrm{T,rel}}^{\mathrm{miss}}$	projections of the track- and calo-based $E_{\mathrm{T}}^{\mathrm{miss}}$
1j $e\mu + \mu e$	$p_{\mathrm{T}}^{\mathrm{miss\,(trk)}}$	track-based $E_{\mathrm{T}}^{\mathrm{miss}}$ with calorimeter jets
1j $ee + \mu\mu$	$p_{\mathrm{T,rel}}^{\mathrm{miss\,(trk)}}$,$E_{\mathrm{T,rel}}^{\mathrm{miss}}$	projections of the track- and calo-based $E_{\mathrm{T}}^{\mathrm{miss}}$
2j $e\mu + \mu e$	$p_{\mathrm{T}}^{\mathrm{miss}}$	track-based $E_{\mathrm{T}}^{\mathrm{miss}}$ with calorimeter jets
VBF $e\mu + \mu e$	-	-
VBF $ee + \mu\mu$	$E_{\mathrm{T}}^{\mathrm{miss}}$, $p_{\mathrm{T}}^{\mathrm{miss}}$	calo-based and track-based $E_{\mathrm{T}}^{\mathrm{miss}}$ with calorimeter jets

Table 6.10: Event selection requirements. Values are given for the analysis of 8 TeV data for $m_H = 125$ GeV in units of GeV.

Objective		ggF-enriched			VBF-enriched
		$n_j = 0$	$n_j = 1$	$n_j \geq 2$ ggF	$n_j \geq 2$ VBF
Preselection					
	All n_j	$p_{\mathrm{T}}^{\ell 1} > 22$ for the leading lepton ℓ_1 $p_{\mathrm{T}}^{\ell 2} > 10$ for the subleading lepton ℓ_2 Opposite-charge leptons $m_{\ell\ell} > 10$ for the $e\mu$ sample $m_{\ell\ell} > 12$ for the $ee/\mu\mu$ sample $\lvert m_{\ell\ell} - m_Z \rvert > 15$ for the $ee/\mu\mu$ sample			
		$p_{\mathrm{T}}^{\mathrm{miss}} > 20$ for $e\mu$ $E_{\mathrm{T,rel}}^{\mathrm{miss}} > 40$ for $ee/\mu\mu$	$p_{\mathrm{T}}^{\mathrm{miss}} > 20$ for $e\mu$ $E_{\mathrm{T,rel}}^{\mathrm{miss}} > 40$ for $ee/\mu\mu$	$p_{\mathrm{T}}^{\mathrm{miss}} > 20$ for $e\mu$ -	No MET requirement for $e\mu$ -
Reject backgrounds	DY	$p_{\mathrm{T,rel}}^{\mathrm{miss\,(trk)}} > 40$ for $ee/\mu\mu$ $f_{\mathrm{recoil}} < 0.1$ for $ee/\mu\mu$ $p_{\mathrm{T}}^{\ell\ell} > 30$ $\Delta\phi_{\ell\ell,\mathrm{MET}} > \pi/2$	$p_{\mathrm{T,rel}}^{\mathrm{miss\,(trk)}} > 35$ for $ee/\mu\mu$ $f_{\mathrm{recoil}} < 0.1$ for $ee/\mu\mu$ $m_{\tau\tau} < m_Z - 25$ -	- - $m_{\tau\tau} < m_Z - 25$ -	$p_{\mathrm{T}}^{\mathrm{miss}} > 40$ for $ee/\mu\mu$ $E_{\mathrm{T}}^{\mathrm{miss}} > 45$ for $ee/\mu\mu$ $m_{\tau\tau} < m_Z - 25$ -
	Misid.	-	$m_{\mathrm{T}}^{\ell} > 50$ for $e\mu$	-	-
	Top	$n_j = 0$ - -	$n_b = 0$ - -	$n_b = 0$ - -	$n_b = 0$ $p_{\mathrm{T}}^{\mathrm{sum}}$ inputs to BDT $\Sigma m_{\ell j}$ inputs to BDT
VBF topology		-	-		m_{jj} inputs to BDT Δy_{jj} inputs to BDT ΣC_ℓ inputs to BDT $C_{\ell 1} < 1$ and $C_{\ell 2} < 1$ $C_{j3} > 1$ for j_3 with $p_{\mathrm{T}}^{j3} > 20$ $O_{\mathrm{BDT}} \geq -0.48$
$H \to WW^* \to \ell\nu\ell\nu$ decay topology		$m_{\ell\ell} < 55$ $\Delta\phi_{\ell\ell} < 1.8$ No m_{T} requirement	$m_{\ell\ell} < 55$ $\Delta\phi_{\ell\ell} < 1.8$ No m_{T} requirement	$m_{\ell\ell} < 55$ $\Delta\phi_{\ell\ell} < 1.8$ No m_{T} requirement	$m_{\ell\ell}$ inputs to BDT $\Delta\phi_{\ell\ell}$ inputs to BDT m_{T} inputs to BDT

For the DF of ggF categories, $p_{\mathrm{T}}^{\mathrm{miss}} > 20\,\mathrm{GeV}$ is required, while for SF channel in $n_j \leq 1$ categories an $E_{\mathrm{T,rel}}^{\mathrm{miss}} > 40\,\mathrm{GeV}$ is required.

Background rejection

Each of the following requirements reduce certain backgrounds and improve the overall significance:

- $\Delta\phi_{ll,E_{\mathrm{T}}^{\mathrm{miss}}}$: Azimuthal angle between the dilepton system and the $p_{\mathrm{T}}^{\mathrm{miss\,(trk)}}$. Events are rejected if angle is close to zero.
- $m_{\tau\tau} < |m_Z - 25|$ GeV ($Z/H \rightarrow \tau\tau$-Veto) : another Z/γ^* background reduction for $n_j \geq 1$ categories. Neutrinos that result from $\tau-$lepton decays tend to be collinear with the visible decay products of the τ. This information can be used to reconstruct the invariant mass of the $di-\tau$ system (called collinear approximation) [69]. This helps to suppress both Z/γ^* and $H \rightarrow \tau\tau$ events.
- p_T^{ll} : Transverse momentum of the dilepton system. This is an additional Z/γ^* background reduction cut that is applied for the $n_j = 0$ categories. In $n_j = 0$ events, the Z/γ^* should not be boosted, therefore, p_T^{ll} should be small.
- $n_b = 0$ (b-Jet Veto) : Top backgrounds have b jet(s) that decay from the top quark(s). Removal of any b-tagged jets in $n_j \geq 1$ categories, including VBF, is a powerful discrimination for top backgrounds.
- f_{recoil} : For the SF lepton combination, this cut removes Z/γ^* events in the $n_j \leq 1$ categories. The f_{recoil} variable measures the strength of the recoil system associated to the two leptons. p_{T}^{j} is used for the $n_j = 1$ instead of $p_{\mathrm{T}}^{\ell\ell}$ used for the $n_j = 0$. The definition is given as :

$$f_{\mathrm{recoil}} = \frac{|\sum_{\mathrm{soft\ jets}} |\mathrm{JVF}| \cdot \vec{p}_{\mathrm{T}}|}{p_{\mathrm{T}}^{\ell\ell}} \tag{6.2}$$

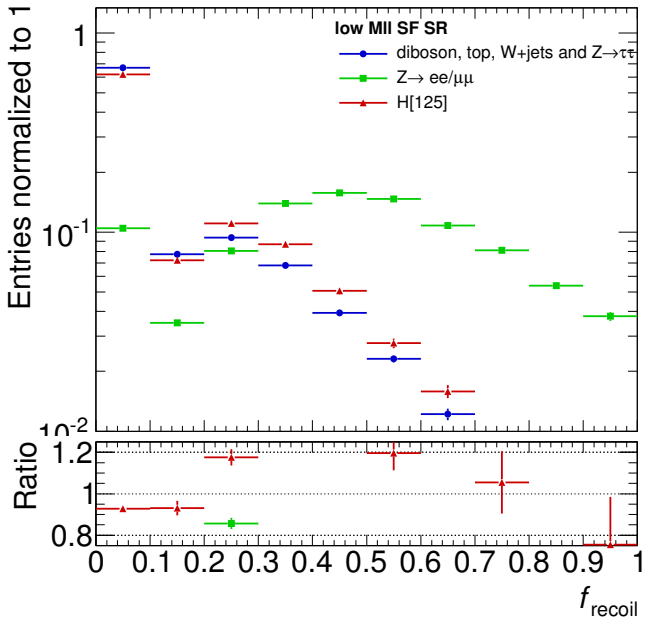

Figure 6.5: Shape of the f_{recoil} variable in the SF $N_{\text{jet}} = 0$ signal region for DY backgrounds, non-$Z/\gamma^* \to ee$, $\mu\mu$ backgrounds and 125 GeV Higgs boson signal. The $p_{\text{T}}^{\ell\ell} > 30$ threshold boosts the dilepton system, creating the shape difference.

Topological cuts to enhance Higgs signal

- $\Delta\phi_{\ell\ell}$: Due to the spin-0 nature of the SM Higgs, leptons from the signal have a tendency to lie parallel to each other. Hence, $\Delta\phi_{\ell\ell} < 1.8$ discriminates the signal from the irreducible non-resonant WW background.
- $m_{\ell\ell}$: The invariant mass of the di-lepton system. Since the leptons in signal events tend to be parallel to each other, their invariant mass also tends to be small.
- m_{T} : is the transverse mass [70] and is used for the statistical fit for the final discrimination. Its definition is

$$m_{\text{T}} = \sqrt{(E_{\text{T}}^{\ell\ell} + E_{\text{T}}^{\text{miss}})^2 - |\boldsymbol{p}_{\text{T}}^{\ell\ell} + \boldsymbol{E}_{\text{T}}^{\text{miss}}|^2},$$

where $E_{\text{T}}^{\ell\ell} = \sqrt{|\boldsymbol{p}_{\text{T}}^{\ell\ell}|^2 + m_{\ell\ell}^2}$. The $p_{\text{T}}^{\text{miss (trk)}}$ is used to improve the resolution of the selection.

VBF Topology Kinematics

The VBF uses a Boosted Decision Tree (BDT) [58] in order to separate the signal from the background. The BDT is trained with the following input variables: $m_{\ell\ell}$, m_{T}, m_{jj}, Δy_{jj}, $\Delta\phi_{\ell\ell}$, $\Sigma\, p_{\mathrm{T}}$, η_{lep} and $\Sigma\, m_{\ell j}$, described below. The final BDT score is used as the final discriminating variable in the likelihood fit.

- $\Sigma\, p_{\mathrm{T}}^{\mathrm{tot}}$: The total transverse momentum $p_{\mathrm{T}}^{\mathrm{tot}}$ of all objects is defined as :

  $$\boldsymbol{p}_{\mathrm{T}}^{l1} + \boldsymbol{p}_{\mathrm{T}}^{\mathrm{l2}} + p_{\mathrm{T}}^{\mathrm{miss}} + \sum \boldsymbol{p}_{\mathrm{T}}^{\mathrm{jets}}$$

  where the missing transverse energy used is $\boldsymbol{p}_{\mathrm{T}}^{\mathrm{miss}}$. This variable rejects QCD multi-jet and $t\bar{t}$ events with soft gluon radiation that recoils against the $\ell\ell + 2j$ system with no high-p_{T} jets.

- Δy_{jj} : The rapidity difference between the two identified jets. VBF processes produce two jets with a rapidity gap. $\Delta y_{jj} = |\, y_{j1} - y_{j2}\,|$.

- m_{jj} : The invariant mass of the two tagging jets.

- *CJV* (Central Jet Veto) [71] : Events are rejected if they have jets with $p_{\mathrm{T}} > 20\,\mathrm{GeV}$ between the two tagging jets which denoted as Central jets.

  $$C_{j3} = \left| \eta_{j3} - \frac{\Sigma\, \eta_{jj}}{2} \right| \Big/ \frac{\Delta\eta_{jj}}{2}, \tag{6.3}$$

  where η_{j3} is the pseudo-rapidity of an extra jet, $\Sigma\, \eta_{jj} = \eta_{j1} + \eta_{j2}$ and $\Delta\eta_{jj} = |\, \eta_{j1} - \eta_{j2}\,|$. If $C_{j3} < 1$, then j_3 is between the tagging jets, and if $C_{j3} > 1$, then j_3 lies outside of the the two tag jets in pseudo-rapidity.

- OLV (Outside Lepton Veto) : This variable discriminates events with leptons that lie outside of the two tagging jets in rapidity.

- η_{lep} : centrality, it calculates an exact position of two leptons with respect to the two tagging jets in the η-plane. This variable extends the idea of the OLV. The definition

of OLV and η_{lep} are followed

$$\mathrm{OLV}_{l_0} = 2 \cdot |\frac{\eta_{l_0} - \bar{\eta}}{\eta_{j_0} - \eta_{j_1}}|$$
$$\mathrm{OLV}_{l_1} = 2 \cdot |\frac{\eta_{l_1} - \bar{\eta}}{\eta_{j_0} - \eta_{j_1}}|$$

$$\eta_{\mathrm{lep}}(\mathrm{centrality}) = \mathrm{OLV}_{l_0} + \mathrm{OLV}_{l_1} \tag{6.4}$$

where $\bar{\eta} = (\eta_{j_0} + \eta_{j_1})/2$, the average η of the two tag jets. If OLV has

$$\mathrm{OLV}_l \begin{cases} = 0 & \text{:the lepton is right in the middle rapidity gap between the two tag jets.} \\ < 1 & \text{:the lepton lies within the rapidity gap between the two tag jets.} \\ > 1 & \text{:the lepton is outside the rapidity gap between the two tag jets.} \end{cases} \tag{6.5}$$

- $\Sigma m_{\ell j}$: the sum of the invariant masses of all four possible lepton-jet pairs. Since the jets in the VBF are closer to the forward region and the lepton still remains in the center of the two jet system, the VBF signal tends to have higher values than the backgrounds.

6.1.3.5 7 TeV Analysis

The 7 TeV analysis is made closer to the 8 TeV analysis even though their data taking conditions were different. Here are some differences from the 8 TeV analysis. The 7 TeV analysis uses the same lepton triggers with the one that the 8 TeV analysis uses but with lower p_{T} threshholds. Regardless of E_{T}, all electrons are required to pass a tight cut-based identification in which the GSF fit is not used and the muon identification also remains the same with respect to 8 TeV ones. The jet selection is identical in the 7 TeV analysis, except that a tighter cut on JVF is used. The used MC tools are consistent for both

analyses, except for the WZ and ZZ backgrounds that are modeled with POWHEG+PYTHIA6. The pile-up events are simulated with PYTHIA6. The event selection criteria are nearly identical to the 8 TeV data analysis. In the SF channel, the $E_{\mathrm{T}}^{\mathrm{miss}}$ is lowered to 35 GeV , while the $p_{\mathrm{T}}^{\mathrm{miss\,(trk)}}$ requirement is not adopted. The $p_{\mathrm{T}}^{\ell\ell}$ is increased to 40 GeV in the $n_j = 0$ channel while the p_{T} of the di-lepton + jet system is required to be > 35 GeV in the $n_j = 1$ channel. f_{recoil} is loosened to 0.5 and to 0.2 in the $n_j = 0$ and $n_j = 1$ categories, respectively. The ggF analysis is not performed in 2 jets, while the VBF analysis is identical.

6.1.4 Signal Extraction

6.1.4.1 ggF Signal

The ggF analysis has two lepton flavor combination categories, SF and DF in three jet multiplicity channels, $n_j = 0, 1,$ and ≥ 2. The $n_j \geq 2$ channel only considers the DF flavor combination. For each variable in Fig 6.6, the top panel compares the observed and the cumulative expected distributions while the bottom panel shows the overlay of the distributions of the individual expected contributions, normalized to unit area to emphasize shape differences.

Fig 6.6 shows the kinematic distributions in the $n_j = 0$. In the DF channel, one observes the background composition change as subsequent selections are applied. Most of Z/γ^* events are suppressed by the $p_{\mathrm{T}}^{\ell\ell} > 30$ GeV cut. Further removal of Z/γ^* and WW backgrounds are achieved by requiring $m_{\ell\ell} < 55$ GeV and $\Delta\phi_{\ell\ell} < 1.8$, since leptons from the spin-0 Higgs boson decay tend to be at small angles to each other. Due to the large Z/γ^* background in the SF channel, there is an additional discriminating kinematic variable (f_{recoil}) that exploits the soft hadronic recoil in the event. The $f_{\mathrm{recoil}} < 0.1$ requirement reduces a large amount of Z/γ^* backgrounds by a factor of seven in the signal region. A summary of the number of events at each cut with 8 TeV data is shown in Table 6.11.

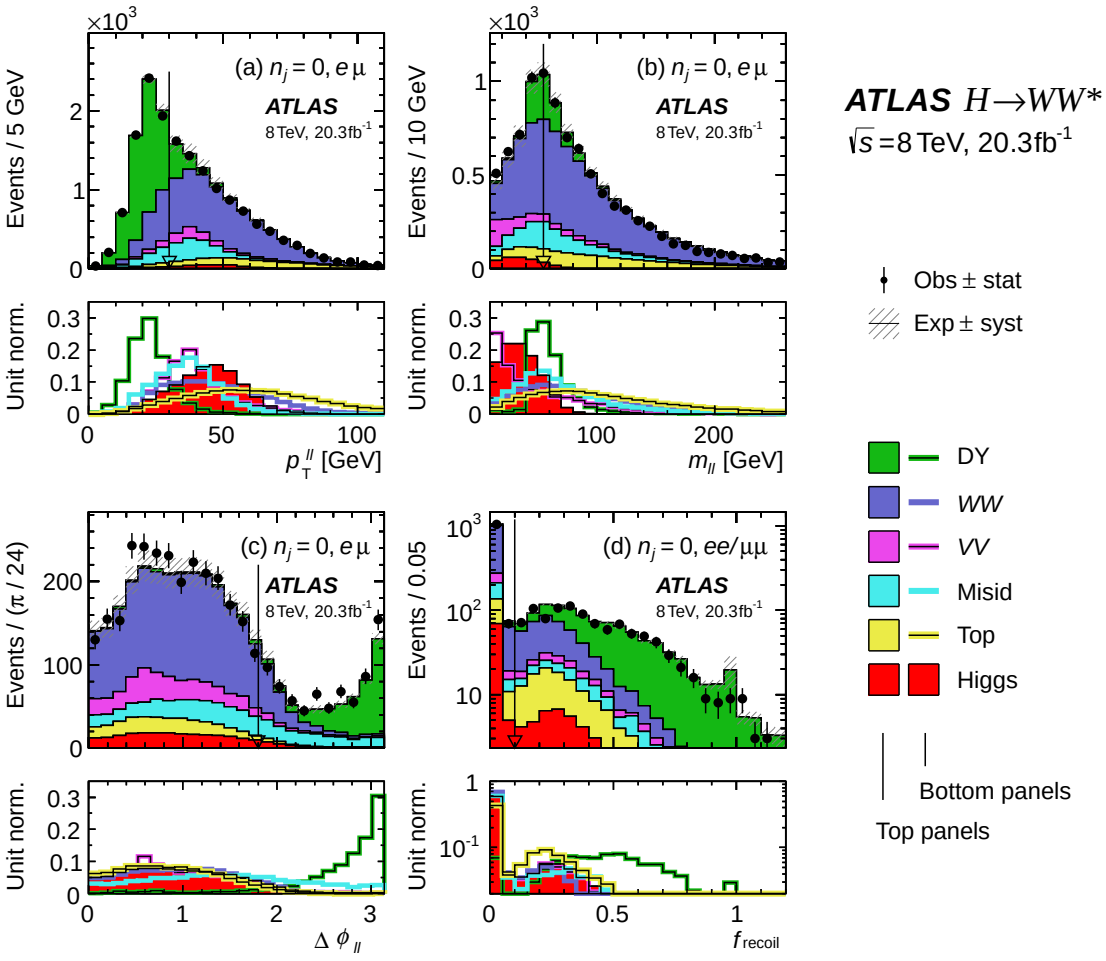

Figure 6.6: Distributions of kinamatic variables for the $n_j = 0$ category; (a) $p_{\mathrm{T}}^{\ell\ell}$, (b) $m_{\ell\ell}$, (c) $\Delta\phi_{\ell\ell}$, and (d) f_{recoil}.

Table 6.11: Event selection table for the $n_j = 0$ category in the 8 TeV data analysis. It is presented separately for the DF and SF channels.

Selection	Summary					Composition of N_{bkg}							
	$N_{\text{obs}}/N_{\text{bkg}}$	N_{obs}	N_{bkg}	N_{sig}		N_{WW}	N_{top}		N_{misid}		N_{VV}	N_{DY}	
				N_{ggF}	N_{VBF}		$N_{t\bar{t}}$	N_t	N_{Wj}	N_{jj}		$N_{ee/\mu\mu}$	$N_{\tau\tau}$
$e\mu$ sample	1.01 ± 0.01	16423	16330	290	12.1	7110	820	407	1330	237	739	115	5570
$\Delta\phi_{\ell\ell,\text{MET}} > \pi/2$	1.00 ± 0.01	16339	16270	290	12.1	7110	812	405	1330	230	736	114	5530
$p_{\text{T}}^{\ell\ell} > 30$	1.00 ± 0.01	9339	9280	256	10.3	5690	730	363	1054	28	571	60	783
$m_{\ell\ell} < 55$	1.11 ± 0.02	3411	3060	224	6.3	1670	141	79	427	12	353	27	350
$\Delta\phi_{\ell\ell} < 1.8$	1.12 ± 0.02	2642	2350	203	5.9	1500	132	75	278	9.2	324	19	12
$\frac{3}{4} m_H < m_{\text{T}} < m_H$	1.20 ± 0.04	1129	940	131	2.2	660	40	21	133	0.8	78	4.3	2.3
$ee/\mu\mu$ sample	1.04 ± 0.01	38040	36520	163	7.2	3260	418	211	504	29	358	31060	685
$\Delta\phi_{\ell\ell,\text{MET}} > \pi/2$	1.05 ± 0.01	35445	33890	163	7.1	3250	416	211	493	26	355	28520	622
$p_{\text{T}}^{\ell\ell} > 30$	1.06 ± 0.01	11660	11040	154	6.8	3010	394	201	396	2.6	309	6700	21
$m_{\ell\ell} < 55$	1.01 ± 0.01	6786	6710	142	5.0	1260	109	64	251	2.0	179	4840	8.7
$p_{\text{T,rel}}^{\text{miss (trk)}} > 40$	1.02 ± 0.02	2197	2160	117	4.3	1097	99	59	133	0.5	106	660	0.3
$\Delta\phi_{\ell\ell} < 1.8$	1.01 ± 0.02	2127	2100	113	4.2	1068	96	57	122	0.5	104	649	0.3
$f_{\text{recoil}} < 0.1$	1.01 ± 0.03	1108	1096	72	2.7	786	41	31	79	0.0	69	91	0.1
$\frac{3}{4} m_H < m_{\text{T}} < m_H$	0.99 ± 0.05	510	517	57	1.3	349	11	8	53	-	31	64	0.1

Fig 6.7 shows the key kinematic distributions for the $n_j = 1$ analysis. Top backgrounds become more dominant becasue top quarks decay to $t \rightarrow W + \bar{b}$, Hence, top events could have one ore more $b-$tagged jets. Events are vetoed if there is a $b-$tagged jet with $p_{\mathrm{T}} > 20\,\mathrm{GeV}$. In the DF category, Z/γ^* and QCD multijet events are further suppressed by requiring m_{T}^{ℓ}, the transverse momentum of lepton, and the $p_{\mathrm{T}}^{\mathrm{miss}}$, since these backgrounds tend to have a small value for this variable.

The definition of m_{T}^{ℓ} is:

$$m_{\mathrm{T}}^{\ell} = max(m_{\mathrm{T}}^{\ell_i}1, m_{\mathrm{T}}^{\ell_i}2); \tag{6.6}$$

$$m_{\mathrm{T}}^{\ell_i} = \sqrt{2\, p_{\mathrm{T}}^{\ell_i} \cdot p_{\mathrm{T}}^{\mathrm{miss}} \cdot (1 - \cos\Delta\phi)}. \tag{6.7}$$

The additional requirement of $m_{\tau\tau} < m_Z - 25\,\mathrm{GeV}$ significantly reduces the remaining $Z/\gamma^* \rightarrow \tau\tau$ contribution in the DF analysis, as seen in Fig 6.7 (b). In the DF analysis, the requirement on $p_{\mathrm{T,rel}}^{\mathrm{miss\,(trk)}}$ is 35 GeV in this category. Other selection criteria are unchanged from the $n_j = 0$ analysis. Table 6.12 summarizes the event selection in the $n_j = 1$ analysis.

For the ggF-enriched $n_j \geq 2$ analysis, events are required to fail the VBF selection. Due to the relatively low statistics of the SF, this analysis only considers DF events. To suppress Z/γ^* and top backgrounds, $n_b = 0$ and $m_{\tau\tau} < m_Z - 25\,\mathrm{GeV}$ requirements are imposed. To ensure to have orthogonality with the VBF and VH analyses [72], some extra requirements are implemented for this analysis as listed below :

- non-VBF selection:
  - VBF cut-based veto: fail of either $\Delta Y_{jj} > 3.6$, $m_{jj} > 600$ GeV, CJV or OLV
  - VBF BDT veto: fail of either CJV, OLV or BDT score > -0.48

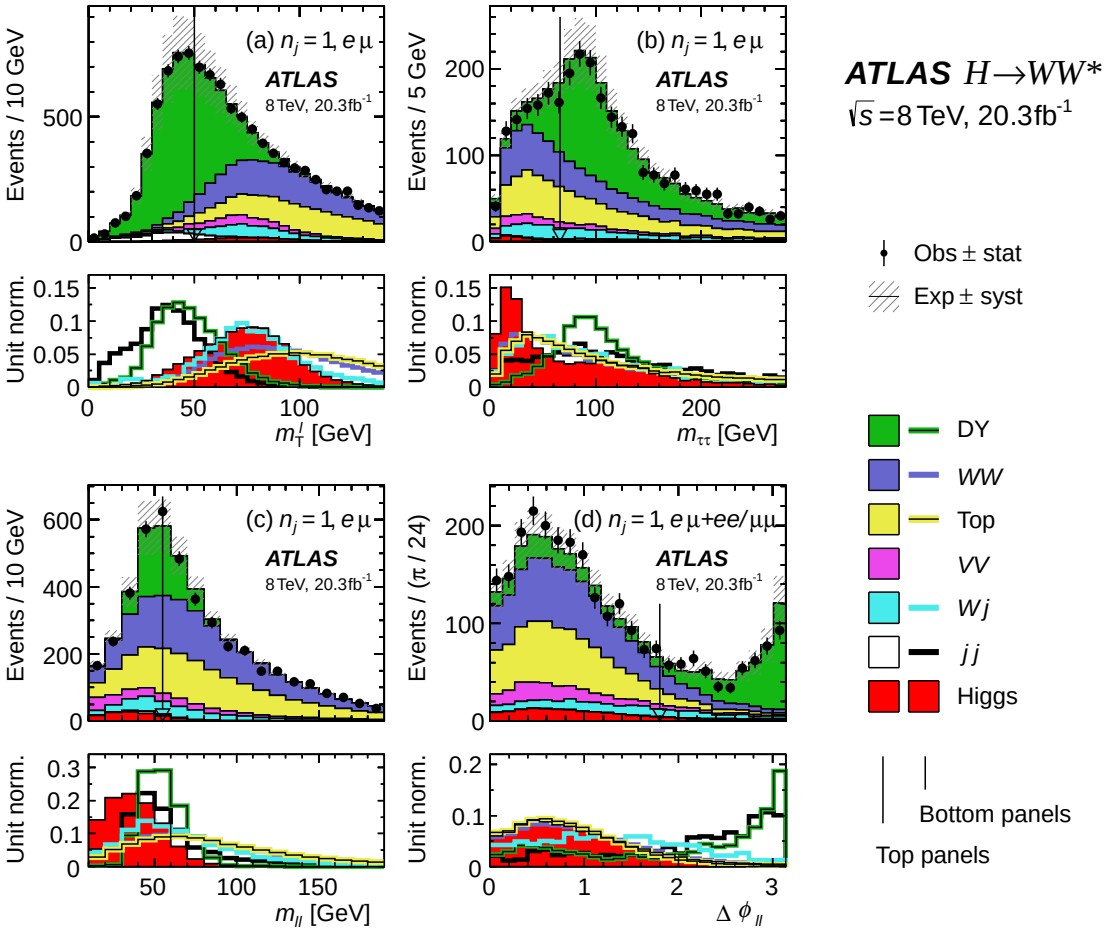

Figure 6.7: Distributions of kinamatic variables for the $n_j = 1$ category; (a) m_{T}^{ℓ}, (b) $m_{\tau\tau}$, (c) $m_{\ell\ell}$, and (d) $\Delta\phi_{\ell\ell}$.

Table 6.12: Event selection table for $n_j = 1$ in the 8 TeV data analysis. It is presented separately for the DF and SF channels.

Selection	Summary					Composition of N_{bkg}							
	$N_{\text{obs}}/N_{\text{bkg}}$	N_{obs}	N_{bkg}	N_{sig}		N_{WW}	N_{top}		N_{misid}		N_{VV}	N_{DY}	
				N_{ggF}	N_{VBF}		$N_{t\bar{t}}$	N_t	N_{Wj}	N_{jj}		$N_{ee/\mu\mu}$	$N_{\tau\tau}$
$e\mu$ sample	1.00 ± 0.01	20607	20700	131	32	2750	8410	2310	663	334	496	66	5660
$n_b = 0$	1.01 ± 0.01	10859	10790	114	26	2410	1610	554	535	268	423	56	4940
$m_{\text{T}}^{\ell} > 50$	1.01 ± 0.01	7368	7280	103	23	2260	1540	530	477	62	366	43	1990
$m_{\tau\tau} < m_Z - 25$	1.02 ± 0.02	4574	4490	96	20	1670	1106	390	311	32	275	21	692
$m_{\ell\ell} < 55$	1.05 ± 0.02	1656	1570	84	15	486	297	111	129	19	139	6.4	383
$\Delta\phi_{\ell\ell} < 1.8$	1.10 ± 0.03	1129	1030	74	13	418	269	102	88	6.1	119	5.0	22
$\frac{3}{4}\, m_H < m_{\text{T}} < m_H$	1.21 ± 0.06	407	335	42	6.6	143	76	30	40	0.5	42	1.1	2
$ee/\mu\mu$ sample	1.05 ± 0.01	15344	14640	61	15	1111	3770	999	178	13	192	8100	280
$n_b = 0$	1.08 ± 0.02	9897	9140	53	12.1	972	725	245	137	10	163	6640	241
$m_{\ell\ell} < 55$	1.16 ± 0.02	5127	4410	48	9.4	351	226	85	73	7.8	79	3420	168
$p_{\text{T,rel}}^{\text{miss (trk)}} > 35$	1.14 ± 0.04	960	842	36	6.9	292	193	73	38	0.2	49	194	2
$\Delta\phi_{\ell\ell} < 1.8$	1.14 ± 0.04	889	783	32	6.3	265	179	68	30	0.2	44	194	2
$f_{\text{recoil}} < 0.1$	1.16 ± 0.05	467	404	20	3.6	188	98	44	17	-	29	26	1
$\frac{3}{4}\, m_H < m_{\text{T}} < m_H$	1.11 ± 0.10	143	129	14	2.0	59	23	11	11	-	11	14	-

- fail of either $\Delta Y_{jj} < 1.2$ or $|m_{jj} - 85\ \text{GeV}| < 15\ \text{GeV}$ (where 85 GeV is the average of the W and Z boson masses)

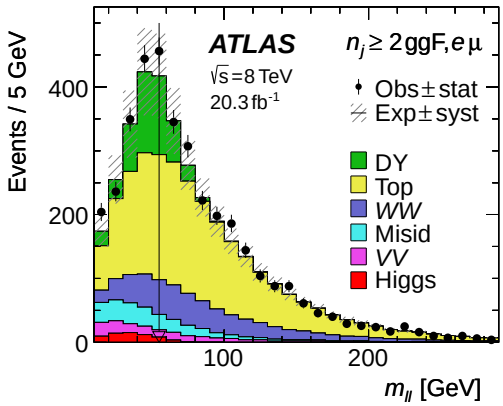

Figure 6.8: The distribution of dilepton invariant mass for the ggF-enriched $n_j \geq 2$ category.

The events in the $n_j \geq 2$ ggF category are contaminated by both the VBF and VH signal production processes, therefore they are included in the analysis category and considered as backgrounds when extracting the ggF only component. The composition of the ggF-enriched $n_j \geq 2$ for each production modes are shown in Table 6.13.

Table 6.13: The expected number of events and fraction for each production mode in the $n_j \geq 2$ channel.

Higgs Production process	ggF	VBF	VH
Number of events	32.47 ± 0.20	6.88 ± 0.11	4.53 ± 0.29
Signal composition [%]	74.0	15.7	10.3

Further selection with $m_{\ell\ell} < 55\,\text{GeV}$ and $\Delta\phi_{\ell\ell} < 1.8$ reduce the dominant top-quark background by 70%, resulting in a signal purity of 3.3%. Fig 6.8 shows the $m_{\ell\ell}$ distribution after the VBF othrogonality cuts are applied. The event selection for this category is summarized in Table 6.14.

Table 6.14: Event selection table for the $n_j \geq 2$ ggF-enriched category in the 8 TeV data analysis. The expected yields from different production modes are shown separately, N_{ggF}, N_{VBF}, and N_{VH}.

Selection	Summary						Composition of N_{bkg}				
	$N_{\text{obs}}/N_{\text{bkg}}$	N_{obs}	N_{bkg}	N_{signal}			N_{WW}	N_{top}	N_{misid}	N_{VV}	N_{DY}
				N_{ggF}	N_{VBF}	N_{VH}					
$e\mu$ category	0.99 ± 0.00	56759	57180	76	29	24	1330	52020	959	324	2550
$n_b = 0$	1.02 ± 0.01	6777	6650	56	23	15	964	3190	407	233	1850
$m_{\tau\tau} < m_Z - 25$	1.06 ± 0.02	3826	3620	49	19	12	610	2120	248	152	485
VBF ortho.	1.05 ± 0.02	3736	3550	44	9.0	12	593	2090	241	148	477
VH ortho.	1.04 ± 0.02	3305	3170	40	8.6	7.4	532	1870	212	132	423
$m_{\ell\ell} < 55$	1.09 ± 0.03	1310	1200	35	7.5	5.0	158	572	124	66	282
$\Delta\phi_{\ell\ell} < 1.8$	1.06 ± 0.03	1017	955	32	6.9	4.5	140	523	99	60	133
$\frac{3}{4} m_H < m_{\text{T}} < m_H$	1.05 ± 0.07	210	200	13.3	2.6	1.9	35	131	16	15	3

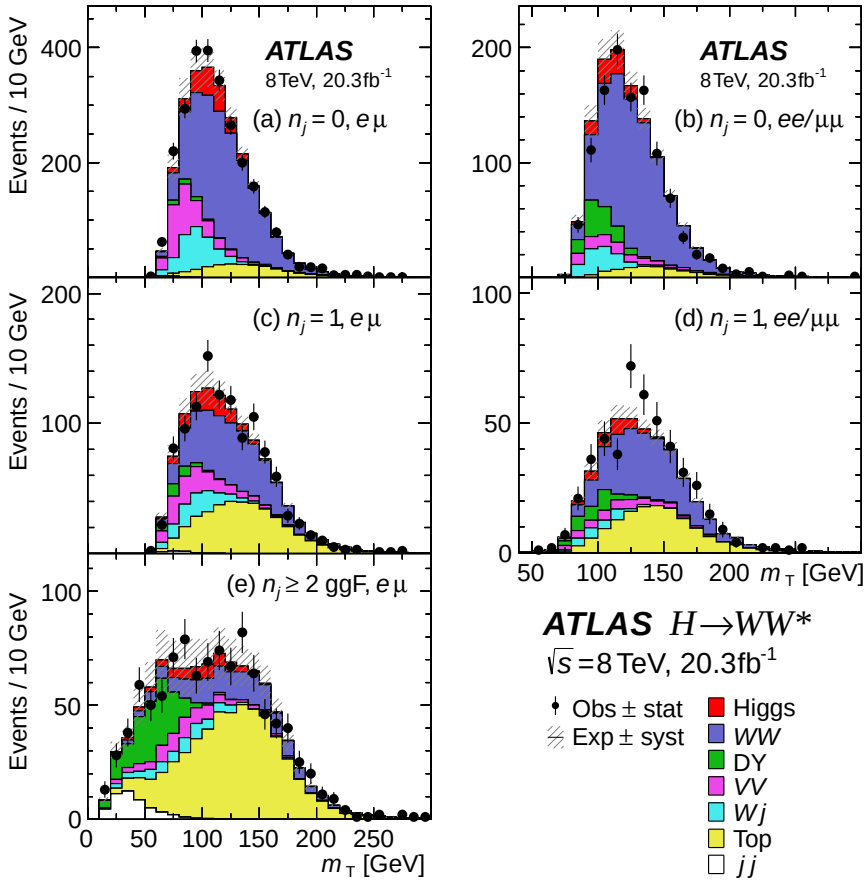

Figure 6.9: Distributions of the transverse mass m_{T} for the $n_j = 0, 1,$ and ≥ 2 ggF-enriched categories in the 8 TeV data analysis. The plots are made after requiring all selections up to the m_{T} requirement.

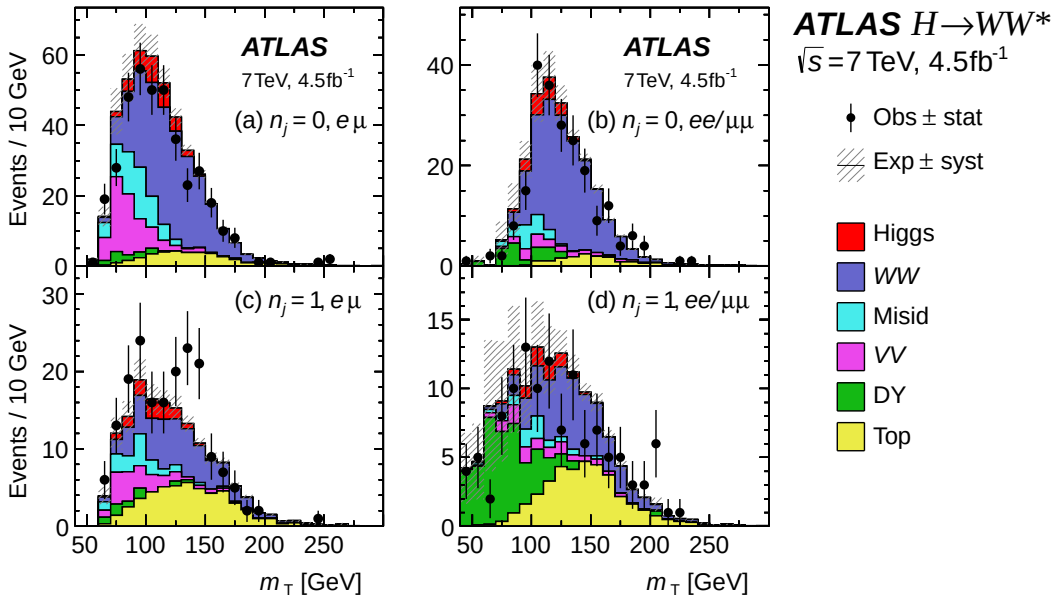

Figure 6.10: Distributions of the transverse mass m_{T} for the $n_j = 0/1$ categories in the 7 TeV data analysis.

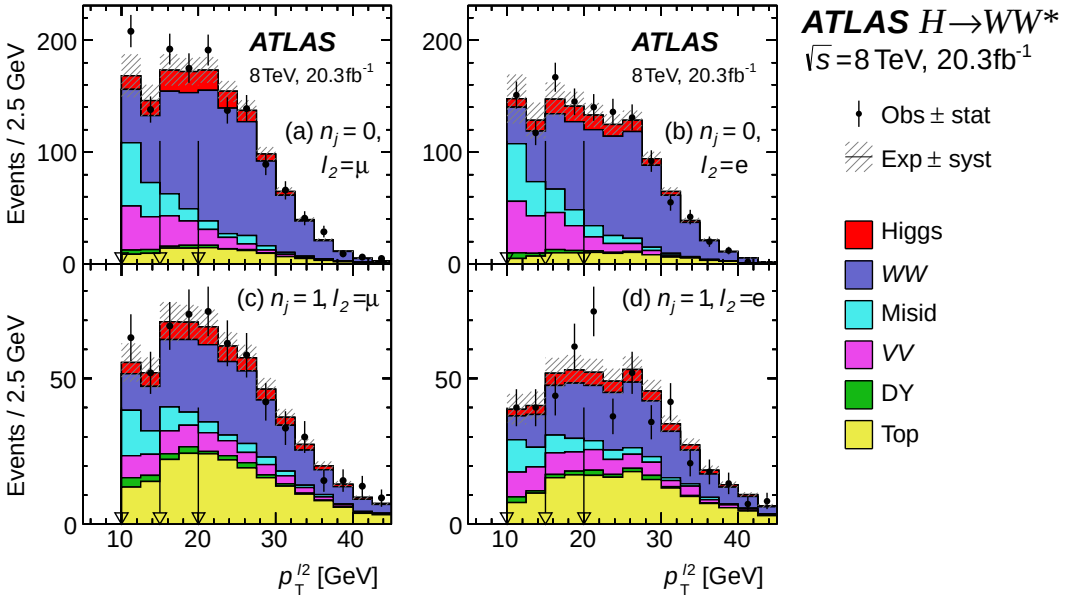

Figure 6.11: Distributions of the sub-leading lepton p_{T} for the 8 TeV data analysis in the DF analysis. These categories are further split into regions based on the sub-leading lepton pT: $10 < p_{\mathrm{T}} < 15$, $15 < p_{\mathrm{T}} < 20$, and $p_{\mathrm{T}} > 20$ GeV.

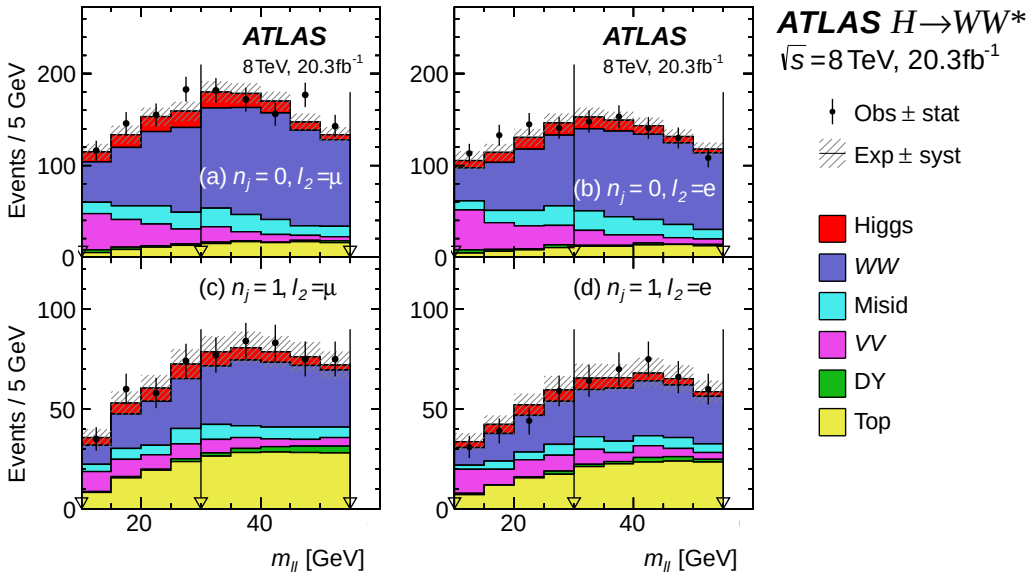

Figure 6.12: Distributions of the dilepton invariant mass $m_{\ell\ell}$ for the 8 TeV data analysis in the DF sample. These categories are further split into regions based on the sub-leading lepton pT: $10 < p_{\mathrm{T}} < 15$, $15 < p_{\mathrm{T}} < 20$, and $p_{\mathrm{T}} > 20$ GeV.

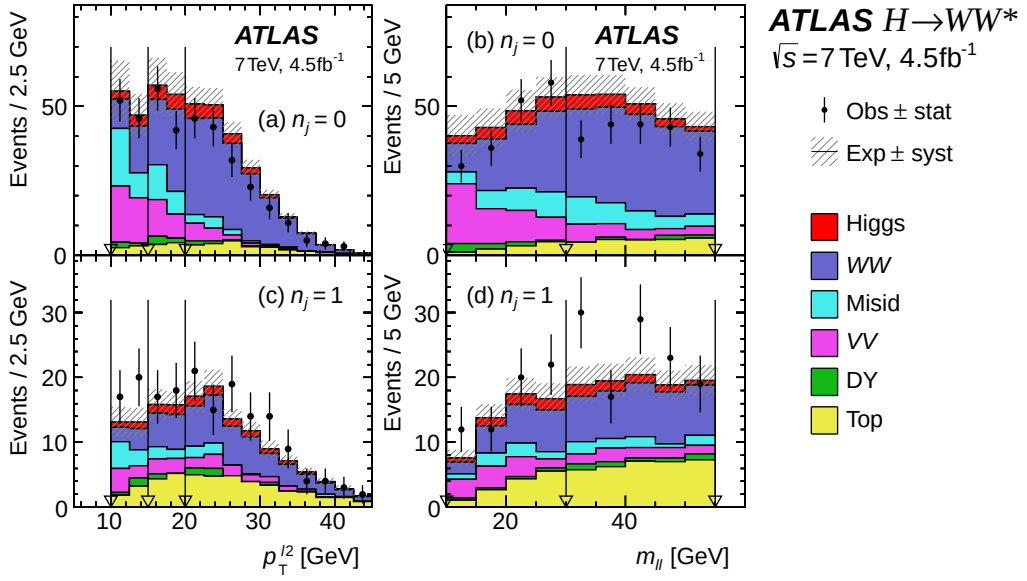

Figure 6.13: Distributions of the sub-leading lepton p_{T} and dilepton invariant mass for the 7 TeV data analysis in the $e\mu$ sample. The plots are made after requiring all selections up to m_{T}. The arrows indicate the bin boundaries.

6.1.4.2 VBF Signal

The VBF-enriched $n_j \geq 2$ analysis uses a boosted decision tree (BDT) in the multi variable analysis(MVA) [58]. The nominal BDT method is cross-checked with a cut-based analysis. Most of the input variables of the BDT analysis have already been discussed in section 6.1.3.4, neverthless, more details are explained below.

In the VBF production, there is no color connection between the two produced jets, thus, these two jets are generally well separated in rapidity [73]. The final BDT discrimination score (O_{BDT}) is calculated. The BDT is trained with 8 input variables: ΣC_ℓ, Δy_{jj}, and m_{jj} for VBF selection; $p_{\mathrm{T}}^{\mathrm{sum}}$ and $\Sigma m_{\ell j}$ for $t\bar{t}$ rejection; and $\Delta\phi_{\ell\ell}$, $m_{\ell\ell}$, and m_{T} for their sensitivity to the $H \to WW^* \to \ell\nu\ell\nu$ signal.

The final BDT score is an average of the binary scores from each of the individual decision trees. The score is binned as $[-1, -0.48, 0.3, 0.78, 1]$ with corresponding bin numbers from 0 to 3. The bin widths are optimized against the expected signal significance. The first bin is dominated by backgrounds, therefore, it is removed from the likelihood fit. The distributions of the input avariables are shown in Fig 6.14 and Fig 6.15 for $e\mu$ and $e\mu + ee/\mu\mu$, respectively.

The BDT training correlation table is shown in Fig 6.17. The event selection summary for the VBF BDT analysis is shown in Table 6.15, while the cut-based analysis for cross-checking is shown in Table 6.16.

Fig 6.18 shows the two cases of candidate events for this study. The top figure is the ggF−enriched $n_j = 0$ category event at 7 TeV, specifically in the $H \to WW^* \to e\nu\mu\nu$ channel. The bottom figure displays the VBF-enriched $e\mu$ event in the $n_j \geq 2$ category.

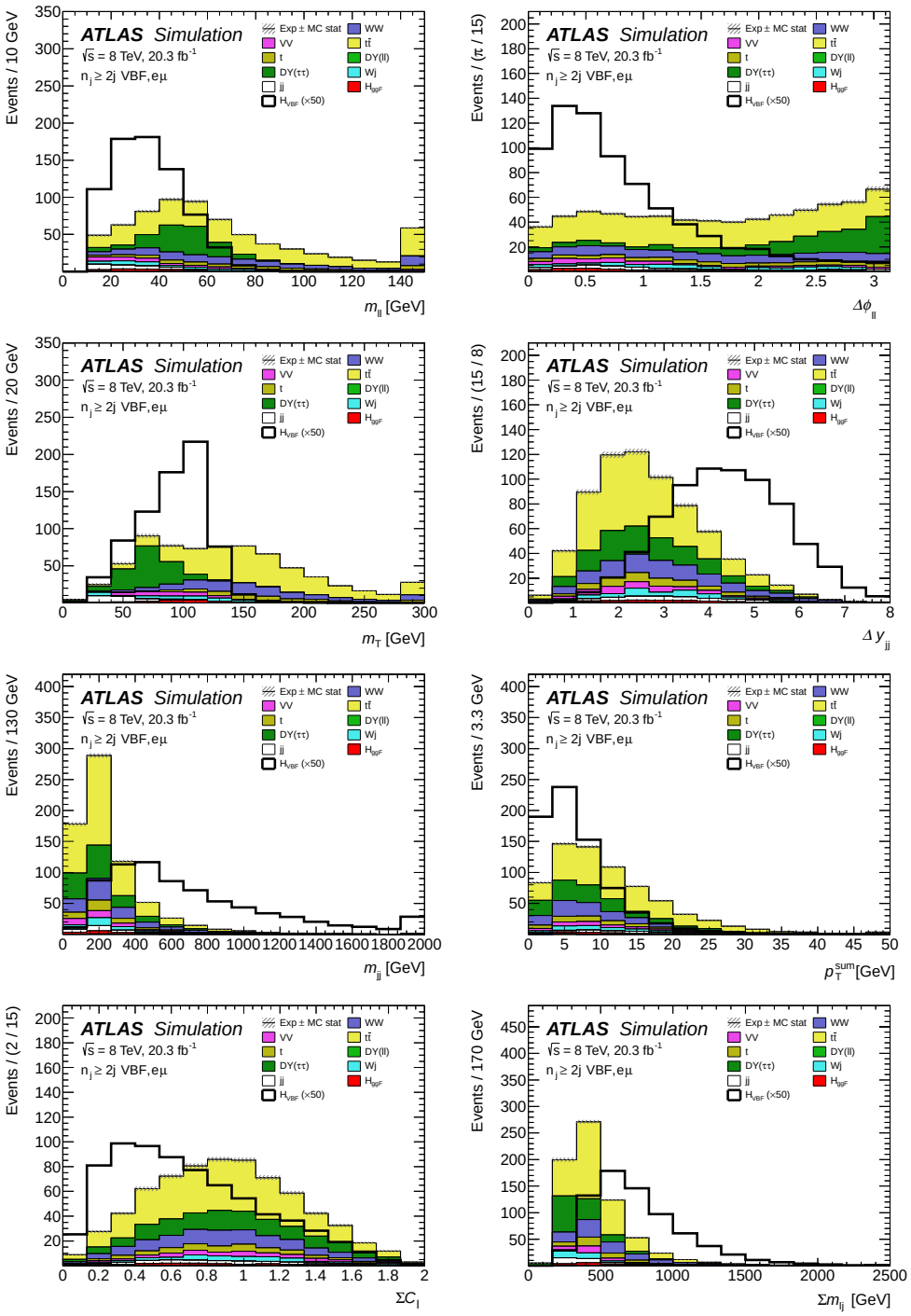

Figure 6.14: Distributions of the variables used as inputs to the training of the BDT in the $e\mu$ sample in the 8 TeV data analysis. The variables are shown after the common preselection and the additional selection requirements in the $n_j \geq 2$ VBF-enriched category.

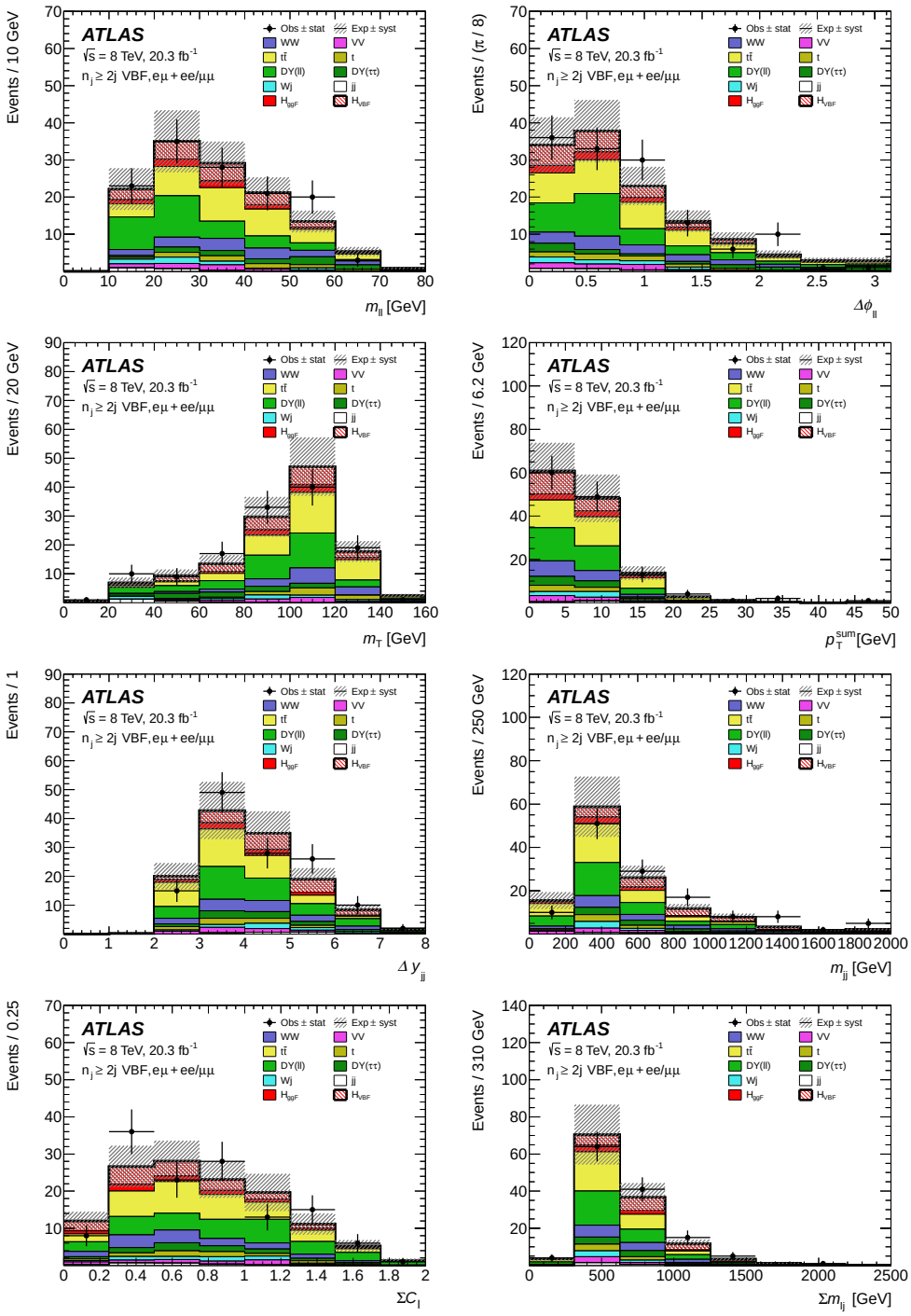

Figure 6.15: Comparisons of the observed and expected distributions of the variables used as inputs to the training of the BDT in the $e\mu + ee/\mu\mu$ samples in the 8 TeV data analysis. The variables are shown after the common preselection and the additional selection requirements in the $n_j \geq 2$ VBF-enriched category.

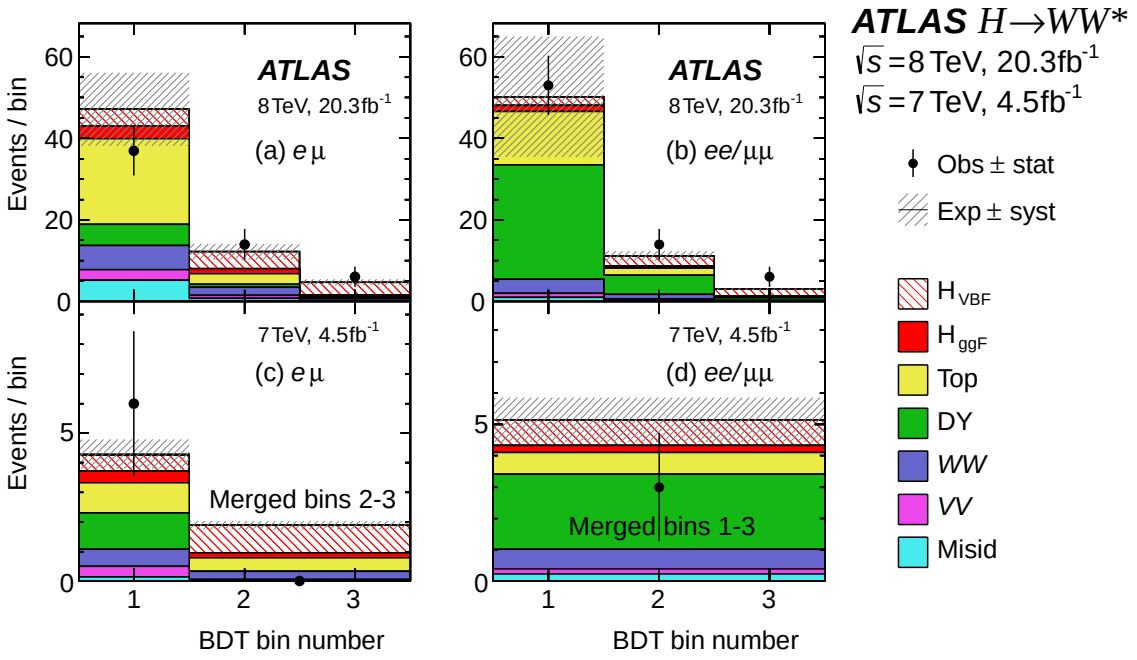

Figure 6.16: Distributions of the BDT output in the $n_j \geq 2$ VBF-enriched category in the 8 and 7 TeV data analyses.

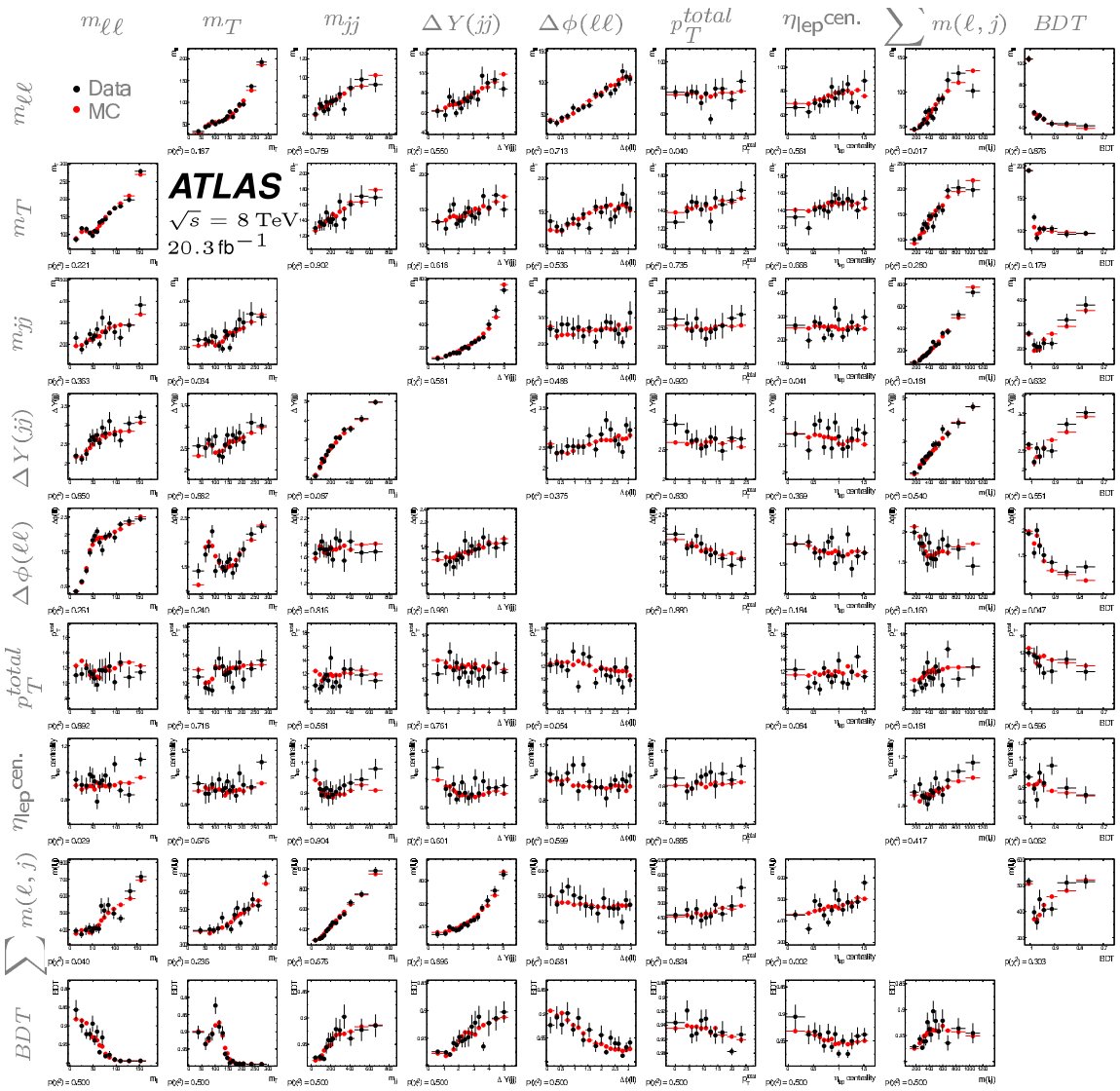

Figure 6.17: Correlation plots between BDT variables in the validation region of BDT bin 0 ($O_{\text{BDT}} < -0.48$). They are shown for each pair of training variable in the BDT as well as the correlation of each training variable with O_{BDT}. The data is indicated by the black points and the red points are shown for the MC model only with the statistical uncertainty.

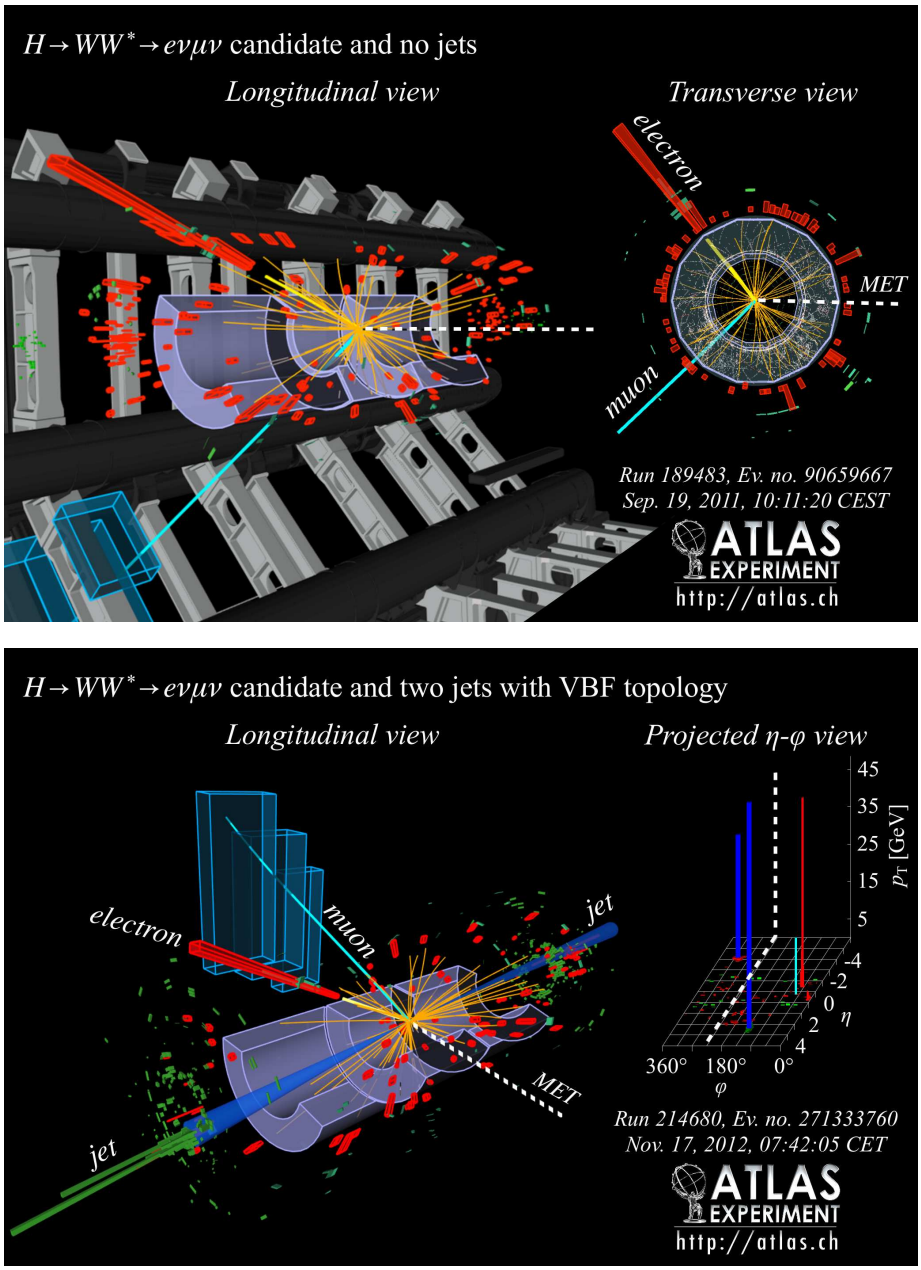

Figure 6.18: Event displays of $H \to WW^* \to e\nu\mu\nu$ candidates in the $n_j = 0$ (top) and $n_j \geq 2$ VBF-enriched (bottom) categories. The neutrinos are represented by missing transverse momentum (MET, dotted line) that points away from the $e\mu$ system. The properties of the first event are $p_{\mathrm{T}}^{e} = 33\,\mathrm{GeV}$, $p_{\mathrm{T}}^{\mu} = 24\,\mathrm{GeV}$, $m_{\ell\ell} = 48\,\mathrm{GeV}$, $\Delta\phi_{\ell\ell} = 1.7$, $p_{\mathrm{T}}^{\mathrm{miss}} = 37\,\mathrm{GeV}$, and $m_{\mathrm{T}} = 98\,\mathrm{GeV}$. The properties of the second event are $p_{\mathrm{T}}^{e} = 51\,\mathrm{GeV}$, $p_{\mathrm{T}}^{\mu} = 15\,\mathrm{GeV}$, $m_{\ell\ell} = 21\,\mathrm{GeV}$, $\Delta\phi_{\ell\ell} = 0.1$, $p_{\mathrm{T}}^{j1} = 67\,\mathrm{GeV}$, $p_{\mathrm{T}}^{j2} = 41\,\mathrm{GeV}$, $m_{jj} = 1.4\,\mathrm{TeV}$, $\Delta y_{jj} = 6.6$, $p_{\mathrm{T}}^{\mathrm{miss}} = 59\,\mathrm{GeV}$, and $m_{\mathrm{T}} = 127\,\mathrm{GeV}$. Both events have a small value of $\Delta\phi_{\ell\ell}$, which is characteristic of the signal. The second event shows two well-separated jets that are characteristic of the VBF production.

Table 6.15: Event selection table for the $n_j \geq 2$ VBF-enriched category in the 8 TeV BDT data analysis. (a) is the event yields after the event selections before the BDT classification and (b) is the event yields in the O_{BDT} bins with the normalization factors applied to the event yields. The expected yields are shown separately depending on the Higgs production modes; the N_{ggF}, N_{VBF}, and N_{VH}.

(a) Before the BDT classification

Selection	Summary						Composition of N_{bkg}									
	$N_{\mathrm{obs}}/N_{\mathrm{bkg}}$	N_{obs}	N_{bkg}	N_{signal}			N_{WW}		N_{top}		N_{misid}		N_{VV}	$N_{\mathrm{Drell\text{-}Yan}}$		
				N_{ggF}	N_{VBF}	N_{VH}	N_{WW}^{QCD}	N_{WW}^{EW}	$N_{t\bar{t}}$	N_t	N_{Wj}	N_{jj}		$N_{ee/\mu\mu}$	$N_{\tau\tau}^{\mathrm{QCD}}$	$N_{\tau\tau}^{\mathrm{EW}}$
$e\mu$ sample	1.04 ± 0.04	718	689	13	15	2.0	90	11	327	42	29	23	31	2.2	130	2
$ee/\mu\mu$ sample	1.18 ± 0.08	469	397	6.0	7.7	0.9	37	3	132	17	5.2	1.2	10.1	168	23	1

(b) Bins in O_{BDT}

$e\mu$ sample																
Bin 0 (not used)	1.02 ± 0.04	661	650	8.8	3.0	1.9	83	9	313	40	26	21	28	2.2	126	1
Bin 1	0.99 ± 0.16	37	37	3.0	4.2	0.1	5.0	1.0	17	3.1	3.3	1.8	2.6	-	4.0	0.2
Bin 2	2.26 ± 0.63	14	6.2	1.2	4.2	-	1.5	0.5	1.8	0.3	0.4	0.3	0.8	-	0.3	0.3
Bin 3	5.41 ± 2.32	6	1.1	0.4	3.1	-	0.3	0.2	0.3	0.1	-	-	0.1	-	0.1	0.1
$ee/\mu\mu$ sample																
Bin 0 (not used)	1.91 ± 0.08	396	345	3.8	1.3	0.8	33	2	123	16	4.1	1.1	8.8	137	20.5	0.5
Bin 1	0.82 ± 0.14	53	45	1.5	2.2	0.1	3.0	0.5	10.4	1.8	0.8	0.2	0.9	26	1.7	0.1
Bin 2	1.77 ± 0.49	14	7.9	0.6	2.5	-	0.8	0.3	1.1	0.2	0.2	-	0.3	4.4	0.3	0.1
Bin 3	6.52 ± 2.87	6	0.9	0.2	1.7	-	0.1	0.2	0.2	-	-	-	-	0.7	-	-

Table 6.16: Event selection table for the $n_j \geq 2$ VBF-enriched category in the 8 TeV cross-check data analysis. The expected yields are shown separately depending on the Higgs production modes; the N_{ggF}, N_{VBF}, and N_{VH}.

Selection	Summary						Composition of N_{bkg}									
	$N_{\text{obs}}/N_{\text{bkg}}$	N_{obs}	N_{bkg}	N_{signal}			N_{WW}		N_{top}		N_{misid}		N_{VV}	$N_{\text{Drell-Yan}}$		
				N_{ggF}	N_{VBF}	N_{VH}	N_{WW}^{QCD}	N_{WW}^{EW}	$N_{t\bar{t}}$	N_t	N_{Wj}	N_{jj}	$N_{ee/\mu\mu}$	$N_{\tau\tau}^{\text{QCD}}$	$N_{\tau\tau}^{\text{EW}}$	
$e\mu$ sample	1.00 ± 0.00	61434	61180	85	32	26	1350	68	51810	2970	847	308	380	51	3260	46
$n_b = 0$	1.02 ± 0.01	7818	7700	63	26	16	993	43	3000	367	313	193	273	35	2400	29
$p_{\text{T}}^{\text{sum}} < 15$	1.03 ± 0.01	5787	5630	46	23	13	781	38	1910	270	216	107	201	27	2010	23
$m_{\tau\tau} < m_Z - 25$	1.05 ± 0.02	3129	2970	40	20	9.9	484	22	1270	177	141	66	132	7.6	627	5.8
$m_{jj} > 600$	1.31 ± 0.12	131	100	2.3	8.2	-	18	8.9	40	5.3	1.8	2.4	5.1	0.1	15	1.0
$\Delta y_{jj} > 3.6$	1.33 ± 0.13	107	80	2.1	7.9	-	11.7	6.9	35	5.0	1.6	2.3	3.3	-	11.6	0.8
$C_{j3} > 1$	1.36 ± 0.18	58	43	1.3	6.6	-	6.9	5.6	14	3.0	1.3	1.3	2.0	-	6.8	0.6
$C_{\ell 1} < 1, C_{\ell 2} < 1$	1.42 ± 0.20	51	36	1.2	6.4	-	5.9	5.2	10.8	2.5	1.3	1.3	1.6	-	5.7	0.6
$m_{\ell\ell}, \Delta\phi_{\ell\ell}, m_{\text{T}}$	2.53 ± 0.71	14	5.5	0.8	4.7	-	1.0	0.5	1.1	0.3	0.3	0.3	0.6	-	0.5	0.2
$ee/\mu\mu$ sample	0.99 ± 0.01	26949	27190	31	14	10.1	594	37	23440	1320	230	8.6	137	690	679	16
$n_b, p_{\text{T}}^{\text{sum}}, m_{\tau\tau}$	1.03 ± 0.03	1344	1310	13	8.0	4.0	229	12.0	633	86	26	0.9	45	187	76	1.5
$m_{jj}, \Delta y_{jj}, C_{j3}, C_\ell$	1.39 ± 0.28	26	19	0.4	2.9	0.0	3.1	3.1	5.5	1.0	0.2	0.0	0.7	3.8	0.7	0.1
$m_{\ell\ell}, \Delta\phi_{\ell\ell}, m_{\text{T}}$	1.63 ± 0.69	6	3.7	0.3	2.2	0.0	0.4	0.2	0.6	0.2	0.2	0.0	0.1	1.5	0.3	0.1

6.1.5 Background Estimation

The major backgrounds encountered in this study are listed here with a short description :

- WW: non-resonant W pair production
- top quarks (Top): t pair production ($t\bar{t}$) and single-top production (t) both have the decay $t \to Wb$. Leptons can come from W bonsons.
- Misidentified leptons (Misid.): W boson production in association with a jet that is misidentified as a lepton (Wj) and dijet or multijet production with two misidentifications (jj) (QCD).
- Other dibosons (VV): $W\gamma$, $W\gamma^*$, WZ, and ZZ
- Drell-Yan (DY): Z/γ^* decay to e or μ pairs ($ee/\mu\mu$) and τ pairs ($\tau\tau$)

The backgorunds giving a small contribution to the analysis are not described in the following but are taken into account in the final results. For the background estimation, a control region (CR) is defined with inverted or enlarged kinematic selection values of the signal region. Details are discussed in the following sections. From the CR, normalization factors (NF, β) and extrapolation factors (α) are used to predict the number of background events in the signal region. The conceptual equation is

$$B_{\mathrm{SR}}^{\mathrm{est}} = B_{\mathrm{SR}} \cdot \underbrace{N_{\mathrm{CR}}/B_{\mathrm{CR}}}_{\text{Normalization factor } \beta} = N_{\mathrm{CR}} \cdot \underbrace{B_{\mathrm{SR}}/B_{\mathrm{CR}}}_{\text{Extrapolation factor } \alpha} \tag{6.8}$$

where N_{CR} and B_{CR} are the observed events in the CR and the MC estimation, respectively, and B_{SR} is the MC estimate in the signal region. The β which is the data-to-MC normalization factor in the CR and the α that is the extrapolation factor from the CR to the SR. Those factors make the study able to estimate the expected number of background events in the SR. The SR is divided into sub-analysis channels based on the jet multiplicities and the final lepton pair combinations as discussed previously. However, the CR is not split into the sub-categories. Thus, the same value of β is used in the same CR. The associated

Table 6.17: Background estimation methods summary. For each background process or process group, a set of three columns indicate whether data (•) or MC (◦) samples are used to normalize the SR yield (N), determine the CR-to-SR extrapolation factor (E), and obtain the SR distribution of the fit variable (V). In general, the methods vary from one row to the next for a given background process.

Category	WW			Top			Misid.			VV			Drell-Yan $ee/\mu\mu$			$\tau\tau$		
	N	E	V	N	E	V	N	E	V	N	E	V	N	E	V	N	E	V
$n_j = 0$																		
$e\mu$	•	◦	◦	•	◦	◦	•	•	•	•	◦	◦	◦	◦	◦	•	◦	◦
$ee/\mu\mu$	•	◦	◦	•	◦	◦	•	•	•	◦	◦	◦	•	•	◦	•	◦	◦
$n_j = 1$																		
$e\mu$	•	◦	◦	•	◦	◦	•	•	•	•	◦	◦	◦	◦	◦	•	◦	◦
$ee/\mu\mu$	•	◦	◦	•	◦	◦	•	•	•	◦	◦	◦	•	•	◦	•	◦	◦
$n_j \geq 2$ ggF																		
$e\mu$	◦	◦	◦	•	◦	◦	•	•	•	◦	◦	◦	◦	◦	◦	•	◦	◦
$n_j \geq 2$ VBF																		
$e\mu$	◦	◦	◦	•	◦	◦	•	•	•	◦	◦	◦	◦	◦	◦	•	◦	◦
$ee/\mu\mu$	◦	◦	◦	•	◦	◦	•	•	•	◦	◦	◦	•	•	◦	•	◦	◦

uncertainties are used as inputs to extract the signal strength later in this study. Most of the background estimations use data, but MC is used to understand the backgrounds that have a lack of statistics in the CR or SR. Table 6.17 summarizes whether a background estimation is purely data-driven, MC normalized to data or pure MC driven. The open circle means the use of MC and the black solid dot is an indication of a data-driven method. The N, E and V indicates whether data driven technique or MC estimation is used for the normalisation factor, the extrapolation factor and the variable distribution respectively.

6.1.5.1 WW Background Estimation

The non-resonant WW is a dominant background in $n_j = 0$ channel and is irreducible. For this background, $m_{\ell\ell}$ is the key discriminating variable in the relatively low

Higgs boson mass range, $m_H < 2m_W$, as seen in Fig 6.6. The CR definition for the WW background is designed to remove the other background contaminations. The following is imposed

- DF events with $p_{\mathrm{T}}^{\mathrm{miss}} > 20$ GeV
- $p_{\mathrm{T}}^{\ell 2} > 15$ GeV
- $\Delta\phi_{\ell\ell} < 2.6$
- $55 < m_{\ell\ell} < 110$ GeV

To avoid the Z/γ^* background, the main background in SF, the CR for the WW events only contains the different lepton flavor combination. Then, $p_{\mathrm{T}}^{\ell\ell} > 30\,\mathrm{GeV}$ for $n_j = 0$ and $m_{\mathrm{T}}^{\ell} > 50\,\mathrm{GeV}$ for $n_j = 1$ are required. By applying $p_{\mathrm{T}}^{\ell 2} > 15\,\mathrm{GeV}$, the W+jets background is suppressed. In the $n_j = 0$ category, the $Z/\gamma^* \to \tau\tau$ background reduction is made with $\Delta\phi_{\ell\ell} < 2.6$ and is made with $|\, m_{\tau\tau} - m_Z \,| > 25\,\mathrm{GeV}$ in the $n_j = 1$. The $m_{\ell\ell}$ range is different depending on the jet multiplicity, $55 < m_{\ell\ell} < 110$ GeV for $n_j = 0$ and $m_{\ell\ell} > 80$ GeV for $n_j = 1$ to maximize the WW yield in the CR. The m_{T} distribution in the CR for $n_j \leq 1$ is shown in Fig 6.19.

The purity of the CR is estimated to be 70% in the $n_j = 0$ and 45% in the $n_j = 1$ categories, respectively. Since the top background is still a dominant background in the $n_j = 1$ category, most of the contamination to this CR is from the top background ($t\bar{t} \to WbWb$). The higher order QCD process not represented with MC modeling is taken into account by varying the re-normalization and factorization scale from one-half to two [74]. The PDF uncertaintys is computed adding in quadrature the largest difference between the nominal PDF set (CT10 [60]) and the MSTW@008 [61] and NNPDF2.3 [62] with the CT10 pdf set error calculated using the eigenvector variations of that PDF set. Underlying event and hadronization uncertainties are taken into account by comparing POWHEG+PYTHIA6 and POWHEG+HERWIG. The matching uncertainties is estimated by comparing POWHEG+HERWIG

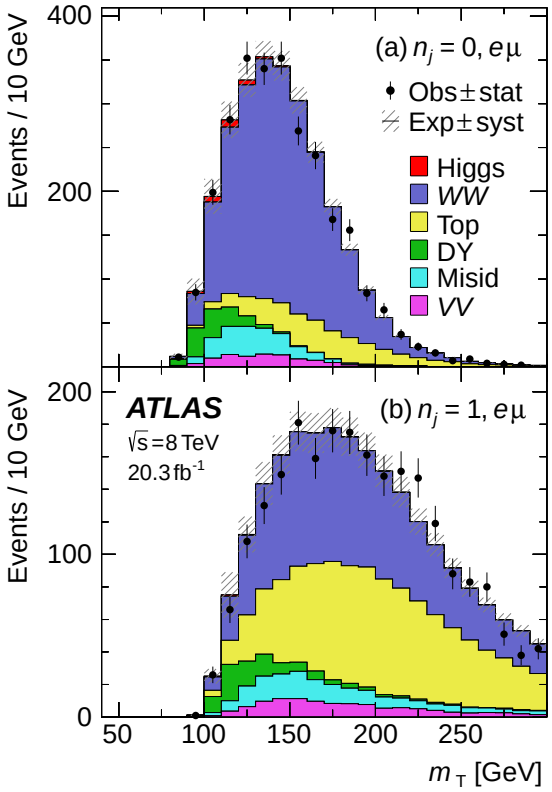

Figure 6.19: *WW* control region distributions of transverse mass.

and aMC@NLO+HERWIG. Finally, higher order electroweak correction are also included by reweigting the MC to NLO [63].

The summary of these uncertainties is shown in Table 6.18 for the $n_j \leq 1$ analysis. The normalization factors is $\beta_{ww}^{0j} = 1.22 \pm 0.03\,(\text{stat.}) \pm 0.10\,(\text{syst.})$ for the $n_j = 0$ and $\beta_{ww}^{1j} = 1.05 \pm 0.05\,(\text{stat.}) \pm 0.24\,(\text{syst.})$ for the $n_j = 1$.

For the case of $n_j \geq 2$, both the VBF− and ggF−enriched categories, SHERPA is used to model *WW* predictions. However, MADGRAPH is used to calculate the uncertainty of the normalization and the factorization scale, which are 27% for the VBF and 19% for the ggF-enriched analysis. The uncertainties of different generators are 8–14% on the O_{BDT} distribution and 1–7% on the m_{T} distribution and the higher order of electroweak renor-

malization uncertainty is 10%. Its 10–16% O_{BDT} uncertainty and 5–17% m_{T} uncertainty are also taken into account.

Table 6.18: Relative WW theoretical uncertainties on the extrapolation factor α for $n_j \leq 1$. Total (Tot) is the sum in quadrature of the uncertainties due to the QCD factorization and re-normalization scales (Scale), the PDFs, the matching between the hard-scatter matrix element to the UE/PS model (Gen), the missing electroweak corrections (EW), and the parton shower and underlying event (UE/PS).

SR category	$n_j = 0$						$= 1$
	Scale	PDF	Gen	EW	UE/PS	Tot	Tot
SR $e\mu$, $10 < m_{\ell\ell} < 30$							
$p_{\mathrm{T}}^{\ell 2} > 20$	0.7	0.6	3.1	−0.3	−1.9	3.8	7.1
	1.2	0.8	0.9	0.7	1.7	2.6	3.9
$15 < p_{\mathrm{T}}^{\ell 2} \leq 20$							
	0.7	1.0	0.4	1.2	2.2	2.8	5.4
$10 < p_{\mathrm{T}}^{\ell 2} \leq 15$							
SR $e\mu$, $30 < m_{\ell\ell} < 55$							
$p_{\mathrm{T}}^{\ell 2} > 20$	0.8	0.7	3.9	−0.4	−2.4	4.8	7.1
	0.8	0.7	1.0	0.5	1.0	2.0	4.5
$15 < p_{\mathrm{T}}^{\ell 2} \leq 20$							
	0.7	0.8	0.5	0.8	1.5	2.1	4.5
$10 < p_{\mathrm{T}}^{\ell 2} \leq 15$							
SR $ee/\mu\mu$, $12 < m_{\ell\ell} < 55$							
$p_{\mathrm{T}}^{\ell 2} > 10$	0.8	1.1	2.4	0.1	−1.2	2.9	5.1

6.1.5.2 Top Background Estimation

The top-background is one of the major backgrounds for the $H \to WW^* \to \ell\nu\ell\nu$ study, especially in the $n_j \geq 1$ category. The W boson associated with $t\bar{t}$ or Wt processes decays with mis-identified jets as leptons. In the $n_j = 0$ category, jets are vetoed in both regions, the CR and the SR, however, the SR is about 3% of the CR and the expected signal contamination by this is less than 1%. For the $n_j = 1$, the CR asks for at least one

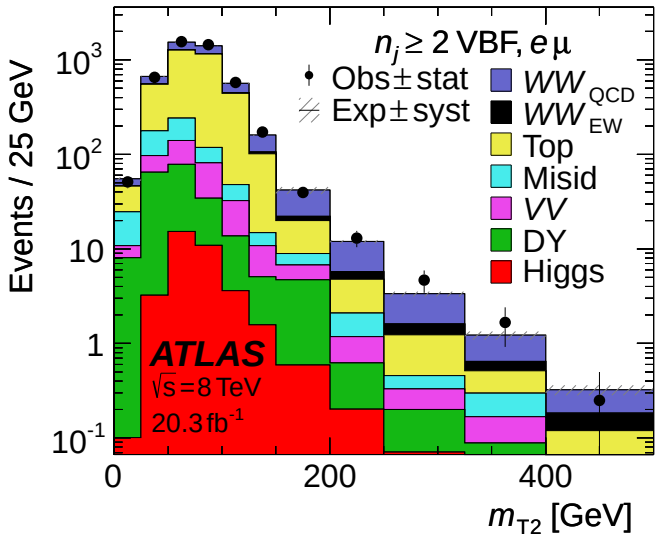

Figure 6.20: WW distribution of m_{T2} in the $n_j \geq 2$ VBF-enriched category.

b jet ($n_b = 1$) while the total number of jets is one ($n_j = 1$). For the $n_j \geq 2$, separate categories are considered for both VBF- and ggF-enriched regions with their own selection requirements.

For $n_j \geq 1$, the WW CR has the following requirements applied:

- DF events with $p_{\mathrm{T}}^{\mathrm{miss}} > 20$ GeV
- $\Delta\phi_{\ell\ell} < 2.8$
- $n_b \geq 1$

The choice of DF reduces the Z/γ^* while the $\Delta\phi_{\ell\ell} < 2.8$ suppress further the $Z/\gamma^* \to \tau\tau$ background in the $n_j \geq 1$ channel. The CR used for the top estimation in the $n_j \geq 1$ channels use all jet multiplicities. Thus, the extrapolation factor (α) is selected the $n_j \geq 1$ events.

For the $n_j = 1$, the $t\bar{t}$ is the largest background after removing the DY background. There are two extrapolation factors considered; one is from top CR to the SR (α_{SR}) and the other is from the top CR to the WW CR (α_{WW}) and it is needed to estimate the top contribution to the WW CR. The definition of the CR is:

- DF events after pre-selection
- $n_b = 1$ in $n_j = 1$ with no additional b jet in $20 < p_{\mathrm{T}} < 25$ GeV
- $m_{\mathrm{T}}^{\ell} > 50$ GeV

Having only DF events reject the Z/γ^*, and $m_{\mathrm{T}}^{\ell} > 50$ GeV suppresses the jj background. Fig 6.21 shows the m_{T} distribution in the CR.

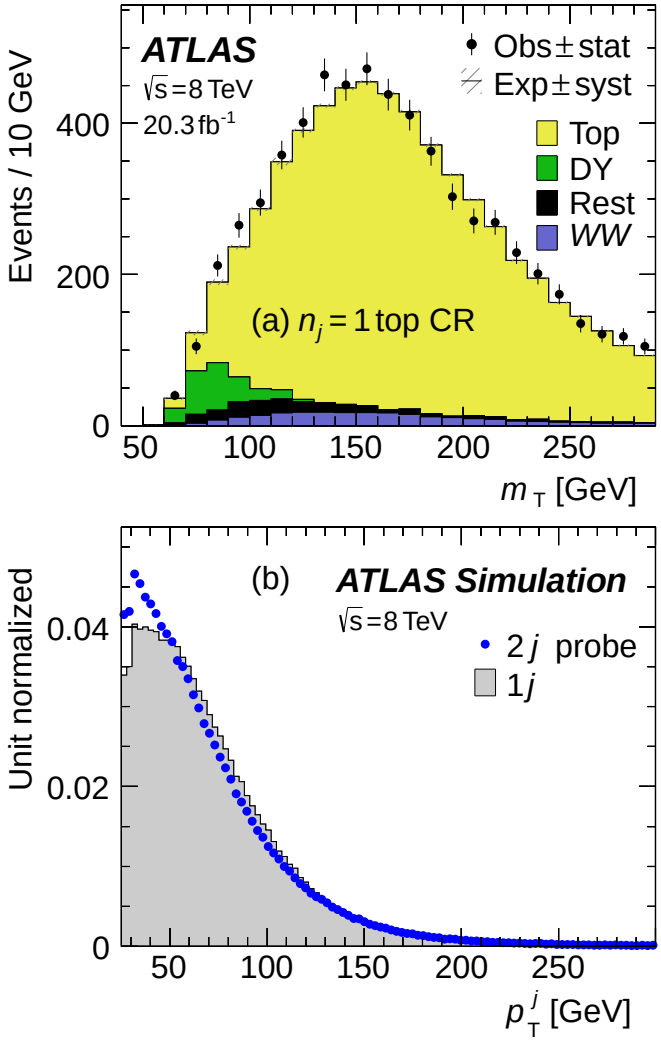

Figure 6.21: (a) transverse mass (m_{T}) and (b) jet p_{T} distributions in top-quark control region (CR).

Since the CR asks for a b-tagged jet, while the SR vetoes on b-tagged jets, a 5% uncertainty on the b-tagging efficiency can affect the estimated yield in the SR as much as 20%. In order to reduce the impact of b-tagging systematics, the b-tagging efficiency is estimated ($\epsilon_{1j}^{\text{est}}$) using the region with 2 jets. As seen in figure 6.21 (b), the p_{T} spectrum of jets in $n_j = 1$ is similar to the spectrum of those in $n_j = 2$. To take into account the small difference, $\epsilon_{1j}^{\text{est}}$ is scaled by the factor $\gamma_{1j} = \epsilon_{1j}/\epsilon_{2j}$ where ϵ_{2j} is the probability that one of the 2 jets is tagged as a b-jet and ϵ_{1j} is the probability to tag a b-jet in the $n_j = 1$ SR. Thus, the estimated b-tagging efficiency in the $n_j = 1$ data is $\epsilon_{1j}^{\text{est}} = \gamma_{1j} \cdot \epsilon_{2j}^{\text{data}}$ and the $\epsilon_{2j}^{\text{data}}$ is the extrapolated efficiency from the $n_j = 2$ data sample. The top-quark background estimate in the SR is then:

$$B_{\text{top},1j}^{\text{est}} = N_{\text{CR}} \cdot \underbrace{\left(\frac{1-\epsilon_{1j}^{\text{est}}}{\epsilon_{1j}^{\text{est}}}\right)}_{\alpha_{\text{data}}^{1j}} \tag{6.9}$$

The value of γ_{1j} is $1.079 \pm 0.002\,(\text{stat.})$ with an experimental systematic uncertainty of 1.4% and a theoretical uncertainty of 0.8%. The largest source for the experimental uncertainty is the b-tagging efficiency systematics. The theoretical uncertainty includes the variation of the renormalization and factorization scales, PDFs, and the parton shower model, as summarized in the Table 6.19.

The calculated normalization factor is $\beta_{\text{top}}^{1j} = 1.06 \pm 0.03\,(\text{stat.})$ and the total estimated top-background uncertainty in this regon is 5%.

For the $n_j \geq 2$ region, there are two regions to study. The first one is the VBF-enriched. In order to reduce background from top-quarks that have a large number of b-jets in the final state, the SR requires a b-jet veto. Therefore the remaining jets are mostly from a light-quark jet from initial-state radiation and also from mis-identificated b-jet that actually comes from a b-jet but not identified as a b-jet. The CR selection is

Table 6.19: Relative top-quark background uncertainties for $n_j \leq 1$. (a) is the uncertainties on the extrapolation procedure for $n_j = 0$ and (b) is the uncertainties on the extrapolation factor α_{top} for $n_j = 1$.

(a) $n_j = 0$

Uncertainty source	$\alpha^{0j}_{\text{MC}}/(\alpha^{1b}_{\text{MC}})^2$	ϵ_{rest}	Total
Experimental	4.4	1.2	4.6
Non-top-quark subtraction	2.7	-	2.7
Theoretical	3.9	4.5	4.9
Statistical	2.2	0.7	2.3
Total	6.8	4.7	7.6

(b) $n_j = 1$.

Regions		Scale	PDF	Gen	UE/PS	Tot
Signal region						
$e\mu$	$(10 < m_{\ell\ell} < 55)$	−1.1	−0.12	−2.4	2.4	3.6
$ee/\mu\mu$	$(12 < m_{\ell\ell} < 55)$	−1.0	−0.12	−2.0	3.0	3.7
WW control region						
$e\mu$	$(m_{\ell\ell} > 80)$	0.6	0.08	2.0	1.8	2.8

made as close as possible to the SR selection. Therefore, the extrapolation factor, α, is the ratio of b-jet efficiency to b-jet inefficiency. For the BDT training, various kinematic variables are involved, including m_{jj}. Fig 6.22 shows the distribution of m_{jj} and the O_{BDT} discriminant. The two highest bins are merged to improve the statistics in the calculation of the nomalization factor, β_i. The Table 6.20 summurize the α and β in each BDT bins.

For the ggf-enriched $n_j \geq 2$ region, no $b-$tagged jet is required in the top background estimation, but $m_{\ell\ell} > 80\,\text{GeV}$ is required to define the CR. With these requirements, the signal contamination is removed and the purity is about 70%. The normalization factor of $\beta = 1.05 \pm 0.03\,(\text{stat.})$ is calculatd. The uncertainty of the extrapolation factor α to the SR is 3.2%. The uncertainty on α is evaluated by varying the MC matrix element generator

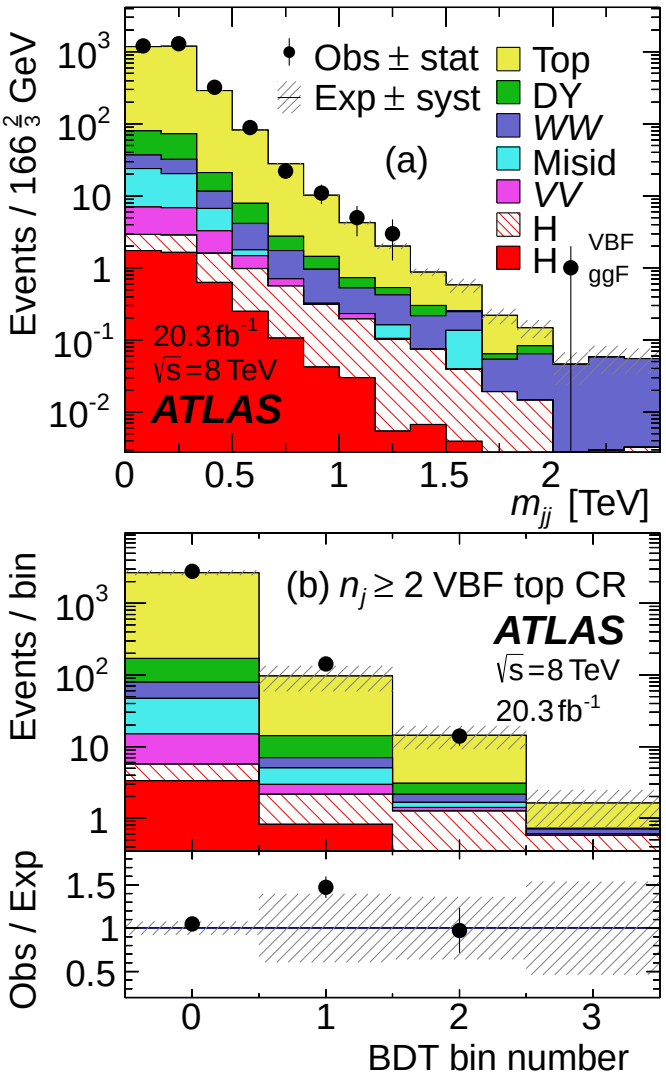

Figure 6.22: (a) m_{jj} and (b) BDT output contributions in the top-quark control region (CR) distributions in the VBF-enriched $n_j \geq 2$ category.

Table 6.20: Relative top-quark background uncertainties for $n_j \geq 2$ VBF on the extrapolation factor α and normalization factor β in bins of O_{BDT}.

O_{BDT} bins	$\Delta\alpha/\alpha$	$\Delta\beta$ Statistical	$\Delta\beta$ Systematic	β
SR bin 0 (unused)	0.04	0.02	0.05	1.09
SR bin 1	0.10	0.15	0.55	1.58
SR bin 2	0.12	0.31	0.36	0.95
SR bin 3	0.21	0.31	0.36	

(3.2%), the parton shower model (1.2%), varying the factorization and the renormalization scale (1.0%) and by varying the PDFs (0.3%).

6.1.5.3 W+jets and QCD Background Estimation

The W+jets and QCD backgrounds come with jets that are mis-identified as leptons. The used method for estimating W+jets and QCD backgrounds is a fake factor method. In this method, two lepton categories are defined, "identified" and "anti-identified" leptons. The "identified" leptons follow the same selection of the SR leptons, while the "anti-identified" leptons are designed to be orthogonal to the leptons in the "identified" category. The W+jets CR has one "identified" lepton and one "anti-identified" lepton coming from the mis-identification of a jet as a lepton. The QCD backgrounds have two leptons that pass "anti-identified" criteria. The details of definitions are in tables below, Table 6.21 and 6.22 for the electron and Table 6.23 and 6.24 for the muon. As can be seen in the tables, lepton isolation cuts are the main differences between the two categories because lepton identification is at the basis of this method.

The SR and CR are defined using the following relations:

$$N_{\text{id+id}} = N^{\text{QCD}}_{\text{id+id}} + N^{\text{W+jet}}_{\text{id+id}} + N^{\text{EW,MC}}_{\text{id+id}} \tag{6.10}$$

$$N_{\text{id+anti-id}} = N^{\text{QCD}}_{\text{id+anti-id}} + N^{\text{W+jet}}_{\text{id+anti-id}} + N^{\text{EW,MC}}_{\text{id+anti-id}} \tag{6.11}$$

$$N_{\text{anti-id+anti-id}} = N^{\text{QCD}}_{\text{anti-id+anti-id}} + N^{\text{W+jet,MC}}_{\text{anti-id+anti-id}} + N^{\text{EW,MC}}_{\text{anti-id+anti-id}} \tag{6.12}$$

where "QCD" denotes the QCD background, the "W+jets" is the W+jets background and "EW, MC" denotes all other background contributions. The extrapolation factor in here,

which is called as a fake factor, is defined as the ratio of the number of objects satisfying the full lepton identification to the number satisfying the anti-identification selection.

$$f_\ell \equiv \frac{N_{\text{id}}}{N_{\text{anti-id}}} \quad (\ell = e \text{ or } \mu). \tag{6.13}$$

Table 6.21: The definition of the identification electron.

Identified Electron
Author 1 or 3
$p_T > 10$ GeV
$\|\eta\| < 2.47$, excluded crack region ($1.37 < \|\eta\| < 1.52$)
$\|z_0 \times \sin(\theta)\| < 0.4$ mm, $\|d_0/\sigma(d_0)\| < 3$
topoEtCone30Corr/$E_T < 0.20$, PtCone40/$E_T < 0.06$ ($10 - 15$ GeV)
topoEtCone30Corr/$E_T < 0.24$, PtCone30/$E_T < 0.08$ ($15 - 20$ GeV)
topoEtCone30Corr/$E_T < 0.28$, PtCone30/$E_T < 0.10$ (≥ 20 GeV)
VeryTight Likelihood ($10 - 25$ GeV)
Medium++ with conversion bit and b-layer requirement (≥ 25 GeV)

Table 6.22: The definition of the anti-identification electron.

Anti-id Electron
Author 1 or 3
$p_T > 10$ GeV
$\|\eta\| < 2.47$, excluded crack region ($1.37 < \|\eta\| < 1.52$)
$\|z_0 \times \sin(\theta)\| < 0.4$ mm, $\|d_0/\sigma(d_0)\| < 3$
$N_{hits}^{SCT} + N_{hits}^{Pixel} \geq 4$
topoEtCone30Corr/$E_T < 0.30$
PtCone30/$E_T < 0.16$
Fails isEM Medium++
Fails the identified electron

Table 6.23: The definition of identification muon.

Identified Muon Definition
STACO Combined Muon
$p_T > 10$ GeV
$\|\eta\| < 2.5$
$\|d_0/\sigma(d_0)\| < 3$
$\|z_0 \times \sin(\theta)\| < 1$ mm
EtCone30Corr/$P_T < 0.06$, PtCone40/$P_T < 0.06$ ($10 - 15$ GeV)
EtCone30Corr/$P_T < 0.12$, PtCone30/$P_T < 0.08$ ($15 - 20$ GeV)
EtCone30Corr/$P_T < 0.18$, PtCone30/$P_T < 0.12$ ($20 - 25$ GeV)
EtCone30Corr/$P_T < 0.30$, PtCone30/$P_T < 0.12$ (≥ 25 GeV)

Table 6.24: The definition of anti-identification muon.

Anti-id Muon Definition
STACO Combined Muon
$p_T > 10$ GeV
$\|\eta\| < 2.5$
d_0 Impact Parameter Requirements Removed
$\|z_0 \times \sin(\theta)\| < 1$ mm
EtCone30Corr/$P_T < 0.15$ ($10 - 15$ GeV)
EtCone30Corr/$P_T < 0.25$ ($15 - 20$ GeV)
EtCone30Corr/$P_T < 0.30$ (≥ 20 GeV)
Track isolation cuts Removed
Fails the identified muon selection

W+jets **estimation**

The estimated *W*+jets events are calculated by the number of *W*+jets events in the *W*+jets CR multiplied by the fake factor as expressed in the equation 6.15.

$$N^{\text{W+jet}}_{\text{id+id}} = f_l \times N^{\text{W+jet}}_{\text{id+anti-id}} \tag{6.14}$$

$$= f_l \times (N_{\text{id+anti-id}} - N^{\text{EW}}_{\text{id+anti-id}} - N^{\text{QCD}}_{\text{id+anti-id}}) \tag{6.15}$$

The extrapolation factor is extracted from the data for this case and is determined as the ratio between the identified and the anti-identified lepton in the *Z*+jets control region samples. The *Z*+jets sample consists of e^+e^- or $\mu^+\mu^-$ final state from *Z* boson. Fig 6.23 shows

the p_{T} distribution of id-leptons and anti-id-leptons in the Z+jets control region. The extrapolation factors are extracted on each bin.

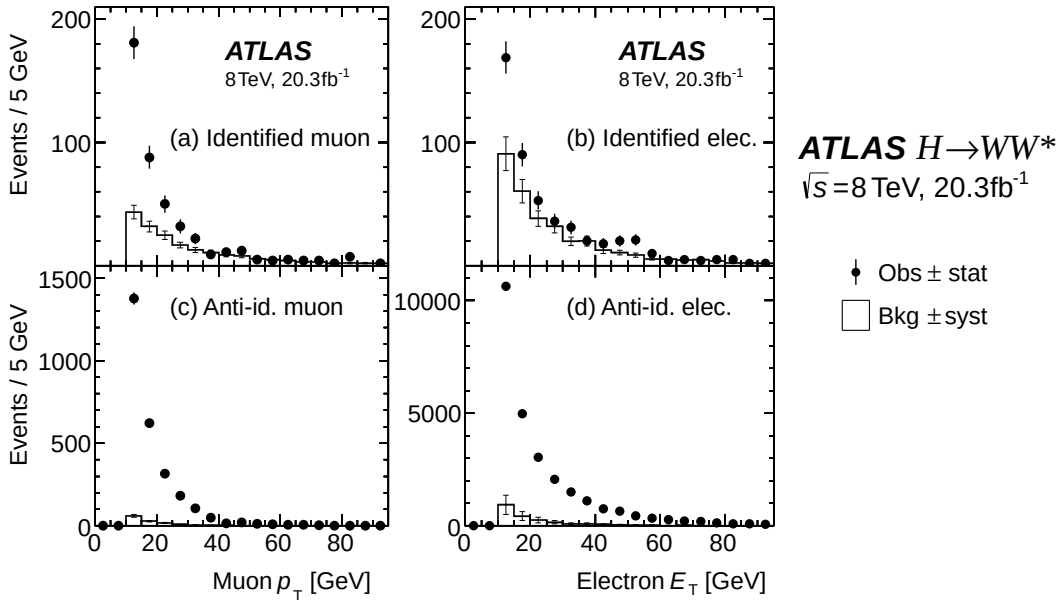

Figure 6.23: Misidentified lepton sample distributions of p_{T} in the Z+jets control sample: (a) identified muon, (b) identified electron, (c) anti-identified muon, and (d) anti-identified electron. The symbols represent the data (Obs); the histograms are the background MC estimates (Bkg) of the sum of electroweak processes other than the associated production of a Z boson and jets.

Since jets behave differently in W+jets and Z+jets, an uncertainty arise from this difference. Therefore, the correction factor is applied to compensate the difference. From the comparison of three different MC tools combination to make MC samples, the correction factors are 0.99 ± 0.20 for anti-identified electrons and 1.00 ± 0.22 for anti-identified muons. Total systematic uncertainties by the correction factors range from 29% to 61% for anti-identified electrons and 25% to 46% for anti-identified muons. The total systematic uncertainty and the correction factors are summarized in Table 6.25. The fake factors and their systematic uncertainties are different for the Opposite Charge (OC) and the Same

Charge (SC) regions used in the analysis due to processes that exhibit charge correlation between the lepton and the fake lepton, like Wc. The sign of the final status would affect to the factors and their uncertainty calculation. Thus, the flavor of decayed jet in W+jets is studied in separated categories, same-charge and opposite-charge regions. Fig. 6.24 shows the extrapolation factor comparison in the same-charged W+jets with ones of Z+jets.

Table 6.25: Relative uncertainties on the extrapolation factor α_{misid} for the determination of the W+jets background. Total is the quadrature sum of the uncertainties due to the correction factor determined with MC simulation (Corr. factor), the number of jets misidentified as leptons in the Z+jets control sample (Stat) and the subtraction of other processes (Other bkg.).

SR p_{T} range	Total		Corr. factor		Stat	Other bkg.
	OC	SC	OC	SC		
Electrons						
10–15 GeV	29	32	20	25	18	11
15–20 GeV	44	46	20	25	34	19
20–25 GeV	61	63	20	25	52	25
≥ 25 GeV	43	45	20	25	30	23
Muons						
10–15 GeV	25	37	22	35	10	3
15–20 GeV	37	46	22	35	18	5
20–25 GeV	37	46	22	35	29	9
≥ 25 GeV	46	53	22	35	34	21

QCD estimation

The QCD or multijet background is defined to have two anti-identified jets as leptons in the events. Therefore, the fake factor should be applied as f^2 respect to the number of QCD events in the SR.

$$N_{\text{QCD Bkg}} = f^2 \times N^{\text{QCD}}_{\text{anti-id+anti-id}} \tag{6.16}$$

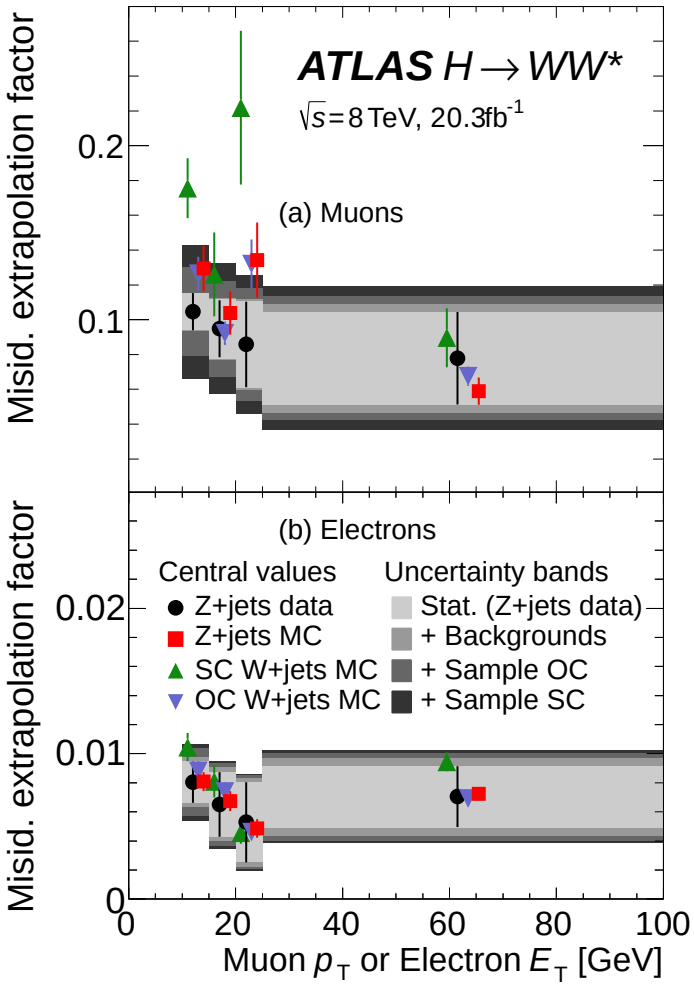

Figure 6.24: Misidentified lepton extrapolation factors, α_{misid}, for anti-identified (a) muons and (b) electrons before applying the correction factor. The symbols represent the central values of the Z+jets data and the three ALPGEN+PYTHIA6 MC samples: Z+jets, opposite-charge (OC) W+jets, and same-charge (SC) W+jets. The bands represent the uncertainties: Stat. refers to the statistical component, which is dominated by the number of jets identified as leptons in Z+jets data; Background is due to the subtraction of other electroweak processes present in Z+jets data; and Sample is due to the variation of the α_{misid} ratios in Z+jets to OC W+jets or to SC W+jets in the three MC samples.

To take into account the impact of the QCD that has one mis-identified lepton, the following relation is used :

$$N^{\text{QCD}}_{\text{id+anti-id}} = 2 \times f \times N^{\text{QCD}}_{\text{anti-id+anti-id}} \tag{6.17}$$

Therefore, the equations are written in this way :

$$N^{W\text{+jets}}_{\text{QCD Bkg}} = f \times N^{\text{QCD}}_{\text{id+anti-id}} = 2 \times f^2 \times N^{\text{QCD}}_{\text{anti-id+anti-id}} = 2 \times N_{\text{QCD Bkg}} \tag{6.18}$$

Table 6.26 shows the estimated number of events for the multijet and W+jets backgrounds in the DF channel for the various jet multiplicities. Those values are extracted from the m_{T} fit with the combination of the statistical and systematic uncertainties. The most systematic uncertainties are from the extrapolation factors and the correlations between extrapolation factors in events with two misidentified leptons are the biggest uncertainty for W+jets background.

6.1.5.4 Dibosons Backgrounds Estimation

Backgrounds from the production of two vector bosons, other than WW, come from $W\gamma$, $W\gamma^*$, WZ and ZZ, and it is referred as VV background. The VV events represent about 10% of the total estimated background in $n_j \leq 1$. The large portion of this background are

Table 6.26: W+jets and multijets estimated yields in the DF category. For $n_j = 0$ and 1, yields for both the opposite-charge (OC) and same-charge (SC) leptons are given. The yields are given before the m_{T} fit for the ggF-enriched categories and after the VBF-selection for the VBF-enriched categories. The uncertainties include statistical and systematic sources.

Category	W+jets yield N_{Wj}		Multijets yield N_{jj}	
	OC	SC	OC	SC
$n_j = 0$	278 ± 71	174 ± 54	9.2 ± 4.2	5.5 ± 2.5
$n_j = 1$	88 ± 22	62 ± 18	6.1 ± 2.7	3.0 ± 1.3
$n_j \geq 2$ ggF	50 ± 22	-	49 ± 22	-
$n_j \geq 2$ VBF	3.7 ± 1.2	-	2.1 ± 0.8	-

$W\gamma$, $W\gamma^*$, and WZ. The normalization for the VV events uses data samples for the DF while the theoretical cross section is used for the SF channel. To study $W\gamma$ and $W\gamma^*$, the reconstruction of photon conversions should be considered. The $W\gamma$ is identified by one leptonic decay from W and a photon conversion to e^+e^- pair in the detector without a track matched in the pixel detector. There are two electrons and they randomly associate one of the two with the prompt lepton, making SS and OS.

The accuracy of photon conversion efficiency is crucial to extract the normalization factor. $Z \to \mu\mu\gamma$ validation samples consisting of either $Z\gamma$ or Z boson production with the final state radiation (FSR) is used to validate the modelling of the photon conversion, where Z decays into $\mu^+\mu^-$ final states. The $\mu^+\mu^-e^\pm$ invariant mass is required to be within 15 GeV from m_Z to reduce contributions from an associated production of a Z boson and hadronic jets. Similarly, the $W\gamma^*$ background also decays into one prompt lepton and one e^+e^- or $\mu^+\mu^-$ pair from the virtual γ^* conversion. In order to validate the $W\gamma^*$ background estimate, a specific $W\gamma^* \to e\nu\mu\mu$ selection is used. The events of $W\gamma^* \to e\nu\mu\mu$ must satisfy $m_{\mu\mu} < 7\,\text{GeV}$, $p_{\text{T}}^{\text{miss}} > 20\,\text{GeV}$ and $\Delta\phi(e,\mu) < 2.8$ for both muons. The distributions of the m_{T} using the electron and the higher-p_{T} muon and the invariant mass of two muons ($m_{\mu\mu}$) are shown in Fig. 6.25(a) and 6.25(b).

The MC simulation is used for the simulation of WZ and ZZ backgrounds. The ZZ backgrounds mostly decay to $e^+e^-\mu^+\mu^-$ in which one of the electron and the muon from each Z bosons are not detected. Their contribution to this background is very small as $Z\gamma^*$ and $Z\gamma$ backgrounds are. The point here is different because they are charge symmetric, we can use the SC region to normalize the $W\gamma$, $W\gamma^*$, and WZ background. Fig 6.26(a) and 6.26(c) shows the distributions of the transverse mass, and Fig 6.26(b) and 6.26(d) shows the sub-leading lepton p_{T}. The normalization factors are $\beta_{0j} = 0.92 \pm 0.07$ (stat.) and $\beta_{1j} = 0.96 \pm 0.12$ (stat.) for the DF channels in the $n_j \leq 1$ categories.

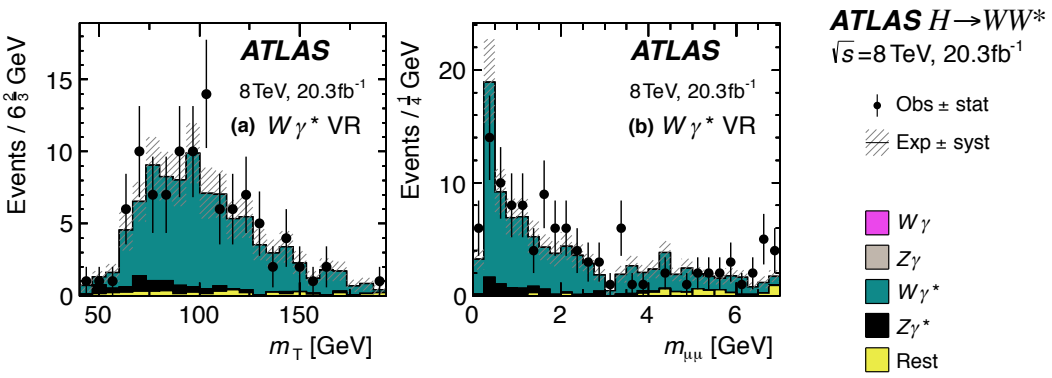

Figure 6.25: (a) $W\gamma^*$ transverse mass using the leading two leptons, and (b) $W\gamma^*$ dimuon invariant mass in $W\gamma^*$ validation region (VR).

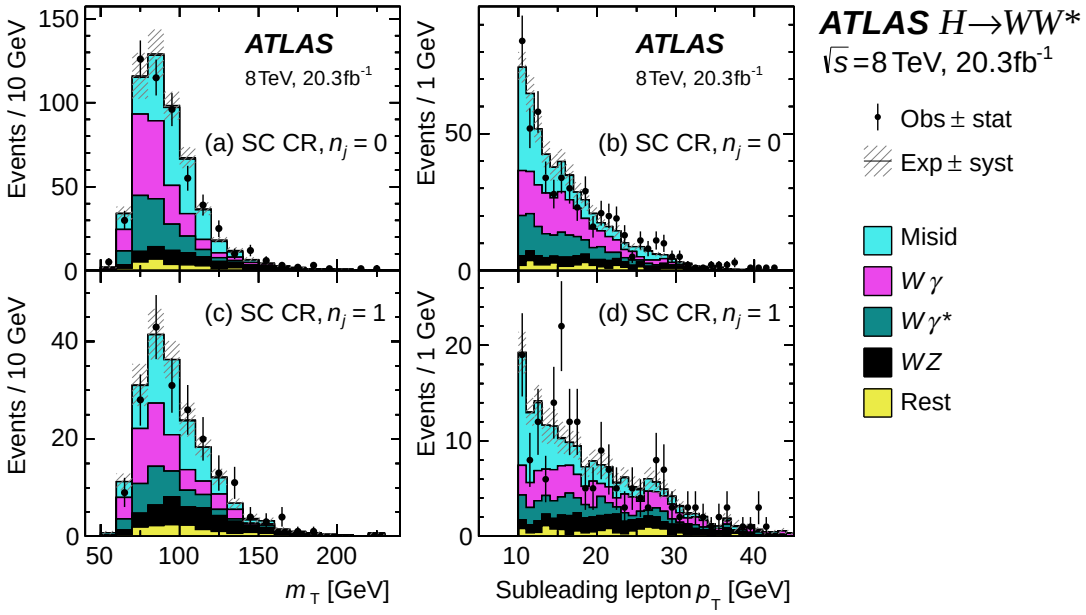

Figure 6.26: Same-charge control region (CR) distributions: (a) transverse mass in the $n_j = 0$ category, (b) subleading lepton p_{T} in the $n_j = 0$ category, (c) transverse mass in the $n_j = 1$ category, and (d) subleading lepton p_{T} in the $n_j = 1$ category. "Rest" consists of contributions not listed in the legend.

Theoretical uncertainties of VV backgrounds are dominated by the scale uncertainty on the prediction in each jet bin. For the $W\gamma$ background, a relative uncertainty of 6% on total cross section is correlated across jet categories, and the uncorrelated jet-bin uncertainties are 9%, 53%, and 100% in the $n_j = 0$, $n_j = 1$, and $n_j \geq 2$ categories, respectively. The total cross section uncertainty is 7% for $W\gamma^*$ events where the cross section uncertainty in each jet bins are 7% ($n_j = 0$), 30% ($n_j = 1$), and 26% ($n_j \geq 2$).

6.1.5.5 Z/γ^* Background Estimation

The Drell-Yan (DY) background consists of two opposite charged leptons. Z/γ^* decays to a pair of leptons; $Z/\gamma^* \to \tau\tau$ and $Z/\gamma^* \to ee$, $\mu\mu$. $Z/\gamma^* \to \tau\tau$ is more abundant in the DF channel and $Z/\gamma^* \to ee$, $\mu\mu$ is a major background in the SF category. The estimation of $Z/\gamma^* \to \tau\tau$ backgrounds is done with a CR that is defined in each jet bin. The $Z/\gamma^* \to ee$, $\mu\mu$ uses data-driven method to handle the complexity of $p_{\mathrm{T}}^{\mathrm{miss}}$ mis-measurement in the SF channel. The $p_{\mathrm{T}}^{Z/\gamma^*}$, reconstructed as $p_{\mathrm{T}}^{\ell\ell}$, is modeled by the ALPGEN + HERWIG. However, its modelling is not accurate to simulate soft interactions, specially for $n_j = 0$ category. Therefore, the correction for mis-modeled $p_{\mathrm{T}}^{Z/\gamma^*}$ is done by re-weighting. The weights are derived from a data-to-MC comparison in the Z peak and applied for $Z/\gamma^* \to ee$, $Z/\gamma^* \to \mu\mu$ and $Z/\gamma^* \to \tau\tau$. Therefore, an extra systematic comes from this treatment and it is propagated to the $Z/\gamma^* \to ee$, $\mu\mu$ background estimation.

$Z/\gamma^* \to \tau\tau$

The $Z/\gamma^* \to \tau\tau$ control region is used to estimate the background for each categorized channels, depending on the jet multiplicity and the production modes. Due to the large contamination from $Z/\gamma^* \to ee$ and $Z/\gamma^* \to \mu\mu$ in the SF channel, the CR is reconstructed using only DF lepton pairs, except in the VBF-enriched $n_j \geq 2$ region. The criteria used to

build the CR for each analysis categories are shown in Table 6.27. The bottom of the table shows the purity and the normalization factors of each categories.

Table 6.27: $Z/\gamma^* \to \tau\tau$ CR and the normalization factors.

$Z/\gamma^* \to \tau\tau$ CR			
$n_j = 0$, DF	$n_j = 1$, DF	$n_j > 2$ ggF , DF	$n_j > 2$ VBF , $DF + SF$
pre-selection $m_{\ell\ell} < 80$ GeV $\Delta\phi_{\ell\ell} > 2.8$	pre-selection $m_{\ell\ell} < 80$ GeV $m_{\tau\tau} > (m_Z - 25\,\text{GeV})$	pre-selection $m_{\ell\ell} < 70$ GeV $\Delta\phi_{\ell\ell} > 2.8$	pre-selection $m_{\ell\ell} < 80$ GeV (75 GeV in $ee/\mu\mu$) $\lvert m_{\tau\tau} - m_Z \rvert < 25$ GeV.
purity = 91% $\beta_{0j} = 1.00 \pm 0.02$ (stat.)	purity = 80% $\beta_{1j} = 1.05 \pm 0.04$ (stat.)	purity = 74% $\beta_{2j} = 1.00 \pm 0.09$ (stat.)	- $\beta = 0.9 \pm 0.3$ (stat.)

Fig 6.27 shows the m_{T} distributions for $n_j \leq 1$. The MC-to-Data agreement is good and the sources of uncertainty are mainly QCD scale variations, PDFs and generator modeling. The used MC generators are ALPGEN + HERWIG and ALPGEN + PYTHIA. An additional source of uncertainty is due to the $p_{\mathrm{T}}^{Z/\gamma^*}$ reweighting in the $n_j = 0$ category, where the impact of different weights derived with the cut $p_{\mathrm{T}}^{\mathrm{miss}} > 20$ GeV in the Z-peak region is evaluated. Table 6.28 shows the uncertainties on the extrapolation factor α to the signal regions and the WW control regions in the $n_j \leq 1$ and $n_j \geq 2$ ggF-enriched categories.

$Z/\gamma^* \to ee, \mu\mu$

The $Z/\gamma^* \to ee, \mu\mu$ CR is designed only in the SF channel where f_{recoil} is a good indicator of the soft hadronic recoil as seen in Fig 6.6 (d). The definition of f_{recoil} is given in section 6.1.3.4.

For the VBF-enriched $n_j \geq 2$ category, $Z/\gamma^* \to ee, \mu\mu$ background is estimated with an ABCD method. The $Z/\gamma^* \to ee, \mu\mu$ BDT shape is derived from a region pure in Z/γ^* at low $m_{\ell\ell}$ and low $p_{\mathrm{T}}^{\mathrm{miss}}$. The normalization factor computed in the region at low $p_{\mathrm{T}}^{\mathrm{miss}}$ is cor-

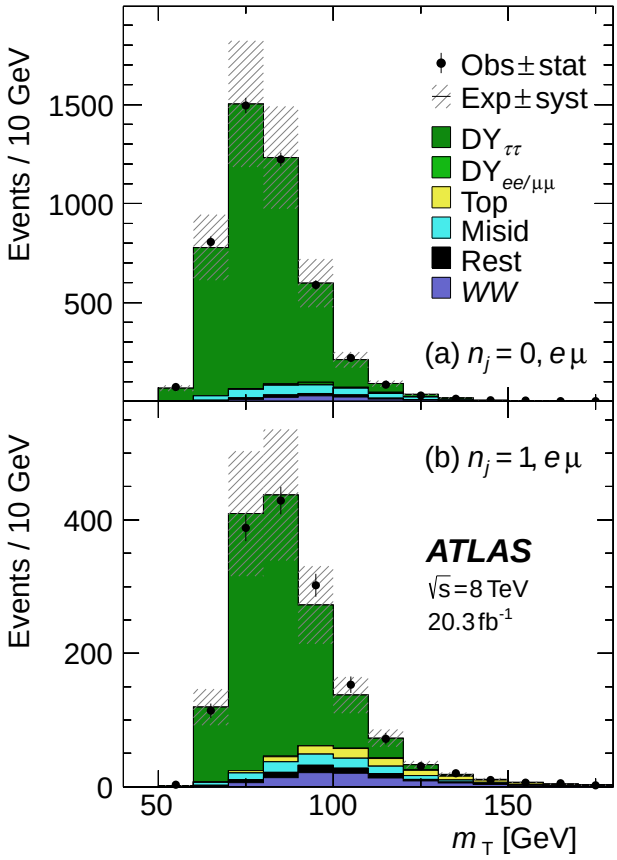

Figure 6.27: $Z/\gamma^* \to \tau\tau$ control region distributions of transverse mass.

Table 6.28: Relative $Z/\gamma^* \to \tau\tau$ uncertainties on the extrapolation factor α, for the $n_j \leq 1$ and $n_j \geq 2$ ggF-enriched categories. Scale, PDF and generator modeling (Gen) uncertainties are reported. For the $n_j = 0$ category, additional uncertainty due to $p_{\mathrm{T}}^{Z/\gamma^*}$ re-weighting is shown.

Regions	Scale	PDF	Gen	$p_{\mathrm{T}}^{Z/\gamma^*}$
Signal regions				
$n_j = 0$	−1.6	1.4	5.7	19
$n_j = 1$	4.7	1.8	−2.0	-
$n_j \geq 2$ ggF	−10.3	1.1	10.4	-
WW control regions				
$n_j = 0$	−5.5	1.0	−8.0	16
$n_j = 1$	−7.2	2.1	3.2	-

rected for the mismodelling of the $p_{\mathrm{T}}^{\mathrm{miss}}$ cut efficiency computed in the Z-peak region. The normalization factor is computed for each bin of the BDT shape, in particular for the first bin and for the bins 2 and 3 merged together. The values obtained are : $\beta_{\mathrm{bin1}} = 1.01 \pm 0.15$ (stat.) and $\beta_{\mathrm{bin2+3}} = 0.89 \pm 0.28$ (stat.)

6.1.5.6 7 TeV Analysis

The 7 TeV analysis is designed to be similar to the 8 TeV analysis in the $n_j \leq 1$ channels. The majority of the background CRs have similar criteria to the 8 TeV analysis while the f_{recoil} cut is looser than the value used at 8 TeV. Due to the lack of statistics, the 7 TeV study uses a multijet sample to extract the extrapolation factor for W+jets backgrounds instead of Z+jets events. For the VBF-enriched $n_j \geq 2$ study, the basic estimation method are same to the 8 TeV analysis. The normalization factors are summarized in Table 6.30 with 8 TeV data ones.

The uncertainties in the 7 TeV analysis are evaluated using the same procedure as the 8 TeV analysis including the estimation of the f_{recoil} selection efficiency for the $Z/\gamma^* \to ee, \mu\mu$ background estimation. The experimental uncertainty is calculated using the likelihood fit. The major uncertainty is from the extrapolation factor in the W+jets estimate which is 29% and 36% for muons and electrons, respectively.

6.1.5.7 Summary

Table 6.29 shows the detailed event yield in the CR of the 8 TeV analysis. They are all normalized with the normalization factor β shown in Table 6.30. The table shows only the statistical uncertainty except for the WW background where, in order to quantify the large deviation from one, the systematic contribution is also included. The value of β is : $1.22 \pm 0.03\,(\mathrm{stat.}) \pm 0.10\,(\mathrm{syst.})$.

Table 6.29: CR event yields for 8 TeV data. All of the background processes are normalized with the corresponding β or with the data-derived methods.

Control regions	Summary			Composition of N_{bkg}						Purity
	N_{obs}	N_{bkg}	N_{sig}	N_{WW}	N_{top}	N_{misid}	N_{VV}	N_{DY}		$N_{\text{bold}}/N_{\text{bkg}}$ (%)
								$N_{ee/\mu\mu}$	$N_{\tau\tau}$	
$n_j = 0$										
CR for WW	2713	2680 ± 9	28	1950	335	184	97	8.7	106	73
CR for top quarks	76013	75730 ± 50	618	8120	56210	2730	1330	138	7200	74
CR for VV	533	531 ± 8	2.2	2.5	1.1	180	327	19	2.7	62
CR for $Z/\gamma^* \to \tau\tau$	4557	4530 ± 30	23	117	16.5	239	33	28	4100	91
$n_j = 1$										
CR for WW	2647	2640 ± 12	4.3	1148	1114	165	127	17	81	43
CR for top quarks	6722	6680 ± 12	17	244	6070	102	50	6	204	91
CR for VV	194	192 ± 4	1.9	1	3.1	65	117	4.7	0.8	61
CR for $Z/\gamma^* \to \tau\tau$	1540	1520 ± 14	18	100	75	84	27	7	1220	80
$n_j \geq 2$ ggF										
CR for top quarks	2664	2660 ± 10	4.9	561	1821	129	101	10	44	68
CR for $Z/\gamma^* \to \tau\tau$	266	263 ± 6	2.6	13	34	18	4.1	0.1	194	74
$n_j \geq 2$ VBF										
CR for top quarks, bin 1	143	142 ± 2	2.1	1.9	130	2.1	0.8	6.3	1.1	92
CR for top quarks, bin 2–3	14	14.3 ± 0.5	1.8	0.6	11.6	0.2	0.2	0.9	0.2	81
CR for $Z/\gamma^* \to \tau\tau$	24	20.7 ± 0.9	2.4	0.9	1.2	0.6	0.2	0.8	17	82

Table 6.30: Control region normalization factors β. The β values scale the corresponding estimated yields in the signal region. The uncertainties are due to the sample size of the corresponding control regions.

Category	WW	Top quarks	VV	$Z/\gamma^* \to \tau\tau$
8 TeV sample				
$n_j = 0$	1.22 ± 0.03	1.08 ± 0.02	0.92 ± 0.07	1.00 ± 0.02
$n_j = 1$	1.05 ± 0.05	1.06 ± 0.03	0.96 ± 0.12	1.05 ± 0.04
$n_j \geq 2$, ggF	-	1.05 ± 0.03	-	1.00 ± 0.09
$n_j \geq 2$, VBF bin 1	-	1.58 ± 0.15	-	0.90 ± 0.30
$n_j \geq 2$, VBF bins 2–3	-	0.95 ± 0.31	-	
7 TeV sample				
$n_j = 0$	1.09 ± 0.08	1.12 ± 0.06	-	0.89 ± 0.04
$n_j = 1$	0.98 ± 0.12	0.99 ± 0.04	-	1.10 ± 0.09
$n_j \geq 2$, VBF bins 1–3	-	0.82 ± 0.29	-	1.52 ± 0.91

Also the normalization factor of the top-quark background in bin-1 of the $n_j \geq 2$ VBF-enriched category shows a deviation from 1 larger than the statistical uncertainty but still is well within the systematic error: $\beta = 1.58 \pm 0.15\,(\text{stat.}) \pm 0.55\,(\text{syst.})$. Other normalization factors are compatible with one inside the shown statistical error.

6.2 Fits in $H \to WW^* \to \ell\nu\ell\nu$

The selected events are used to extract the signal strength and to quantify the significance of the observed excess. A likelihood function is built using all the events in both signal regions and control regions and is maximized with respect to the signal strengths, the background normalization factors and the nuisance parameters used to implement the systematic uncertainties. This procedure is called "fitting". In this section, details of the fitting procedure are described and the final fitting results are shown.

6.2.1 Fit regions

The fitting procedure is designed to reduce the expected error on the signal strength parameter (μ). The final kinematic variables for the fitting procedure are the transverse mass (m_{T}) for the ggF analysis and the BDT score (O_{BDT}) for the VBF analysis. Tables 6.31 and 6.32 list up the SR and the CR that are used in the fitting procedure with the sub-analysis categories in the SR as explained in section 6.1.4. The SR, then, is divided into bins based on the values of the fit variables, $m_{\ell\ell}$ and $p_{\mathrm{T}}^{\ell 2}$, and two regions distinguished by the cases where the subleading lepton is an electron or a muon. The profiled CR are included in the fit procedure and the relative normalization factors are extracted from the fit itself, while the non-profiled CRs don't enter directly in the fit but are used to estimate the backgrounds that are included in the fit procedure. They are shown in Table 6.32 for completeness.

The DF samples in $n_j \leq 1$ are categorized into twelve kinematic regions as listed in Table 6.31, two regions in $m_{\ell\ell}$, three regions in $p_{\mathrm{T}}^{\ell 2}$, and two regions for the sub-leading lepton flavors, denoted as $12 = 2 \cdot 3 \cdot 2$. Since the DF samples in the $n_j \leq 1$ regions is the most sensitive channel, the statistics are enough to make this fine binning. However, the SF samples in the $n_j \leq 1$ regions are relatively less sensitive, thus, only one bin is designed

for the fit. The control regions that are included in the likelihood is the profiled CRs and it determine the normalization of the backgrounds accordingly.

For the final fitting procedure, the m_{T} is used for the ggF production mode analysis. The m_{T} distribution in the $n_j = 0$ category is binned with ten bins. The bin boundaries are chosen in such a way that the signal distributes uniformly in each bin. The lowest bin and the highest bin have the worse signal/background ratio and their boundaries are at 80 GeV and 130 GeV. The lowest bin has a high contamination of Wj and $Z/\gamma^* \to \tau\tau$ background while the highest bin is contaminated by top-quarks and WW background. The remaining 8 bins distribute between 80 and 130 GeV with a bin width of about 6 GeV. The m_{T} distribution for the $n_j = 1$ category follows the same strategy as the $n_j = 0$ category but is in six bins with 10 GeV granularity. The ggF-enriched $n_j \geq 2$ category has a specific bin boundaries $[0, 50, 80, 130, \infty]$ GeV. The VBF-enriched $n_j \geq 2$ category is fitted using O_{BDT} score distribution that is binned according the bin boundaries: $[-1, -0.48, 0.3, 0.78, 1]$. The S/B ratio increases with increasing values of O_{BDT}, therefore the lowest bin is not used in the fit because it is completely dominated by backgrounds. The other three bins, 1, 2, and 3, are used in the fit. The bin boundaries are chosen to maximize the expected significance for the VBF process. Fig 6.28 visualizes the fitting procedure for the $n_j = 0$ case as an example.

6.2.2 Fitting tools

As discussed in chapter 5, the likelihood function is used in the fit. $\mathcal{L}(\mu, \theta|N)$ is a function of the signal strength parameter μ and nuisance parameters $\theta = \{\theta_a, \theta_b, \ldots\}$ in the shown number of event sets $\mathbf{N} = \{N_A, N_B, \ldots\}$. The likelihood function used in this study is given in Eq. 6.19.

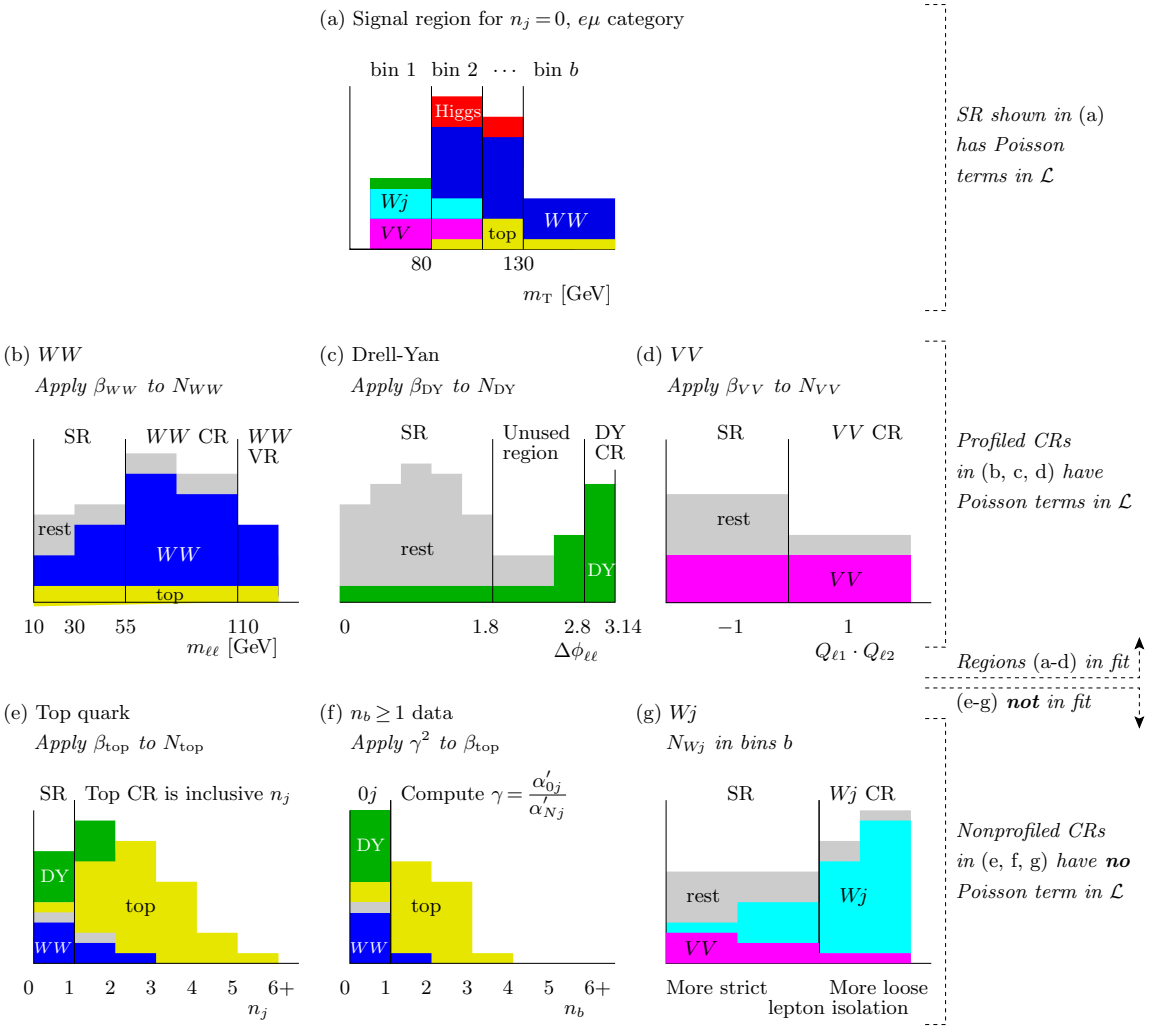

Figure 6.28: Simplified illustration of the fit regions for $n_j = 0$, $e\mu$ category. The figure in (a) is the variable-binned m_{T} distribution in the signal region for a particular range of $m_{\ell\ell}$ and $p_{\mathrm{T}}^{\ell 2}$ specified in Table 6.31 and Table 6.32; the m_{T} bins are labeled $b = 1, 2, \ldots$; the histograms are stacked for the five principal background processes—WW, top, Misid. (mostly Wj), VV, DY (unlabeled)—and the Higgs signal process. The figures in (b, c, d) represent the distributions that define the various profiled control regions used in the fit with a corresponding Poisson term in the likelihood $\mathcal{L}$. Those in (e, f, g) represent the non-profiled control regions that do not have a Poisson term in $\mathcal{L}$, but determine parameters that modify the background yield predictions. A validation region (VR) is also defined in (b).

Table 6.31: The fitting region definitions for the SR. These categories are represented in the Poisson terms in the $\mathcal{L}$ (Eq. 6.19)

Signal region categories

SR category i				Fit var.
n_j, flavor	$\otimes m_{\ell\ell}$	$\otimes p_{\mathrm{T}}^{\ell 2}$	$\otimes \ell_2$	
$n_j = 0$				
DF	$\otimes [10, 30, 55]$	$\otimes [10, 15, 20, \infty]$	$\otimes [e, \mu]$	m_{T}
SF	$\otimes [12, 55]$	$\otimes [10, \infty]$		m_{T}
$n_j = 1$				
DF	$\otimes [10, 30, 55]$	$\otimes [10, 15, 20, \infty]$	$\otimes [e, \mu]$	m_{T}
SF	$\otimes [12, 55]$	$\otimes [10, \infty]$		m_{T}
$n_j \geq 2$ ggF				
DF	$\otimes [10, 55]$	$\otimes [10, \infty]$		m_{T}
$n_j \geq 2$ VBF				
DF	$\otimes [10, 50]$	$\otimes [10, \infty]$		O_{BDT}
SF	$\otimes [12, 50]$	$\otimes [10, \infty]$		O_{BDT}

Table 6.32: The fitting region definitions for the CR. These categories are represented in the Poisson terms in the $\mathcal{L}$ (Eq. 6.19).

Control regions that are profiled (•) and non-profiled (◦)

CR	Profiled?	Sample	Notable differences vs. SR
$n_j = 0$			
	•	DF	$55<m_{\ell\ell}<110$, $\Delta\phi_{\ell\ell}<2.6$, $p_{\mathrm{T}}^{\ell 2}>15$
WW			
Top	◦	DF	$n_j = 0$ after presel., $\Delta\phi_{\ell\ell} < 2.8$
Wj	◦	Same	One anti-identified ℓ
jj	◦	Same	Two anti-identified ℓ
VV	•	DF	Same-charge ℓ (only used in DF)
DY, SF	•	SF	$f_{\mathrm{recoil}} > 0.1$ (only used in SF)
DY, $\tau\tau$	•	DF	$m_{\ell\ell} < 80$, $\Delta\phi_{\ell\ell} > 2.8$
$n_j = 1$			
	•	DF	$m_{\ell\ell}>80$, $\lvert m_{\tau\tau}-m_Z\rvert>25$, $p_{\mathrm{T}}^{\ell 2}>15$
WW			
Top	•	DF	$n_b = 1$
Wj	◦	Same	One anti-identified ℓ
jj	◦	Same	Two anti-identified ℓ
VV	•	DF	Same-charge ℓ (only used in DF)
DY, SF	•	SF	$f_{\mathrm{recoil}} > 0.1$ (only used in SF)
DY, $\tau\tau$	•	DF	$m_{\ell\ell} < 80$, $m_{\tau\tau} > m_Z - 25$
$n_j \geq 2$ ggF			
Top	•	DF	$m_{\ell\ell} > 80$
Wj	◦	Same	One anti-identified ℓ
jj	◦	Same	Two anti-identified ℓ
DY, $\tau\tau$	•	DF	$m_{\ell\ell} < 70$, $\Delta\phi_{\ell\ell} > 2.8$
$n_j \geq 2$ VBF			
Top	•	Both	$n_b = 1$
Wj	◦	Same	One anti-identified ℓ
jj	◦	Same	Two anti-identified ℓ
DY, SF	◦	SF	$E_{\mathrm{T}}^{\mathrm{miss}}<45$ (only used in SF)
DY, $\tau\tau$	◦	Both	$m_{\ell\ell} < 80$, $\lvert m_{\tau\tau} - m_Z \rvert < 25$

$$\mathcal{L} = \underbrace{\prod_{i,b}^{\text{Table 6.31 \& 6.32}} f\Big(N_{ib}\,\Big|\,\mu\cdot S_{ib}\cdot\prod_{r}^{\text{Syst. in Signal}}\nu_{br}(\theta_r) + \sum_{k}^{\text{Table 6.1}}\beta_k\cdot B_{kib}\cdot\prod_{s}^{\text{Syst. in Fitting}}\nu_{bs}(\theta_s)\Big)}_{\text{Poisson for SR with signal strength } \mu\text{; predictions } S,\,B} \cdot \underbrace{\prod_{l}^{\text{Table 6.32 •}} f\Big(N_l\,\Big|\,\sum_{k}^{\text{Table 6.1}}\beta_k\cdot B_{kl}\Big)}_{\text{Poisson for profiled CRs}} \cdot \underbrace{\prod_{t}^{\text{Syst. in } \{r,s\}} g(\vartheta_t|\theta_t)}_{\text{Gauss. for syst.}}$$
$$\cdot \underbrace{\prod_{k}^{\text{Table 6.1}} f(\xi_k\,|\,\zeta_k\cdot\theta_k)}_{\text{Poiss. for MC stats}} \tag{6.19}$$

The likelihood is built using the follwing factors:

- Poisson function $f(N_{ib}\,|\,\ldots)$ used to model the event yield in each bin b of the variable fit to extract the signal yield for each category i
- Poisson function $f(N_l\,|\,\Sigma_k\,\beta_k\,B_{kl})$ used to model the event yield in each control region l with the total background yield summed over processes k (B_{kl})
- Gaussian functions $g(\vartheta_t\,|\,\theta_t)$ used to model the systematic uncertainties t
- Poisson functions $f(\zeta_k\,|\,\ldots)$ used to account for the MC statistics k

The SR is treated in the first term, it includes the number of signal events scaled by the signal strength μ, and the sum of the background yields in the SR. The total expected number of event in the SR, then, $\lambda = \mu\cdot S + \Sigma_k\,B_k$ while the Poisson function f for the probability is given as $f(N\,|\,\lambda) = e^{-\lambda}\lambda^N/N!$. The β_k is the normalization factor of background k, and the ν is the corresponding functions that parameterize the impact of the systematic uncertainties θ. The CR is treated in the second term and is described with the function $f(N_l\,|\,\lambda_l)$ for the different CRs, denoted as l. The expected events yields in each CR regions is $\lambda_l = \Sigma_k\,\beta_k\cdot B_{kl}$, where the B_{kl} is the estimate of background k in a certain CR, l. The third term is the term for the systematic uncertainties where the Gaussian p.d.f. constraint is adopted. As described in section 5.3, the Gaussian p.d.f. has two different form of Gaussian functions; $\nu(\theta) = (1+\epsilon)^\theta$ and $\nu_b(\theta) = 1 + \epsilon_b\cdot\theta$. These different forms of functions are used for the normalization uncertainties and the shape uncertainties, respectively.

The fourth term is for the statistical uncertainties. This term uses the Poisson distribution $f(\xi \mid \lambda)$, where ξ is the central value of the background estimation and the $\lambda = \zeta \cdot \theta$.

Beside the first term, all other terms are dealing with the background estimation, however, they all affect the prediction of the S and B_k in the first term. As seen in the overall $\mathcal{L}$, given in the equation 6.19, the multiplication of all the terms is maximized respect to μ and $\boldsymbol{\theta}$ to evaluated at $\vartheta = 0$ and $\xi = \zeta$.

The test statistics is the negative profile-likelihood ratio.

$$q(\mu) = -2 \ln \frac{\mathcal{L}(\mu, \boldsymbol{\theta})}{\mathcal{L}_{\max}}\bigg|_{\boldsymbol{\theta} = \hat{\boldsymbol{\theta}}_\mu}, \tag{6.20}$$

where the numerator is the conditional fit of $\boldsymbol{\theta}$ with a fixed value of μ and the denominator is unconditional maximized fit results respect to μ and $\boldsymbol{\theta}$. The major results in the study are computed with this test statistics, i.e. p_0 which is the test for q_0 in the equation 6.20 at the $\mu = 0$ and measures the probability of accidental fluctuation of background to mimic the signal like events.

6.2.3 Systematic Uncertainties

In the likelihood fit, uncertainties are included in the nuisance parameter treatments. The uncertainties are categorized into several areas based on their sources, the experimental uncertainty, the theory uncertainty and the statistical uncertainty. The most major source of the experimental uncertainty are the jet energy scale (JES) and the jet energy resolution (JER), and the b-tagging efficiency. The lepton resolution and identification, the trigger efficiency, the missing transverse momentum measurement, and the luminosity calculation also contribute to the experimental uncertainty. Table 6.33 summarizes the systematic uncertainties for the signal and background yield at 8 TeV. The luminosity uncertainty (Lumi) is 2.8% for all categories at 8 TeV [75] while it is 1.8% at 7 TeV. The

JES uncertainties, coming from many different source, are further divided in different categories by the physical source of the uncertainty, such as MC modeling, pile-up and so on. The associated uncertainty of JER lies in a range between 2% and 40% depending on the p_{T} and the η. The b jet tagging uncertainty ranges from 1% from 7.8%. The uncertainty of the mis-identification rate for the light-quark jets has a dependency from p_{T} and η, and ranges from 9 to 19%. The c-jet impact on the b jet tagging lies in the range $6-14\%$. The lepton related uncertainties are estimated from the $Z \to ee, \mu\mu$, $J/\psi \to ee, \mu\mu$, and $W \to e\nu, \mu\nu$ decay samples [48, 46]. The $E_{\mathrm{T}}^{\mathrm{miss}}$ is affected by soft object selections as well as hard object selections. Therefore, the jet energy and lepton momentum reconstruction can be big sources of uncertainties. And, also the low-energy modeling for the soft term impacts to the uncertainty. The $p_{\mathrm{T}}^{\mathrm{miss}}$ also takes into account the track information in the reconstruction, thus, the track-related soft objects are major sources of uncertainty.

The experimental uncertainties are correlated across all backgrounds in the SR and CR, therefore, the uncertainty of the extrapolation factor α is applied to the all the study. However, if the uncertainty is less than 1%, the systematic is neglected and this pruning procedure leads the study achieving more stable for the fitting procedure. The influence of experimental uncertainty on the m_{T} shape to extract the signal yield is used all backgrounds except W+jets and multi-jets and its impact is not significant because the normalization uncertainty of the individual background dominates the total uncertainty. The theory uncertainties of the m_{T} shape in some backgrounds for ggF are calculated and are included in the total uncertainty. For the $n_j \geq 2$ VBF-enriched category, the O_{BDT} output distribution is used to calculate the theoretical uncertainty.

Table 6.34 summarizes the post-fit uncertainty results for all sub-analysis categories. The table shows in three sub-divisions, the experimental and the theoretical, along with the total uncertainty. In each categories are listed up the signal and backgrounds.

Table 6.33: Sources of systematic uncertainty (in %) on the predicted signal yield (N_{sig}) and the cumulative background yields (N_{bkg}). The values are post-fit and given for the 8 TeV analysis.

(a) Uncertainties on N_{sig} (in %)

	$n_j = 0$	$n_j = 1$	$n_j \geq 2$ ggF	$n_j \geq 2$ VBF
ggF H, jet veto for $n_j = 0$, ϵ_0	8.1	14	12	-
ggF H, jet veto for $n_j = 1$, ϵ_1	-	12	15	-
ggF H, $n_j \geq 2$ cross section	-	-	-	6.9
ggF H, $n_j \geq 3$ cross section	-	-	-	3.1
ggF H, total cross section	10	9.1	7.9	2.0
ggF H acceptance model	4.8	4.5	4.2	4.0
VBF H, total cross section	-	0.4	0.8	2.9
VBF H acceptance model	-	0.3	0.6	5.5
$H \to WW^*$ branch. fraction	4.3	4.3	4.3	4.3
Integrated luminosity	2.8	2.8	2.8	2.8
Jet energy scale & reso.	5.1	2.3	7.1	5.4
$p_{\text{T}}^{\text{miss}}$ scale & resolution	0.6	1.4	0.1	1.2
f_{recoil} efficiency	2.5	2.1	-	-
Trigger efficiency	0.8	0.7	-	0.4
Electron id., iso., reco. eff.	1.4	1.6	1.2	1.0
Muon id., isolation, reco. eff.	1.1	1.6	0.8	0.9
Pile-up model	1.2	0.8	0.8	1.7

(b) Uncertainties on N_{bkg} (in %)

WW theoretical model	1.4	1.6	0.7	3.0
Top theoretical model	-	1.2	1.7	3.0
VV theoretical model	-	0.4	1.1	0.5
$Z/\gamma^* \to \tau\tau$ estimate	0.6	0.3	1.6	1.6
$Z/\gamma^* \to ee$, $\mu\mu$ est. in VBF	-	-	-	4.8
Wj estimate	1.0	0.8	1.6	1.3
jj estimate	0.1	0.1	1.8	0.9
Integrated luminosity	-	-	0.1	0.4
Jet energy scale & reso.	0.4	0.7	0.9	2.7
$p_{\text{T}}^{\text{miss}}$ scale & resolution	0.1	0.3	0.5	1.6
b-tagging efficiency	-	0.2	0.4	2.0
Light- and c-jet mistag	-	0.2	0.4	2.0
f_{recoil} efficiency	0.5	0.5	-	-
Trigger efficiency	0.3	0.3	0.1	-
Electron id., iso., reco. eff.	0.3	0.3	0.2	0.3
Muon id., isolation, reco. eff.	0.2	0.2	0.3	0.2
Pile-up model	0.4	0.5	0.2	0.8

Table 6.34: Composition of the post-fit uncertainties (in %) on the total signal (N_{sig}), total background (N_{bkg}), and individual background yields in the signal regions. The values are given for the 8 TeV analysis.

Sample	Total error	Stat. error	Expt. syst. err.	Theo. syst. err.
$n_j = 0$				
N_{sig}	16	-	6.7	15
N_{bkg}	2.5	1.5	1.2	1.7
N_{WW}	4.2	2.4	2.3	2.6
N_{top}	7.4	2.3	4.2	5.6
N_{misid}	17	-	9.9	14
N_{VV}	9.9	4.8	4.6	7.4
$N_{\tau\tau}$ (DY)	34	1.7	33	7.2
$N_{ee/\mu\mu}$ (DY)	30	14	26	5.5
$n_j = 1$				
N_{sig}	22	-	5.3	22
N_{bkg}	3	1.7	1.4	2.1
N_{WW}	7.7	5.5	2.7	4.6
N_{top}	5	3.4	2.9	2.3
N_{misid}	18	-	11	14
N_{VV}	14	8.9	6.1	8.5
$N_{\tau\tau}$ (DY)	27	3.3	26	6.3
$N_{ee/\mu\mu}$ (DY)	39	27	26	7.4
$n_j \geq 2$ ggF-enriched				
N_{sig}	23	-	8.6	22
N_{bkg}	4.2	1.5	2.2	3.2
N_{WW}	20	-	8.7	18
N_{top}	7.9	2.6	3.4	6.7
N_{misid}	29	-	16	24
N_{VV}	32	-	9.6	31
$N_{\tau\tau}$ (DY)	18	8	13	10
$N_{ee/\mu\mu}$ (DY)	15	-	14	4
$n_j \geq 2$ VBF-enriched				
N_{sig}	13	-	6.8	12
N_{bkg}	9.2	4.7	6.4	4.5
N_{WW}	32	-	14	28
N_{top}	15	9.6	7.6	8.5
N_{misid}	22	-	12	19
N_{VV}	20	-	12	15
$N_{\tau\tau}$ (DY)	40	25	31	2.9
$N_{ee/\mu\mu}$ (DY)	19	11	15	-

Table 6.35: Impact on the signal strength $\hat{\mu}$ from the pre-fit and post-fit variations of the nuisance parameter uncertainties, Δ_θ. The + (−) column header indicates the positive (negative) variation of Δ_θ and the resulting change in $\hat{\mu}$ is noted in the entry (the sign represents the direction of the change). The right-hand side shows the pull of θ and the data-constraint of Δ_θ. The pulls are given in units of standard deviations (σ) and Δ_θ of ±1 means no data-constraint. The rows are ordered by the size of a change in $\hat{\mu}$ due to varying θ by the post-fit uncertainty Δ_θ.

Systematic source	Impact on $\hat{\mu}$					Impact on $\hat{\theta}$	
	Pre-fit $\Delta_{\hat{\mu}}$		Post-fit $\Delta_{\hat{\mu}}$		Plot of post-fit $\pm\Delta_{\hat{\mu}}$	Pull, $\hat{\theta}$ (σ)	Constr., Δ_θ
	+	−	+	−			
ggF H, PDF variations on cross section	−0.06	+0.06	−0.06	+0.06		−0.06	± 1
ggF H, QCD scale on total cross section	−0.05	+0.06	−0.05	+0.06		−0.05	± 1
WW, generator modeling	−0.07	+0.06	−0.05	+0.05		0	± 0.7
Top quarks, generator modeling on α_{top} in ggF cat.	+0.03	−0.03	+0.03	−0.03		−0.40	± 0.9
Misid. of μ, OC uncorrelated corr. factor α_{misid}, 2012	−0.03	+0.03	−0.03	+0.03		0.48	± 0.8
Integrated luminosity, 2012	−0.03	+0.03	−0.03	+0.03		0.08	± 1
Misid. of e, OC uncorrelated corr. factor α_{misid}, 2012	−0.03	+0.03	−0.02	+0.03		−0.06	± 0.9
ggF H, PDF variations on acceptance	−0.02	+0.02	−0.02	+0.02		−0.03	± 1
Jet energy scale, η intercalibration	−0.02	+0.02	−0.02	+0.02		0.45	± 0.95
VBF H, UE/PS	−0.02	+0.02	−0.02	+0.02		0.26	± 1
ggF H, QCD scale on ϵ_1	−0.01	+0.03	−0.01	+0.03		−0.10	± 0.95
Muon isolation efficiency	−0.02	+0.02	−0.02	+0.02		0.13	± 1
VV, QCD scale on acceptance	−0.02	+0.02	−0.02	+0.02		0.09	± 1
ggF H, UE/PS	-	−0.02	-	−0.02		0	± 0.9
ggF H, QCD scale on acceptance	−0.02	+0.02	−0.02	+0.02		0	± 1
Light jets, tagging efficiency	+0.02	−0.02	+0.02	−0.02		0.21	± 1
ggF H, generator modeling on acceptance	+0.01	−0.02	+0.01	−0.02		0.10	± 1
ggF H, QCD scale on $n_j \geq 2$ cross section	−0.01	+0.02	−0.01	+0.02		−0.04	± 1
Top quarks, generator modeling on α_{top} in VBF cat.	−0.01	+0.02	−0.01	+0.02		−0.16	± 1
Electron isolation efficiency	−0.02	+0.02	−0.02	+0.02		−0.14	± 1
					-0.1 -0.05 0 0.05 0.1		

The fit of the nuisance parameters impact to the measurement of signal strength, $\hat{\mu}$. Thus, checking the impact of certain nuisance parameters (NP) on $\hat{\mu}$ before and after the fitting procedure is necessary. The impact of a single nuisance parameter θ is assessed by considering its effect on the signal strength, in this following definition.

$$\Delta_{\hat{\mu},\pm} = \hat{\mu}(\hat{\theta} \pm \Delta_\theta) - \hat{\mu}(\hat{\theta}), \tag{6.21}$$

where $\hat{\mu}$ is the post-fit value of the signal strength. The top 20 list of the effective nuisance parameters to the signal strength is shown in Table 6.35 in the pre and the post fit condition.

6.2.4 Signal Yield and Distributions

The expected signal and background contributions are used to fit the data in both signal and control regions within given uncertainties. Individual normalization factors (β) can be changed by the background process in the post fit thus the NPs (θ) can have a different value from their nominal values.

The post-fit yields are summarized for the 7 TeV and the 8 TeV analyses. Each categories are normalized with individual normalization factors and are scaled with individual signal strengths. The comparison of the pre-fit and the post-fit turns out to have a significant changes. Table 6.36 summarizes the post-fit signal yields with uncertainties (stat. + syst.) into the division of the jet multiplicity and the lepton flavor composition. The N_{signal} columns is the expected signal yields in each production modes, ggF and VBF. The yields and uncertainties includes the impact from the pulls and the data-constraints of NPs. Following figures are the post-fit distributions of the m_{T} and the O_{BDT} that is used for the final fit. Fig. 6.29 shows the m_{T} distributions for the variation of jet multiplicities and the $m_{\ell\ell}$ and the $p_{\text{T}}^{\ell 2}$ in $n_j \leq 1$. Under different conditions, the background contributions are changed, i.e. the WW process is the dominated background contribution in $n_j = 0$; but the VV and W+jets processes become very significant in Fig. 6.29 (d). By adding the Higgs

Table 6.36: Signal region yields with uncertainties. The tables give the ggF- and VBF-enriched post-fit yields for each n_j category, separated for the 8 and 7 TeV data analyses.

(a) 8 TeV data sample

Channel	Summary				Composition of N_{bkg}						
	N_{obs}	N_{bkg}	N_{signal}		N_{WW}	N_{top}		N_{misid}		N_{VV}	N_{DY}
			N_{ggF}	N_{VBF}		N_t	$N_{t\bar{t}}$	N_{Wj}	N_{jj}		
$n_j = 0$	3750	3430 ± 90	300 ± 50	8 ± 4	2250 ± 95	112 ± 9	195 ± 15	360 ± 60	16 ± 5	420 ± 40	78 ± 21
DF, $\ell_2 = \mu$	1430	1280 ± 40	129 ± 20	3.0 ± 2.1	830 ± 34	41 ± 3	73 ± 6	149 ± 29	10.1 ± 3.6	167 ± 21	14 ± 2.4
DF, $\ell_2 = e$	1212	1106 ± 35	97 ± 15	2.5 ± 0.6	686 ± 29	33 ± 3	57 ± 5	128 ± 31	3.8 ± 1.5	184 ± 23	14 ± 2.4
SF	1108	1040 ± 40	77 ± 15	2.4 ± 1.7	740 ± 40	39 ± 3	65 ± 5	82 ± 16	2 ± 0.5	68 ± 7	50 ± 21
$n_j = 1$	1596	1470 ± 40	102 ± 26	17 ± 5	630 ± 50	150 ± 10	385 ± 20	108 ± 20	8.2 ± 3.0	143 ± 20	51 ± 13
DF, $\ell_2 = \mu$	621	569 ± 19	45 ± 11	7.4 ± 2	241 ± 20	58 ± 4	147 ± 7	51 ± 11	5.7 ± 2.0	53 ± 10	13.8 ± 3.3
DF, $\ell_2 = e$	508	475 ± 18	35 ± 9	6.1 ± 1.4	202 ± 17	45 ± 3	119 ± 6	37 ± 9	2.3 ± 0.9	60 ± 10	9.3 ± 2.5
SF	467	427 ± 21	22 ± 6	3.6 ± 1.8	184 ± 15	46 ± 4	119 ± 10	19 ± 4	0.2 ± 0.1	31 ± 4	28 ± 12
$n_j \geq 2$, ggF $e\mu$	1017	960 ± 40	37 ± 11	13 ± 1.4	138 ± 28	56 ± 5	480 ± 40	54 ± 25	62 ± 22	56 ± 18	117 ± 21
$n_j \geq 2$, VBF	130	99 ± 9	7.7 ± 2.6	21 ± 3	11 ± 3.5	5.5 ± 0.7	29 ± 5	4.7 ± 1.4	2.8 ± 1.0	4.4 ± 0.9	38 ± 7
DF bin 1	37	36 ± 4	3.3 ± 1.2	4.9 ± 0.5	5.0 ± 1.5	3.0 ± 0.6	15.6 ± 2.6	3.2 ± 1.0	2.3 ± 0.8	2.3 ± 0.7	3.6 ± 1.5
DF bin 2	14	6.5 ± 1.3	1.4 ± 0.5	4.9 ± 0.5	1.7 ± 0.7	0.3 ± 0.4	2.0 ± 1.0	0.4 ± 0.1	0.3 ± 0.1	0.7 ± 0.2	0.6 ± 0.2
DF bin 3	6	1.2 ± 0.3	0.4 ± 0.3	3.8 ± 0.7	0.3 ± 0.1	0.1 ± 0.0	0.3 ± 0.1	-	-	0.1 ± 0.0	0.2 ± 0.1
SF bin 1	53	46 ± 6	1.7 ± 0.6	2.6 ± 0.3	3.1 ± 1.0	1.7 ± 0.3	10.1 ± 1.6	0.9 ± 0.2	0.2 ± 0.1	1.0 ± 0.3	28 ± 5
SF bin 2	14	8.4 ± 1.8	0.7 ± 0.3	3.0 ± 0.4	0.9 ± 0.3	0.3 ± 0.2	1.2 ± 0.5	0.2 ± 0.1	-	0.3 ± 0.1	5.2 ± 1.7
SF bin 3	6	1.1 ± 0.4	0.2 ± 0.2	2.1 ± 0.4	0.1 ± 0.1	0.1 ± 0.0	0.2 ± 0.1	-	-	-	0.5 ± 0.3

(b) 7 TeV data sample

$n_j = 0$	594	575 ± 24	49 ± 8	1.4 ± 0.2	339 ± 24	20.5 ± 2.1	38 ± 4	74 ± 15	1.3 ± 0.6	79 ± 10	23 ± 6
DF, $\ell_2 = \mu$	185	186 ± 8	19 ± 3	0.5 ± 0.0	116 ± 8	7 ± 1	14 ± 2	19 ± 5	-	24 ± 3	4.8 ± 1
DF, $\ell_2 = e$	195	193 ± 12	15 ± 2.4	0.5 ± 0.0	95 ± 7	5.3 ± 0.5	10 ± 1	37 ± 9	1.1 ± 0.5	41 ± 6	4.1 ± 0.9
SF	214	196 ± 11	16 ± 3.1	0.5 ± 0.1	128 ± 10	8 ± 1	14 ± 2	18 ± 4	0.2 ± 0.1	14 ± 2	14 ± 5
$n_j = 1$	304	276 ± 15	16 ± 4	3.2 ± 0.3	103 ± 15	22 ± 2	58 ± 6	20 ± 4	3.2 ± 1.6	32 ± 8	38 ± 6
DF, $\ell_2 = \mu$	93	75 ± 4	5.7 ± 1.6	1.2 ± 0.1	33 ± 5	7 ± 1	18 ± 2	5 ± 1	-	9 ± 2	2.7 ± 0.4
DF, $\ell_2 = e$	91	76 ± 5	4.5 ± 1.2	0.9 ± 0.1	28 ± 4	6 ± 1	16 ± 2	10 ± 2	0.7 ± 0.3	14 ± 4	2.3 ± 0.7
SF	120	125 ± 9	5.3 ± 1.6	1.2 ± 0.2	43 ± 6	9 ± 1	24 ± 3	5 ± 1	2.5 ± 1.4	9 ± 2	33 ± 6
$n_j \geq 2$, VBF	9	7.8 ± 1.8	0.9 ± 0.3	2.7 ± 0.3	1.2 ± 0.4	0.3 ± 0.1	1.6 ± 0.8	0.4 ± 0.1	0.1 ± 0.0	0.5 ± 0.2	3.4 ± 1.5
DF bin 1	6	3.0 ± 0.9	0.4 ± 0.2	0.6 ± 0.1	0.5 ± 0.2	0.2 ± 0.1	0.9 ± 0.5	0.1 ± 0.0	0.1 ± 0.0	0.3 ± 0.1	0.8 ± 0.6
DF bin 2–3	0	0.7 ± 0.2	0.2 ± 0.1	1.1 ± 0.1	0.2 ± 0.1	-	0.3 ± 0.2	-	-	-	-
SF bins 1–3	3	4.1 ± 1.3	0.3 ± 0.1	1.0 ± 0.1	0.5 ± 0.2	0.1 ± 0.0	0.4 ± 0.3	0.3 ± 0.1	-	0.2 ± 0.1	2.5 ± 1.1

signal at the mass $m_{\mathrm{T}} = 125$ GeV, the data-to-MC agreement is improved. For the m_{T} distribution of the SF channel for $n_j \leq 1$ is shown in Fig 6.30. For the ggF-enriched $n_j \geq 2$ region, Fig 6.31 shows the m_{T} distribution that contains significant contributions of the top-quark and the $Z/\gamma^* \to \tau\tau$ backgrounds. The analysis of VBF-enriched $n_j \geq 2$ region requires some extra works. The m_{T} distribution is used as the discriminate variables. The m_{T} and the m_{jj} are divided into three and two bins between 80 GeV and 130 GeV for the m_{T} and ≤ 1 TeV for the m_{jj}. Thus, there are 6 defined regions as seen in Fig 6.32, (a) is the m_{T} distribution and (b) shows the scatter plot of the m_{jj} versus the m_{T}. Fig 6.33 shows the O_{BDT} and the m_{T} distributions are shown for DF (a) and SF (b). The m_{T} plot is a distribution after combining all three O_{BDT} bins. The m_{T} distribution for the 7 GeV is shown in Fig 6.34 that has similar tendency with the 8 TeV.

Fig 6.35 is the summary distribution that combines all the lepton flavor compositions and the jet multiplicity categories in $n_j \leq 1$ for the 7 TeV and the 8 TeV. The top figure displays the signal and backgrounds distribution, and if the backgrounds contributions are removed from the top plots, the distribution remains with the SM Higgs signal at $m_H = 125$ GeV scaled by the observed combined signal strength and the data residuals with respect to the total estimated background. The significant excess is observed in the figure.

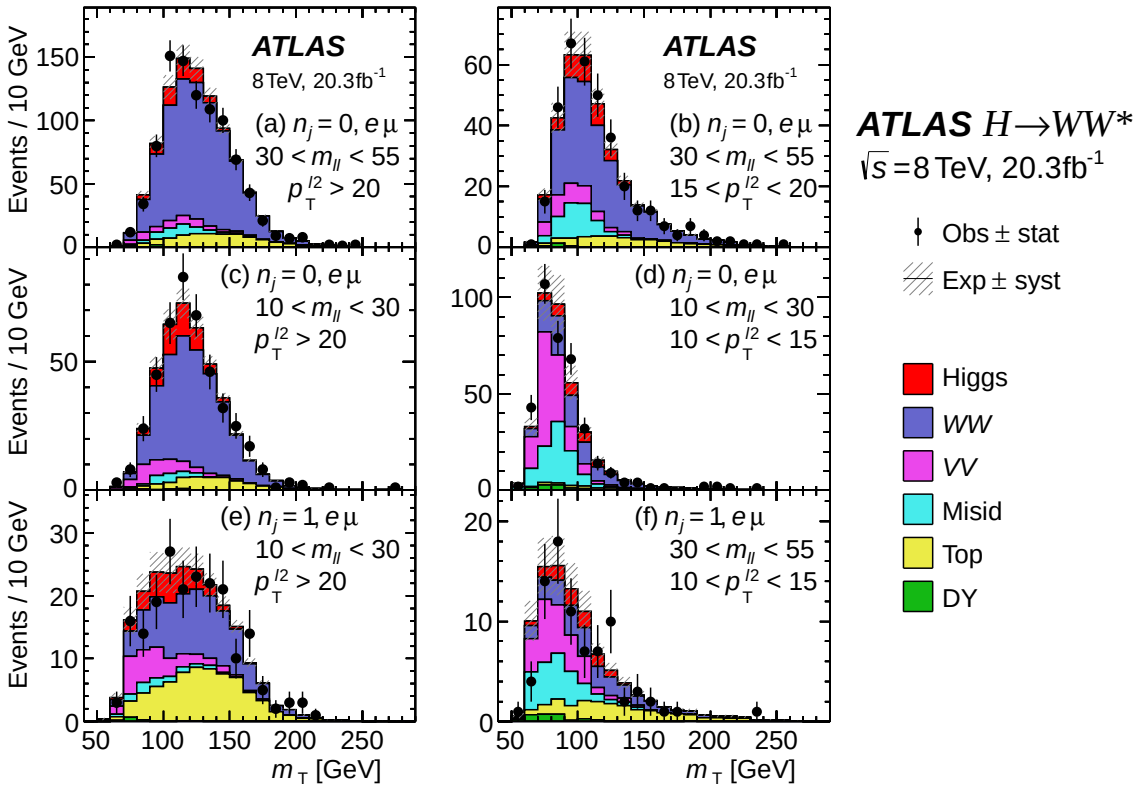

Figure 6.29: Post-fit transverse mass distributions in the DF $n_j \leq 1$ categories in the 8 TeV data analysis, for specific $m_{\ell\ell}$ and $p_{\mathrm{T}}^{\ell 2}$ ranges. The plots are made after applying all the selection requirements (see Tables 6.11 and 6.12). The signal processes are scaled with the observed signal strength μ from the fit to all the regions and the background normalization include the post-fit β values and effects from the pulls of the nuisance parameters.

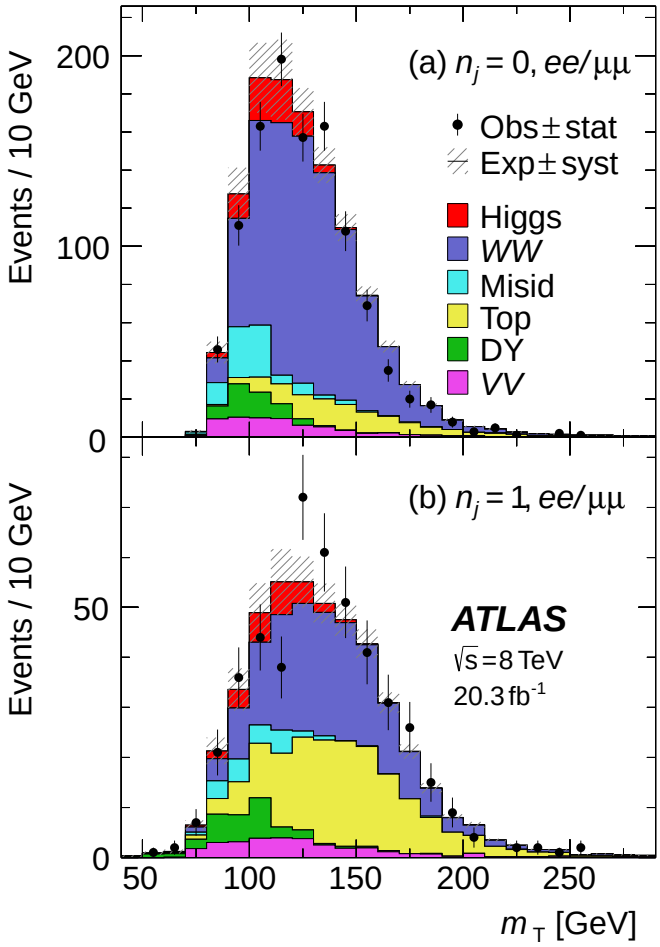

Figure 6.30: Post-fit transverse mass distributions in the $n_j \leq 1$, SF categories in the 8 TeV analysis.

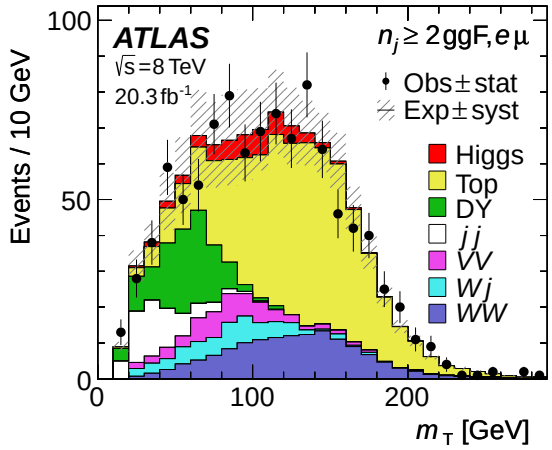

Figure 6.31: Post-fit transverse mass distribution in the $n_j \geq 2$ ggF-enriched category in the 8 TeV analysis.

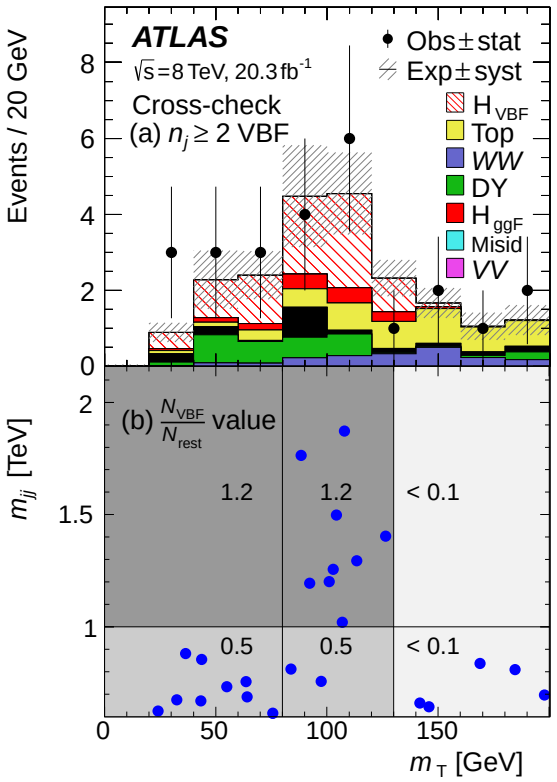

Figure 6.32: Post-fit distributions in the cross-check analysis in the $e\mu + ee/\mu\mu$ $n_j \geq 2$ VBF-enriched category in the 8 TeV data analysis: (a) m_{T} and (b) m_{jj} versus m_{T} scatter plot for data. For each bin in (b), the ratio $N_{\mathrm{VBF}}/N_{\mathrm{rest}}$ is stated in the plot, where N_{rest} includes all processes other than the VBF signal.

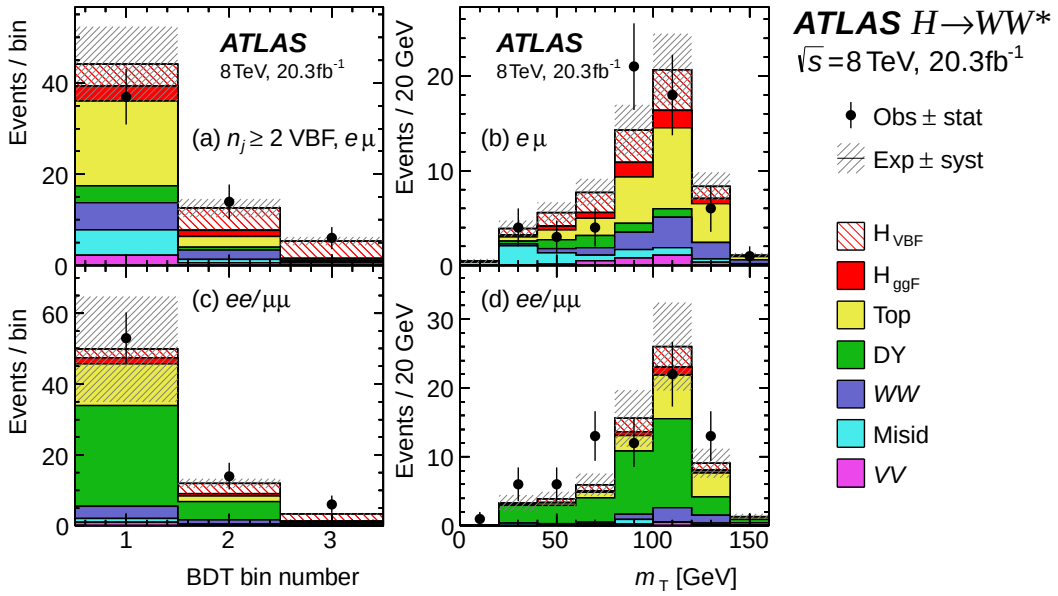

Figure 6.33: Post-fit BDT and transverse mass distributions in the $n_j \geq 2$ VBF-enriched category in the 8 TeV data analysis: (a) BDT output in DF, (b) m_{T} in DF, (c) BDT output in SF, and (d) m_{T} in SF. For (b) and (d), the three BDT bins are combined.

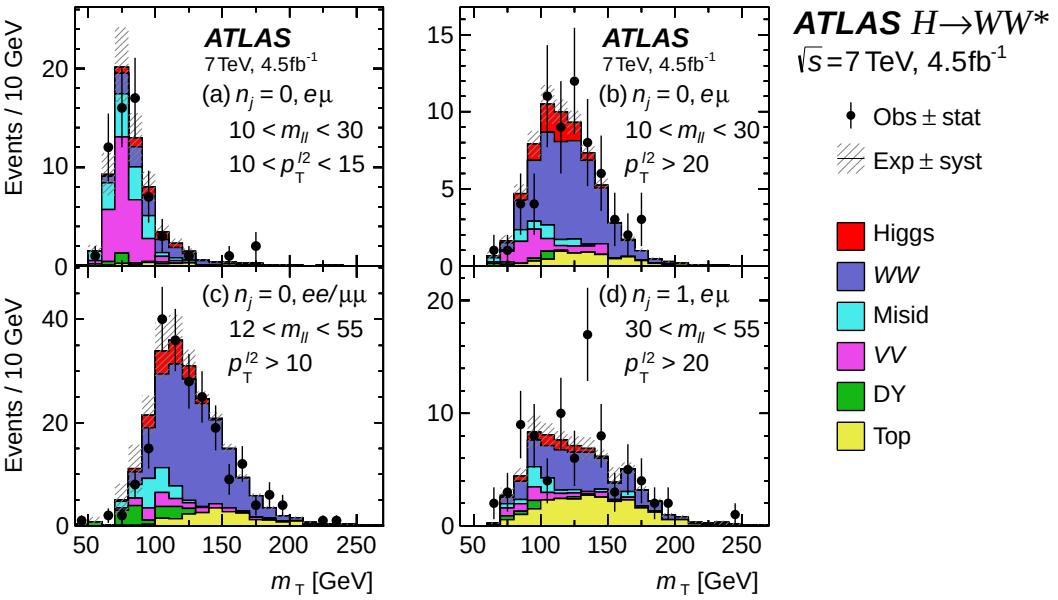

Figure 6.34: Post-fit transverse mass distributions in the $n_j \leq 1$ categories in the 7 TeV data analysis, for specific $m_{\ell\ell}$ and $p_{\mathrm{T}}^{\ell 2}$ ranges. The plots are made after applying all the selection requirements.

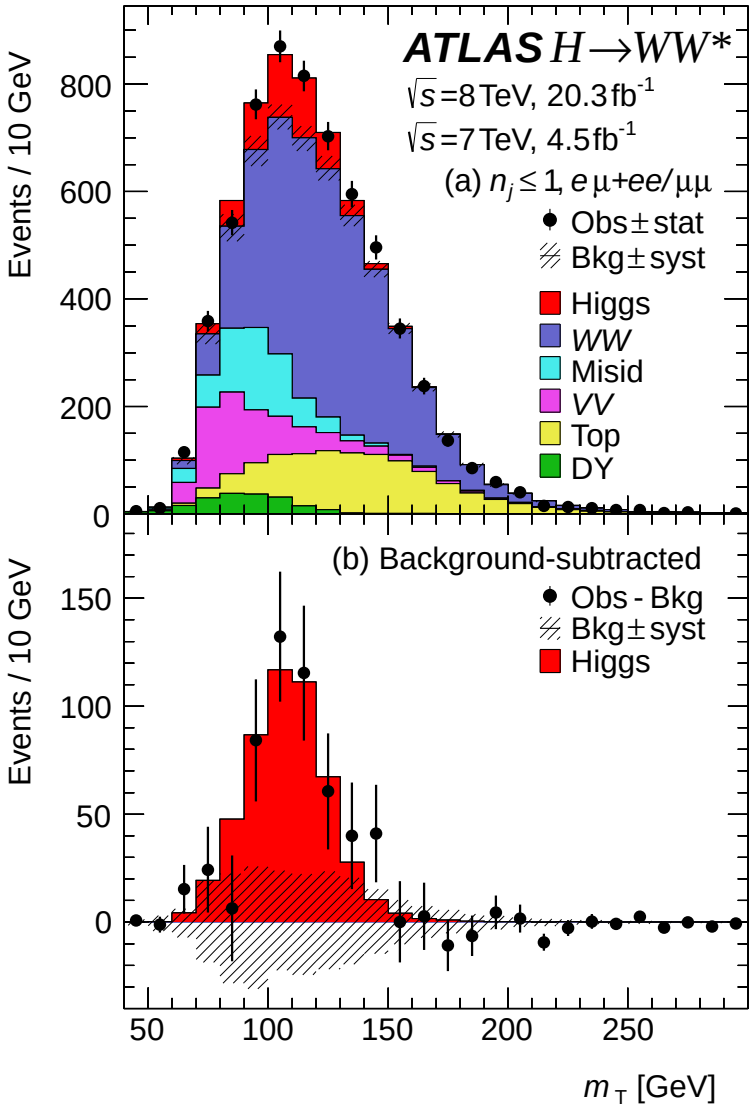

Figure 6.35: Post-fit of combined m_{T} distributions for $n_j \leq 1$ and for all lepton compositions in the 7 and 8 TeV data analyses. The plot (b) shows the residuals of the data with respect to the estimated background compared to the expected distribution for an SM Higgs boson with $m_H = 125$ GeV; the error bars on the data are statistical ($\sqrt{N_{\mathrm{obs}}}$). The uncertainty on the background (shown as the shaded band around 0) is at most about 25 events per m_{T} bin and partially correlated between bins. Background processes are scaled by post-fit normalization factors and the signal processes by the observed signal strength μ from the likelihood fit to all regions. Their normalizations also include effects from the pulls of the nuisance parameters.

CHAPTER 7

Results

All sub-analyses with the 7 and the 8 TeV datasets are combined and the results are extracted at the mass $m_H = 125.36 \pm 0.41$ GeV corresponding to the measured Higgs boson mass in the ATLAS detector using the $ZZ \to 4\ell$ and $\gamma\gamma$ decay modes [12]. The Likelihood ($\mathcal{L}$) fit is used to test the model. In this chapter, the results of $H \to WW^* \to \ell\nu\ell\nu$ analysis are presented as well as the SM Higgs compatibility.

7.1 Observation of the SM Higgs Boson

Numerical evidence of the Higgs boson from the $H \to WW^* \to \ell\nu\ell\nu$ channel is obtained from the exclusion limit plot and the local p_0 plot. The SM Higgs boson compatibility can be verified with the measurement of the signal strength, μ. In this study, the resolution focuses on the low mass SM Higgs. Before the Higgs boson discovery in 2012, the CL_S exclusion test was used over a lager mass range to find the Higgs boson. Even after the discovery, it is used for the further confirmation of the result. From the exclusion plot in Fig 7.1 (top), any observation or expectation that is below the limit $\mu = 1$ (solid blue line) would exclude a SM Higgs boson at a particular mass. Thus, in the absence of signal, we expect to exclude a Higgs with $m_H > 114$ GeV (dashed black line). With observed data, the range is changed to above 132 GeV which agrees to the result of the Higgs mass measurement done with $ZZ \to 4\ell$ and $\gamma\gamma$ decay channels at the Higgs mass $m_H = 125.36$ GeV. The p_0 tests the probability that the background only model can fluctuate to produce any excess as mimicking the signal observation in data. The tested Higgs mass is 125.36 GeV for each mass point. From the bottom plot of Fig 7.1, the minimum

p_0 is around $m_H \approx 130\,\text{GeV}$. This probability can be converted in terms of the standard deviation which is the local significance (Z_0). The corresponding Z_0 is 6.1 standard deviation (σ) at the Higgs mass $m_H = 125.36\,\text{GeV}$. Based on the 5σ rule (see section 5.2), this is considered as a discovery of the Higgs particle in the $H \to WW^* \to \ell\nu\ell\nu$ channel. The granularity in this plot is 5 GeV, thus, the actual measurement of the mass can be differ from 130 GeV with $\pm 5\,\text{GeV}$ uncertainty range.

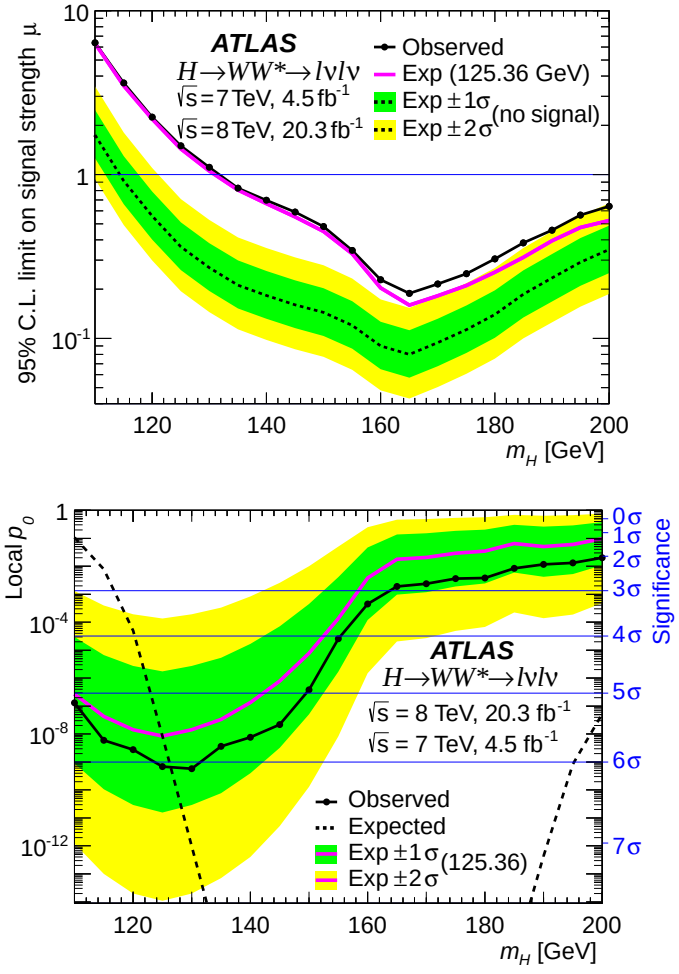

Figure 7.1: CL_S exclusion plot for $110 \le m_H \le 200\,\text{GeV}$ (top). The observed values are shown as a solid line with points where the limit is evaluated. Local p_0 as a function of m_H (bottom). The observed values are shown as a solid line with points where p_0 is evaluated.

In order to verify that the observed Higgs boson is compatible to the SM Higgs boson, the observed best fit of the signal strength ($\hat{\mu}$) should be in good agreement with the SM Higgs model value: $\hat{\mu} = 1$ means an excess consistent with a SM Higgs; $\hat{\mu} = 0$ means no excess is observed, while $\hat{\mu}$ that differs significantly from 1 or 0 means an excess is observed that is inconsistent with a SM Higgs boson. The $\hat{\mu}$ as a function of m_H is compatible with $\hat{\mu} = 1$ around 125 GeV area and it reaches very close to zero around the $m_H > 160\,\text{GeV}$ as shown in Fig 7.2. The behavior of the $\hat{\mu}$ plot is inversely proportional with the branching ratio ($\sigma \cdot \mathcal{B}$) of $H \to WW^*$ as it increases until $m_H \approx 160\,\text{GeV}$ and saturates after that.

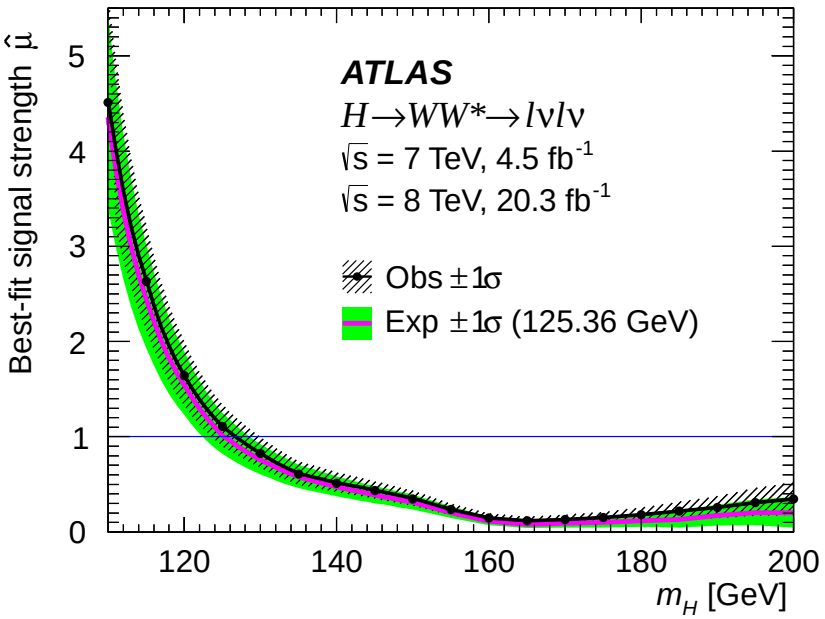

Figure 7.2: Best-fit signal strength $\hat{\mu}$ as a function of m_H. The observed values are shown as a solid line with points where $\hat{\mu}$ is evaluated. The expected values for $m_H = 125.36\,\text{GeV}$ are shown as a solid line without points. The dashed and shaded (solid) bands represent the one standard deviation uncertainties for the observed (expected) values.

The two-dimensional $\mathcal{L}$ with respect to m_H and μ is shown in Fig 7.3. In the top figure, the minimum point of the observation, which is represented by the black cross, is at 128 GeV with $\hat{\mu} = 0.94$. The result of $\hat{\mu}$ is consistent within one sigma of the SM Higgs model. $\hat{\mu} = 1$ and the mass lies in the tolerable accordance range to the Higgs mass measured by $H \to ZZ \to 4\ell$ and $H \to \gamma\gamma$ final state channels. The granularity of m_H in this plot is 1 GeV.

The signal strength ($\hat{\mu}$) in this figure has a dependency on $\sigma \cdot \mathcal{B}$, where $\mathcal{B}$ is the branching ratio of the Higgs decay and σ is the cross section. Removing these influences in calculation of $\hat{\mu}$ do not effect on the result of the minimum but the overall plot tendencies are changed. The bottom left plot shows contours of the negative log likelihood ratio as a function of m_H and $b = (\sigma \cdot \mathcal{B})_{\text{obs}}/(\sigma_{\text{SM}} \cdot \mathcal{B}_{128})$. $\mathcal{B}$ is canceled on each sides, thus, the signal strength μ is left with dependency of σ. The contour size is much smaller and less correlated between b and m_H (than between μ and m_H). A slightly positive slope can be observed due to the cross section dependency as it increases as a function of m_H. The bottom right plot shows the result after removing the impact of σ and $\mathcal{B}$ as seen in the definition on the y-axis : $S = (\sigma \cdot \mathcal{B})_{\text{obs}}/(\sigma_{125.36} \cdot \mathcal{B}_{125.36})$. Therefore, the result shows the signal strength μ as a function of m_H with no impact of the branching fraction and the cross section. The slope of the plot goes a bit negative because the likelihood calculation is now proportional to the signal selection efficiency of m_H. The acceptance also contributes to this behavior. The colored areas correspond up to 3 σ range.

7.2 The Evidence of VBF Higgs Production

One of the achievements in this $H \to WW^* \to \ell\nu\ell\nu$ analysis is getting an observation level of the significance in the $n_j \geq 2$, a VBF-enriched signal region (SR). Unlike the ggF study done with the cut based method, a BDT MVA method is used for the VBF analysis.

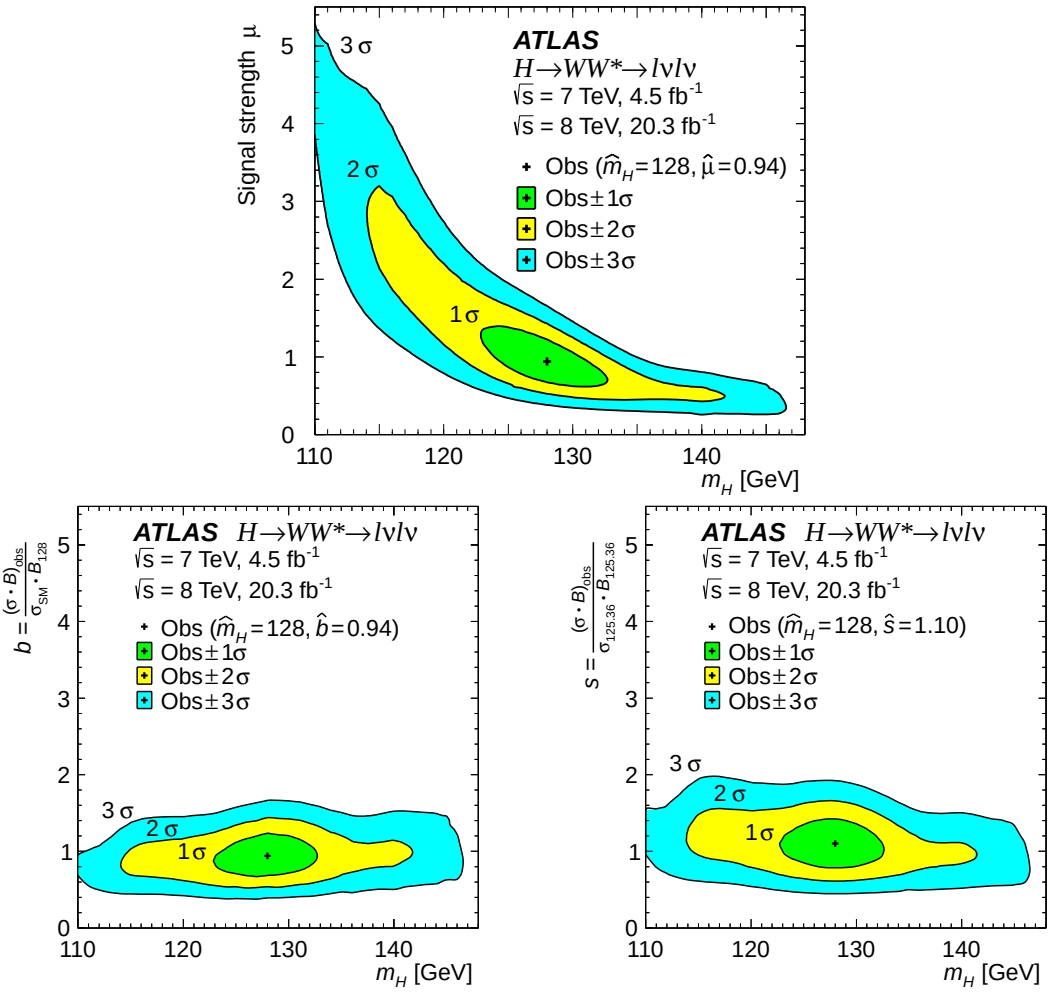

Figure 7.3: Observed signal strength μ as a function of m_H as evaluated by the likelihood fit. The shaded areas represent the one, two, and three standard deviation contours with respect to the best fit values $\hat{m}_H$ and $\hat{\mu}$. The top plot represents the regular calculation that includes of the branching fraction ($\mathcal{B}$) and the cross section (σ) while the bottom two remove the influences from them, removing $\mathcal{B}$ (bottom left) and removing both impacts, $\mathcal{B}$ and σ (bottom right).

Since the ggF contribution is still significant in the VBF SR, the ggF signal has to be profiled when the VBF significance is measured, meanwhile, the global significance is fixed. Fig 7.4 shows the ratio $\mu_{\text{VBF}}/\mu_{\text{ggF}}$ plot at the Higgs mass $m_H = 125.36$ GeV along with μ_{ggF} and μ_{VBF} plots at the bottom.

The μ_{VBF}/μ_{ggF} is introduced as a new parameter of interest (POI) in the calculation and the result is :

$$\frac{\mu_{VBF}}{\mu_{ggF}} = 1.26\,^{+0.61}_{-0.45}\,(\text{stat.})\,^{+0.50}_{-0.26}\,(\text{syst.}) = 1.26\,^{+0.79}_{-0.53}. \tag{7.1}$$

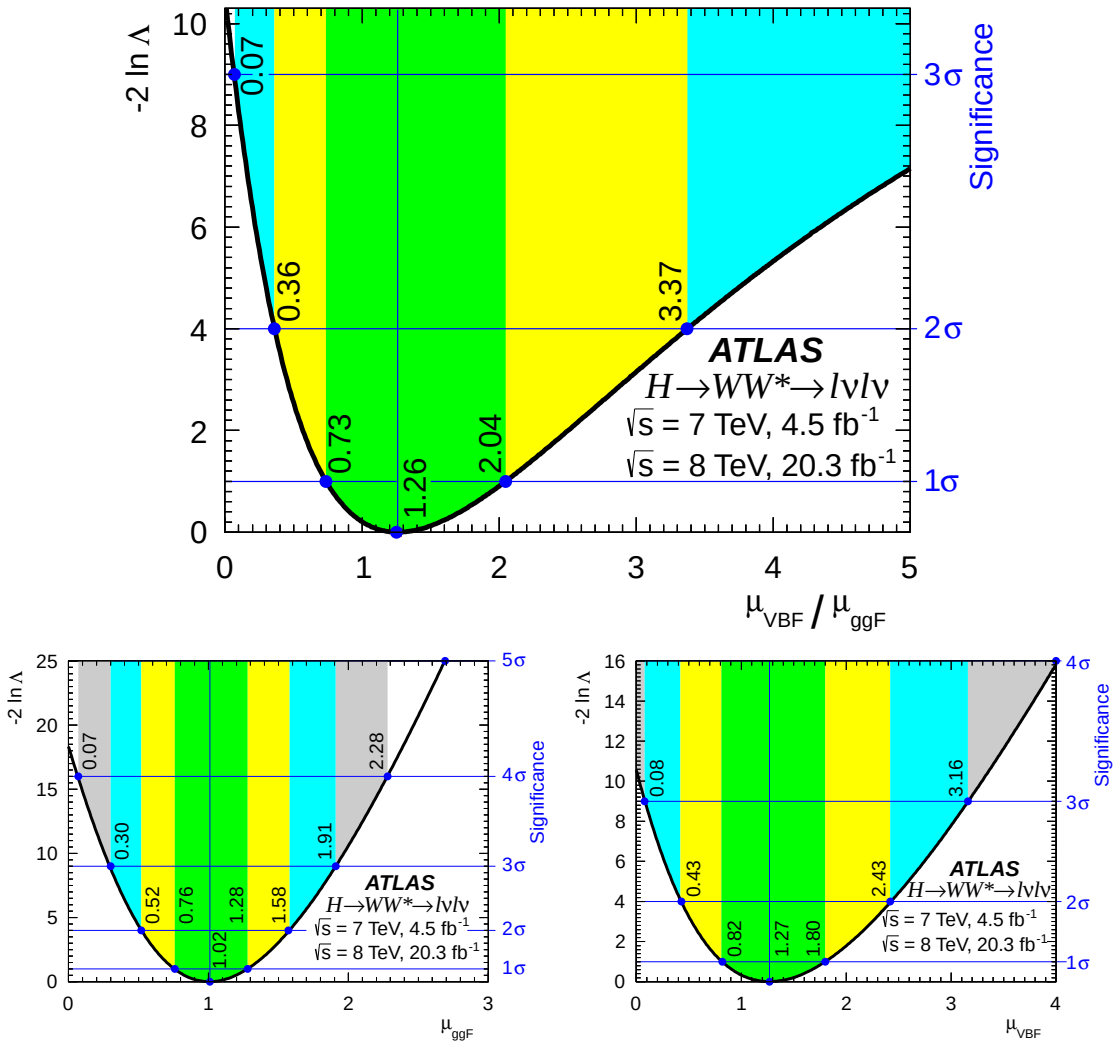

Figure 7.4: Likelihood scan of a function of μ_{VBF}/μ_{ggF} (top), μ_{ggF} (bottom left) and μ_{VBF} (bottom right). The colored area represents the standard deviation uncertainty around the central value represented by the vertical line. For the top plot, a new parameter of interest, μ_{VBF}/μ_{ggF},has been introduced in the calculation. For the bottom plots, μ_{ggF} is profiled when μ_{VBF} is calculated and vice versa.

which is a ratio between the signal strength of the VBF production mode over the one for the ggF production mode.

This agrees to the results of the individual production modes that are shown at the bottom figures of Fig. 7.4. The likelihood lies above 3 σ at $\mu_{\mathrm{VBF}}/\mu_{\mathrm{ggF}} = 0$ in the top figure of Fig. 7.4. This is the equivalent to the result that $\mu_{\mathrm{VBF}} = 0$ hypothesis testing on p-value returns more than 3 σ (3.2 standard deviations (σ)), as shown in the bottom left of Fig. 7.4. This is the evidence of the existence of the Higgs particle for the VBF production in $H \to WW^* \to \ell\nu\ell\nu$. The VBF results can be improved as the LHC takes more data in the coming years.

7.3 Signal strength μ

As already mentioned in the chapter 5, the signal strength (μ) is one of the indicators that characterizes whether the observed particle is the SM Higgs boson or not. This SM Higgs compatibility check can be done not only at the combination level of the analysis but also at the level of sub-analysis. The nominal Higgs mass m_H is 125.36 GeV to match with other ATLAS Higgs studies. The combined μ including all categories is :

$$\begin{aligned}
\mu &= 1.09 \ {}^{+0.16}_{-0.15}\,(\text{stat.}) \ {}^{+0.08}_{-0.07}\left(\begin{matrix}\text{expt.}\\ \text{syst.}\end{matrix}\right) \ {}^{+0.15}_{-0.12}\left(\begin{matrix}\text{theo.}\\ \text{syst.}\end{matrix}\right) \ \pm 0.03\left(\begin{matrix}\text{lumi.}\\ \text{syst.}\end{matrix}\right) \\
&= 1.09 \ {}^{+0.16}_{-0.15}\,(\text{stat.}) \ {}^{+0.17}_{-0.14}\,(\text{syst.}) \\
&= 1.09 \ {}^{+0.23}_{-0.21}.
\end{aligned} \tag{7.2}$$

while the expected value is $1\ {}^{+0.16}_{-0.15}\,(\text{stat.})\ {}^{+0.17}_{-0.13}\,(\text{syst.})$. The individual results by the production modes, the ggF and the VBF, are :

$$\begin{aligned} \mu_{\mathrm{ggF}} &= 1.02 \pm 0.19 \,{}^{+0.22}_{-0.18} = 1.02 \,{}^{+0.29}_{-0.26} \\ \mu_{\mathrm{VBF}} &= 1.27 \,{}^{+0.44}_{-0.40} \,{}^{+0.30}_{-0.21} = 1.27 \,{}^{+0.53}_{-0.45}. \end{aligned} \tag{7.3}$$

(stat.) (syst.)

with split uncertainties based on their sources. The statistical uncertainty is simply from the number of events in the SR while the control regions (CR) are profiled. However, the statistical uncertainties from MC samples, from non-profiled CR in Table 6.32, and from fake-factors for the W+jets background are treated as the experimental uncertainty. The theoretical uncertainties include the acceptance and the cross section uncertainties, the normalization uncertainty and the extrapolation factor uncertainty besides W+jets. Separate measurements of the ggF and the VBF are done as the each other signals are profiled while they are measured to avoid the contamination from each other signals. For example, μ_{VBF} is measured while μ_{ggF} is treated as a background (profiled) and vice versa. The VH signal is included in the VBF. Therefore, the terms of μ_{VBF} takes the VH production into account. The 2-dimensional likelihood of the signal strength of the ggF and the VBF is seen in Fig 7.5. The dashed red contours are the expected values. As seen in the figure, the minimum of the observation is consistent with the SM model, represented with the empty circle at (1, 1). Table 7.1 summarizes the result of the study with detail uncertainties for μ, μ_{ggF}, and μ_{VBF} .

Table 7.2 summarizes the significance and the signal strength measurements in all categories. The strongest signal source is $n_j = 0$ in the $e\mu$ (DF) channel followed by the VBF in the DF category. The $ee/\mu\mu$ (SF) analyses, in general, tends to have a weaker significance than the DF analyses due to the low statistics in the signal region. Among the SF analyses, the VBF in the SF category has a significantly high value compared with other SF categories. The results of the signal strengths mostly agree to the SM Higgs model in the DF analysis.

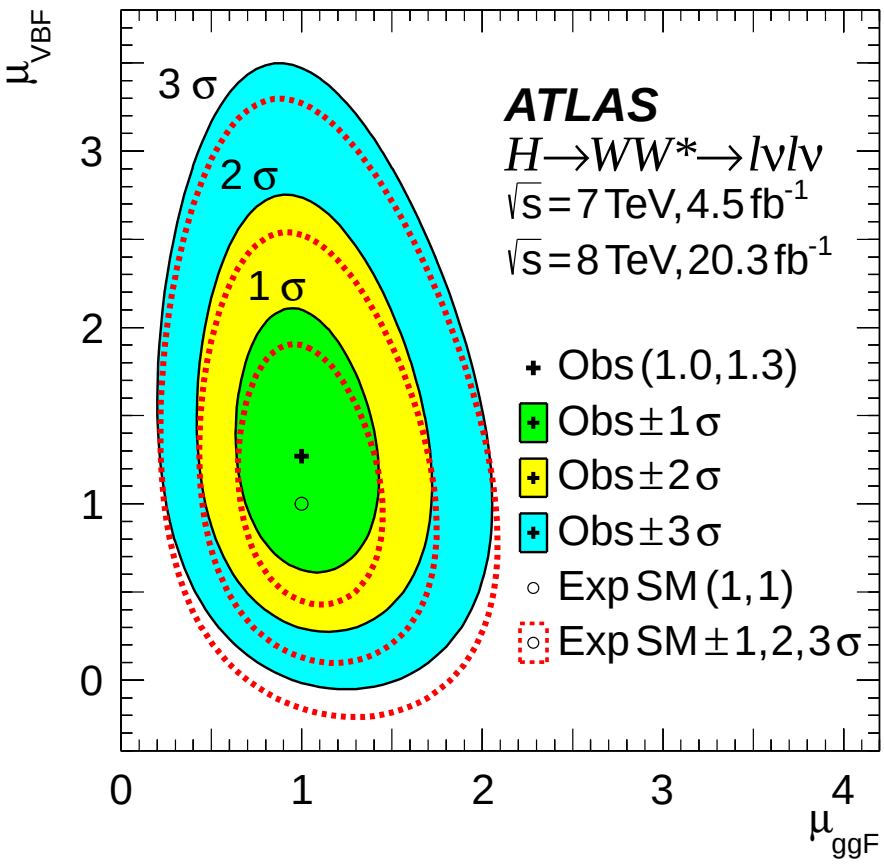

Figure 7.5: Likelihood scan as a function of μ_{ggF} and μ_{VBF}. The best-fit observed (expected SM) value is represented by the cross symbol (open circle) and its one, two, and three standard deviation contours are shown by solid lines surrounding the filled areas (dotted lines). The *x*- and *y*-axis scales are the same to visually highlight the relative sensitivity.

Table 7.1: Summary of uncertainties on the signal strength μ (left) as well as μ_{ggF} (middle) and μ_{VBF} (right). The "profiled signal region" indicates the contribution of the uncertainty on the ggF signal yield to the μ_{VBF} measurement and vice versa. The measured values are done at $m_H = 125.36\,\text{GeV}$.

Source	Observed $\mu = 1.09$			Observed $\mu_{ggF} = 1.02$			Observed $\mu_{VBF} = 1.27$		
	Error +	Error −	Plot of error (scaled by 100)	Error +	Error −	Plot of error (scaled by 100)	Error +	Error −	Plot of error (scaled by 100)
Data statistics	0.16	0.15		0.19	0.19		0.44	0.40	
Signal regions	0.12	0.12		0.14	0.14		0.38	0.35	
Profiled control regions	0.10	0.10		0.12	0.12		0.21	0.18	
Profiled signal regions	-	-	-	0.03	0.03		0.09	0.08	
MC statistics	0.04	0.04		0.06	0.06		0.05	0.05	
Theoretical systematics	0.15	0.12		0.19	0.16		0.22	0.15	
Signal $H \to WW^* \mathcal{B}$	0.05	0.04		0.05	0.03		0.07	0.04	
Signal ggF cross section	0.09	0.07		0.13	0.09		0.03	0.03	
Signal ggF acceptance	0.05	0.04		0.06	0.05		0.07	0.07	
Signal VBF cross section	0.01	0.01		-	-	-	0.07	0.04	
Signal VBF acceptance	0.02	0.01		-	-	-	0.15	0.08	
Background WW	0.06	0.06		0.08	0.08		0.07	0.07	
Background top quark	0.03	0.03		0.04	0.04		0.06	0.06	
Background misid. factor	0.05	0.05		0.06	0.06		0.02	0.02	
Others	0.02	0.02		0.02	0.02		0.03	0.03	
Experimental systematics	0.07	0.06		0.08	0.08		0.18	0.14	
Background misid. factor	0.03	0.03		0.04	0.04		0.02	0.01	
Bkg. $Z/\gamma^* \to ee, \mu\mu$	0.02	0.02		0.03	0.03		0.01	0.01	
Muons and electrons	0.04	0.04		0.05	0.04		0.03	0.02	
Missing transv. momentum	0.02	0.02		0.02	0.01		0.05	0.05	
Jets	0.03	0.02		0.03	0.03		0.15	0.11	
Others	0.03	0.02		0.03	0.03		0.06	0.06	
Integrated luminosity	0.03	0.03		0.03	0.02		0.05	0.03	
Total	0.23	0.21		0.29	0.26		0.53	0.45	
			-30 -15 0 15 30			-30 -15 0 15 30			-60 -30 0 30 60

Table 7.2: Signal significance Z_0 and signal strength μ.

Sample	Signal significance			Expected		Observed uncertainty						Observed central value	
				Tot. err.		Tot. err.		Stat. err.		Syst. err.			
	Exp. Z_0	Obs. Z_0	Bar graph of observed Z_0	+	−	+	−	+	−	+	−	μ_{obs}	μ_{obs} ± stat. (thick) ± total (thin)
$n_j = 0$	3.70	4.08		0.35	0.30	0.37	0.32	0.22	0.22	0.30	0.23	1.15	
$e\mu$, $\ell_2 = \mu$	2.89	3.07		0.41	0.36	0.43	0.38	0.30	0.29	0.32	0.24	1.08	
$e\mu$, $\ell_2 = e$	2.36	3.12		0.49	0.44	0.54	0.48	0.38	0.37	0.39	0.30	1.40	
$ee/\mu\mu$ category	1.43	0.71		0.74	0.70	0.68	0.66	0.45	0.44	0.51	0.50	0.47	
$n_j = 1$	2.60	2.49		0.51	0.41	0.50	0.41	0.33	0.32	0.38	0.26	0.96	
$e\mu$ category	2.56	2.83		0.51	0.42	0.56	0.45	0.35	0.35	0.43	0.29	1.16	
$ee/\mu\mu$ category	1.02	0.21		1.12	0.98	1.02	0.97	0.80	0.76	0.63	0.61	0.19	
$n_j \geq 2$, ggF, $e\mu$	1.21	1.44		0.96	0.83	0.91	0.84	0.70	0.68	0.70	0.49	1.20	
$n_j \geq 2$, VBF-enr.	3.38	3.84		0.42	0.36	0.45	0.38	0.36	0.33	0.27	0.19	1.20	
$e\mu$ category	3.01	3.02		0.48	0.40	0.47	0.39	0.40	0.35	0.24	0.16	0.98	
$ee/\mu\mu$ category	1.58	2.96		0.84	0.67	0.97	0.78	0.83	0.71	0.51	0.33	1.98	
All n_j, all signal	5.76	6.06		0.23	0.20	0.23	0.21	0.16	0.15	0.17	0.14	1.09	
ggF as signal	4.34	4.28		0.30	0.24	0.29	0.26	0.19	0.19	0.22	0.18	1.02	
VBF as signal	2.67	3.24		0.50	0.43	0.53	0.45	0.44	0.40	0.30	0.21	1.27	

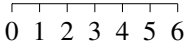

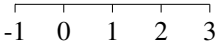

7.4 Higgs Coupling Measurement

In order to verify whether the observed Higgs boson corresponds to the SM Higgs model, its properties should be measured. The spin and the coupling are typical properties to show the compatibility to the SM Higgs. Here, the coupling of the observed Higgs particle is measured. The LHC Higgs cross section working group has suggested an interim framework for such studies in this reference [74], therefore, the process of the coupling measurement follows this guideline. The testing is performed under the assumption of $m_H = 125.36$ GeV.

The ggF production cross section is proportional to κ_F^2 through the top-quark or bottom-quark loops at the production vertex, and the VBF production cross section is proportional to κ_V^2. The branching fraction $\mathcal{B}_{H\to WW^*}$ is proportional to κ_V^2 and inversely proportional to a linear combination of κ_F^2 and κ_V^2. The denominator corresponds to the total decay width in terms of the fermionic and bosonic decay amplitudes [74]. Therefore, the formulae are

$$\begin{aligned} \mu_{\mathrm{ggF}} &\propto \frac{\kappa_F^2 \cdot \kappa_V^2}{(\mathcal{B}_{H\to f\bar{f}} + \mathcal{B}_{H\to gg})\,\kappa_F^2 + (\mathcal{B}_{H\to VV})\,\kappa_V^2} \\ \mu_{\mathrm{VBF}} &\propto \frac{\kappa_V^4}{(\mathcal{B}_{H\to f\bar{f}} + \mathcal{B}_{H\to gg})\,\kappa_F^2 + (\mathcal{B}_{H\to VV})\,\kappa_V^2}. \end{aligned} \tag{7.4}$$

The small contribution from $\mathcal{B}_{H\to\gamma\gamma}$ depends on both κ_F and κ_V and is not explicitly shown. $\mathcal{B}_{H\to f\bar{f}} + \mathcal{B}_{H\to gg}$ is given as ≈ 0.75 and limited by $\kappa_F^2 > 1/3\kappa_V^2$. Therefore, μ_{ggF} does not depend on κ_F^2 but only the κ_V^2 dependency is left over. Meanwhile, only μ_{VBF} is sensitive to κ_F^2. Thereby, the relative coupling strengths to fermions is extracted only from μ_{VBF}. The 2-dimensional likelihood scan of those two coupling strengths is showed in Fig 7.6 for both the observed and the expected. The best fit values of the measured relative coupling strengths are:

$$\begin{aligned} \kappa_F &= 0.93 \;{}^{+0.24}_{-0.18}\;{}^{+0.21}_{-0.14} = 0.93 \;{}^{+0.32}_{-0.23} \\ \kappa_V &= 1.04 \;{}^{+0.07}_{-0.08}\;{}^{+0.07}_{-0.08} = 1.04 \;\pm 0.11. \end{aligned} \tag{7.5}$$

(stat.) (syst.)

As seen in Fig 7.6, the uncertainty of κ_V is smaller than the one for κ_F. Since κ_F is governed by μ_{VBF}, the effects of the VBF rapidly decrease when $\kappa_F \gg \kappa_V$. Thus, this leads the result that leaves the 3 σ contour open and the resolution of κ_F is broad. The recommended framework for the coupling study $\mu_{\mathrm{VBF}} = 0$ excludes $\kappa_F \gg \kappa_V$.

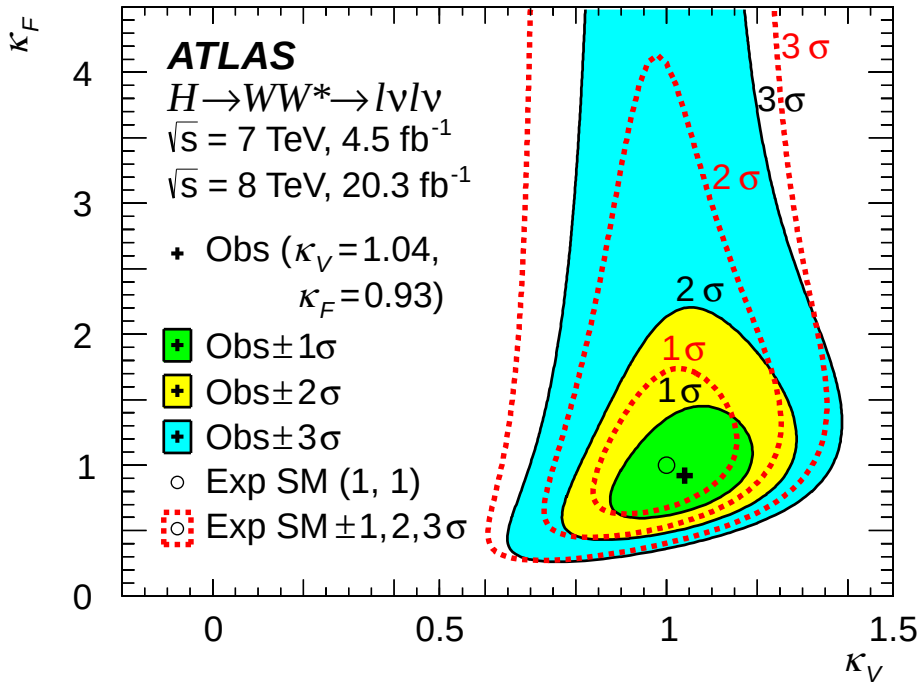

Figure 7.6: Likelihood scan as a function of κ_V and κ_F. The best-fit observed (expected SM) value is represented by the cross symbol (open circle) and its one, two, and three standard deviation contours are shown by solid lines surrounding the filled areas (dotted lines).

Their correlation is $\rho = 0.47$ where the correlation is derived from the co-variance matrix constructed from the second-order mixed partial derivatives of the likelihood, evaluated at the best-fit values of κ_F and κ_V.

7.5 Cross Section Measurement

The measured signal strengths are used to calculate $\sigma \cdot \mathcal{B}_{H \to WW^*}$. This study is categorized by the production modes and the center of mass energy. The uncertainty treatments are different with the nominal study as those of QCD, PDF and the branching ratio are fixed at the nominal values.

Inclusive Cross Section

The equation used for the inclusive cross section measurement is :

$$\begin{aligned} (\sigma \cdot \mathcal{B}_{H \to WW^*})_{\text{obs}} &= \frac{(N_{\text{sig}})_{\text{obs}}}{\mathcal{A} \cdot C \cdot \mathcal{B}_{WW \to \ell\nu\ell\nu}} \cdot \frac{1}{\int L \, \mathrm{d}t} \\ &= \hat{\mu} \cdot (\sigma \cdot \mathcal{B}_{H \to WW^*})_{\text{exp}}. \end{aligned} \tag{7.6}$$

where $\mathcal{A}$ is the kinematic and geometric acceptance, C is a correction factor that indicates the ratio of the number of measured events with respect to the number of events produced in the fiducial phase space of the detector. Thus, the actual acceptance is the product of these two, $\mathcal{A} \times C$. Therefore, in this measurement, the $\hat{\mu}$ is the measured signal strength with the specific uncertainty treatment condition described previously. There are three different cases, the 7 and the 8 TeV in the ggF and the 8 TeV in the VBF. Due to the lack of statistics, 7 TeV in VBF study was not performed. The results are following.

$$
\begin{aligned}
\mu_{ggF}^{7TeV} &= 0.57 \quad {}^{+0.52}_{-0.51} \quad {}^{+0.36}_{-0.34} \quad {}^{+0.14}_{-0.004} \\
\mu_{ggF}^{8TeV} &= 1.09 \quad \pm 0.20 \quad {}^{+0.19}_{-0.17} \quad {}^{+0.14}_{-0.09} \\
\mu_{VBF}^{8TeV} &= 1.45 \quad {}^{+0.48}_{-0.44} \quad {}^{+0.38}_{-0.24} \quad {}^{+0.11}_{-0.06} \\
&\qquad\qquad (\text{stat.}) \quad (\text{syst.}) \quad (\text{sig.})
\end{aligned}
\tag{7.7}
$$

And the corresponding cross sections measurement results are:

$$
\begin{aligned}
\sigma_{ggF}^{7TeV} \cdot \mathcal{B}_{H\to WW^*} &= 2.0 \quad \pm 1.7 \quad {}^{+1.2}_{-1.1} \quad = 2.0 \quad {}^{+2.1}_{-2.0} \quad \text{pb} \\
\sigma_{ggF}^{8TeV} \cdot \mathcal{B}_{H\to WW^*} &= 4.6 \quad \pm 0.9 \quad {}^{+0.8}_{-0.7} \quad = 4.6 \quad {}^{+1.2}_{-1.1} \quad \text{pb} \\
\sigma_{VBF}^{8TeV} \cdot \mathcal{B}_{H\to WW^*} &= 0.51 \; {}^{+0.17}_{-0.15} \quad {}^{+0.13}_{-0.08} \quad = 0.51 \; {}^{+0.22}_{-0.17} \quad \text{pb.} \\
&\qquad\qquad (\text{stat.}) \quad (\text{syst.})
\end{aligned}
\tag{7.8}
$$

while the expected cross-section values are 3.3 ± 0.4 pb, 4.2 ± 0.5 pb, and 0.35 ± 0.02 pb, respectively.

Fiducial Cross Section

The fiducial cross section measurement requires the definition of a region with a clear understanding of the performance of the detector. This study aims to have the theoretical predictions with minimum uncertainties on the kinematics of signal and any jets in the event. Table 7.3 summarizes the requirements for the defined fiducial volume.

In the given fiducial volume, the definition of the cross section is the following :

$$
\begin{aligned}
\sigma_{\text{fid}} &= \frac{(N_{\text{sig}})_{\text{obs}}}{C} \cdot \frac{1}{\int L \, \mathrm{d}t} \\
&= \hat{\mu} \cdot (\sigma \cdot \mathcal{B}_{H\to WW^*\to e\nu\mu\nu})_{\text{exp}} \cdot \mathcal{A},
\end{aligned}
\tag{7.9}
$$

The uncertainty is smaller than the inclusive case because it does not include the signal yield extrapolation effect. The largest uncertainty is from the jet multiplicity requirements

Table 7.3: Fiducial volume definitions for fiducial cross sections.

Type	$n_j = 0$	$n_j = 1$
Preselection	$p_{\mathrm{T}}^{\ell 1} > 22$	
	$p_{\mathrm{T}}^{\ell 2} > 10$	
	Opposite charge ℓ	
	$m_{\ell\ell} > 10$	
	$p_{\mathrm{T}}^{\nu\nu} > 20$	
n_j-dependent	$\Delta\phi_{\ell\ell,\nu\nu} > \pi/2$	-
	$p_{\mathrm{T}}^{\ell\ell} > 30$	-
	-	$m_{\mathrm{T}}^{\ell} > 50$
	-	$m_{\tau\tau} < 66$
	$m_{\ell\ell} < 55$	$m_{\ell\ell} < 55$
	$\Delta\phi_{\ell\ell} < 1.8$	$\Delta\phi_{\ell\ell} < 1.8$

on the QCD scale which is totally theoretical. The correction factor C is evaluated with MC samples for $n_j = 0$ and $n_j = 1$ events. The used correction factors are

$$\begin{aligned} C_{0j}^{\mathrm{ggF}} &= 0.507 \pm 0.027 \\ C_{1j}^{\mathrm{ggF}} &= 0.506 \pm 0.022. \end{aligned} \tag{7.10}$$

The experimental systematic uncertainty is approximately 5%, and using MCs, POWHEG +HERWIG, POWHEG+PYTHIA8 and POWHEG+PYTHIA6, the theoretical uncertainties are calculated. The uncertainty from different MC tools is negligible, approximately 2%. According to the simulation, the fraction of measured signal events within the fiducial volume is 85% for $n_j = 0$ and 63% for $n_j = 1$.

Since the VBF contributions is not negligible in the ggF yield, $\mathcal{A}$ would be differed by jet multiplicities and the effect of the theoretical uncertainties on the VBF signal yield is included in the systematic uncertainties on the cross sections. Thereby the new acceptance for the study is

$$\begin{aligned} \mathcal{A}_{0j}^{\text{ggF}} &= 0.206 \pm 0.030 \\ \mathcal{A}_{1j}^{\text{ggF}} &= 0.075 \pm 0.017. \end{aligned} \tag{7.11}$$

And the signal strengths used are:

$$\begin{aligned} \mu_{0\,j,e\mu}^{\text{ggF}} &= 1.39 \quad \pm 0.27 \quad {}^{+0.21}_{-0.19} \quad {}^{+0.27}_{-0.17} \\ \mu_{1\,j,e\mu}^{\text{ggF}} &= 1.14 \quad {}^{+0.42}_{-0.41} \quad {}^{+0.27}_{-0.26} \quad {}^{+0.42}_{-0.17} \\ &\qquad\qquad \text{(stat.)} \quad \text{(syst.)} \quad \text{(sig.)} \end{aligned} \tag{7.12}$$

and the corresponding fiducial cross sections, evaluated at $m_H = 125.36$ GeV and using the 8 TeV data, are:

$$\begin{aligned} \sigma_{\text{fid},0j}^{\text{ggF}} &= 27.6 \quad {}^{+5.4}_{-5.3} \quad {}^{+4.1}_{-3.9} \quad = 27.6 \quad {}^{+6.8}_{-6.6} \text{ fb} \\ \sigma_{\text{fid},1j}^{\text{ggF}} &= 8.3 \quad {}^{+3.1}_{-3.0} \quad {}^{+2.0}_{-1.9} \quad = 8.3 \quad {}^{+3.7}_{-3.5} \text{ fb.} \\ &\qquad\qquad \text{(stat.)} \quad \text{(syst.)} \end{aligned} \tag{7.13}$$

while the expected values are 19.9 ± 3.3 fb and 7.3 ± 1.8 fb, respectively.

CHAPTER 8

Conclusions

With a good performance of the ATLAS detector, 25 fb^{-1} data were collected from 2011 to 2013 and were analyzed for the study of $H \to WW^* \to \ell\nu\ell\nu$. The results of this study are significant as the observed statistical significance (6.1σ) indicates a clear discovery.

The analysis is optimized to maximize the signal yield against the backgrounds and is divided into categories with the number of associated jets and the lepton flavor combinations, as well as the production modes.

The most sensitive channel is the ggF-enriched production mode with no associated jet in the different flavor lepton combination channel followed by the different flavor lepton combination channel in the VBF production mode. The $n_j > 2$ in ggF-enriched channel has only a different lepton flavor combination and the study for this channel is done over the events that are orthogonal to VBF events. The VBF study is significantly improved by changing the analysis method from the cut-based to the Boosted Decision Tree (BDT) method in the multi-variate analysis (MVA).

A fit was performed to reduce the expected error on the signal strength (μ). The m_{T} distribution and the O_{BDT} distribution are used for the fit procedure of the ggF and the VBF categories, respectively. After combining all results from the different sub-channels, a Higgs boson signal excess is observed in the Higgs mass range below 132 GeV. There is a clear 6.1σ observed excess at the mass $m_H = 125.36$ GeV. The compatibility check to the SM Higgs boson followed. The Higgs coupling is measured for this purpose by

utilizing the measured μ for each production modes, the ggF and the VBF. The measured signal strengths are :

$$\begin{aligned} \mu &= 1.09\ ^{+0.23}_{-0.21} \\ \mu_{\mathrm{ggF}} &= 1.02\ ^{+0.29}_{-0.26} \\ \mu_{\mathrm{VBF}} &= 1.27\ ^{+0.53}_{-0.45}. \end{aligned} \tag{8.1}$$

These results agree to the SM Higgs, where $\mu = 1$. Obtained μ_{ggF} and μ_{VBF} are used for the Higgs coupling measurement. The relative Higgs coupling strength to bosons, κ_V, and the one to fermions, κ_F, agree with the SM prediction. The measured Higgs coupling constants are :

$$\begin{aligned} \kappa_F &= 0.93\ ^{+0.24}_{-0.18}\ ^{+0.21}_{-0.14} &&= 0.93\ ^{+0.32}_{-0.23} \\ \kappa_V &= 1.04\ ^{+0.07}_{-0.08}\ ^{+0.07}_{-0.08} &&= 1.04\ \pm 0.11. \end{aligned} \tag{8.2}$$

(stat.) (syst.)

Using the signal strength μ, cross sections can also be calculated. The inclusive cross section is calculated for the ggF and the VBF production modes in the form of $\sigma \cdot \mathcal{B}$ at the different center of mass energy ($\sqrt{s}$), 7 and 8 TeV, as follows :

$$\begin{aligned} \sigma^{7\mathrm{TeV}}_{\mathrm{ggF}} \cdot \mathcal{B}_{H\to WW^*} &= 2.0\ ^{+2.1}_{-2.0}\ \mathrm{pb} \\ \sigma^{8\mathrm{TeV}}_{\mathrm{ggF}} \cdot \mathcal{B}_{H\to WW^*} &= 4.6\ ^{+1.2}_{-1.1}\ \mathrm{pb} \\ \sigma^{8\mathrm{TeV}}_{\mathrm{VBF}} \cdot \mathcal{B}_{H\to WW^*} &= 0.51\ ^{+0.22}_{-0.17}\ \mathrm{pb}. \end{aligned} \tag{8.3}$$

The fiducial cross sections are also calculated in the exclusive $n_j = 0$ and $n_j = 1$ categories, where the uncertainty can be minimized. The obtained values are :

$$\sigma^{\mathrm{ggF}}_{\mathrm{fid},0j} = 27.6\ ^{+5.4}_{-5.3}\ ^{+4.1}_{-3.9} = 27.6\ ^{+6.8}_{-6.6}\ \mathrm{fb}$$
$$\sigma^{\mathrm{ggF}}_{\mathrm{fid},1j} = 8.3\ ^{+3.1}_{-3.0}\ ^{+2.0}_{-1.9} = 8.3\ ^{+3.7}_{-3.5}\ \mathrm{fb}. \quad (8.4)$$

(stat.) (syst.)

The LHC starts new runs in 2015 with higher $\sqrt{s}$ and is expected to collect up to $100\,\mathrm{fb}^{-1}$ of data, as seen in Fig 8.1. Thus, a significant improvement is expected in the $H \to WW^* \to \ell\nu\ell\nu$ analysis, in particular for the Higgs property study. With increased amount of data, the signal strengths can be measured with smaller uncertainty [77]. Noticeable improvement also awaits in the Higgs coupling measurements as well, especially for the κ_F thanks to higher statistics of VBF signal [78].

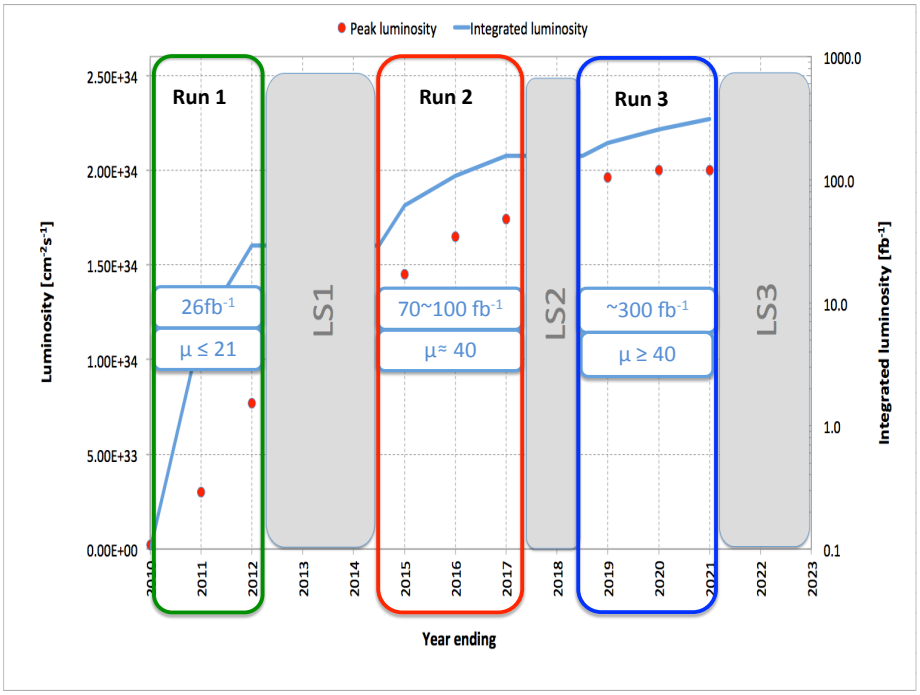

Figure 8.1: Expected luminosity performance in Run II that starts from 2015.

REFERENCES

[1] S. L. Glashow, Nucl. Phys. **22**, 579 (1961); S. Weinberg, Phys. Rev. Lett. **19**, 1264 (1967); A. Salam, in *Proceedings of the Nobel Symposium* (Stockholm, 1968), p. 367.

[2] F. Englert and R. Brout, Phys. Rev. Lett. **13**, 321 (1964); P. W. Higgs, Phys. Lett. **12**, 132 (1964); Phys. Rev. Lett. **13**, 508 (1964); G. S. Guralnik, C. R. Hagen, and T. W. B. Kibble, *ibid.* 585 (1964); P. W. Higgs, Phys. Rev. **145**, 1156 (1966); T. W. B. Kibble, *ibid.* **155**, 1554 (1967).

[3] ATLAS Collaboration, Phys. Lett. B **716**, 1 (2012); CMS Collaboration, *ibid.* 30 (2012).

[4] Lyndon Evans and Philip Bryant (editors), JINST **3**, S08001 (2008).

[5] The European Organization for Nuclear Research (CERN), http://home.web.cern.ch

[6] Glen Cowan, Statistical Data Analysis, Clarendon Press, Oxford, 1998.

[7] Louise Lyon, Statistics for Nuclear and Particke Physicists, Cambridge University Press, 1986.

[8] "Standard Model" Wikipedia: The Free Encyclopedia. Wikimedia Foundation, Inc. 4 April 2002. Web. 27 January 2015. http://en.wikipedia.org/wiki/Standard_Model

[9] J. Goldstone, Field theories with Superconductor solutions, Il Nuovo Cimento V.19, 154164 (1961)

[10] "Higgs cross sections and decay branching ratios", LHC Cross Section Working Group, CERN Report 3,
https://twiki.cern.ch/twiki/bin/view/LHCPhysics/CrossSections

[11] CMS Collaboration, Eur. Phys. J. C **74**, 3076 (2014); Phys. Rev. D **89**, 092007 (2014).

[12] ATLAS Collaboration, Phys. Rev. D **90**, 052004 (2014).

[13] "Taking a Closer Look at LHC", Xabier Cid Vidal & Ramon Cid, Santiago, SPAIN, http://www.lhc-closer.es

[14] Computer-generated diagram of an LHC dipole Schema d'un dipole du LHC, CERN, 1998, http://cds.cern.ch/record/39731

[15] LHC quadrupole cross section, CERN, 1998, http://cds.cern.ch/record/841485

[16] "Integrated luminosity summary plots for 2011-2012 data taking", Luminosity Public Results, CERN, https://twiki.cern.ch/twiki/bin/view/AtlasPublic/LuminosityPublicResults

[17] ATLAS Collaboration, JINST **3**, S08003 (2008).

[18] "MobiDick4", MobiDICK team, CERN, https://twiki.cern.ch/twiki/bin/viewauth/Atlas/MobiDick4.

[19] R. Placakyte, XXXI PHYSICS IN COLLISION, (2011).

[20] V.N. Gribov, L.N. Lipatov, Sov. J. Nucl. Phys. 15, 438, 675 (1972); L.N. Lipatov, Sov. J. Nucl. Phys. 20, 94 (1975); G. Altarelli, G. Parisi, Nucl. Phys. B126, 298 (1977); Yu. L. Dokshitzer,Sov. Phys. JETP 46, 641 (1977); G. Curci, W. Furmanski, and R. Petronzio, Nucl.Phys. B175, 27 (1980); S. Moch, J. Vermaseren, and A. Vogt, Nucl.Phys. B688, 101 (2004); A. Vogt, S. Moch, and J. Vermaseren, Nucl.Phys. B691, 129 (2004);

[21] A.D. Martin, W.J. Stirling, R.S. Thorne, G. Watt, Eur. Phys. J. C63, 189 (2009)

[22] P. M. Nadolsky et al, Phys. Rev. D78, 013004 (2008)

[23] Bo Andersson, G. Gustafson, G. Ingelman, and T. Sjostrand. Parton Fragmentation and String Dynamics. Phys.Rept., 97:31145, 1983.

[24] B.R. Webber. A QCD Model for Jet Fragmentation Including Soft Gluon Interference. Nucl.Phys., B238:492, 1984.

[25] ATLAS Collaboration, Report No. ATLAS-CONF-2012-064, http://cds.cern.ch/record/1459529.

[26] P. Bartalini et al, Multi-Parton Interactions at the LHC, http://arxiv.org/abs/1111.0469

[27] P. Nason, J. High Energy Phys. 11 (2004) 40.

[28] T. Sjöstrand, S. Mrenna, and P. Skands, J. High Energy Phys. 05 (2006) 026.

[29] T. Sjöstrand, S. Mrenna, and P. Skands, Comput. Phys. Commun. **178**, 852 (2008).

[30] G. Corcella, I. G. Knowles, G. Marchesini, S. Moretti, K. Odagiri, P. Richardson, M. H. Seymour, and B. R. Webber, J. High Energy Phys. 01 (2001) 010.

[31] J. M. Butterworth, J. R. Forshaw, and M. H. Seymour, Z. Phys. C **72**, 637 (1996).

[32] T. Gleisberg, S. Höche, F. Krauss, M. Schönherr, S. Schumann, F. Siegert, and J. Winter, J. High Energy Phys. 02 (2009) 007.

[33] M. L. Mangano, F. Piccinini, A. D. Polosa, M. Moretti, and R. Pittau, J. High Energy Phys. 07 (2003) 001.

[34] B. P. Kersevan and E. Richter-Was, Comput. Phys. Commun. **184**, 919 (2013).

[35] N. Kauer, J. High Energy Phys. 12 (2013) 082.

[36] S. Agostinelli *et al.* (GEANT4 Collaboration), Nucl. Instr. Meth. A**506**, 250 (2003).

[37] ATLAS Collaboration, Eur. Phys. J. C **70**, 823 (2010).

[38] ATLAS Collaboration, Report No. ATLAS-PHYS-PUB-2010-013, http://cds.cern.ch/record/1300517.

[39] E Barberio, et al, Journal of Physics: Conference Series 119 (2008) 032008, 2008

[40] Wolfgang Lukas, Journal of Physics: Conference Series 396 (2012) 022031, 2012

[41] P. F. Akesson et al., ATLAS Tracking Event Data Model, Report No. ATL-SOFT-PUB-2006-004, http://cds.cern.ch/record/973401

[42] ATLAS Collaboration, Eur. Phys. J. C **72**, 1909 (2012).

[43] ATLAS Collaboration, Report No. ATLAS-CONF-2012-047, http://cds.cern.ch/record/1449796.

[44] ATLAS Collaboration, Report No. ATLAS-CONF-2014-032, http://cds.cern.ch/record/1706245

[45] ATLAS Collaboration, Phys. Lett. B **726**, 88 (2013); *ibid.* **734**, 406 (2014).

[46] ATLAS Collaboration, Report No. ATLAS-CONF-2014-032, http://cds.cern.ch/record/1706245.

[47] Particle Data group (PDG) pocket book (2012)

[48] ATLAS Collaboration, Eur. Phys. J. C **74**, 3130 (2014).

[49] N. J. Hadley. Cone algorithm for jet finding. D note 904, November 1989.

[50] Matteo Cacciari, Gavin P. Salam, Gregory Soyez, J. High Energy Phys. (4),JHEP04(2008)063 (2008)

[51] M. Cacciari and G. Salam, Phys. Lett. B **641**, 57 (2006); M. Cacciari, G. Salam, and G. Soyez, J. High Energy Phys. 04 (2008) 063.

[52] ATLAS Collaboration, Report No. CERN-PH-EP-2013-222, arXiv:1406.0076.

[53] ATLAS Collaboration, Report No. ATLAS-CONF-2013-083, http://cds.cern.ch/record/1570994.

[54] ATLAS Collaboration, Report No. ATLAS-CONF-2011-102, http://cds.cern.ch/record/1369219.

[55] ATLAS Collaboration, Eur. Phys. J. C **72**, 1844 (2012).

[56] G. Cowan, K. Cranmer, E. Gross, and O. Vitells, Eur. Phys. J. C **71**, 1554 (2011).

[57] A. L. Read, J. Phys. **G28**, 2693 (2002).

[58] L. Breiman, J. Friedman, R. Olshen, and C. Stone, *Classification and Regression Trees* (Chapman and Hall, New York, 1984); Y. Freund and R. E. Schapire, J. Com-

put. Syst. Sci. **55**, 119 (1997); J. Friedman, Comput. Stat. Data Anal. **38**, 267 (2002).

[59] C. Nelson, Phys. Rev. D **37**, 1220 (1988); M. Dittmar and H. Dreiner, Phys. Rev. D **55**, 167 (1997).

[60] H.-L. Lai, M. Guzzi, J. Huston, Z. Li, P. M. Nadolsky, J. Pumplin, and C.-P. Yuan, Phys. Rev. D **82**, 074024 (2010).

[61] A. D. Martin, W. J. Stirling, R. S. Thorne, and G. Watt, Eur. Phys. J. C **63**, 189 (2009).

[62] R. D. Ball *et al.* (NNPDF Collaboration), Nucl. Phys. **B867**, 244 (2012).

[63] A. Bierweiler, T. Kasprzik, and J. H. Kühn, J. High Energy Phys. 12 (2013) 071.

[64] H.-C. Cheng and Z. Han, J. High Energy Phys. 12 (2008) 063.

[65] J. Pumplin, D. R. Stump, J. Huston, H.-L. Lai, P. M. Nadolsky, and W.-K. Tung, J. High Energy Phys. 07 (2002) 012.

[66] A. Sherstnev and R. S. Thorne, Eur. Phys. J. C **55**, 553 (2009).

[67] ATLAS Collaboration, Report No. ATLAS-CONF-2014-046, http://cds.cern.ch/record/1741020.

[68] ATLAS Collaboration, Report No. ATLAS-CONF-2012-158, http://cds.cern.ch/record/1493601.

[69] R. K. Ellis, I. Hinchliffe, M. Soldate, and J. J. Van der Bij, Nucl. Phys. **B297**, 221 (1988); T. Plehn, D. Rainwater, and D. Zeppenfeld, Phys. Rev. D **61**, 093005 (2000); ATLAS Collaboration, Report No. CERN-OPEN-2008-020, p. 1280, arXiv:0901.0512.

[70] A. J. Barr, B. Gripaios, and C. G. Lester, J. High Energy Phys. 07 (2009) 072.

[71] V. Barger, R. J. N. Phillips, and D. Zeppenfeld, Phys. Lett. B **346**, 106 (1995).

[72] ATLAS Collaboration, Report No. ATLAS-CONF-2015-005, http://cds.cern.ch/record/2002123.

[73] D. Rainwater and D. Zeppenfeld, Phys. Rev. D **60**, 113004 (1999)

[74] S. Heinemeyer *et al.* (LHC Higgs Cross Section Working Group), Report No. CERN-2013-004, arXiv:1307.1347.

[75] ATLAS Collaboration, Eur. Phys. J. C **73**, 2518 (2013).

[76] LHC Higgs Cross Section Working Group, Report No. LHCHXSWG-2012-001, 2012, http://arxiv.org/pdf/1209.0040.pdf

[77] Chelstowska, M, Schaefer, D, Long, J, Valencic, N, Arnaez, O, $H \rightarrow WW^*$ ingredients for the 2013 ECFA studies, ATL-COM-PHYS-2013-1289, https://cds.cern.ch/record/1598896

[78] H. Kim, Report No. ATLAS Physics workshop - Ready for Run-2, https://indico.cern.ch/event/301300/session/13/contribution/90/material/slides/0.pdf

BIOGRAPHICAL STATEMENT

Hee Yeun Kim was born in South Korea, in 1976. She received her B.S. and M.S. degree from Dongguk University, Korea, in 1998 and 2000, respectively, and Ph.D. degrees from The University of Texas at Arlington in 2015, all in Physics. From 2000 to 2001, she worked in Korea Institute of Science and Technology (KIST) as research scientist in the Microelectromechanical systems (MEMS) lab. From 2001, she joined the Intelligent Microsystem Center of KIST as a technical advisor for the overal project. Since she started a career in the High Energy Physics, she performed researche at the European Organization for Nuclear Research (CERN) with A Torodial LHC Apparatus (ATLAS), one of the major experiments of the Large Hadron Collider (LHC) after building her acdemic career at the UTA for 2 year. She contributed the Higgs study, particulary the mesurment of the Higgs coupling strengths in $H \to WW^* \to \ell\nu\ell\nu$ channel. She is a member of APS and an active member of ATLAS.